Quarterly Reviews of Biophysics **34**, 2 (2001), pp. 105–267. © 2001 Cambridge University Press
DOI: 10.1017/S0033583501003687 Printed in the United Kingdom

Intermolecular forces in biology

Deborah Leckband[1] and Jacob Israelachvili[2]

[1] Department of Chemical Engineering, and the Center for Biophysics and Computational Biology, University of Illinois, Urbana-Champaign, Illinois 61801, USA
[2] Department of Chemical Engineering, and Materials Department, University of California, Santa Barbara, California 93106, USA

0. Abbreviations 106

1. Introduction: overview of forces in biology 108
- 1.1 Subtleties of biological forces and interactions 108
- 1.2 Specific and non-specific forces and interactions 113
- 1.3 van der Waals (VDW) forces 114
- 1.4 Electrostatic and 'double-layer' forces (DLVO theory) 122
  - 1.4.1 Electrostatic and double-layer interactions at very small separation 126
- 1.5 Hydration and hydrophobic forces (structural forces in water) 131
- 1.6 Steric, bridging and depletion forces (polymer-mediated and tethering forces) 137
- 1.7 Thermal fluctuation forces: entropic protrusion and undulation forces 142
- 1.8 Comparison of the magnitudes of the major non-specific forces 146
- 1.9 Bio-recognition 146
- 1.10 Equilibrium and non-equilibrium forces and interactions 150
  - 1.10.1 Multiple bonds in parallel 153
  - 1.10.2 Multiple bonds in series 155

2. Experimental techniques for measuring forces between biological molecules and surfaces 156
- 2.1 Different force-measuring techniques 156
- 2.2 Measuring forces between surfaces 161
- 2.3 Measuring force–distance functions, *F(D)* 161
- 2.4 Relating the forces between different geometries: the 'Derjaguin Approximation' 162
- 2.5 Adhesion forces and energies 164
  - 2.5.1 An example of the application of adhesion mechanics of biological adhesion 166
- 2.6 Measuring forces between macroscopic surfaces: the surface forces apparatus (SFA) 167
- 2.7 The atomic force microscope (AFM) and microfiber cantilever (MC) techniques 173
- 2.8 Micropipette aspiration (MPA) and the bioforce probe (BFP) 177
- 2.9 Osmotic stress (OS) and osmotic pressure (OP) techniques 179
- 2.10 Optical trapping and the optical tweezers (OT) 181
- 2.11 Other optical microscopy techniques: TIRM and RICM 184
- 2.12 Shear flow detachment (SFD) measurements 187
- 2.13 Cell locomotion on elastically deformable substrates 189

3. Measurements of equilibrium (time-independent) interactions 191
- 3.1 Long-range VDW and electrostatic forces (the two DVLO forces) between biosurfaces 191
- 3.2 Repulsive short-range steric–hydration forces 197
- 3.3 Adhesion forces due to VDW forces and electrostatic complementarity 200

https://doi.org/10.1017/S0033583501003687 Published online by Cambridge University Press

3.4 Attractive forces between surfaces due to hydrophobic interactions: membrane adhesion and fusion 209
3.4.1 Hydrophobic interactions at the nano- and sub-molecular levels 211
3.4.2 Hydrophobic interactions and membrane fusion 212
3.5 Attractive depletion forces 213
3.6 Solvation (hydration) forces in water: forces associated with water structure 215
3.7 Forces between 'soft-supported' membranes and proteins 218
3.8 Equilibrium energies between biological surfaces 219

4. Non-equilibrium and time-dependent interactions: sequential events that evolve in space and time 221
4.1 Equilibrium and non-equilibrium time-dependent interactions 221
4.2 Adhesion energy hysteresis 223
4.3 Dynamic forces between biomolecules and biomolecular aggregates 226
4.3.1 Strengths of isolated, noncovalent bonds 227
4.3.2 The strengths of isolated bonds depend on the activation energy for unbinding 229
4.4 Simulations of forced chemical transformations 232
4.5 Forced extensions of biological macromolecules 235
4.6 Force-induced *versus* thermally induced chemical transformations 239
4.7 The rupture of bonds in series and in parallel 242
4.7.1 Bonds in series 242
4.7.2 Bonds in parallel 244
4.8 Dynamic interactions between membrane surfaces 246
4.8.1 Lateral mobility on membrane surfaces 246
4.8.2 Intersurface forces depend on the rate of approach and separation 249
4.9 Concluding remarks 253

5. Acknowledgements 255

6. References 255

0. Abbreviations

AChR	acetylcholine receptor
AFM	atomic force microscope
BFP	bioforce probe
CD2	cell surface adhesion protein
CPK®	space-filling atomic models
De	Deborah number
DGDG	di-glucosyl diglyceride
DHP	di-hexadecyl phosphate
DL	double layer
DLPC	di-lauryl phosphatidyl choline
DLVO	Derjaguin–Landau–Verwey–Overbeek
DMPC	di-meristoly phosphatidyl choline
DMPG	di-meristoly phosphatidyl glycerol

https://doi.org/10.1017/S0033583501003687 Published online by Cambridge University Press

DNA	deoxyribonucleic acid
DPPC	di-palmitoyl phosphatidyl choline
DPPE	di-palmitoyl phosphatidyl ethanolamine
DPPG	di-palmitoyl phosphatidyl glycerol
DSPE	di-steroyl phosphatidyl ethanolamine
DSPG	di-steroyl phosphatidyl glycerol
Fab′	antigen binding fragment of an antibody molecule
FECO	fringes of equal chromatic order
FFM	friction force microscope
GCMC	Grand Canonical Monte Carlo (computer simulation)
HMG	high mobility group
IEP (pI)	isoelectric point (pH at the IEP)
ICAM	intercellular adhesion molecule 1
Ig	immunoglobulin
JKR	Johnson–Kendall–Roberts
LCT	lower critical temperature
LFA3	lymphocyte antigen 3
LFM	lateral force microscope
LR	ligand–receptor
MARCKS	myristoylated alanine rich C kinase substrate
MC	micro-cantilever (force measuring technique)
MC	Monte Carlo (computer simulation)
MD	molecular dynamics (computer simulation)
MHC	major histocompatibility complex
MGDG	monogalactosyl diglyceride
MPA	micropipette aspiration
OP	osmotic pressure
OS	osmotic stress
OT	optical tweezers
PB	Poisson–Boltzmann (equation)
PC	phosphatidyl choline
PE	phosphatidyl ethanolamine
PEG	polyethylene glycol
PEI	polyethylene imine
PEO	polyethylene oxide
PG	physophatidyl glycerol
PMF	potential of mean force
PMMA	polymethyl methacrylate
PSD	position sensitive detector
PTFE	polytetrafluoro ethylene (Teflon)
PVC	polyvinyl chloride
pzc	point of zero charge
QCM	quartz crystal microbalance
R_F	Flory radius
R_g	radius of gyration
RBC	red blood cell

https://doi.org/10.1017/S0033583501003687 Published online by Cambridge University Press

RICM	reflection interference contrast microscopy
RL	receptor–ligand
SFA	surface forces apparatus
SFD	shear flow detachment
SMD	steered molecular dynamics
SNARE	receptors for intracellular membrane fusion (SNAp REceptor)
SOPC	stearoyl oleoyl phosphatidyl choline
SPM	scanning probe microscope
STM	scanning tunneling microscope
TIRM	total internal reflection microscopy
UCT	upper critical temperature
VDW	van der Waals
WLC	worm like chain (model)

I. Introduction: overview of forces in biology

1.1 Subtleties of biological forces and interactions

While the intermolecular forces between biological molecules are no different from those that arise between any other types of molecules, a 'biological interaction' is usually very different from a simple chemical reaction or physical change of a system. This is due in part to the higher complexity of biological macromolecules and systems that typically exhibit a hierarchy of self-assembling structures ranging in size from proteins to membranes and cells, to tissues and organs, and finally to whole organisms. Moreover, interactions do not occur in a linear, stepwise fashion, but involve competing interactions, branching pathways, feedback loops, and regulatory mechanisms.

In addition, biological interactions are essentially 'dynamic' rather than 'static': biological systems are never at thermodynamic equilibrium, and are not, rigorously speaking, closed systems. While it may be common to investigate processes in isolation, *in vivo* they are coupled to other reactions or interactions that control the many biological processes, which together maintain the organism. A 'complete' biological interaction, even if such a concept could be clearly defined, would involve a sequence of tightly orchestrated events, whose effects propagate out in both space and time in a regulated manner.

The events shown in Fig. 1, associated with electrical signal transduction at the synaptic junction between neurons, clearly illustrates these principles. This is a classic example of how the interactions between membranes or biomolecules vary in space and in time in a coordinated fashion to effect precisely controlled, highly directional electrical signal propagation. In a resting neuron, the voltage across the presynaptic membrane is constant, and the voltage-sensitive sodium channels are closed (Fig. 1(*a*)). A balance between energy-dependent ion pumping and passive ion leakage through pores in the membrane generates the steady-state transmembrane ion distribution and the voltage drop across the membrane (resting potential). However, a suprathreshold change in the membrane potential (Fig. 1(*A*)) stimulates the directional propagation of a transient, highly localized reversal of the membrane potential along the presynaptic neuron. The resulting large, local change in the electrostatic field induces a transient conformational change in the voltage-sensitive channels.

https://doi.org/10.1017/S0033583501003687 Published online by Cambridge University Press

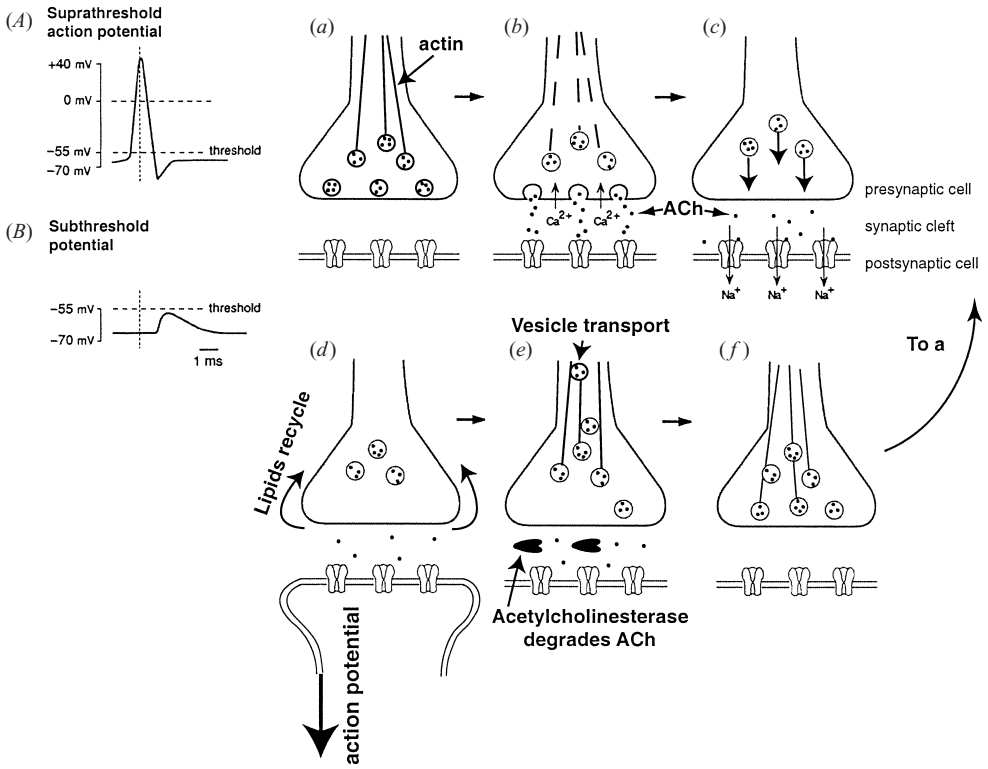


Fig. 1. Sequence of changing interactions during synaptic transmission. At the synaptic junction, a suprathreshold action potential (*A*) opens ion channels in the presynaptic membrane (*a*). This allows calcium ions to enter the cell, triggers synaptic vesicle fusion with the membrane, and releases the vesicle contents (ACh) into the synaptic cleft (*b*). The released acetylcholine binds receptors on the postsynaptic cell membrane (*c*) and induces an action potential (*A*) in the postsynaptic cell (*d*). A subthreshold membrane depolarization (*B*) will fail to stimulate this response in the postsynaptic cell. Lipid recycling (*d*), acetylcholinesterase degradation of residual acetylcholine (*e*) and reassembly of synaptic vesicles ($e \rightarrow f$) restore the system to its initial resting state (*a*).

The channels undergo a conformational change and open (Fig. 1 (*b*)). This locally reverses the membrane potential. Above a certain potential change, the channels become inactivated and relax back to their initial state.

At the synapse, voltage-sensitive calcium channels also open (Fig. 1 (*b*)) and calcium enters the cell. Synaptic vesicles are stockpiled near the presynaptic membrane, and may be organized by the actin cytoskeleton. Calcium triggers the dissolution of the actin mesh and lowers the repulsive energy barrier between the vesicles and the presynaptic membrane. This transforms the repulsion between them into an attraction. The released vesicles diffuse to the membrane, and fusion proteins both dock the vesicles and induce membrane fusion. The fusion releases neurotransmitter into the synaptic cleft (Fig. 1 (*b*)). The neurotransmitter (acetylcholine) diffuses across the narrow intercellular gap and binds to ligand-activated channels (acetylcholine receptor, AChR) on the postsynaptic membrane (Fig. 1 (*c*)). Neurotransmitter binding induces a conformational change in the AChR, which opens and triggers a local change in the membrane potential (Fig. 1 (*c*)). If this potential change exceeds the threshold potential (Fig. 1 (*A*)), it will trigger an identical sequence of events in the

https://doi.org/10.1017/S0033583501003687 Published online by Cambridge University Press

postsynaptic cell (Fig. 1(*d*)). If it is subthreshold (Fig. 1(*B*)), there will be no further electrical transmission.

A variety of mechanisms rapidly restore the presynaptic cell to the resting state: acetylcholinesterase degrades any remaining neurotransmitter in the synaptic cleft (Fig. 1(*e*)), and active mechanisms transport fresh membrane components along the actin cytoskeleton to be assembled into new synaptic vesicles (Fig. 1(*e*)). Calcium is scavenged, the cytoskeleton reassembles, fusion proteins are recycled, and synaptic vesicles are again stockpiled near the presynaptic membrane (Fig. 1(*f*)). Finally, inactive ion channels relax back to their closed state (Fig. 1(*a*)).

This precisely timed, spatially controlled, directional process results from a highly regulated sequence of molecular rearrangements and protein conformational changes arising from transient changes in the forces acting between the different membranes and proteins (including actin and ligand-gated channels) in the system. The membrane lipids, proteins, and ions, such as calcium, in the solution, mediate these forces.

This is but one example of how biological systems are poised to exploit the often subtle changes in the intermolecular or surface forces between biomolecules and biosurfaces to trigger a rapid, precisely orchestrated sequence of events. The steps shown in Fig. 1 involve time-dependent perturbations in the forces exerted on or between specific proteins, transient changes in interbilayer forces, changes in actin–vesicle interactions, receptor–ligand (RL) interactions, ligand-gated channels, and diffusion within the membranes, through the cytoplasm, or across the synaptic cleft.

Some interactions are at 'steady-state' – requiring a continuous but constant input of energy, as in biosynthetic and anabolic pathways. Determining the forces that mediate these interactions, their time-dependence, and their modulation by cellular components will provide us with a fundamental understanding of the physical basis of these interactions and the mechanisms used to execute these processes.

These forces and their time-dependent changes give rise to a rich variety of dynamic interactions characteristic of 'living systems'. Understanding the fundamental physical basis of biological interactions and the manner in which they occur hinges on our knowledge of the basic physical interactions that control them. For example, fusion proteins – such as those that mediate fusion in Fig. 1(*b*) – overcome the repulsive barriers to membrane adhesion and enable the membranes to fuse. The *dynamics* of bond breakage and reformation determine other behavior as, for example, how neutrophils roll along the vascular endothelium.

Such questions concerning the physical principles that control the mechanisms of biological association and the organization and stability of biological structures motivated the rapid development of several force-measuring techniques. These powerful tools led to an explosion in studies that revealed the fundamental mechanical properties of isolated motor proteins, the forces between biological membranes, and the molecular mechanisms that determine the strength of cell adhesion, to name only a few examples.

Here we provide a comprehensive review of the forces that mediate biological interactions, and the different force probe techniques used to investigate their ranges, magnitudes and changes over time. We discuss recent experimental and theoretical understanding of the occurrence, relative strengths, and biological manifestations of intermolecular and intersurface forces such as van der Waals and electrostatic forces, steric, hydration and hydrophobic interactions, and various 'entropy-driven' forces. Some of these forces are short-ranged and therefore determine adhesion and binding energies; others are long-ranged

https://doi.org/10.1017/S0033583501003687 Published online by Cambridge University Press

'colloidal' forces that determine steering and docking, or the equilibrium finite separation between cell membranes. We further describe their measurements in the laboratory using model systems under *in vitro* conditions, and how the results allow us to better understand the interactions that control events *in vivo*. The emphasis is on interactions at the molecular level (between proteins, lipids or biomembranes) but with illustrations of when and how these manifest themselves both at the microscopic level (of cellular organelles or whole cells) and the macroscopic level. Examples are also given that show how to calculate or estimate the strength and range of these interactions, and to identify which type of attractive or repulsive force controls a particular interaction.

The complexity of biological interactions – which often involve many different molecules or aggregate structures, occur over large distances, and evolve in time – prevents their rigorous understanding in terms of the fundamental laws of physics or even chemistry. Non-linear and non-equilibrium effects are the norm rather than the exception – a stimulus or interaction triggers a series of reactions or processes. These can involve branching pathways, feedback mechanisms, and amplification, so that the initial stimulus can effect several different outcomes. While each of these steps can be described in terms of elemental processes and associated free energy changes, the overall processes are difficult to model.

In this review we therefore attempt to convey, not only the importance of equilibrium forces, but also the essential *dynamic* nature of biological interactions. In the latter case, direct measurements are invaluable because there are as yet no rigorous physical or thermodynamic rules that quantitatively predict such behavior or its consequences. The many examples given here were chosen to illustrate the power of these relatively new experimental approaches for probing both the physical forces that control interactions in biology and the way in which they change over time.

It is worth starting by defining some of the terms that will be used. The terms *energy*, E, in units of joule (J), *force*, F, in units of newtons ($1\ \mathrm{N} = 10^5$ dyne $= 100$ gm), and *pressure*, P, in units of force/area ($1\ \mathrm{N\,m^{-2}} = 1$ pascal $= 1\ \mathrm{Pa} = 10^{-5}$ atm), will be used in the conventional sense. The *interaction potential*,[1] $E(D)$, and *force-function*, $F(D)$, are also used in the conventional sense to indicate the variation of the energy E or force F with the distance D between two molecules or surfaces. The two are related via

$$F(D) = -\mathrm{d}E(D)/\mathrm{d}D \tag{1}$$

which defines the force at a specified separation distance D as the negative of the energy gradient at D. In contrast to the specific term *force*, the looser term *interaction*, when used on its own, will mean not only the interaction energy or force between two entities, but also the overall effect that the force has on the whole system, such as any molecular configurational changes, membrane shape changes, or other subtle effects far from the interaction 'site' that can arise when two molecules or membranes come together as a consequence of an attractive force between them. Other terms involving forces and interactions, such as the difference between *non-specific* and (*bio*)*specific* interactions, will be defined as they are introduced.

Self-assembling structures will be used to denote complex nano- or micro-structures such as protein aggregates, protein–lipid membranes, and certain intracellular organelles such as vesicles, that form spontaneously from the constituent molecules in solution and that are thermodynamically stable. This does not apply to all structures, especially more complex aggregates, cells and organs. Such structures do not normally self-assemble spontaneously in

[1] Also known as the *pair potential* or *interaction energy*.

https://doi.org/10.1017/S0033583501003687 Published online by Cambridge University Press

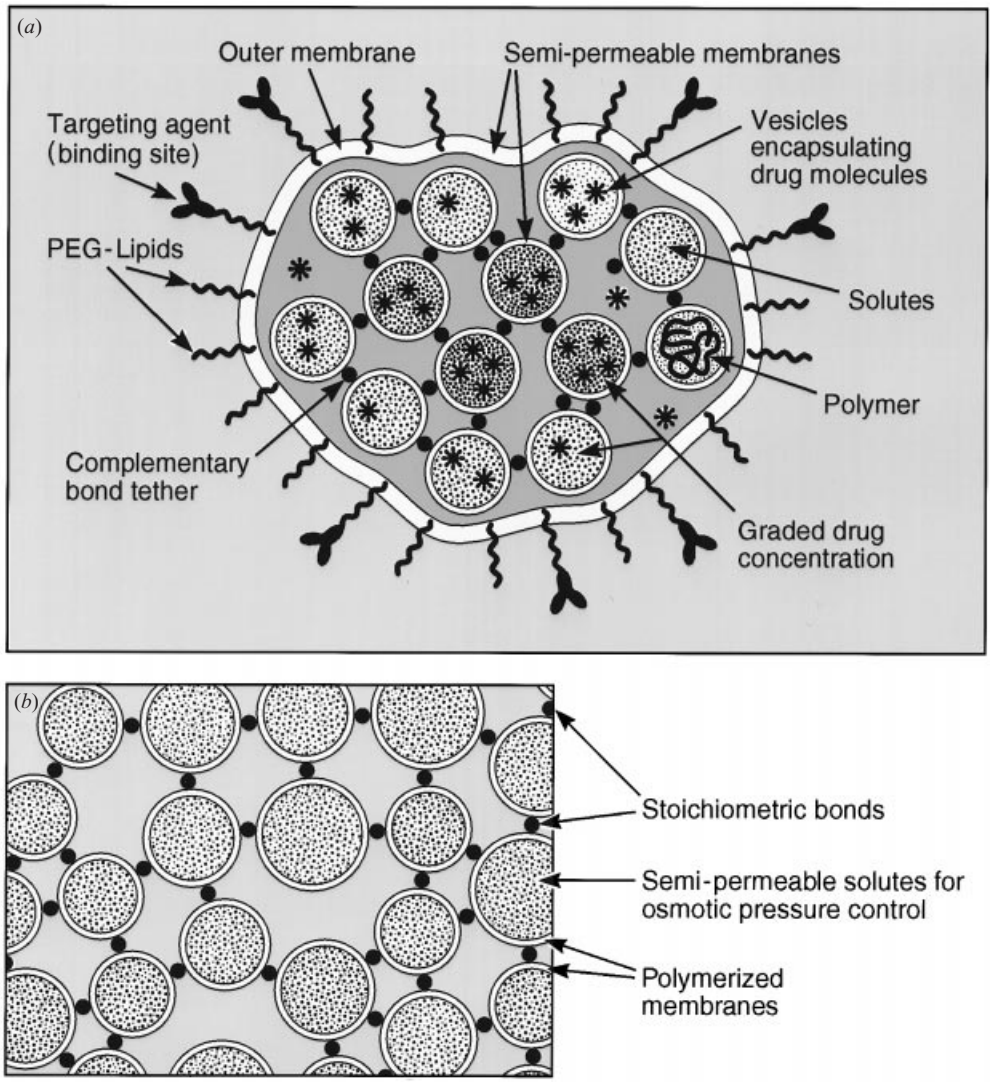


Fig. 2. Examples of bioengineered structures for drug-delivery and tissue engineering applications. (*a*) A biomimetic cell or 'vesosome' that can function as a drug- or gene-delivery vehicle. Target-specific molecules on the outer membrane surface ensure that the carrier becomes attached to a particular organ or tissue where it slowly releases a drug contained in small internal vesicles. (*b*) An adaptable biomaterial or artificial tissue, composed of vesicles held together by specific complementary bonds. Changing the osmotic balance between the internal and external compartments by light or voltage stimulation, for example, can alter the stiffness or viscoelastic properties of the material.

solution,[2] but are assembled step-by-step by energy requiring mechanisms of the cell or organ. Their maintenance also usually requires a continuous input of energy.

By using similar principles of self-assembly, it is now within our reach to artificially construct 'biomimetic' structures in the laboratory (cf. Fig. 2). This is one of the routes being taken to bioengineer new drug-delivery vehicles, artificial tissues, and new biomaterials.

[2] In the sense that one cannot simply throw all the chemical ingredients into a beaker containing the right (physiological saline) solution at the right temperature, and then wait for the biological structure to assemble spontaneously.

https://doi.org/10.1017/S0033583501003687 Published online by Cambridge University Press

Table 1. *Non-specific physical interactions*

Name/type of interaction or bond	Special features
van der Waals	A force that exists between all bodies. Usually attractive, but can be repulsive.
Electrostatic (also Coulomb, ionic, double-layer)	A force that exists only between charged molecules (ions) or surfaces. Can be attractive or repulsive.
Steric (also hard-core repulsion, structural force in liquids)	The short-range quantum-mechanical repulsive force that defines the geometry or shape of a molecule.
Thermal fluctutation (also osmotic, entropic, steric-hydration, protrusion, undulation, depletion, overlap)	A temperature-dependent force associated with the local concentration and configurational entropy of atoms or molecular groups that enhances the 'steric' repulsion. Usually repulsive.
Hydrogen bonding	A special electrostatic binding (attractive) interaction involving positively charged H atoms covalently bound to electronegative atoms. Directional.
Hydrophobic	A special attractive interaction in water between inert, non-polar molecules or surfaces.

Here, a knowledge of the pertinent forces between the constituent molecules is required if one is to successfully manipulate these forces at each stage of the assembly process.

1.2 Specific and non-specific forces and interactions

Non-specific forces are those that arise between many different types of atoms, molecules, molecular groups or surfaces, and that can usually be described in terms of a generic interaction potential or force-function. The major physical forces that fall into this category are listed in Table 1, and are described in detail in Sections 1.3–1.7.

Specific interactions arise when a unique combination of physical forces or bonds between two macromolecules act together cooperatively in space to give rise to a (usually) strong but non-covalent bond. Because such specific interactions typically arise from a synergy of multiple geometric, steric, ionic and directional bonds (see Table 1) they are also referred to as 'complementary', 'lock-and-key', 'ligand–receptor (LR)' and 'recognition' interactions.

In what follows we attempt to describe current understanding of all of the above-mentioned forces and their implications, but we restrict ourselves to 'physical' forces, i.e. those in which the interacting molecules retain their main characteristics during an interaction. Thus, we avoid consideration of covalent (chemical) bonds. That would take us into the world of biochemical reactions, which is well outside the scope of this review. However, it is important to note that physical 'bonds' can be just as strong as covalent or chemical bonds, especially in the case of ionic and complementary bonds.[3]

The strengths of the non-specific physical forces between two molecules, particles, or

[3] The term 'bond' is difficult to define and has caused much confusion. Strictly, the term bond, for example, a chemical bond such as a C–C bond, applies only to the association of atoms (not molecules) and the overlap of electron clouds, is of *short-range* ($\sim 0{\cdot}1$ nm), *stoichiometric* (associated with a coordination number or valency per atom), and is *directional* in space. Hydrogen bonds fall into this category, but van der Waals (VDW), ionic and hydrophobic bonds do not since they can arise between well-separated molecules or even large particles, and they lack directionality (or are only weakly directional).

https://doi.org/10.1017/S0033583501003687 Published online by Cambridge University Press

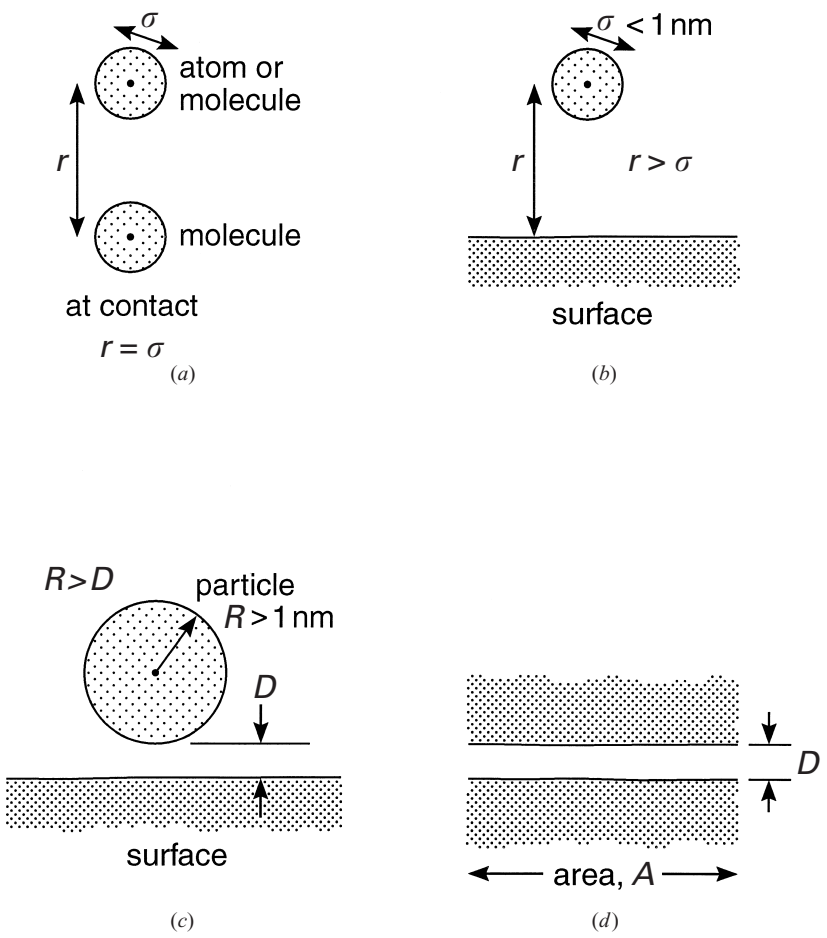


Fig. 3. Common geometries: (*a*) interacting small molecules of diameter σ, (*b*) small molecules of diameter σ, (*c*) spherical particles of radius R interacting with a plane, and (*d*) planar surfaces, close and far apart. Different generic interaction potentials $E(r)$ or $E(D)$ and force-laws $F(r)$ or $F(D)$ apply in each case depending on the type of force. The expression for the force or energy in one geometry is often related to that in another geometry by simple equations such as the 'Derjaguin Approximation' which relates the force $F(D)$ between two spherical particles of radii R_1 and R_2 to the energy per unit area $E(D)$ between two flat surfaces of the same materials at the same separation D by Eq. (32): $F(D) = 2\pi[R_1R_2/(R_1+R_2)]E(D)$. Putting $R_1 = R_2 = R$ gives the force between two identical spheres of radius R as $F(D) = \pi R E(D)$, while putting $R_2 = \infty$ gives the force between a single sphere or macromolecule of radius R and a flat surface as $F(D) = 2\pi R\ E(D)$.

extended surfaces depend on their separation D but also on their size and shape. Fig. 3 shows the more common geometries for which the non-specific interaction potentials will be described.

1.3 van der Waals (VDW) forces

VDW forces arise from the fluctuations in the electric dipole moments of molecules which become correlated as the molecules come closer together, giving rise to an attractive force (in the same way that two rotating magnets become aligned and attract each other as they

https://doi.org/10.1017/S0033583501003687 Published online by Cambridge University Press

approach). There is therefore always a VDW force between any two molecules or surfaces, which has a power-law dependence on the separation r or D that can be written as

$$E(D) = -C_{\mathrm{VDW}}/D^6$$

so that

$$F(D) = -\mathrm{d}F(D)/\mathrm{d}D = -6C_{\mathrm{VDW}}/D^7, \tag{2}$$

where the constant C_{VDW} depends on the optical properties and geometry of the interacting bodies. Table 2 lists the VDW energy and force-laws for some common geometries. This force can be attractive or repulsive, but is always attractive between similar molecules or materials. The interaction between macroscopic bodies or surfaces is generally described in terms of the Hamaker constant, A, which, for two bodies **1** interacting across a medium **2** is given by the 'Lifshitz theory' as (see Israelachvili, 1991)

$$A = \tfrac{3}{4}kT\left(\frac{\epsilon_1-\epsilon_2}{\epsilon_1+\epsilon_2}\right)^2 + \frac{3I}{16\sqrt{2}}\frac{(n_1^2-n_2^2)^2}{(n_1^2+n_2^2)^{\frac{3}{2}}}, \tag{3}$$

where ϵ_1, ϵ_2 and n_1, n_2 are the static dielectric constants and refractive indices of the two phases, I is their ionization potential, which is close to 2×10^{-18} J for most materials, and T is the temperature. For some of the classic papers on the theory and application of VDW forces see London (1937), Hamaker (1937), Lifshitz (1956) and Dzyaloshinskii *et al.* (1961). For more recent reviews see Mahanti & Ninham (1976), Hunter (1987) and Israelachvili (1991).

For non-conducting (non-metallic) solids and liquids interacting in vacuum or air ($\epsilon_2 = n_2 = 1$) their Hamaker constants are typically in the range $(5\text{–}10)\times10^{-20}$ J, while for interactions in a liquid medium such as water, the Hamaker constants are typically an order of magnitude smaller and in the range $(0{\cdot}5\text{–}1{\cdot}5)\times10^{-20}$ J. For example, $A \sim 0{\cdot}8\times10^{-20}$ J for lipid bilayers (Israelachvili, 1994), and is estimated at $A \sim (1{\cdot}0\text{–}1{\cdot}5)\times10^{-20}$ J for proteins interacting in water or salt solutions, the values being slightly lower in high salt (Marra, 1985).

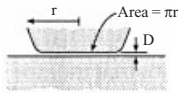
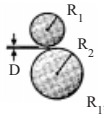
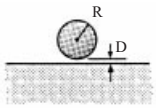
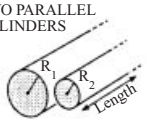
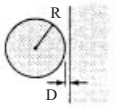
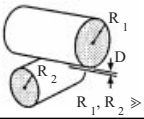
For inert non-polar surfaces, e.g. of hydrocarbons, the Lifshitz theory has been found to apply even at molecular contact, where it can predict the surface energies (or tensions) of solids and liquids. Thus, for hydrocarbon surfaces interacting in air or vacuum the Hamaker constant is typically $A = 5\times10^{-20}$ J. Inserting this value into the appropriate equation for two flat surfaces (Table 2) and using a 'cut-off' distance of $D = D_0 \approx 0{\cdot}165$ nm when the two surfaces are in contact,[4] we obtain for the surface energy γ (which is conventionally defined as half the interaction energy at contact):

$$\gamma = \frac{A}{24\pi D_0^2} \approx 24\ \mathrm{mJ\ m^{-2}}, \tag{4}$$

[4] The cut-off distance D_0 represents the effective separation between two surfaces or particles in contact. It is not a rigorously defined quantity. One expects it to be close to an atomic or molecular dimension and, indeed, values in the range 0·15–0·4 nm, when put into the appropriate equations in Table 2, usually provide good estimates of actual binding energies and adhesion forces. For the purpose of crude estimates of the strengths of interaction forces and energies, a 'universal' cut-off separation of $D_0 = 0{\cdot}165$ nm is sometimes used for macroscopic *surfaces*, and $D_0 = 0{\cdot}3\text{–}0{\cdot}4$ nm for individual *atoms* or *small molecules* (Israelachvili, 1991).

https://doi.org/10.1017/S0033583501003687 Published online by Cambridge University Press

Table 2. *VDW interaction potential $E(D)$ and force $(F = -\mathrm{d}E/\mathrm{d}D)$ between macroscopic bodies of different geometries as shown in Fig. 3*

Geometry of bodies with surfaces D apart ($D \ll R$)		van der Waals interaction*	
		Energy, E	Force, F
Two atoms or small molecules	TWO ATOMS or SMALL MOLECULES 	$-C_{VDW}/r^6$	$-6C_{VDW}/r^7$
Two flat surfaces (per unit area)	TWO FLAT SURFACES 	$E_0 = -A/12\pi D^2$	$-A/6\pi D^3$
Two spheres or macromolecules of radii R_1 and R_2	TWO SPHERES 	$\frac{-A}{6D}\left(\frac{R_1R_2}{R_1+R_2}\right)$	$\frac{-A}{6D^2}\left(\frac{R_1R_2}{R_1+R_2}\right)$ Also $F = 2\pi\left(\frac{R_1R_2}{R_1+R_2}\right)E_0$
Sphere or macromolecule of radius R near a flat surface	SPHERE ON FLAT 	$-AR/6D$	$-AR/6D^2$ Also $F = 2\pi RE_0$
Two parallel cylinders or rods of radii R_1 and R_2 (per unit length)	TWO PARALLEL CYLINDERS 	$\frac{-A}{12\sqrt{2}D^{3/2}}\left(\frac{R_1R_2}{R_1+R_2}\right)^{\frac{1}{2}}$	$\frac{-A}{8\sqrt{2}D^{5/2}}\left(\frac{R_1R_2}{R_1+R_2}\right)^{\frac{1}{2}}$
Cylinder of radius R near a flat surface (per unit length)	CYLINDER ON FLAT 	$\frac{-A\sqrt{R}}{12\sqrt{2}D^{3/2}}$	$\frac{-A\sqrt{R}}{8\sqrt{2}D^{5/2}}$
Two cylinders or filaments of radii R_1 and R_2 crossed at 90°	CROSSED CYLINDERS 	$\frac{-A\sqrt{R_1R_2}}{6D}$	$\frac{-A\sqrt{R_1R_2}}{6D^2}$ Also $F = 2\pi\sqrt{R_1R_2}E_0$

* The Hamaker constant is defined by Eq. (3). A negative force F implies attraction (A positive), a positive force means repulsion (A negative).

How to use this table: for interactions in aqueous solutions between weakly polar organic surfaces, such as two membranes or proteins, the Hamaker constant, A, is typically of order 1×10^{-20} J. For example, between two biomembranes of area 10 nm × 10 nm = 10^{-16} m^2 in contact at a separation of D = 0·25 nm in water (i.e. separated by one 'hydration' layer of water molecules), the adhesion energy E, force F, and pressure P between them will be, respectively, $E = (1 \times 10^{-20})(10^{-16})/12\pi(0{\cdot}25 \times 10^{-9})^2 = 4{\cdot}2 \times 10^{-19}$ J = 100 kT, $F = (1 \times 10^{-20})(10^{-16})/6\pi(0{\cdot}25 \times 10^{-9})^3 = 3{\cdot}4 \times 10^{-9}$ N = 3·4 nN 0·34 μg, and $P = F/\text{area} = 3{\cdot}4 \times 10^{-9}/10^{-16} = 3 \times 10^7$ N m^{-2} (Pa) = 300 atm. Other examples and comparison with experimental values are given in the main text.

https://doi.org/10.1017/S0033583501003687 Published online by Cambridge University Press

a value that is typical for hydrocarbon solids and liquids (cf. $\gamma = 27{\cdot}5$ mJ m^{-2} for hexadecane). For liquids, γ is usually referred to as the 'surface tension' and is expressed in units of force/length (N m^{-1}), which is dimensionally and numerically the same as energy/area (J m^{-2}).

The good agreement between theory and experiment using an equation that is strictly valid only for macroscopic bodies at separations larger than molecular dimensions is fortuitous: the Lifshitz theory of VDW forces assumes that matter is a structureless continuum and it should therefore not apply at the molecular level. Nevertheless, the equations of Table 2, when used with the Hamaker constants determined by Eq. (3), do appear to apply quite well even for small particles and molecules at contact separations. This allows one readily and easily to estimate the strengths of adhesion forces and binding energies, as illustrated further in the following two examples:

First, one can estimate the binding energy and adhesion or 'detachment' force between a spherical particle such as a vesicle of radius $R = 10$ nm (diameter = 20 nm) and a flat surface in water. This knowledge may be required, for example, to ascertain whether the binding energy is greater or less than the thermal energy kT, which will determine the adhesion lifetime. Or it may be used to estimate the force needed to mechanically detach a vesicle from a surface (using one or other of the experimental techniques described later) to establish whether the adhesion is governed only by VDW forces. Thus, using the appropriate equation from Table 2 for the sphere-on-flat geometry, with a Hamaker constant of $A = 1 \times 10^{-20}$ J and a cut-off distance of $D_0 = 0{\cdot}4$ nm (allowing for one layer of strongly bound water molecules on each surface), we estimate

$$E = -AR/6D_0 \approx 4 \times 10^{-20} \text{ J} \approx 10\ kT \quad \text{for the binding energy,}$$

and

$$F = -AR/6D_0^2 \approx 1 \times 10^{-10}\ N \approx 100 \text{ pN} \quad \text{for the adhesion (detachment) force,}$$

whereas between two planar membranes in contact, we estimate

$$E = -A/12\pi D_0^2 \approx 1{\cdot}7 \text{ mJ m}^{-2} \quad \text{for the energy per unit area,}$$

and

$$F = -A/6\pi D_0^3 \approx 8{\cdot}3 \times 10^6 \text{ N m}^{-2} \approx 80 \text{ atm} \quad \text{for the adhesive pressure (force per unit area).}$$

The value of 10 kT obtained for the vesicle–surface interaction energy implies that the vesicle–surface 'bond' will have a lifetime of order 1 s or less before the vesicle–detaches spontaneously due to its thermal energy (Brownian motion). This is much longer than the thermal vibrational time of the vesicle or its constituent molecules, but not long enough to make this a permanent bond. Only for bond strengths in excess of 25 kT can the binding be considered as long-lived (on the scale of hours or days). The value of 100 pN (10^{-10} N or 0·001 μg) obtained for the detachment force, F, is typical of what is measured between small round tips and flat surfaces using the atomic force microscope (AFM), described later.

The simple equations of Table 2 for the VDW forces between *macroscopic* bodies, which are in terms of the Lifshitz–Hamaker constants of the materials, can often be used to estimate the interaction forces and energies between small molecules (which are usually difficult to calculate exactly). As an example of this, we apply the Liftshitz theory to the contact energy in air of two small molecules such as methane, CH_4, of radii $R \approx 0{\cdot}2$ nm (diameter $\sigma \approx$

https://doi.org/10.1017/S0033583501003687 Published online by Cambridge University Press

0·4 nm). Using the equation in Table 2 for the sphere-on-sphere geometry, with a Hamaker constant of $A = 5 \times 10^{-20}$ J as is appropriate for hydrocarbons, and a cut-off distance of $D_0 =$ 0·4 nm (the molecular diameter), we estimate

$E = -AR/12D_0 = 2{\cdot}1 \times 10^{-21}$ J for the binding energy.

For the VDW interaction of individual atoms and small molecules in contact a more accurate theory – the 'London' theory – should strictly be applied. The London equation for the VDW interaction energy (pair potential) for two atoms or small molecules of diameter σ whose centers are at a distance D apart is (cf. Eq. (2))

$$E(D) = -C_{\mathrm{VDW}}/D^6, \tag{5}$$

where C_{VDW} is a constant which for methane is $C = 102 \times 10^{-79}$ J m^{-6} (Israelachvili, 1991). Putting $D = \sigma = 0{\cdot}4$ nm into this equation, we obtain a more rigorously calculated binding energy for two methane molecules of $E = 2{\cdot}4 \times 10^{-21}$ J, which is also very close to the measured value (Israelachvili, 1991). But note that it is also very close (within 15 %) of the value of $2{\cdot}1 \times 10^{-21}$ J predicted above by the Lifshitz equation for macroscopic bodies. As regards the binding *force*, a value of $F(D) = -6C_{\mathrm{VDW}}/\sigma^7 \approx 40$ pN is obtained which is typical for the strength of the VDW force between two non-polar atoms or small molecules.[5]

The above examples serve to illustrate how the simple equations of Table 2 can be used to *estimate* the VDW interaction energies and forces between molecules, particles and surfaces of different geometries at *all* separations, including contact, even for relatively small molecules and molecular groups. Further examples of this will be given later.

But this generalization does not mean that one may calculate each and every binding interaction in this simple way, namely using equations for macroscopic particles at the molecular (nanoscopic) level. The problem is that the cut-off distance D_0 is an unknown factor that depends sensitively on the nature of the repulsive short-range forces; it may be less than or significantly greater than the 0·2–0·4 nm assumed in the above calculations. There is also the likely involvement of other adhesive forces. The VDW force is a relatively weak force compared to some of the other binding forces that can arise, such as ionic, H-bonding, and hydrophobic forces, and these forces, when present, often dominate the interaction.

In addition, the structure or topography of a macromolecule or surface also influences the strength of binding, and this factor is often more important than the attractive force-law. This 'structure' is defined by the sizes of the atoms and their arrangement within a macromolecule or at a surface, and is manifested by the repulsive 'steric' force between them (cf. Table 1) that determines how close two molecules or surfaces can get. The stabilizing repulsive forces essentially determine the cut-off separations, D_0, which in turn determines how effective the attractive forces can be.

In many cases of biological interest, the shapes of a macromolecular surface are too convoluted to be described by a simple cut-off distance, D_0, and only a detailed analysis of the discrete shapes and sizes of the interacting molecules at the atomic scale can determine how they can fit together so as to maximize the number of VDW contacts or 'bonds'. This

[5] Note that this value corresponds to an energy of $\sim 1\ kT$ (a typical energy for a VDW bond) acting over a distance of ~ 1 Å (a typical length of a VDW bond), namely $F =$ energy/length $\approx (4 \times 10^{-21}\ \mathrm{J})/(1 \times 10^{-10}\ \mathrm{m}) = 4 \times 10^{-11}\ \mathrm{N} = 40$ pN, which is an alternative way of estimating the force needed to rupture a VDW bond.

https://doi.org/10.1017/S0033583501003687 Published online by Cambridge University Press

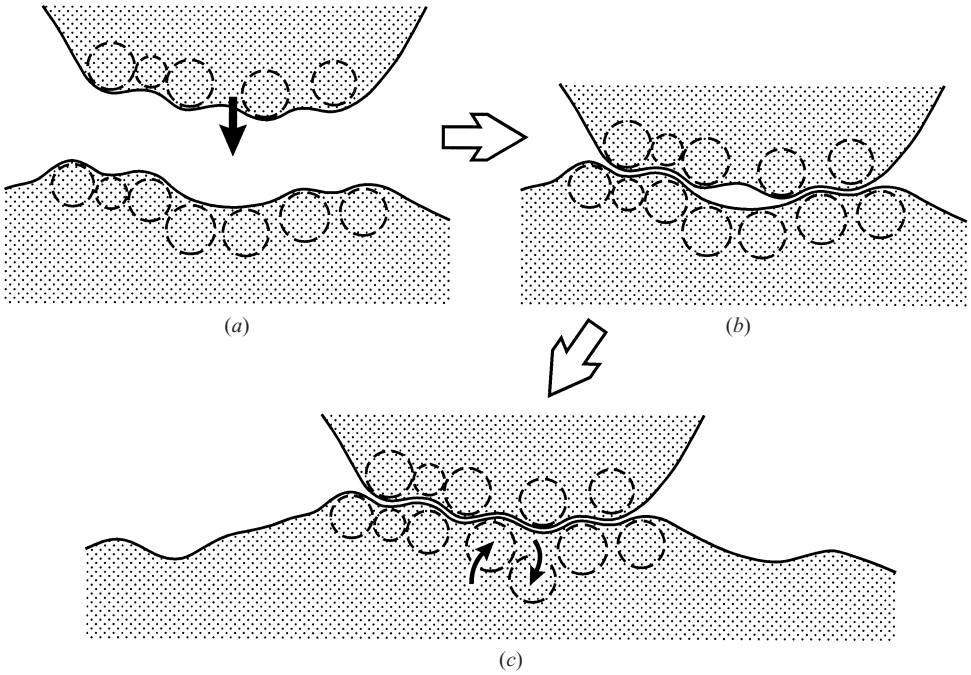


Fig. 4. Geometric Complementarity (also known as VDW complementarity) in which the final adhesion of two surfaces (*a*) depends on the way they can fit together at the atomic scale, either naturally (*b*) or after some local rearrangement of the atomic positions (*c*). Note that the upper surface or molecule may not be able to bind to the lower surface at any other location.

is known as 'VDW' or 'geometric complementarity' (Dean, 1987) and is illustrated in Fig. 4. Furthermore, if one or both of the interacting macromolecules or surfaces has some flexibility, its surface groups may be able to rearrange themselves to further enhance of the overall binding energy. This type of 'complementary adaptation' or 'induced fit' interaction begins to look increasingly like a specific interaction – which indeed it is – where only two unique molecules or surfaces are able to recognize each other, that is, fit together in a specific orientation with a high binding energy.

The way complementary and induced-fit interactions enhance adhesion is difficult to model theoretically or to express in terms of a generic equation such as a simple force-law or potential function. The coupling of binding and protein folding was only recently addressed theoretically by Shoemaker *et al.* (2000). Additionally these complex processes can now be theoretically computed or 'simulated' by molecular dynamics (MD) computer simulations, examples of which will be given in Section 4.

Figure 5 shows another example of adhesion enhancement that depends on the ability of molecules or submolecular groups to rearrange. Here, however, the interaction is much less specific: it involves the slow diffusive intermixing of molecular groups across an interface, which increases the number of VDW contacts. It can arise between any two polymer-like molecules or surfaces that do not have a fixed structure. Such processes can be slow – proceeding over hours or days, during which time both the effective adhesion energy and force continue to increase (often by a factor of 1000 or more), and the interacting species lose their original structure.

https://doi.org/10.1017/S0033583501003687 Published online by Cambridge University Press

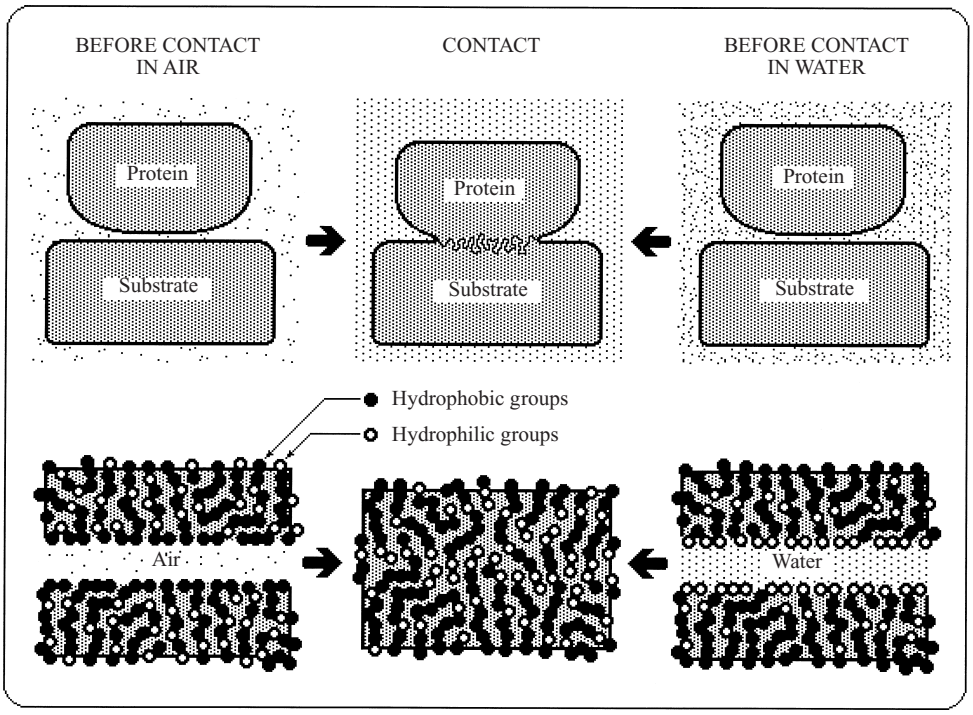


Fig. 5. Interdiffusion of biopolymer surfaces during protein–substrate or cell–substrate adhesion. This leads to time-dependent (ageing) effects, which are manifested by a slow increase in the molecular contact area and the intrinsic adhesion force. Both molecular-level interdiffusion across the interface (reptation) and bulk flow at the boundaries (viscous creep) can occur.

There are several systems where such interdiffusion mechanisms may play an important biological function. For example, the intercellular space in tissues comprises many different proteins and carbohydrate polymers in a very dense matrix. Investigations have focused on the possible specific, i.e. receptor-mediated, interactions between the different matrix components but the non-specific interpenetration of the polymers may also increase the structural integrity of the intercellular scaffolding. In addition, during biofilm formation, bacteria adhering to substrata secrete a dense carbohydrate matrix in which the bacteria are embedded (Gristina, 1987). Although several protein receptors have been identified that promote bacterial adhesion (Soto & Hultgren, 1999), the interpenetration of carbohydrate chains into the surrounding material may also contribute to the robust adhesion of many biofilms to various materials. This dense, secreted matrix also protects bacterial populations from diffusable toxins, and contributes to the robustness of bacterial infections associated with implanted devices (Gristina, 1987). One could also imagine how the interpenetration of the glycocalyces of bacterial and mammalian cells could enhance bacterial adhesion and hence pathogenicity. In these complex biological systems, the molecular bases of the time-evolution or ageing processes of biofilms or intercellular junctions are unknown. The secretion of polymers with sticky side chains might be the sole basis of the time-dependent increase in the strength of bacterial adhesion. Studies of bacterial adhesion have focused primarily on the specific binding interactions. However, non-specific interdiffusion may also play an important function by increasing the contact between the interacting materials and thereby enhancing the resultant adhesion.

https://doi.org/10.1017/S0033583501003687 Published online by Cambridge University Press

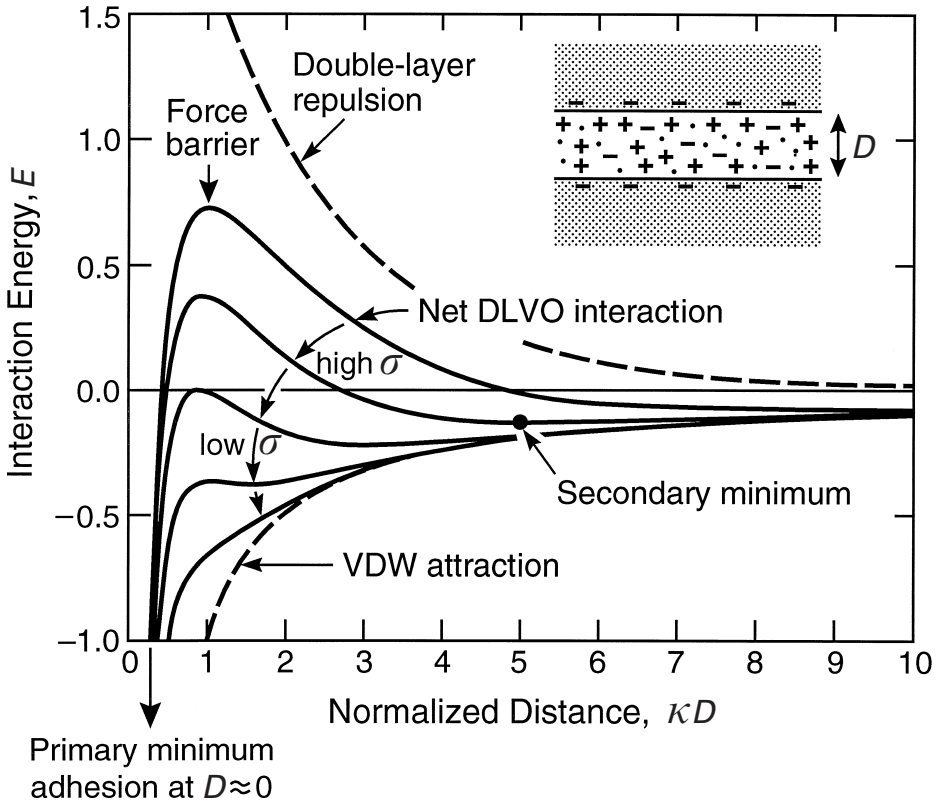


Fig. 6. Schematic DLVO plots showing how the attractive VDW and repulsive electrostatic double-layer (DL) forces together determine the total interaction potential between two charged surfaces in aqueous electrolyte solutions at different surface charge densities σ or potentials ψ_o which are related by Eq. (8). The DLVO theory has been found to adequately describe the long-range forces between similarly charged colloidal and some bio-colloidal surfaces in aqueous solutions. However, at small and contact separations in liquids, continuum models such as the Lifshitz theory of VDW forces and the Poisson–Boltzmann (PB) Equation of electrostatic interactions break down and/or other forces take-over to determine the final adhesion. Experimental examples of these forces are given in Section 3.

There are serious limitations to modeling binding mechanisms and energies of interactions between biomolecules on the basis of the VDW forces with a cut-off separation determined from data on static crystal structures. Additional repulsive forces often arise between biological surfaces owing to (1) a strongly bound primary hydration shell or layer that prevents two surfaces from approaching closer than 0·5 nm, and (2) the thermal motion of soft, fluid-like surfaces and protruding flexible surface groups that give rise to a thermal fluctuation or steric-hydration force (Table 1). Both of these forces are discussed in more detail below. They can prevent two hydrated surfaces from approaching closer than 0·5–2·0 nm and in this way drastically reduce their adhesion or binding energy. For example, since the VDW energy and force between two spherical particles varies as $-1/D$ and $-1/D^2$, respectively, if two such particles come into contact in water at a cut-off separation of $\sim$ 2·0 nm, their binding energy and adhesion force would be, respectively, a factor of 10 and 100 lower than if they came into true molecular contact at a separation of $\sim$ 0·2 nm.

https://doi.org/10.1017/S0033583501003687 Published online by Cambridge University Press

1.4 Electrostatic and 'double-layer' forces (DLVO theory)

In addition to the VDW force, the other major long-range force that almost always exists between two macromolecules or surfaces in aqueous solutions is the electric 'double-layer' (DL) force (Fig. 6). These two forces make up the two forces of the so-called DLVO theory of colloid stability,[6] after Derjaguin & Landau (1941), and Verwey & Overbeek (1948), who independently developed the theory during the Second World War. The long-range electrostatic interaction energy between two similarly charged macromolecules or surfaces is usually repulsive and roughly an exponentially decaying function of their separation:

$$E(D) \approx +C_{\mathrm{ES}}\, \mathrm{e}^{-\kappa D}, \tag{6}$$

where C_{ES} is a constant – analogous to the VDW interaction constant C_{VDW} in Eq. (2) – that depends on the geometry of the interacting surfaces, their surface charge density and the solution conditions (Table 3). The factor $1/\kappa$ is the Debye length (the characteristic decay length of the interaction) that depends only on the solution conditions, namely on the type (monovalent, divalent) and concentration of electrolyte present and on the temperature. The Debye length falls with increasing ionic strength and valence of the ions in the solution, and for aqueous electrolyte (salt) solutions at 37 °C (310 K) the Debye length (in nm) is

$$\begin{aligned} 1/\kappa = \kappa^{-1} &= 0{\cdot}30/[\mathrm{NaCl}]^{\frac{1}{2}}\ \mathrm{nm} \quad \text{for 1:1 electrolytes such as NaCl} \\ &= 0{\cdot}18/[\mathrm{CaCl_2}]^{\frac{1}{3}}\ \mathrm{nm} \quad \text{for 1:2 or 2:1 electrolytes such as } \mathrm{CaCl_2}, \end{aligned} \tag{7}$$

where the concentration units [NaCl] and [$CaCl_2$] are in moles/liter (M). For example, for NaCl solutions, $1/\kappa \approx 10$ nm at 1 mM NaCl, 0·8 nm at 0·15 M (physiological conditions), and 0·3 nm at 1 M. In totally pure water at pH 7, where $[H^+] = [OH^-] = 10^{-7}$ M, the Debye length is 950 nm, or about 1 μm.

The constant C_{ES} can be calculated by solving the so-called PB equation or by more rigorous theories (Verwey & Overbeek, 1948; Ninham & Parsegian, 1971; Chan *et al*. 1980a; Ohshima *et al*. 1983; Sharp & Honig, 1990; Ohshima, 1994, 1995). There are many approximate expressions for this interaction, some of which are in terms of the surface charge density σ, others are in terms of the surface potential ψ_o, which is easier to measure,[7] while still others take into account 'charge-regulation' effects where neither the surface charge nor the potential remain constant during an interaction (Hogg *et al*. 1966; Gingell & Parsegian, 1972; Gregory, 1973, 1975; Chan *et al*. 1976, 1980b; Ohshima *et al*. 1983; Hunter, 1987; Israelachvili, 1991; Evans & Wennerstrom, 1999a). There is also a simple relation between σ and ψ_o, given by the Graham equation for monovalent 1:1 electrolytes such as NaCl at $T = 37$ °C (310 K):

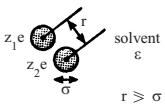
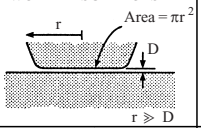
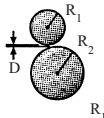
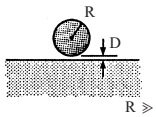
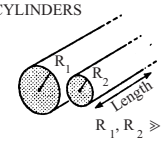
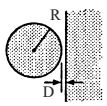
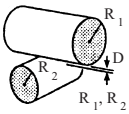
$$\sigma = 0{\cdot}116 \sinh(\psi_o/53{\cdot}4)\ [\mathrm{NaCl}]^{\frac{1}{2}}\ \mathrm{C\ m^{-2}} \tag{8}$$

[6] A colloid is a dispersion of colloidal particles (defined as particles whose dimensions are larger than molecular dimensions, which usually implies an aggregate of many molecules). A stable colloid is one whose particles remain suspended in solution indefinitely. An unstable colloid is one whose particles eventually coalesce (also referred to as coagulation or flocculation) and precipitate out of solution, resulting in a two-phase system.

[7] However, the measured potential across an interface contains contributions from two different layers: (i) ψ_s, from the fixed or bound surface charges or dipoles in the so-called Stern layer, and (ii) ψ_o, from the 'free' ions in the diffuse DL which are assumed to obey Boltzmann statistics on which the theory and various equations of DL forces are based. Electrophoresis and streaming potential measurements usually give the closest values for ψ_o which is also referred to as the Zeta potential to distinguish it from the total surface potential (Hunter, 1987).

https://doi.org/10.1017/S0033583501003687 Published online by Cambridge University Press

Table 3. *Electric 'double-layer' interaction energy $E(D)$ and force $(F = -\mathrm{d}E/\mathrm{d}D)$ between macroscopic bodies of different geometries (cf. Fig. 3) based on the PB equation (a continuum, mean-field theory)*

Geometry of bodies with surfaces D apart ($D \ll R$)		Electric 'double-layer' interaction*	
		Energy, E	Force, F
Two ions or small charged molecules	TWO IONS IN WATER 	$+\dfrac{z_1z_2e^2}{4\pi\varepsilon\varepsilon_0 r}\dfrac{e^{-\kappa(r-\sigma)}}{(1+\kappa\sigma)}$	$\dfrac{+z_1z_2e^2}{4\pi\varepsilon\varepsilon_0 r^2}\dfrac{(1+\kappa r)}{(1+\kappa\sigma)}e^{-\kappa(r-\sigma)}$
Two flat surfaces (per unit area)	TWO FLAT SURFACES 	$(\kappa/2\pi)\,Ze^{-\kappa D}$	$(\kappa^2/2\pi)\,Ze^{-\kappa D}$
Two spheres or macromolecules of radii R_1 and R_2	TWO SPHERES 	$\left(\dfrac{R_1R_2}{R_1+R_2}\right)Ze^{-\kappa D}$	$\kappa\left(\dfrac{R_1R_2}{R_1+R_2}\right)Ze^{-\kappa D}$
Sphere or macromolecule of radius R near a flat surface	SPHERE ON FLAT 	$RZe^{-\kappa D}$	$\kappa\,RZe^{-\kappa D}$
Two parallel cylinders or rods of radii R_1 and R_2 (per unit length)	TWO PARALLEL CYLINDERS 	$\dfrac{\kappa^{1/2}}{\sqrt{2\pi}}\left(\dfrac{R_1R_2}{R_1+R_2}\right)^{\frac{1}{2}}Ze^{-\kappa D}$	$\dfrac{\kappa^{3/2}}{\sqrt{2\pi}}\left(\dfrac{R_1R_2}{R_1+R_2}\right)^{\frac{1}{2}}Ze^{-\kappa D}$
Cylinder of radius R near a flat surface (per unit length)	CYLINDER ON FLAT 	$\kappa^{1/2}\sqrt{\dfrac{R}{2\pi}}\,Ze^{-\kappa D}$	$\kappa^{3/2}\sqrt{\dfrac{R}{2\pi}}\,Ze^{-\kappa D}$
Two cylinders or filaments of radii R_1 and R_2 crossed at 90°	CROSSED CYLINDERS 	$\sqrt{R_1R_2}\,Ze^{-\kappa D}$	$\sqrt{R_1R_2}\,Ze^{-\kappa D}$

* For interactions between similarly charged (ionized) surfaces in aqueous solutions of monovalent electrolyte ($z = 1$) at $T = 37$ °C (310 K) where the unit of electrolyte concentration [NaCl] is mole/*liter* (M). The interaction constant Z is defined by Eq. (10) in terms of surface potential ψ_o, but it can also be expressed in terms of the surface charge density σ by applying the Graham Equation, Eq. (8).

https://doi.org/10.1017/S0033583501003687 Published online by Cambridge University Press

where σ is in units of Coulombs per unit area (C m^{-2}), where 1 C m^{-2} corresponds to one electronic charge[8] e per 0·16 nm^2 or 16 Å^2 (1 nm^2 = 100 Å^2), and where ψ_o is in millivolts (mV). For example, Eq. (8) shows that a surface potential of $\psi_o = -75$ mV across a physiological saline solution of 0·15 M NaCl at 37 °C would be generated by a surface charge density of $\sigma = 0{\cdot}086$ C m^{-2} = 0·54 charges per nm^2 or 1 charge per 185 Å^2. This would correspond to discrete anionic charges e on the surface (e.g. of carboxyl COO^- groups on a protein or membrane surface) separated from each other by an average distance of about 1·4 nm (14 Å).

At 37 °C the double-layer pressure (force per unit area) between two surfaces interacting at constant surface potential in a monovalent salt solution is given by the approximate expression:[9]

$$P = 64\, kT\rho_\infty \tanh^2(ze\psi_o/4\, kT)e^{-\kappa D} = (1{\cdot}65 \times 10^8)\tanh^2(\psi_o/107)[\mathrm{NaCl}]e^{-\kappa D}\ \mathrm{N\ m^{-2}}, \qquad (9)$$

where ρ_∞ is the total ion concentration in units of number density (m^{-3}), [NaCl] is the salt concentration in units of mole/liter (M) as before, and ψ_o is in millivolts (mV). We may note from this expression that the double-layer repulsion generally increases with increasing surface potential ψ_o, as expected, but saturates at high potentials ($\psi_o > 150$ mV) as $\tanh(\psi_o/107)$ approaches unity.[10] Equation (9) also shows that the repulsion decays more rapidly with increasing salt, as the Debye screening length $1/\kappa$ falls, but that the short-range force *increases* with increasing salt concentration (since $e^{-\kappa D} \to 1$ as $D \to 0$). However, this latter effect is not general but depends on the geometry of the interacting particles (cf. Table 3).

Table 3 lists approximate expressions for the double-layer interaction between similarly charged surfaces of different geometries. The various equations are all expressed in terms of the constant, Z, defined by

$$Z = 64\pi\epsilon\epsilon_0(kT/e)^2 \tanh^2(ze\psi_o/4\, kT) = (9{\cdot}38 \times 10^{-11})\tanh^2(\psi_o/107)\ \mathrm{J\ m^{-1}} \qquad (10)$$

for a monovalent electrolyte ($z = 1$) at 37 °C. The constant Z is analogous to the Hamaker constant A for the VDW force, and – apart from the electrolyte valence z – depends only on the properties of the *surfaces*. The other terms that appear in the expressions for the interaction energies and forces, such as κ and [NaCl], depend only on the *solution* conditions and on the separation D between the surfaces.

In aqueous solutions, since VDW and electrostatic forces usually occur together, it is common practice to plot the two forces together when describing the net interaction of two surfaces. These two forces have come to be known as the two forces of the Derjaguin–Landau–Verwey–Overbeek theory (the DLVO theory). Figure 6 shows how these two forces, acting together, can determine whether an interaction will be attractive at all separations, repulsive at all separations, or weakly attractive at some finite separation – at the 'secondary minimum' – with an energy or force barrier separating it from the more adhesive 'primary minimum'. These subtleties arise because the two forces have very different distance dependencies – the one being a power law, the other an exponential – which asymptote differently at small, intermediate, and large separations. In addition, these two

[8] $1\ e = -1{\cdot}60 \times 10^{-19}$ C by definition.

[9] When expressed in terms of Z, defined by Eq. (10), the DL pressure between two planar surfaces can be written as: $P = (\kappa^2/2\pi)Ze^{-\kappa D}$ N m^{-2} (see Table 3).

[10] $\tanh x = (e^x - e^{-x})/(e^x + e^{-x})$, $\tanh x \approx x$ for $x \ll 1$, $\tanh x \approx 1$ for $x \gg 1$.

https://doi.org/10.1017/S0033583501003687 Published online by Cambridge University Press

forces are differently affected by changes in the surface and solution conditions: the VDW force being little affected, the double-layer force being very much affected, even changing from repulsion to attraction under certain conditions. For example, in the case of *asymmetric* surfaces, such as when the two surfaces have opposite charges as occurs when the solution pH is above the pI of one surface but below that of the other, the DL force is attractive. An experimental example of this is given in Section 3.1 (Fig. 33).

Returning to the previous example of a negatively charged membrane surface where $\psi_0 = -75$ mV in 0·15 M NaCl solution at $T = 37$ °C, Eq. (10) gives $Z = 3{\cdot}44 \times 10^{-11}$ J m^{-1}. The electric DL interaction between a vesicle of radius $R = 10$ nm at a separation of $D = 0{\cdot}4$ nm from a membrane surface having the same surface potential will therefore be (cf. Table 3):

$$E_{\mathrm{DL}} = +2{\cdot}1 \times 10^{-19}\ \mathrm{J} \approx +50\ kT \quad \text{for the energy,}$$

and

$$F_{\mathrm{DL}} = +2{\cdot}64 \times 10^{-10}\ \mathrm{N} \approx 260\ \mathrm{pN} \quad \text{for the (repulsive) force.}$$

These values may be compared with the values previously estimated in Section 1.3 for the attractive VDW interaction for the same system at the same separation, namely $E_{\mathrm{VDW}} = -4{\cdot}0 \times 10^{-20}$ J ($\sim 10\ kT$) for the energy, and $F_{\mathrm{VDW}} = -100$ pN for the (attractive) force. Clearly, at a separation of 0·4 nm the DL repulsion wins out over the VDW attraction. However, at even smaller separations, below about 0·2 nm, corresponding to one layer of water molecules between the surfaces, the VDW force eventually wins out, as illustrated in Fig. 6. This corresponds to adhesion or binding in the 'primary' minimum. However, at such small separations additional (short-range) forces generally participate in – if not dominate – the interaction, such as repulsive hydration and thermal fluctuation forces or attractive specific forces. The DL force, too, may become modified at small separations, as discussed below.

As illustrated in Fig. 6, the net DLVO interaction is expected to be attractive both at very small and very large separations. In the case of the parameters used in the above example: $\psi_0 = -75$ mV, [NaCl] = 0·15 M, $T = 37$ °C, $A = 10^{-20}$ J – which are fairly typical of physiological conditions – it can be readily verified using the equations of Tables 2 and 3 that as D increases the net force changes sign, becoming again attractive, at $D = 5{\cdot}1$ nm. The maximum adhesion force in the 'secondary' minimum occurs at $D = 6{\cdot}6$ nm where $F_{\mathrm{ad}} = -3 \times 10^{-13}$ N ($\sim 0{\cdot}3$ pN). The maximum adhesion *energy*, however, occurs at $D = 5{\cdot}1$ nm (when the force is zero) where $E_{\mathrm{min}} = -2{\cdot}8 \times 10^{-21}$ J $\approx 0{\cdot}7\ kT$. This energy is not large enough to bind the $R = 10$ nm radius vesicle to the surface for any appreciable time before the thermal energy drives them apart. However, since the interaction energy and force scale in direct proportion to the size or radius R of the vesicle or cell, the binding energy for larger particles could be large enough to result in effective adhesion. Thus, for a vesicle or small cell of radius $R = 0{\cdot}5$ μm (50 times larger), the adhesion energy will be $\sim 33\ kT$ which is now strong enough to hold the particle to the surface for many hours (assuming the absence of other forces, including hydrodynamic detachment forces due to flow, which are discussed in Section 2.12). Actually, the strong adhesion force will also deform the soft vesicle membrane, causing it to flatten against the flat surfaces. This will cause the effective adhesion energy to increase above the value of $33\ kT$ calculated for rigid, non-deforming particles (see Fig. 4 and Section 2.5).

https://doi.org/10.1017/S0033583501003687 Published online by Cambridge University Press

1.4.1 Electrostatic and double-layer (DL) interactions at very small separations

In the limit of small D (typically D below 1·5 nm in physiological saline solutions), the DL interaction energy depends on whether the surfaces remain at constant potential ψ_o, as assumed in the above equations, or at constant charge σ, when the short-range electrostatic repulsion exceeds that predicted by the above equations. In most cases, the interaction lies somewhere in between these two limits.[11] In the 'constant charge' case, as D falls below 1·5 nm (or below the Debye length), the DL force per unit area between two surfaces approaches the 'osmotic limit' of the trapped counterions; that is, the limiting DL pressure between two approaching surfaces is simply the osmotic pressure P of the excess ions (counterions) that are electrostatically trapped in the aqueous gap between them:[12]

$$P(D \to 0) = +\rho kT = +2\sigma kT/ze D \quad \text{for } D < \kappa^{-1}, \tag{11}$$

where z is the valence of the counterions. For example, for the case considered above of two membrane surfaces of charge density $\sigma = 0{\cdot}086$ C m^{-2} in 0·15 M NaCl solution at 37 °C, if the surface charge density remains constant rather than the surface potential, the repulsive pressure between the two surfaces at $D = 0{\cdot}4$ nm will have increased from 5·4 MPa (as determined by Eq. (9)) to 46·0 MPa (as determined by Eq. (11)).

From Eq. (11) it is apparent that, unlike at constant potential when the DL repulsion remains finite as $D \to 0$, at constant charge, the force becomes infinitely repulsive and independent of the salt concentration. However, the VDW attraction, which goes as $-1/D^3$ between two flat surfaces, still wins out over the DL repulsion as D approaches zero – unless some other short-range repulsive force dominates over both of them. Equation (11) also gives insight into the physical meaning of the difference between an interaction at constant charge and one at constant potential: at constant surface charge density, σ, the total *number* of counterions between the surfaces remains constant as they approach; the counterion *concentration*, $\rho = 2\sigma/zeD$, therefore increases as does the repulsive pressure, $P = \rho kT$. In contrast, at constant potential, the *concentration* ρ of counterions between the surfaces now remains approximately constant (and the surface charge density σ falls) as the surfaces approach.[12] When this happens, the pressure $P = \rho kT$ also remains approximately constant as $D \to 0$, which makes it weaker than the constant charge interaction. Note that in the limit of $D \to 0$ at constant ψ_o, ρ and T, Eq. (9) predicts that the pressure between two planar surfaces, $P = 64\, kT\rho_\infty \tanh^2 (ze\psi_o/4\, kT)e^{-\kappa D}$, approaches a constant, distance-independent value once D falls below the Debye length.

Unlike the continuum equations for the VDW forces that still apply, albeit approximately, at contact separations, the continuum, mean-field equations for the double-layer interaction

[11] Interactions at constant surface charge density are easy to understand: the surface ionizable groups are fully dissociated and remain that way at all separations D. Interactions at constant potential occur when the surface ionizable groups (the co-ions) are not fully dissociated but are in equilibrium with the local concentration of counterions near them. As two surfaces approach each other, the counterion clouds become compressed resulting in an increase in the local counterion concentration at each surface. To offset this increase, some of the counterions bind to the surface co-ions, thereby neutralizing them and reducing the surface charge density.

[12] The osmotic pressure (OP) limit is basically the same as the pressure of an ideal gas, $PV = RT$, or $P = \rho kT$, where ρ is the concentration in units of number density (number of molecules per unit volume). The counterion concentration in the gap ρ is related to the surface charge density σ by the requirement of overall charge neutrality, namely total number of counterions of valence z in gap = $\rho \times$ volume $= \rho \times D \times$ area $= 2(\sigma/ze) \times$ area, so that $\rho = 2\sigma/zeD$.

https://doi.org/10.1017/S0033583501003687 Published online by Cambridge University Press

can break down *completely* at small distances regardless of whether the interaction is at constant charge or constant potential. Such effects arise from a combination of 'discrete co-ion' effects (a charged surface is made up of discrete charged sites, not a smeared out charge), 'finite ion size' effects, counterion 'charge fluctuation' and counterion 'condensation' effects, none of which are considered in the simple mean-field theories based on the PB equation. Thus, there are situations when the DL interaction at short-range is attractive even between similarly charged surfaces, i.e. between *symmetric* surfaces. Such attractive electrostatic forces arise from a combination of 'ion correlation' or 'charge fluctuation' effects (Jonsson & Halle, 1980; Guldbrand *et al*. 1984), and 'ion condensation' effects (Manning, 1969). The attractive ion correlation force acts in addition to (rather than replacing) the PB repulsion, i.e. it enhances the Hamaker constant. This force, together with the other ion-specific, short-range interactions discussed above, affects the net DLVO interaction potential by lowering the force barrier, moving it further out, and enhancing the final adhesion in the primary minimum. This is particularly evident in the presence of divalent counterions such as calcium (cf. Fig. 38 and Table 6). In the former, there is an additional VDW-like attraction between the mobile and therefore highly polarizable counterions located at each surface, which pulls the two surfaces together. The additional attractive force F_{ic} due to ion correlation effects is believed to have the same form as the VDW interaction. For example, Lau *et al*. (2000) have proposed that between two planar charged surfaces at $D > \kappa^{-1}$ the ion correlation or charge fluctuation force can be written as, $F_{\mathrm{ic}} = -C_{\mathrm{ic}}kT/D^3$, where $C_{\mathrm{ic}} \approx 0{\cdot}05\ kT$ is a universal constant at ambient temperatures. This expression can also be written as $F_{\mathrm{ic}} = -A_{\mathrm{ic}}/6\pi D^3$ which gives an additional term to the Hamaker constant (cf. Eq. (3)) due to ion-correlations of $A_{\mathrm{ic}} \approx 6\pi \times 0{\cdot}05\ kT \approx 4 \times 10^{-21}$ J. This is only a modest contribution, is smaller than predicted by computer simulations (Jonsson & Halle 1980; Guldbrand *et al*. 1984), and is too small to account for the much larger effects observed, especially with divalent counterions, described in Section 3.1.

In the case of 'ion condensation', which is also known as Manning condensation (Manning, 1969), the counterions collapse onto the co-ions on the surfaces. This lowers the effective surface charge density and, in turn, the DL repulsion. Ion-condensation forces usually occur in the presence of divalent or trivalent counterions such as calcium. Manning condensation is very geometry-dependent and is particularly effective between planar surfaces such as two membrane surfaces and, to a lesser extent, between cylindrical or filamentous structures such as DNA. Neither of these types of surfaces are ever 'fully charged' or ionized – their fraction of charged sites being typically well below 25%. This is in marked contrast to small *spherical* structures such as ions or small micelles in solution that are usually between 25 and 100% dissociated. Both ion-correlation and ion-condensation forces can significantly enhance adhesion. They are related (Rouzina & Bloomfield, 1996; Shklovskii, 1999) but are difficult to separate, quantify or simulate and, so far, do not appear to be describable by a single simple force-law or potential function. Experimental examples of both of these interactions are given in Sections 3 and 4.

There are other limitations of the simple continuum or 'mean field' equations for the DL force at small separations arising from the assumption that the surface charges are smeared out uniformly over the surfaces rather than existing at discrete sites. Biological surfaces, unlike many simple colloidal surfaces or synthetic polyelectrolytes, expose a mixture of both positive (cationic or basic) and negative (anionic or acidic) groups rather than just one type of charge. Such surfaces or polymers are known as amphoteric surfaces or polymers. Furthermore, these charges usually reside at, or have some flexibility around,

https://doi.org/10.1017/S0033583501003687 Published online by Cambridge University Press

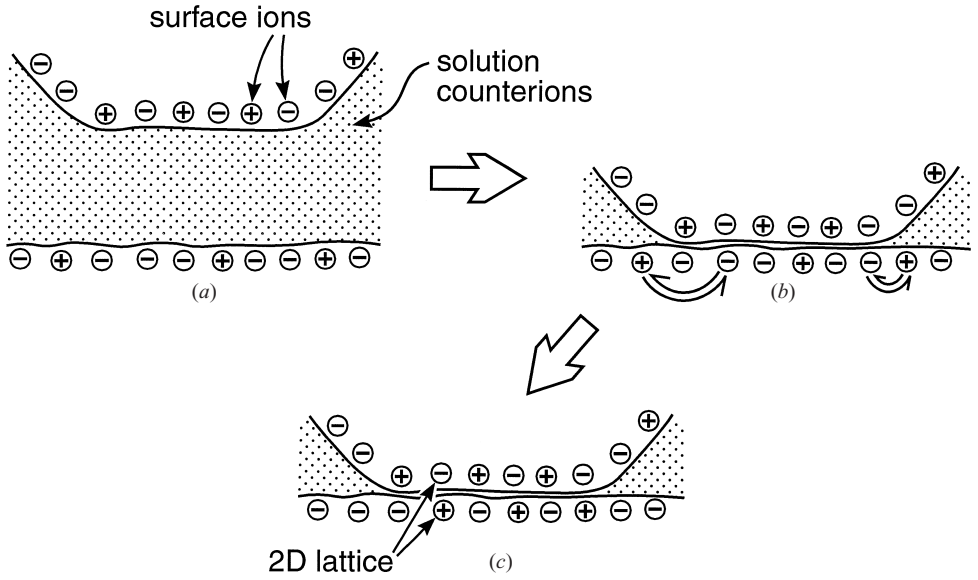


Fig. 7. Electrostatic complementarity. Schematic of two amphoteric surfaces, composed of both positive (basic) and negative (acidic) groups, but with more negative charges than positive charges. In this schematic, the upper surface has six anionic sites and four cationic sites, the lower surface has seven anionic and three cationic sites. Each surface is therefore overall negatively charged, which is the way they appear from afar. These surfaces will therefore repel each other at large separations (panel (*a*)) due to the DL interaction, but attract each other when in contact (panel (*b*)) due to the preponderance of favourable ion-pair interactions. Note, however, that the attraction requires the two surfaces to 'dock' in a highly specific way, which really changes the interaction from being 'nonspecific' at long-range to highly 'specific' at short-range, for example, the binding may occur only when the two surfaces are positioned as shown and at no other orientation or location (note, too, that the two surfaces or molecules can be of the same type, simply exposing different charges at different locations). Local 'induced fit' rearrangements ($b \rightarrow c$) can further enhance the adhesion, and cause the charged sites at the binding site to order into a quasi 2D lattice. Electrostatic complementarity cannot arise between simple polyelectrolytes or surfaces that contain only one type of charged group, e.g. only acidic or basic groups, although a fairly strong, but non-specific, adhesion can arise between negative sites on opposite surfaces or groups by the bridging of divalent counterions such as Ca^{2+}.

discrete sites on the surfaces of proteins or membranes. Such 'discrete ion effects' can result in an enhanced attraction, or reduced repulsion, of the electrostatic interaction at very small separations due to the formation of discrete ionic bonds between two amphoteric surfaces. This is known as 'electrostatic complementarity' (Dean, 1987), which is similar to the 'VDW complementarity' or 'geometric complementarity' discussed earlier (cf. Fig. 4), but electrostatic complementarity is much more effective in changing a weak, non-specific interaction into a strong, highly specific one.

The presence of both negative and positive charges on surfaces can cause the interaction to change sign, from repulsion to attraction, as the two surfaces approach each other, even in the case of symmetric surfaces. How this occurs is illustrated in Fig. 7 which shows two amphoteric surfaces whose mean or surface-averaged charge density is negative, i.e. both surfaces have more negative charges than positive charges (Fig. 7(*a*)). This gives rise to a long-range *repulsive* DL force because this force is determined by the *mean* charge density σ of the surfaces. However, at smaller separations, depending on the distance between the charges on the surfaces and the Debye length, individual ions begin to see each other as

https://doi.org/10.1017/S0033583501003687 Published online by Cambridge University Press

discrete entities rather than a smeared out charge, and the individual Coulombic interactions of ionic pairs now determine the net interaction. As can be seen in Fig. 7(*b*), strongly attractive ionic bonds can develop between most of the ions on the two surfaces, leaving only a few that repel each other.

Biological macromolecules often exploit charge complementarity to enhance both RL, the binding free energies and the rates of biomolecular association. For example, in many protein–DNA complexes, positively charged amino acids on the protein interact with the negatively charged phosphate groups of the DNA backbone (McCammon & Harvey, 1987; Sharp & Honig, 1990; Zacharias *et al*. 1992; Honig & Nicolls, 1995; McCammon, 1998). In other cases, such as the binding between cytochrome c and cytochrome b5 shown in Fig. 8, the precise organization of charges in the binding sites of proteins facilitates protein–protein docking (Wendoloski *et al*. 1987; McCammon, 1998). Changing the sign of any one of the lysine residues in the binding site of cytochrome c dramatically reduces the affinity and the cytochrome b5 binding energy (Rodgers *et al*. 1988). Such quasi-specific interactions are also crucial in determining the binding of lipid bilayers and protein adhesion to lipid membranes (Peitzsch *et al*. 1995; Murray *et al*. 1997; Arbuzova *et al*. 1998).

Complementary electrostatic interactions can be further enhanced when the molecular structures or surfaces are flexible. This flexibility allows local changes in structure to occur so that each cation faces an anion on the opposite surface (Fig. 7(*c*)). It is then possible to end up with a 2D ionic lattice at the interface and where *all* of the ionic bonds are now attractive. Such 'induced fit' interactions can result in very strong binding as well as significant rearrangements/conformational changes of the interacting species.

A similar mechanism to electrostatic complementarity arises between surfaces exposing complementary hydrogen-bonding groups – the one exposing H-donors, the other exposing H-acceptors (i.e. electronegative atoms such as oxygen that expose lone-pair electrons). Indeed, it is well established that the H-bond is essentially an electrostatic interaction between a charge and a dipole (Coulson, 1961), which is why it is intermediate in strength between an ionic bond (between two charges) and a VDW bond (between two dipoles).

A second type of electrostatic complementarity that involves a less stringent arrangement of charges plays an important role in biological recognition. This is particularly evident when the charges are distributed nonuniformly over irregularly shaped macromolecules. This mechanism takes advantage of the longer-ranged DL forces between heterogeneous but complementary charged patches on the associating molecules or surfaces (Sharp & Honig, 1990). The electrostatic potential distributions surrounding proteins or DNA often closely match those of the associating ligands even though the charges generating these fields may not form salt-bridges when the molecules finally bind. This more diffuse complementarity enhances bimolecular association rates (Northrup *et al*. 1984; Sharp & Honig, 1990; Honig & Nicolls, 1995; Kozack *et al*. 1995; McCammon, 1998). Electrostatic potential calculations have suggested that the 3D spatial inhomogeneity of the electrostatic field generates intermolecular steering torques that pre-orient molecules and guide ligands to the receptor binding sites (Northrup *et al*. 1984; Kozack *et al*. 1995; McCammon, 1998). At large distances, molecular tumbling averages out any orientation dependence of the intermolecular pair potentials, but at intermediate separations the focused electrostatic fields guide the ligand along a low energy trajectory to the binding site. The resultant rate enhancement has been demonstrated in Brownian dynamics simulations, and, indirectly by kinetic measurements of association rates (Northrup *et al*. 1984; Kozack *et al*. 1995; McCammon, 1998).

https://doi.org/10.1017/S0033583501003687 Published online by Cambridge University Press

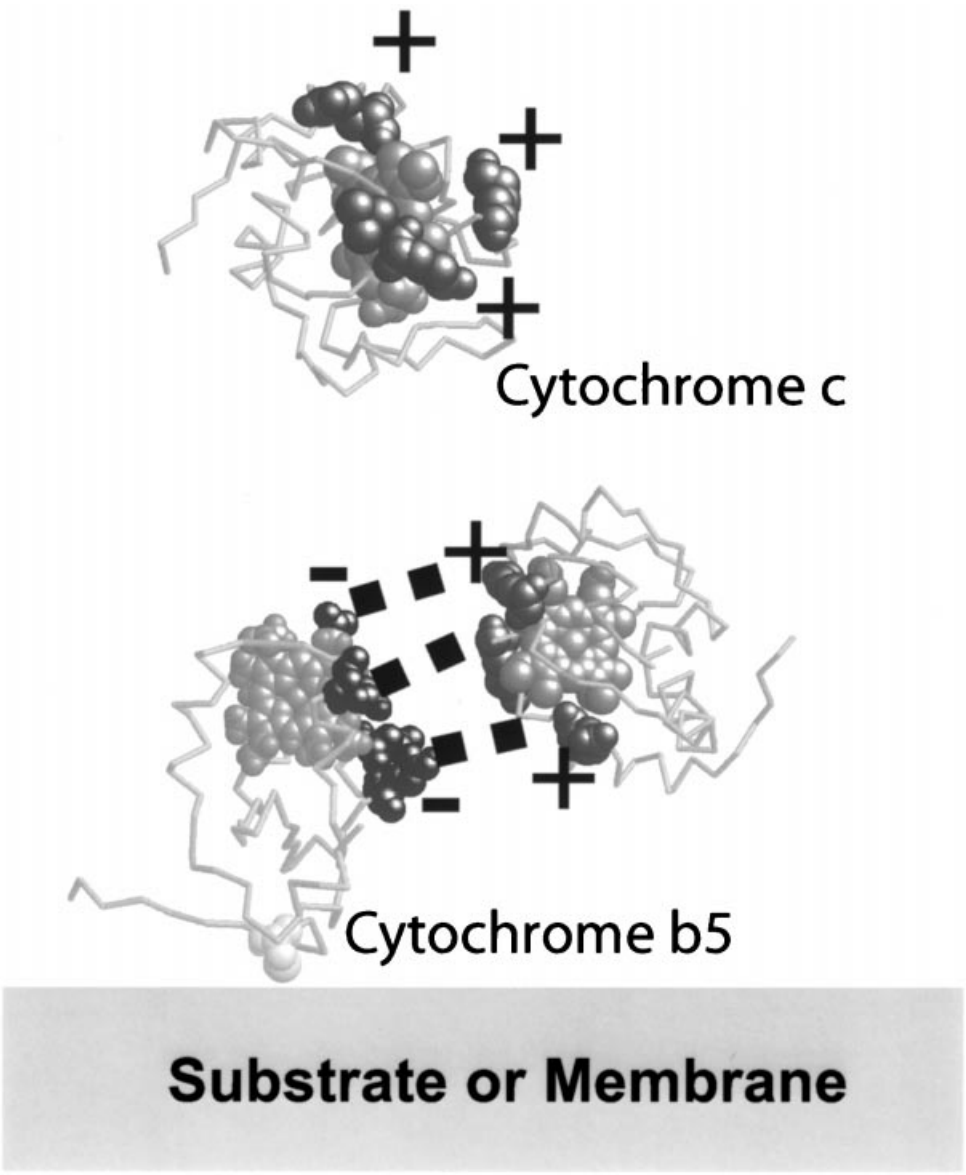


Fig. 8. Electrostatic complementarity between two different (heterologous) proteins. Negatively charged cytochrome b5 on a lipid membrane binds to soluble cytochrome c. The cytochrome c contains several positively charged lysines surrounding the binding site (dark grey CPK models). When the proteins dock, the negatively charged residues near the binding site of cytochrome b5 (black CPK structures) form ion pairs with the lysines of cytochrome c. The ion pairs are indicated by the bold, dashed lines.

The interaction of negatively charged superoxide dismutase with the superoxide anion is an excellent example of the use of such a guidance mechanism to enhance reaction rates. The cleft-shaped dielectric boundary formed by the binding site focuses the surrounding positive electrostatic field due to the metal center in the binding site, and this funnels the superoxide anion to the active site of the negatively charged macromolecule (Klapper *et al.* 1986). The

https://doi.org/10.1017/S0033583501003687 Published online by Cambridge University Press

rapid enzymatic oxidation of superoxide supports this functional role of the protein charge distribution.

Importantly, the charges that contribute to electrostatic complementarity at short-range can also contribute to the complementary, long-range DL 'steering' force. The converse does not necessarily occur. For example, a ring of charge surrounding the binding site of the 4-4-20 anti-fluorescein antibody funnels the negatively charged fluorescein into the binding pocket, but the outer charged residues do not contribute to the binding energy (Herron *et al*. 1989; Bedzyk *et al*. 1990). Conversely, positively charged lysines in the binding site of cytochrome c contribute to the positive electrostatic potential that orients cytochrome b5 (Wendoloski *et al*. 1987). At the same time, short-range salt-bridges between the lysines of cytochrome c and the negatively charged amino acids in the cytochrome b5 binding site stabilize the heterologous protein complex (Rodgers *et al*. 1988) (Fig. 8). Thus, the role played by surface charge clusters and the long-range 'focusing fields' which they generate differs from the more specific electrostatic complementarity described above. Importantly, although these focusing fields do not necessarily contribute to the binding energy or to the binding specificity, they do significantly alter the *dynamics*, i.e. the *rates*, of bimolecular association.

1.5 Hydration and hydrophobic forces (structural forces in water)

When a liquid is in contact with a surface or confined within a restricted space between two surfaces it ceases to behave as a structureless medium, and the short-range forces between two surfaces can no longer be described by simple continuum theories or by equations such as those listed in Tables 2 and 3. For example, at small surface separations – below about 10 molecular diameters – the VDW force between two rigid hydrophilic surfaces or solute molecules in water is no longer a smoothly varying attraction. Instead, there now arises an additional 'solvation' force that generally oscillates with distance, varying between attraction and repulsion, with a periodicity equal to the diameter σ of the water molecule (Israelachvili, 1983; Kjellander & Marcelja, 1985a, b; Tarazona & Vichente, 1985; Henderson & Lozada-Cassou, 1986, 1994; McGuiggan & Israelachvili, 1990). For soft (flexible or mobile) surfaces the short-range solvation force can be smoothly repulsive (not oscillatory), while for hydrophobic surfaces it can be smoothly attractive. Recent advances in understanding these three types of solvation force (also referred to 'structural' or 'hydration' forces when the solvent is water) will now be reviewed.

Historically, hydration forces have been something of a mystery, both experimentally and theoretically. They were first proposed many years ago by Langmuir (1938) and others to 'explain' the unexpected stability of uncharged colloidal particles such as coacervates (giant vesicles) in solution, and subsequent experiments showed them to be monotonically repulsive, roughly exponential, and with a range of about 20 Å. The idea that these forces are due to 'water structuring' at surfaces gained steady popularity, and the exponential decay length of ~ 2 Å was believed to be due to some characteristic property of water such as its size. However, as theoretical work and computer modeling failed to confirm the existence of any type of exponentially repulsive hydration force associated with water structuring other interpretations for their origin – based on the properties of the interacting *surfaces* rather than the *medium* – were offered and supported by further experimental and theoretical work (Pfeiffer *et al*. 1989; Israelachvili & Wennerström, 1990, 1992, 1996, 1997; Granfeldt *et al*. 1991; Marcelja, 1997). We return to these smoothly varying hydration forces later in this

https://doi.org/10.1017/S0033583501003687 Published online by Cambridge University Press

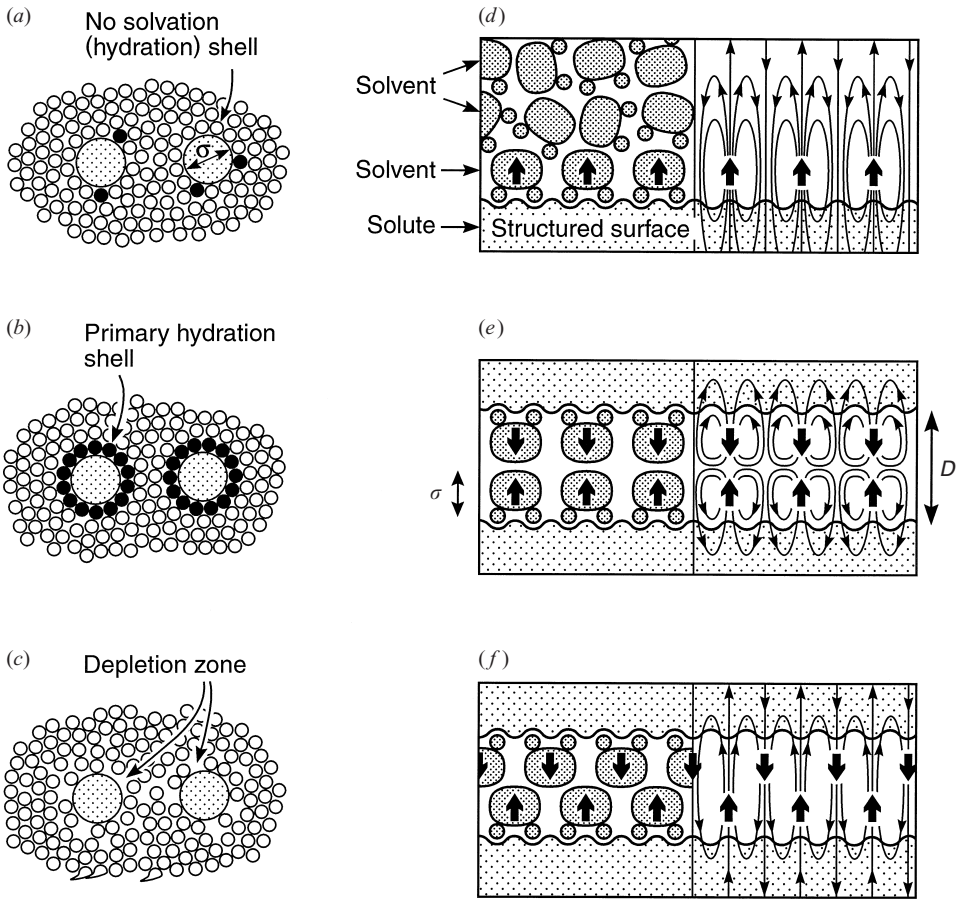


Fig. 9. Schematic diagrams of water structure or organization, which can be both positional and orientational, around different kinds of solute molecules (*a*, *b*, *c*), at a single 'structured' surface (*d*), and between two structured surfaces (*e*, *f*). Whenever the water structure is altered as two solutes or surfaces approach each other there arises a structural or solvation force between them that can be attractive, repulsive or oscillatory (Fig. 10). (*d*) Primary hydration shell of tightly bound water around a structured hydrophilic surface. The ordered dipolar water molecules generate an electric field as shown on the right. (*e*) Two surfaces as in panel (*d*) that approach each other in water: if the bound water molecules are exactly opposite each other as shown, their dipole fields oppose each other (right-hand side), the electrostatic field energy increases, and the ensuing contribution to the structural force is monotonically (exponentially) repulsive (Israelachvili & Wennerström, 1996). (*f*) If the bound water molecules are staggered, their dipole fields complement each other, the electrostatic energy decreases, and the ensuing structural force contribution is monotonically attractive down to 'contact' at $D = 2\sigma$. This is the favored interaction between two such surfaces. At larger separations, beyond 2σ, in addition to the monotonic electrostatic contribution, there is also the oscillatory contribution to the overall structural force that depends on the size and shape of the solvent molecules.

section, and first describe the oscillatory force that is now believed to be the generic solvation force in liquids, i.e. the force due to *solvent–solvent* interactions (as opposed to *surface–surface* or *surface–solvent* interactions such as the two complementary interactions shown in Figs. 4 and 7).

A short-range oscillatory force-law, varying between attraction and repulsion, and with a periodicity equal to some dimension of the solvent molecules such as their diameter, arises

https://doi.org/10.1017/S0033583501003687 Published online by Cambridge University Press

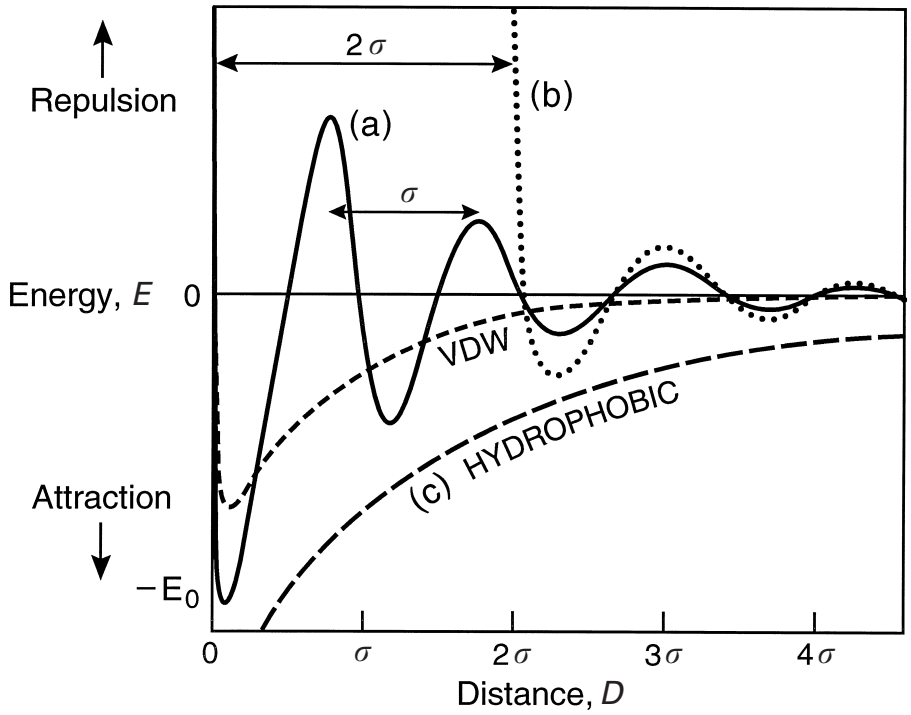


Fig. 10. Different types of hydration force curves: oscillatory, monotonically attractive (hydrophobic), monotonically repulsive, or a combination of these over different distance regimes. The letters adjacent to each force curve refer to the types of solute- or surface-induced water structuring shown in Fig. 9. Curve (a): schematic of oscillatory force between two surfaces in a liquid such as water. Any double-layer force that arises from the presence of a surface charge appears to be simply additive with the oscillatory force (Christenson & Horn, 1983). Curve (b): solvation force between 'solvated' or 'hydrated' hydrophilic surfaces in water, where the first layer of strongly bound water molecules provide a steric barrier at $D \approx 2\sigma$. The strong binding of a single layer of water molecules to a surface or polyelectrolyte (forming a primary 'hydration shell') can come about from strong H-bonds and does not require that the surface groups be charged. Curve (c): attractive solvation forces due to electrostatic effects (Fig. 9(*f*)) or the hydrophobic interaction (Fig. 9(*c*)).

between any two rigid surfaces as they approach each other in a liquid. This force is oscillatory because the two approaching surfaces force the liquid molecules between them to order into quasi-discrete layers that are energetically or entropically favored (and correspond to the free energy minima) while fractional layers are disfavored (energy maxima). The effect is quite general and arises with all simple liquids when they are confined between two smooth rigid surfaces, both flat and curved (Figs. 9 and 10). Oscillatory forces are now well understood theoretically, at least for simple liquids (Christenson & Horn, 1985; Tarazona & Vichente, 1985; Henderson & Lozada-Cassou, 1986, 1994; Christenson, 1988; Israelachvili, 1991). In a first approximation the oscillatory force law (Fig. 10) may be described by an exponentially decaying cosine function of the form

$$E(D) \approx -E_0 \cos(2\pi D/\sigma) e^{-D/\sigma} \quad \text{per unit area,} \tag{12}$$

where both theory and experiments show that the oscillatory period and the characteristic decay length of the envelope, σ, are close to some dimension (usually the diameter) of the confined molecules. Oscillatory forces are characterized by having multiple adhesive minima

https://doi.org/10.1017/S0033583501003687 Published online by Cambridge University Press

at discrete surface separations but of different strengths (energy well depths), with a final deep 'primary minimum' of magnitude $-E_0$ at contact ($D = 0$), where no solvent molecules remain between the surfaces. The final adhesion minimum is essentially the same as the 'depletion force' energy at contact, described later, and is approximately given by the osmotic limit (see footnote 12) as $E_0 \approx -\rho kT\sigma \approx -kT/\sigma^2$. This can exceed the contribution from the continuum VDW force (Christenson & Yaminsky, 1993), as shown schematically in Fig. 10(*a*). For example, for spherical solvent molecules of diameter $\sigma \approx 0{\cdot}25$ nm (cf. water) between two inert surfaces, the contribution from the oscillatory solvation force to the contact energy will be of order $E_0 \approx -4{\cdot}2 \times 10^{-21}/(2{\cdot}5 \times 10^{-9})^2 \approx -67$ mJ m^{-2}, which corresponds to a surface or interfacial energy of $\gamma = E_0/2 \approx 33$ mJ m^{-2} (see depletion and hydrophobic interactions below).

If there is a strong solute–solvent or surface–solvent bond (Fig. 9(*b*, *d*)), a protective solvent shell or layer is formed, and the primary minimum is now much weaker and occurs farther out – at a separation corresponding to two solvent molecules as shown in Fig. 10(*b*). Such effects are particularly common for strongly hydrophilic groups and surfaces in aqueous solutions. A primary solvation or hydration shell around a macromolecule, ionic group or polymer chain acts not only to reduce the final adhesion strength, but also to increase the excluded volume of the hydrated solute molecule in solution. This enhances the repulsive entropic (osmotic) interaction between them, as discussed further below. It is important to appreciate that these two effects, each of which acts to enhance the repulsion between two hydrated groups, are thermodynamically quite different: the first, primary binding, is enthalpically driven, while the second, is an entropy-driven process. Recently, these two processes have been experimentally measured and distinguished in a calorimetric study of phospholipid hydration by Markova *et al.* (2000).

Between two *hydrophobic* surfaces or two hydrophobic patches on surfaces, the hydration force is monotonically attractive. Direct force measurements have shown that the hydrophobic force is long-ranged, that it has a different distance-dependence, and that it is much stronger than the theoretically expected VDW force between non-polar molecules or surfaces. A hydrophobic surface is one that is non-polar and inert to water in the sense that it cannot bind to water molecules via ionic or hydrogen bonds. Hydrocarbons and fluorocarbons are hydrophobic, as is air (e.g. air bubbles), and the strongly attractive hydrophobic force has many important biological manifestations and consequences.

In recent years there has been a steady accumulation of experimental data, including direct force measurements using the surface forces apparatus (SFA) and atomic force microscope (AFM), on the force laws between various hydrophobic surfaces in aqueous solutions. These surfaces include surfaces coated with surfactant monolayers exposing hydrocarbon or fluorocarbon groups and surfaces that have been rendered hydrophobic by chemical methylation or plasma etching (Christenson & Claesson, 2001). These studies have found that the hydrophobic force-law between two macroscopic surfaces is of surprisingly long range, decaying roughly exponentially out to a separation of about 10 nm, and then more gradually farther out. The hydrophobic force can be far stronger than the VDW attraction, especially between hydrocarbon surfaces for which the Hamaker constant is quite small.

As might be expected, the magnitude of the hydrophobic attraction depends on the 'hydrophobicity' (or decreasing 'hydrophilicity') of surfaces, although these are not straightforward to define or quantify. A common criterion in surface science is to consider a smooth surface as being partially hydrophobic if the contact angle θ of water on it is in the

https://doi.org/10.1017/S0033583501003687 Published online by Cambridge University Press

range 75–90°, and fully or strongly hydrophobic if $\theta = 100$–$115°$, higher values being uncommon. This would correspond to interfacial energies of the water–hydrocarbon interface of $\gamma_i = 6$–30 mJ m^{-2} for partially hydrophobic surfaces, and $\gamma_i = 40$–55 mJ m^{-2} for fully hydrophobic surfaces.[13] Based on experimental force-distance measurements (described in Section 3.4) the hydrophobic interaction between two hydrophobic surfaces in water in the range 4–10 nm is roughly exponential and given by

$$E(D) = -2\gamma_i e^{-D/\lambda_0} \quad \text{per unit area,} \tag{13}$$

where $\lambda_0 = 1$–2 nm, and where between two fully hydrophobic surfaces, $\gamma_i = 40$–55 mJ m^{-2}, this value being the *interfacial energy* of the pure hydrocarbon–water interface which, by definition, is half the *adhesion energy*, E_0, at contact, $D = 0$. In the case of partially hydrophobic surfaces, for example, a heterogeneous surface whose hydrophobic area is only a fraction f ($0 < f < 1$) of the total area, the constant γ_i in Eq. (13) becomes replaced by $f\gamma_i$. Such situations arise, for example, when lipid bilayers are stretched, mechanically or osmotically, so that they expose more of their hydrocarbon chains than in the unstressed state when the hydrocarbon chains are shielded from the aqueous phase by the hydrophilic headgroups (Helm *et al*. 1992).

At a separation below 10 nm the hydrophobic force appears to be insensitive or only weakly sensitive to changes in the type and concentration of electrolyte ions in the solution. The absence of a 'screening' effect by ions attests to the non-electrostatic origin of this interaction. In contrast, some experiments have shown that at separations greater than 10 nm the attraction does depend on the intervening electrolyte, and that in dilute solutions, or solutions containing divalent ions, it can continue to exceed the VDW attraction out to separations of 80 nm (Christenson *et al*. 1989, 1990).

The long-range hydrophobic interaction, which has so far been measured directly only between macroscopic surfaces, may not necessarily extrapolate to molecular or sub-molecular groups such as single methyl groups, a paraffin chain or a hydrophobic amino-acid group. There is still no direct evidence that the water structure near the relatively flat, macroscopic surfaces, the forces associated with which are studied by SFA and AFM force measurements, is the same as near a highly curved or heterogeneous surface such as that of a protein residue. Thus, we still can not say much about the *range* of the hydrophobic interactions between small molecular groups. However, the *strength* of the hydrophobic interaction is well known between small molecules in contact in water where – as in the case of macroscopic surfaces – it is significantly stronger than can be accounted for by the VDW force. Moreover, measurements made on macroscopic surfaces, when extrapolated to shorter distances (below 2 nm) and scaled appropriately to molecular dimensions, *do* predict the correct values for the adhesion or binding energy of small hydrophobic molecules in water. Thus, based on such *macroscopic* measurements,[14] the following approximate expressions for the hydrophobic interaction energies between *molecular* hydrocarbon groups in water were obtained (employing the conversion 1 J/molecule $= 1{\cdot}44 \times 10^{20}$ kcal mol^{-1} at 25 °C):

Between two spherical groups each of radius R,

$$E_0 \approx -0{\cdot}7 \times 10^{-10} R\, e^{-D/D_0} \text{ J} \approx -1{\cdot}0 \times 10^{10} R\, e^{-D/D_0} \text{ kcal mol}^{-1}; \tag{14a}$$

[13] These values are based on the Young–Dupré Equation: $\gamma_i = \gamma_{sL} = \gamma_s - \gamma_L \cos\theta$, using $\gamma_s = 25$–30 mJ m^{-2} for the hydrophobic surface, and $\gamma_L = 72$ mJ m^{-2} for water.

[14] These measurements, by Israelachvili & Pashley (1984), were made in the range 4–10 nm between surfactant monolayer-coated surfaces that were not fully hydrophobic.

https://doi.org/10.1017/S0033583501003687 Published online by Cambridge University Press

between two parallel cylinders of radius R (e.g. two hydrocarbon chains) *per unit length*,

$$E_0 \approx -1{\cdot}25 \times 10^{-6} \sqrt{R}\, e^{-D/D_0} \text{ J m}^{-1} = -1{\cdot}8 \times 10^{14} \sqrt{R}\, e^{-D/D_0} \text{ kcal mol}^{-1} \text{ m}^{-1}, \quad (14b)$$

where $D_0 \approx 1{\cdot}0$ nm is the characteristic decay constant for the short-range hydrophobic interaction. For example, the above expressions predict that the hydrophobic binding energy (the free energy of dimerization) for two methane, cyclohexane or benzene groups ($R =$ 0·2–0·3 nm) in contact ($D = 0$, $e^{-D/D_0} = 1$) is

$$E_0 \approx 0{\cdot}7 \times 10^{-10} R \approx 1{\cdot}8 \times 10^{-20} \text{ J} \approx 4\, kT \approx 2{\cdot}5 \text{ kcal mol}^{-1} \text{ at } 25\ ^\circ\text{C},$$

while for two hydrocarbon chains ($R = 0{\cdot}2$ nm) in contact along their length, where the CH_2–CH_2 distance ℓ along a hydrocarbon chain is 0·125 nm, the energy would be given by Eq. (14b) as $E_0 \approx 1{\cdot}25 \times 10^{-6} \sqrt{R\ell} \approx 2{\cdot}2 \times 10^{-21}$ J $\approx 0{\cdot}5\, kT \approx 0{\cdot}3$ kcal mol^{-1} per CH_2 group. All of these values are in good agreement with measured values for the hydrophobic free energies of dimerization of small hydrocarbon groups in water, which fall in the range 2·0–2·7 kcal mol^{-1} for methane, cyclohexane and benzene, and 150–300 cal mol^{-1} per CH_2 for hydrocarbon chains in contact in water (Tanford, 1980; Tucker *et al*. 1981; Israelachvili & Pashley, 1984). If Eqs. (14a) and (14b) also hold at medium to long range, i.e. between small hydrophobic groups that are not in contact, they predict that the hydrophobic interaction energy will be greater than kT at separations D below 1·5 nm (15 Å) between two small hydrophobic groups, and at $D < 2{\cdot}1$ nm (21 Å) between two hydrocarbon chains of length $\ell = 2$ nm (20 Å).

The long-range nature of the hydrophobic interaction[15] has a number of important consequences. In non-biological systems, it is responsible for the rapid coagulation of hydrophobic particles in water and the ease with which water films rupture on hydrophobic surfaces. The consequences of such strong long-range forces, especially if they are also long-ranged at the molecular level, could be very significant for understanding many biological processes: the hydrophobic interaction is the main interaction responsible for stabilizing macromolecules such as proteins and DNA (Cantor & Schimmel, 1980). This contrasts with H-bonds, which are more involved in determining the internal structure.[16] Long-ranged hydrophobic forces may contribute to the rapid and directed folding of proteins, and hydrophobic forces are increasingly being implicated in the adhesion and fusion of biological membranes and cells, as discussed in Section 3.4.

The origin of the hydrophobic force is still unknown. The experimental and theoretical situation has recently been reviewed by Christenson & Claesson (2001). Luzar *et al*. (1987) carried out a Monte Carlo simulation of the interaction between two hydrophobic surfaces

[15] Conventionally, the term *hydrophobic interaction* refers to the free energy of solubilizing a hydrophobic group in water, e.g. the energy needed to take a single liquid alkyl chain from bulk hydrocarbon liquid into water (Kauzmann, 1959; Tanford, 1980). The hydrophobic *force* refers more specifically to the force between two hydrophobic groups in water, e.g. the force between two alkyl chains as a function of their separation. Confusingly, the term 'hydrophobic interaction' is also sometimes used for the 'hydrophobic force' or 'hydrophobic pair potential'.

[16] While H-bonds may be strong as well as directional, their effective strength in binding a H-bonding pair inside a globular protein or ordered helical structure such as DNA has to be compared to their energy in the dissociated (denatured) state in solution, where they can usually form even stronger hydrogen bonds with the solvent water molecules (Voet & Voet, 1995). For example, the measured contribution of a single H-bond to protein stability is 3–6 kcal mol^{-1} (Creighton, 1993) compared to 2·5–10 kcal mol^{-1} in solution or in some alternative configuration (Joesten & Schaad, 1974). In contrast, the strength of hydrophobic bonding is automatically measured relative to the dissociated state of the interacting species in aqueous solution.

https://doi.org/10.1017/S0033583501003687 Published online by Cambridge University Press

across water at separations below 1·5 nm. They obtained a decaying oscillatory force superimposed on a monotonically attractive curve. More recent work (Lum *et al*. 1999; Leung & Luzar, 2000; Luzar & Leung, 2000; Bratko *et al*. 2001) suggests that hydrophobic surfaces or patches generate a depleted region of water around them (cf. Fig. 9(*c*)) that gives rise to a long-range attractive 'depletion force', similar to the depletion force between surfaces in solutions containing non-adsorbing polymers, described below.

It has also been suggested that the hydrophobic force is a kind of enhanced VDW force arising from the peculiar dielectric and proton-hopping properties of water. Other models have suggested an electrostatic origin for this force, postulating the existence of fluctuating or transient charges on hydrophobic surfaces; but the apparent lack of sensitivity of hydrophobic forces to ionic changes make this explanation unlikely. Whatever is the true picture, it is questionable whether the hydrophobic force should be viewed as an ordinary type of structural force – simply reflecting the geometric packing of the water molecules. However, it is conceivable that the H-bonding network in liquid water could extend or be correlated over a much larger region of space than normal molecular correlations. Whatever the answer, it is clear that the situation in water is governed by much more than the simple molecular packing effects that seem to dominate the solvation or structural forces in simpler liquids.

1.6 Steric, bridging and depletion forces (polymer-mediated and tethering forces)

Many biological surfaces expose flexible polymer-like hydrophilic groups into the aqueous phase, such as polysaccharides, ligand groups at the ends of tethers, and lipids with long headgroups. In these cases the chains are usually attached (chemically bound) to the membrane or protein surface at one end. In other cases, free (unattached) polymers or polyelectrolytes such as hyaluronic acid or mucin also exist in solution. In either case, the presence of these polymers, whether bound or free, can dominate the interaction forces between two surfaces. For reviews on polymer interaction forces see (Patel & Tirrell, 1989; Ploehn & Russel, 1990).

Steric forces arise between surfaces containing bound coils when they approach each other in aqueous solution. In a theta solvent, where the segments do not interact strongly with each other or repel each other in the solution (as occurs with polysaccharides, PEO and PEG[17]), the forces between the polymer-covered surfaces are monotonically repulsive. They have an exponential form at separations larger than R_g or R_F and increase more steeply closer in. The magnitude of the repulsion depends on the surface coverage of the chains, Γ. Simple approximate equations for the interaction energies and pressures between two flat surfaces are (see Israelachvili, 1991)

at low coverages (mushrooms, $s > R_F$): $E(D) \approx +36\Gamma kT e^{-D/R_F}$ J m^{-2}

$$P(D) = -dE/dD \approx +36(\Gamma kT/R_F)e^{-D/R_F} \text{ N m}^{-2}, \quad (15)$$

at high coverage (brushes, $s < R_F < L$):[18] $E(D) \approx +32\Gamma kT(L/s)\, e^{-D/L}$ J m^{-2}

$$P(D) = -dE/dD \approx +32(\Gamma kT/s)\, e^{-D/L} \text{ N m}^{-2}, \quad (16)$$

[17] Traditionally, polyethylene glycol (PEG) referred to low MW chains (< 20 kDa), while polyethylene oxide (PEO) to higher MW chains. This distinction is no longer used, and PEO and PEG are often used interchangeably. In this text, they refer to the same polymer.

[18] Equation (16) is an approximate form of the Alexander–de Gennes Equation for the interaction between two polymer brush layers (de Gennes, 1987). This equation was originally developed for high

https://doi.org/10.1017/S0033583501003687 Published online by Cambridge University Press

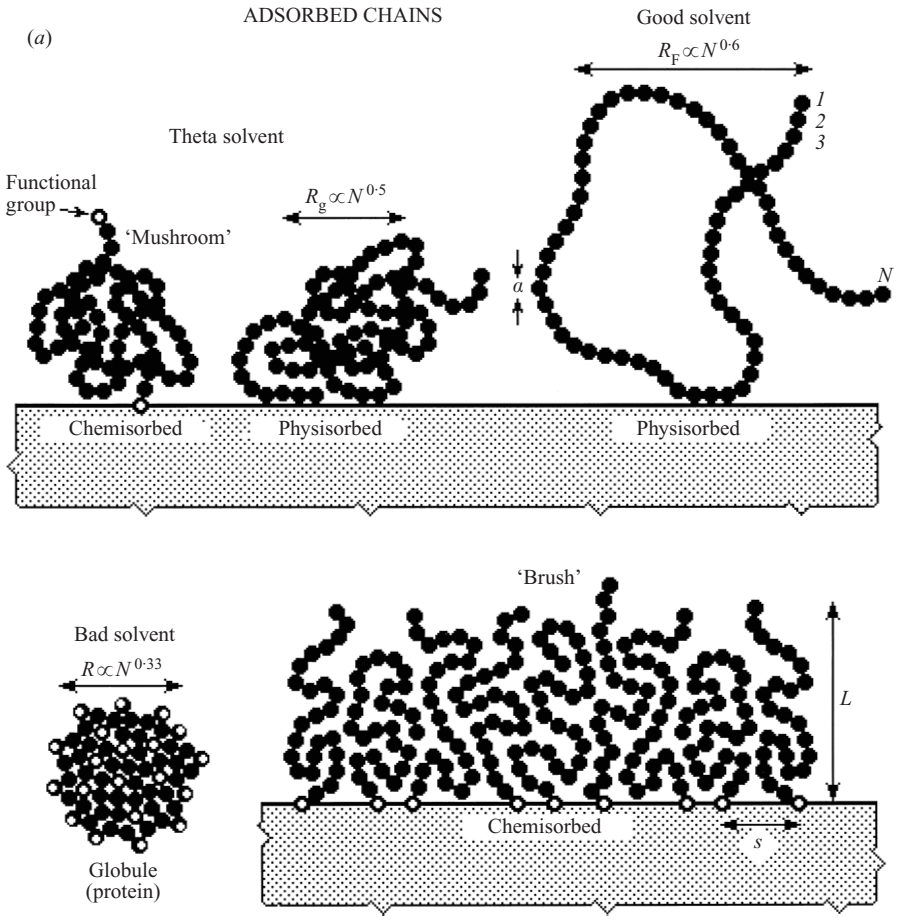


Fig. 11. For legend see opposite.

where the coverage $\Gamma = 1/s^2$ is in units of number of molecules per square meter. We may note that the main difference between low coverage and high coverage is that in the latter case the magnitude of the interaction energy is 'magnified' by L/s – the ratio of the brush layer thickness to the distance between polymer attachment sites on the surface.

As a numerical example of steric forces, if polymer chains of MW 10000 Da having a Flory radius of $R_F = 5$ nm are attached to a surface at a coverage near close packing (where $s = R_F$), the repulsive pressure between two planar surfaces at $D = 2{\cdot}5$ nm and $T = 37$ °C will be $P = -\mathrm{d}E/\mathrm{d}D = +36(\Gamma kT/R_F)\mathrm{e}^{-D/R_F} = 7{\cdot}5 \times 10^5$ Pa or 7·5 atm. This is of the same order as the DL repulsion between two charged membrane surfaces at this separation.[19] Some real examples of steric forces are given in Section 3.2.

MW coils but it has been found to quantitatively account for the forces between surfaces exposing short-chained but flexible segments, such as bilayers with head-groups consisting of a few hydrophilic, but uncharged, groups such as ethylene oxide (EO) and sugar groups (see Fig. 12(*a*, *b*) and Section 3.2). The exact Alexander–de Gennes equation for the pressure is: $P(D) = +(kT/s^3)[(2L/D)^{\frac{9}{4}} - (D/2L)^{\frac{3}{4}}]$ for $D < 2L$.

[19] For example, for two surfaces with a surface potential of $\psi_0 = -75$ mV in 0·15 M NaCl, Eq. (9) predicts a pressure of $P = 3{\cdot}6 \times 10^5$ Pa at $D = 2{\cdot}5$ nm.

https://doi.org/10.1017/S0033583501003687 Published online by Cambridge University Press

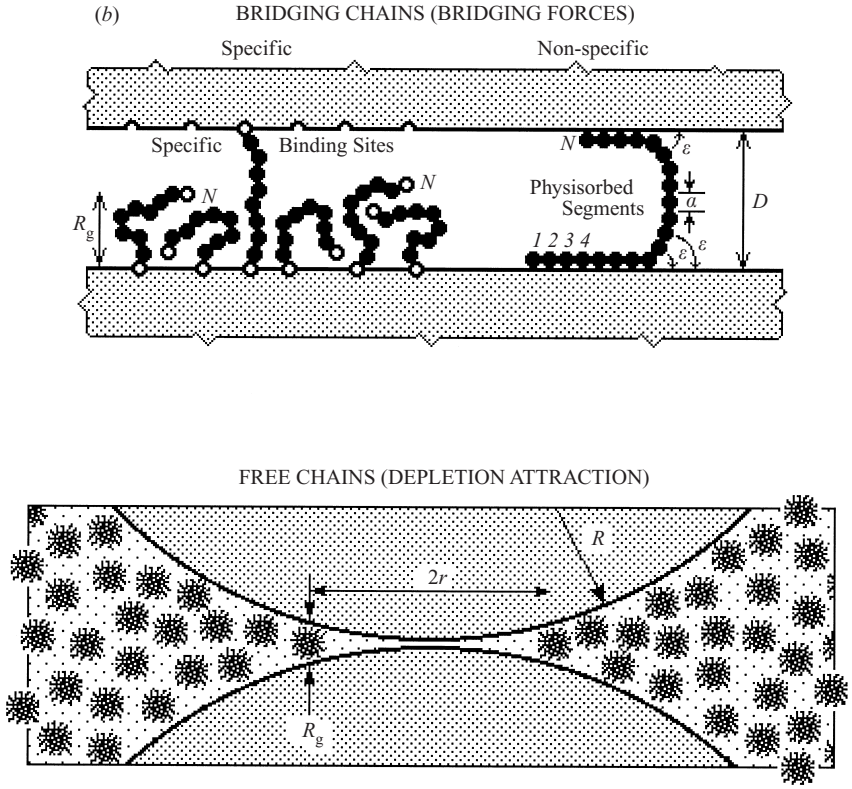


Fig. 11. Surface bound and free coils (polymer chains) in solution. (*a*) The binding to a surface can be via chemical bonds (chemisorption) or physical bonds (physisorption). (*b*) The forces between such surfaces can be attractive or repulsive or both, i.e. attractive at large separations but repulsive at small separations, or vice versa. The swollen radii of chains in solution, R, varies as $R \propto N^n$ where N is the number of monomer units (segments) and n is some number (exponent) that usually lies between 0·33 and 0·60 depending on the flexibility of the coil and on the solvent – the better the 'solvent quality' the more the segments repel each other, the more 'expanded' is the coil in solution, and the higher is n. Four regimes have special significance: in the 'fully stretched' or 'fully extended' regime, $R \propto N$, where R is now the length of the polymer coil; in a 'good solvent' the segments are very hydrophilic or highly charged and $R_F \propto N^{0·6}$ where R_F is known as the Flory radius; in a 'theta solvent' the segments do not attract or repel each other in solution and $R_g \propto N^{0·5}$ where R_g is known as the radius of gyration; finally, in the 'collapsed state', $R \propto N^{1/3}$, the polymer totally collapses into a solvent-free solid particle such as a globular protein. A distinction is also made between coils that are well separated on a surface, known as 'mushrooms', and those that strongly overlap, known as 'brushes'. In the case of end-adsorbed brushes, each coil is attached to the surface at one end only, is separated from its neighbor by a distance s ($s < R_F$), and extends away from the surface by a mean distance L (the brush layer thickness, where $L > R_F$).

A surface-bound polymer may contain functional groups along its chain or a specific ligand group at its free end. When the guest molecule or membrane approaches a host that exposes binding sites for these functional groups, a '*bridging*' attraction can result between the two structures once they are close enough for some initial binding to occur (Fig. 11). Following this initial binding, the two structures will be pulled further together, thereby allowing for even more bonds to form. The resulting 'bridging' force can be of long range – much longer than the radius of gyration, R_g, or Flory radius, R_F, because a significant fraction of groups actually extend well beyond R_g at any moment, and these instantly bind to the opposite surfaces (Jeppesen *et al*. 2001).

https://doi.org/10.1017/S0033583501003687 Published online by Cambridge University Press

There is no simple expression for the bridging energy $E(D)$ or force $F(D) = -\mathrm{d}E(D)/\mathrm{d}D$ between two specific binding sites that are linked together by a single flexible tether composed of N monomer units each of length σ (Fig. 11). Various theoretical analyses of *freely jointed chains* have predicted (i) the force is attractive and diverges as D approaches the fully extended tether length, $D \to L_{\max} = N\sigma$, (ii) it is zero ($F = 0$) at the equilibrium separation near $D \approx R_g = \sqrt{N}\sigma$, as might be expected, and (iii) it diverges again (repulsively) as $D \to 0$ due to the steric-entropic compression of the chains. The three limiting forms for the force per bridging molecule are (note that $L_{\max} = \sqrt{N}R_g$):

$$\text{For } D \to L_{\max}: \quad F(D) \approx -NkT/(L_{\max} - D) \tag{17a}$$

$$\text{For } D \approx R_g: \quad F(D) \approx 3\,kT(D - R_g)/R_g^2 \tag{17b}$$

$$\text{For } D \to 0: \quad F(D) \approx \frac{NkT}{D}\left(\frac{R_g}{D}\right)^n \quad \text{where } n = 0\text{–}2. \tag{17c}$$

We may note that for small displacements about the equilibrium separation at $D \sim R_g$ the force is linear in D and, therefore, 'elastic-like' (cf. deGennes, 1976; Pincus, 1976, 1977). The energy is therefore parabolic around $D \sim R_g$. Thus, as could have been expected, the tendency is for a stretched coil to pull its ends together, but further compression is resisted once the coil reaches its equilibrium configuration. In the alternative *worm-like chain* (WLC) model (Bustamante *et al.* 1994), where the tether is viewed as an elastic element, the limiting force corresponding to the fully stretched tether is given by $F(D) = -L_{\max}^2 kT/4L_p(L_{\max} - D)^2$ as $D \to L_{\max}$, where L_p is the persistence length. This equation differs from Eq. (17a) mainly in the squared term in brackets in the denominator.

In contrast to the situation for end-attached or end-functionalized chains, there are no general expressions for the bridging forces between non-specifically adsorbed chains where each segment can bind to both surfaces. Such systems also depend on the previous history, exhibit very slow conformational relaxation times, and are rarely at equilibrium over reasonable time scales. Figure 11 also shows a bridging mechanism involving a homopolymer[20] where, as each additional segment binds to one of the surfaces, it pulls it closer to the other surface by a distance $\Delta D = -\sigma$ and the energy changes by $\Delta E = -\epsilon$, this being the binding energy per segment. The attractive energy and force for such a system is therefore given by

$$E(D) = \epsilon(L_{\max} - D)/\sigma$$

and

$$F(D) = -\mathrm{d}E/\mathrm{d}D = -\epsilon/\sigma \quad \text{per bridging molecule, for } D < L_{\max}. \tag{18}$$

For example, if $\epsilon = 10\,kT = 4{\cdot}3 \times 10^{-20}$ J (at 37 °C) and $\sigma = 0{\cdot}4$ nm, the pulling force will be $\sim 1{\cdot}1 \times 10^{-10}$ N or ~ 110 pN per tether. Note that this bridging force is constant, i.e. it is independent of D. However, between two spherical particles the net force will vary linearly with D as determined by the Derjaguin Approximation (see Fig. 3). Such 'linear' bridging forces have been measured between certain surfaces (Ruths *et al.* 1997), but they are by no means general. In other cases bridging forces appear to be exponentially attractive (Israelachvili *et al.* 1984) or to follow some power-law distance dependence, as represented by Eq. (17).

[20] In a *homopolymer* each segment is chemically the same. Biological polymers such as a polypeptide chain are *heteropolymers* where each segment is different.

https://doi.org/10.1017/S0033583501003687 Published online by Cambridge University Press

Strongly adhesive bridging forces but of a different kind also arise between charged surfaces that are bridged or cross-linked by divalent counterions such as Ca^{2+} whose two positive charges can bring together two negative charges. Such ionic bridges can occur both *out-of-plane*, between two surfaces, and *in-plane*, on a single surface. An example of the latter is the bringing together of the anionic headgroups of phosphatidylserine or phosphatidylglycerol lipids in a monolayer or bilayer composed of a mixture of charged and uncharged lipids. Divalent and multivalent ion bridges can have a dramatic effect both on the internal structure of a membrane (causing phase separation, clustering and local changes in membrane curvature) and on the gross membrane structure (causing stacking).

Depletion forces arise when polymers are free in solution, i.e. when they are not attached or adsorbed to either surface (Fig. 11*b*). Depletion forces are often used in biomedical experiments to induce cells to adhere or fuse to form 'hybrid' cells (hybridomas) (Boni *et al.* 1981, 1984; Poste & Nicholson, 1978). For example, PEO is commonly used to fuse cells of different types such as mouse cells and human cells. This is a common method used to produce immortal B-cells for making monoclonal antibodies, melanoma cells in monoclonal antibody production, and in hybridoma production (Sowers, 1987). Depletion forces have a similar *entropic* origin to the first potential energy minimum of the oscillatory solvation force (Fig. 10). They were first proposed by Asakura & Oosawa (1954, 1958) in order to account for the unexpected attractive forces that are generated between large colloidal particles upon dissolving non-adsorbing polymer and small colloidal particles in the solution. This force arises from the osmotic pressure between (*a*) the bulk solution that contains polymer at a concentration ρ, and (*b*) the 'depletion zone' of radius r between the two surfaces that is free of polymer (Fig. 11*b*). An osmotic pressure difference is generated because the water is driven out into the bulk solution (as if there were a semi-permeable membrane surrounding the depletion zone) which acts to drive the two surfaces together. The depletion pressure between two flat surfaces is therefore the same as the osmotic pressure and is given by

$$P = -\rho kT, \tag{19}$$

where ρ is in units of number of molecules per unit volume (m^{-3}) so that P is in units of J m^{-3}, which is the same as N m^{-2} or Pa. For example, for a 5 % by weight solution of PEO of MW 8000 Da in water (for which $R_g = 5$ nm), the attractive pressure will be[21] $P = 0{\cdot}05(6{\cdot}022 \times 10^{29})(4{\cdot}3 \times 10^{-21})/8000 = 1{\cdot}6 \times 10^{4}$ N m^{-2} at 37 °C. Note that just as in the case of the linear bridging force described above, this force is constant and independent of the separation D between the surfaces. However, the force acts over a finite distance of about R_g, so that it corresponds to an interaction energy that varies linearly with distance according to

$$E(D) = -\int \rho kT \times \mathrm{d}D = -\rho kT(R_g - D) = -E_0(1 - D/R_g) \quad \text{per unit area (for } D < R_g), \tag{20}$$

i.e. the energy is zero at $D > R_g$ then decreases linearly to $E_0 = E(0) = -\rho R_g kT$ at contact ($D = 0$). One may calculate the depletion force between two curved surfaces such as two vesicles (Kuhl *et al.* 1996) by applying the Derjaguin Approximation (cf. Fig. 3). Thus, for two vesicles of radius R (Fig. 11*b*) their adhesion force due to the depletion effect is

$$F = \pi R E_0 = -\pi R R_g \rho kT. \tag{21}$$

Using the above values for a PEO solution ($\rho = 3{\cdot}8 \times 10^{24}$ m^{-3} and $R_g = 5$ nm) two vesicles

[21] The conversion of concentration C_W in units of weight % in water to ρ in number of molecules per unit volume (m^{-3}) is given by: $\rho = 6{\cdot}022 \times 10^{29}\, C_W/M$, where M is the polymer MW in Da.

https://doi.org/10.1017/S0033583501003687 Published online by Cambridge University Press

of radius $R = 100$ nm will therefore experience an enhanced adhesion force due to depletion of $F = 25$ pN. This may be compared with the (maximum) contribution from the VDW force for this system which is of order $F_{ad} = AR/12D_0^2 = 500$ pN (assuming $D_0 = 0{\cdot}4$ nm). The depletion attraction is generally weak except in the case of high concentrations of low MW polymers: thus, in the above example, if $\rho = 10\,\%$ and $R_g = 1$ nm the depletion force would be 10 times stronger. Furthermore, it is strictly the *activity* and not the *concentration* that should be used for ρ in Eqs. (19)–(21). For some polymers, such as PEO and PEG, their activities can be much larger than their concentrations. This significantly enhances the depletion forces they generate. Experimental measurements of these forces, and their comparison with theoretical expectations, are described in Section 3.5.

In the case of pure liquids or solvents between two inert, non-adsorbing surfaces, e.g. water between two hydrophobic surfaces, one expects there to be an oscillatory force between them whose final primary minimum is essentially the same as the depletion energy at contact (Section 1.5). In this case we may associate R_g with σ, and ρ with $1/\sigma^3$ so that we obtain

$$E_0 \approx -kT/\sigma^2 \tag{22}$$

which in the case of water ($\sigma = 0{\cdot}25$ nm) gives $E_0 = -66$ mJ m^{-2} at room temperature. This energy is very close to the (measured) hydrophobic energy at contact of ~ 100 mJ m^{-2} (which, by definition, is twice the interfacial energy of $\gamma_i \approx 50$ mJ m^{-2}). While the contact energy appears to be reasonably well-predicted by a simple depletion mechanism, the long-range non-oscillatory nature of measured hydrophobic forces suggests a more complex cooperative process.

However, as mentioned above, recent analytic theories (Lum *et al*. 1999) and GCMC[22] simulations (Luzar *et al*. 1987; Luzar & Leung, 2000; Bratko *et al*. 2001) do indicate that a depletion-like mechanism is responsible for the hydrophobic interaction, where the region immediately adjacent to a hydrophobic surface is more vapor-like than liquid-like. The predicted interaction potential is oscillatory at long range but becomes monotonic closer in (below the Kelvin radius, but in practice depending on the surface area and time!) and the final adhesion energy is more complex than given by Eq. (22): the numerator is larger than kT and is also related to the high energy of the unsaturated H-bonds of the water molecules in the depletion layer.

1.7 Thermal fluctuation forces: entropic protrusion and undulation forces

Monotonically repulsive thermal fluctuation forces (also known as steric–hydration forces when the solvent is water) are a subset of the steric forces described above when the surfaces themselves are flexible or expose flexible short-chained molecular groups. The main requirement is that the surfaces are not smooth or rigid, but dynamically rough or 'fluid-like'.[23] As illustrated in Fig. 12, such situations occur with surfaces that expose mobile

[22] In contrast to a simple MC simulation, a GCMC simulation includes a bulk reservoir with which the molecules in the gap can exchange and which ensures constancy of the chemical potential throughout the system or 'ensemble'. GCMC simulations are much more realistic for modeling interactions in a medium than MC simulations.

[23] Biological surfaces and interfaces are especially difficult to categorize into smooth or rough, hard or soft, rigid or flexible. Thus, a membrane surface exposing polysaccharide chains could be treated as a rigid surface with end-grafted polymer chains if the chains are long, but as a soft undulating membrane if the chains are short.

https://doi.org/10.1017/S0033583501003687 Published online by Cambridge University Press

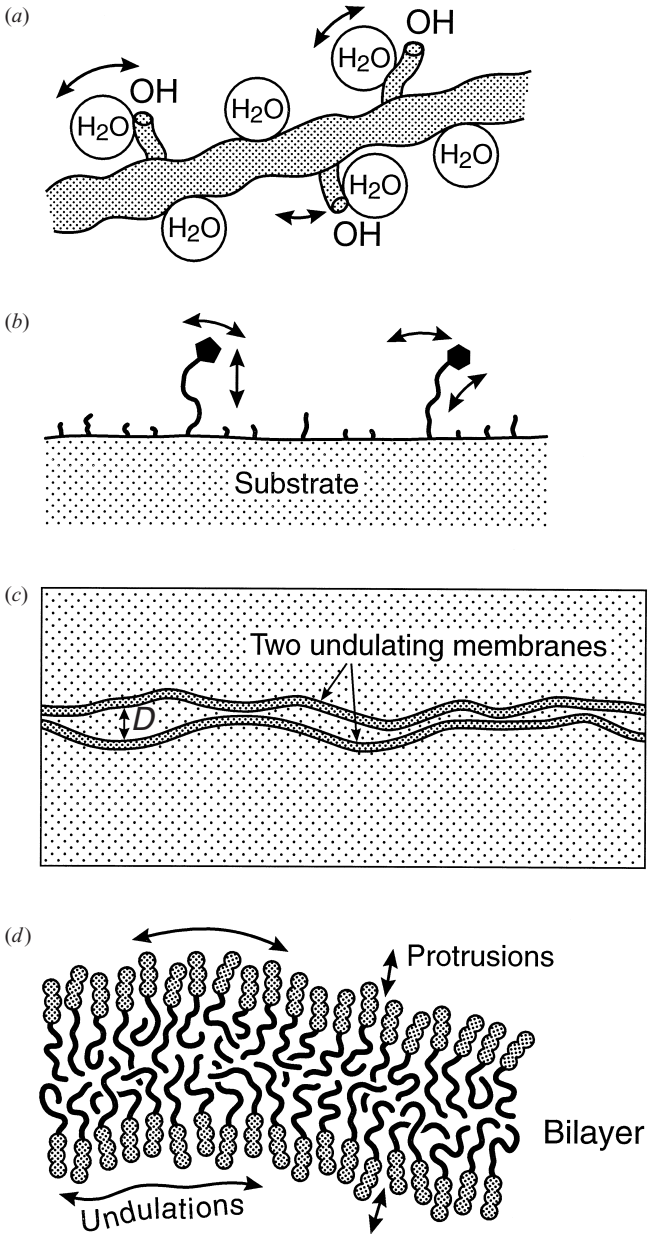


Fig. 12. Schematic illustrations of different types of mobile surfaces that give rise to repulsive thermal fluctuation forces. (*a*) and (*b*): short, protruding hydrophilic side chains from polymer backbones or surfaces. (*c*) and (*d*): membrane undulations and molecular-level protrusions of hydrophilic lipid headgroups. Such flexible chains interact like end-grafted polymer chains and give rise to a short-range entropic repulsion in water which has often been erroneously attributed to water structure (Israelachvili & Wennerström, 1992). Indeed, rather than keep surface chemical groups apart in the solvent, these interactions are an expression of intermittent collisions (i.e. contact) between the surface groups.

groups, for example, surfaces of micelles, bilayers, emulsions, soap films, biomembranes, biopolymers, polyelectrolytes, and rigid colloidal surfaces with protruding 'hairs' or tether groups as occur in lubricating oils, paints and toners. In many cases, the protruding molecular

https://doi.org/10.1017/S0033583501003687 Published online by Cambridge University Press

groups are 'hydrated', namely there is a strongly bound first layer of water, but beyond that the liquid behaves more or less with its bulk fluid properties. When two such surfaces approach, a monotonically repulsive steric force arises as soon as the outermost mobile groups overlap. These forces must be distinguished from the oscillatory solvation forces that arise between *smooth* and *rigid* surfaces that are usually also crystalline and highly structured. Any intrinsic oscillations are smeared out between fluid-like surfaces because the thermal or Brownian motion of the molecular groups at these interfaces make them dynamically 'rough' at any instant, even though the surfaces may appear to be perfectly smooth on a time average. This smearing out is also reflected in the structure of stacked lamellae: X-ray diffraction studies (Caffrey, 1983) have shown that thin clay sheets adopt only discrete separations between each other when pressed together in water, corresponding to discrete layers of water molecules. In contrast, stacked lipid bilayers show no such 'quantized' periodicity but change their separation continuously in water. It appears that oscillatory forces, which are common in the interactions of hard colloidal particles, clay sheets and structured materials (e.g. at grain boundaries), are far less common in biology where surfaces tend to be soft or 'fluid-like'.

Thermal fluctuation forces are usually of short-range and repulsive, and are very effective at stabilizing the attractive VDW forces at some small but finite separation that can reduce the adhesion energy or force by up to three orders of magnitude or eliminate it altogether. It is mainly for this reason that fluid-like micelles and bilayers, biological membranes, emulsion droplets (in salad dressings) or gas bubbles (in beer) adhere to each other only very weakly.

Because of their short range it was, and still is, commonly believed that these short-range repulsive 'hydration' forces arise from water ordering or structuring effects, and that they reflect some unique or characteristic property of water. However, it is now known that these repulsive forces also exist in other liquids (Persson & Bergerstahl, 1985; McIntosh & Simon, 1994). Moreover, they appear to become stronger with *increasing* temperature, which is unlikely for a force that originates from solvent ordering effects. Recent experiments, theory and computer simulations (Granfeldt *et al*. 1991; Israelachvili & Wennerström, 1992) have shown that these repulsive forces have an entropic origin – arising from the osmotic repulsion between exposed thermally mobile surface groups once these overlap in a liquid. These forces therefore have the same origin as the 'steric' forces between polymer-coated surfaces in liquids which were described in Section 1.6, and indeed we shall see later that the same theory can account quantitatively for the measured short-range 'hydration' forces between lipid bilayers and other fluid-like interfaces. Thus, thermal fluctuation forces can be successfully modeled in terms of the steric–entropic repulsion between surfaces exposing short polymer-like chains or tethers that are attached to the surface at one end but are otherwise free in the solution (Israelachvili & Wennerström, 1992). Theoretically, the entropic short-range repulsion between two lipid bilayers or micelles exposing hydrophilic headgroups attached to the ends of hydrophobic hydrocarbon chains that can protrude in and out of the membrane (see *protrusions* in Fig. 12(*d*)) is expected to be roughly exponential and given by the approximate expressions (Israelachvili, 1991)

$$\text{for the energy} \qquad E(D) \approx +3\Gamma kT\,\mathrm{e}^{-D/\lambda_0}\ \mathrm{J\ m^{-2}}$$

$$\text{for the pressure} \quad P(D) = -\mathrm{d}E/\mathrm{d}D \approx +3(\Gamma kT/\lambda_0)\,\mathrm{e}^{-D/\lambda_0}\ \mathrm{N\ m^{-2}}, \tag{23}$$

where Γ is the surface density of protruding molecules in units of m^{-2}, and λ_0 is the decay

https://doi.org/10.1017/S0033583501003687 Published online by Cambridge University Press

length which typically ranges from 0·1 to 0·3 nm depending on the hydrophobicity or hydrophobic energy per unit length of the chains attached to the protruding hydrophilic groups. At small separations, below 0·5–1·0 nm, the repulsion increases more steeply and asymptotes to infinity as D approach zero. Thus, true molecular contact where all the water is forced out from between the two surfaces is prevented unless the hydrated groups are also squeezed out. Numerical and experimental examples for protrusion forces are given in the next sub-section and in Section 3.2.

Comparing Eq. (23) for the protrusion force (Fig. 12(*d*)) with Eqs. (15) and (16) for the steric repulsion between surface-bound polymers (Fig. 12(*a*, *b*)) shows them to be formally the same. Indeed, both have the same (entropic) origin, and are close to exponential at intermediate distances but increase steeply to infinity as $D \to 0$. At small separations, these entropic, temperature-dependent forces have a similar origin to the pressure of a gas, given by Boyle's Law, $P = RT/V$, or the osmotic pressure of a solution, given by $P = \rho RT$.[24] It is for this reason that the repulsion always diverges as $D \to 0$ (just as the pressure diverges as $V \to 0$ or as $\rho \to \infty$). This is known as the 'osmotic limit' (see footnote 12).

Another type of thermal fluctuation force is the *undulation* force, arising from long wavelength thermal ripples of membranes that become confined as two membranes approach each other (Fig. 12(*c*)). This confinement reduces the entropy of the system which results in a repulsive *undulation* force that follows a power-law distance dependence given by (see Helfrich, 1978; Servuss & Helfrich, 1989):

$$P(D) \approx +kT/K_c D^3 \text{ N m}^{-2}, \tag{24}$$

where K_c is the curvature or bending modulus of the membrane which, typically, lies in the range $K_c = 10^{-21}$ J $= 0{\cdot}1$–$10\ kT$. These forces have a similar magnitude and the same distance dependence as the VDW force but are of opposite sign. Membrane undulations are further discussed in Section 3.2.

An important conceptual consequence of recent theoretical and experimental understanding of thermal fluctuation forces is that they have been able to quantitatively account for the mysterious repulsive 'hydration' forces in terms – not of water structure, but of the osmotic pressure of confining surface-bound hydrophilic groups. With this interpretation, there should be no thick 'hydration layers' preventing membranes, proteins, ligands, receptors and other hydrophilic surfaces or groups from coming into contact with each other. Indeed, it is this very contact or molecular collisions that gives rise to the short-range repulsion. Furthermore, in the case of membranes, vesicles and cell–cell interactions, including membrane fusion, there should be no thick 'hydration barrier' that must be 'overcome' before the surfaces or molecular groups on the opposing surfaces can interact directly with each other, adhere or fuse. The only real hydration barrier being the first layer of water molecules directly in contact with the surfaces, i.e. the primary hydration shell of strongly bound water (which may or may not be present). Likewise, the effect of a 'dehydrating agent' or 'water-structure breaker' is likely to be greater on the nearby surfaces than on the water.

[24] These simple equations assume point molecules. In practice, if the interacting hydrophilic groups are large or carry a primary hydration shell of strongly bound water molecules (cf. Fig. 12*a*), their finite excluded volume b must be included as a correction term in the above equations. In a first approximation, this may be done by replacing all free volumes V by $(V-b)$, or densities $\rho = 1/V$ by $1/(V-b) = \rho/(1-\rho b)$. As can be readily seen, this acts to enhance the osmotic repulsion.

https://doi.org/10.1017/S0033583501003687 Published online by Cambridge University Press

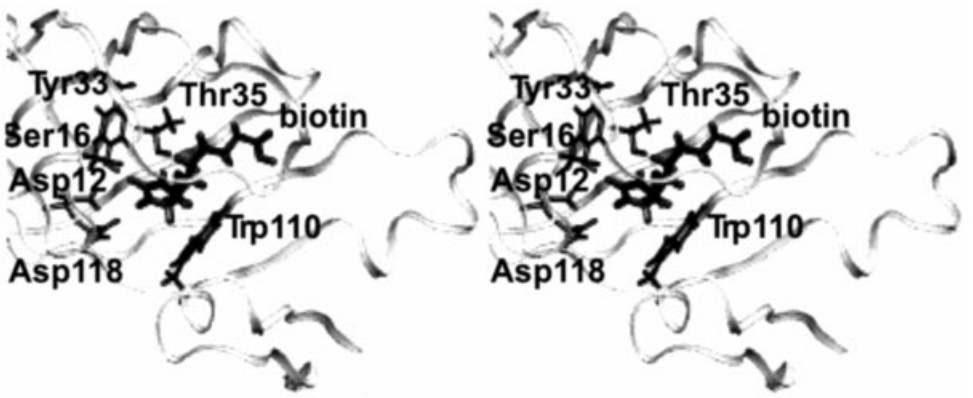


Fig. 13. Structure of biotin (ligand, black stick structure) bound within the avidin (receptor, grey backbone) binding pocket. Several different intermolecular forces or 'bonds' stabilize this complex. The ureideo ring of the biotin head forms hydrogen bonds and complementary electrostatic interactions with the side chains of Asp118, Asp12 and Ser16. The tyrosines on the protein also interact with the aromatic region of the biotin. In addition, several nonpolar side chains form complementary VDW and hydrophobic contacts with the long hydrocarbon tail of the biotin. (Reprinted with permission from *Biophys. J.* **72**, 1568–1581 (1997).)

1.8 Comparison of the magnitudes of the major non-specific forces

The protrusion force is of short-range (effective only at $D < 2$ nm), but it is strong because Γ in Eq. (23) is usually large. This occurs because all the molecules at the interface, for example, all the lipids in Fig. 12(*d*), participate in the interaction. Thus, for two lipid bilayers where each headgroup occupies an area of $a = 0{\cdot}70$ nm^2 ($\Gamma = 1/a = 1{\cdot}4 \times 10^{18}$ m^{-2}), for $\lambda_0 = 0{\cdot}2$ nm, the repulsive protrusion pressure at $D = 0{\cdot}4$ nm will be $P = +12$ MPa (about 120 atm). For reasons discussed in the previous section, this value is similar to the other steric forces between surfaces exposing short- or long-chained polymer coils or tethered groups. More importantly, this value may be compared with the *attractive* VDW pressure, $P = -A/6\pi D^3$, which is of order -8 MPa, and the repulsive DL pressure which is of order $+5$ MPa, at the same separation.[25] Clearly, these three values are very similar in magnitude, indicating that these three major forces between biological surfaces are delicately balanced. On the other hand, the hydrophobic interaction, when it arises between two fully hydrophobic surfaces or patches, greatly exceeds all the other non-specific interactions both in magnitude and range. Thus, at the same separation of $D = 0{\cdot}4$ nm, the attractive hydrophobic pressure, $P \approx -2(\gamma_i/\lambda_0)e^{-D/\lambda_0}$, will of order 50 MPa for $\gamma_i = -50$ mJ m^{-2} and $\lambda_0 = 1{\cdot}5$ nm. This value is a factor of 5–10 greater than any of the other three non-specific interactions discussed just above.

1.9 Bio-recognition

Biospecific interactions are a particular class of highly complementary, non-covalent bonds between biological molecules. The nature of these bonds is exemplified by the high degree of shape and chemical complementarity exhibited in the crystal structures of RL complexes. Figure 13 shows the crystal structure of biotin in the binding site of avidin (Izrailev *et al.* 1997). This complex has one of the highest affinities known at 10^{15} M^{-1}, which corresponds

[25] Calculated using the same typical values for charged bilayer membranes as in previous calculations.

https://doi.org/10.1017/S0033583501003687 Published online by Cambridge University Press

to a binding free energy of $\sim 35\ kT$ at room temperature. The different, labeled amino acids in the figure all contribute to the total biotin binding energy. This is typical of recognition interactions, which are stabilized by multiple interactions between the receptor and ligand. In the case of avidin, the head of the biotin contacts Tyr33, Ser16, Asp118, Trp110, Asp12, and the tail forms contacts with Thr35 and Arg114 (Izrailev *et al*. 1997). These involve ionic (electrostatic and hydrogen-bonding) interactions, as well as van der Waals and hydrophobic interactions.

Another distinguishing characteristic of this and other recognition interactions is the close geometrical and chemical fit between the ligand and binding pocket. The ureideo ring of biotin, for example, is positioned tightly in the binding pocket, and forms short-range hydrogen and electrostatic bonds with Ser16, Asp12 and Asp118. Due to the power law distance dependence of most intermolecular potentials at short separations, small decreases in the separation distance dramatically increase the attraction. For example, reducing the distance between the ureideo ring and Trp110 from 0·5 nm to 0·2 nm, which could arise from conformational changes in the protein backbone, increases the VDW attraction by nearly three orders of magnitude.

In addition to the geometric complementarity, chemical complementarity is also essential in recognition, particularly between polar and ionic groups. Hydrogen bonds are directional, and the relative orientations of H-bonding chemical groups can tune the binding energy. The amino-acid side-chains in streptavidin's binding pocket (Fig. 13) are precisely positioned to optimize several different physical bonds with the biotin. The close chemical and physical fits that are illustrated in Fig. 13 are distinguishing attributes of all biological recognition interactions.

Because of the strong dependence of the binding energy on local geometry and chemistry, the bond energy falls off rapidly with distance. Biospecific bonds are therefore typically short-ranged. Indeed, the range of the specific biotin–streptavidin bond is < 1 nm (Izrailev *et al*. 1997). In some cases the forces originating in the binding site do extend beyond the protein surface (Northrup *et al*. 1984; Klapper *et al*. 1986; Sharp & Honig, 1990; McCammon, 1998). As already mentioned, long-range electrostatic fields due to charges either in or around the binding site sometimes extend several nanometers from the protein surface. This gives rise to a long-range steering force, which directs the ligands to the binding pocket (McCammon, 1998). However, these electrostatic forces alone do not distinguish between different charged molecules and are therefore nonspecific.

Two characteristics are often used to define the specificity of 'biospecific' bonds: (1) the affinity or binding energy relative to kT, and (2) the structural and chemical uniqueness of the binding site. Binding energies of only a few kT per participating bond ensure that the lifetime of the complex will be sufficient to effect chemical or physical changes in the receptor and/or ligand. Since bond lifetimes are proportional to $e^{\Delta E_{act}/kT}$, two or three weak bonds acting together can change a short-lived association (with a lifetime $\tau_0 < 10^{-8}$ s) to a long-lived complex, with $\tau_0 > 1$ s.[26] In addition, the structural uniqueness or 'geometric fit' ensures that only the ligand or structurally similar molecules can partition into the binding

[26] For example, if the lifetime of a typical H-bond of energy $\sim 10\ kT$ is 10^{-8} s, if we assume all break simultaneously, then three H-bonds acting together will have a lifetime of $10^{-8} \times e^{30}/e^{10} = 5$ s. This is ~ 500 million longer due to a mere three-fold increase of the binding energy. In reality the lifetime will be much shorter because the bonds can break sequentially. The lifetime is, however, still much greater than for a single bond.

https://doi.org/10.1017/S0033583501003687 Published online by Cambridge University Press

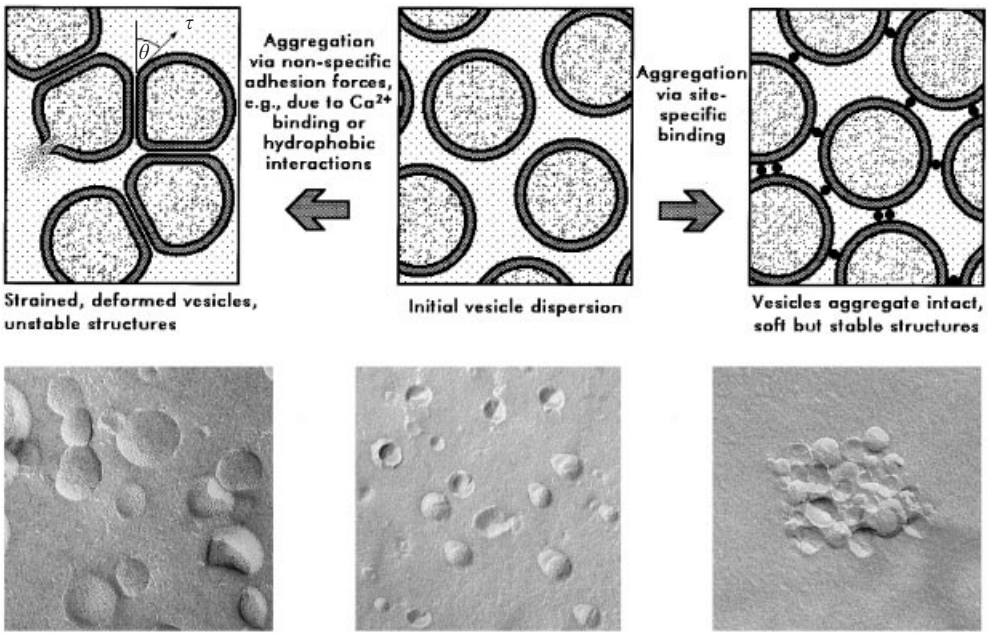


Fig. 14. *Left*: vesicles aggregating via non-specific forces, showing deformation stresses. *Right*: stress-free aggregation via site-specific binding, showing no deformations. Controlled self-assembly of such stable multivesicular aggregates or 'vesosomes' can now be bioengineered in the laboratory (Chiruvolu *et al*. 1994; Walker *et al*. 1997; Zasadzinski, 1997) and offers a path towards the processing of biomimetic microstructures and biomaterials such as those shown in Fig. 2. Also, by measuring the deformations, such as the contact angles, θ, of adhering vesicles, one can estimate the stress on the bilayers or membranes and/or the adhesion energy between them (cf. Eq. (44)) which can then be compared with other, more direct measurements, or with the phase diagrams of the lipid–water mixture (Bailey *et al*. 1990; Chiruvolu *et al*. 1995).

pocket. The extent of this preferential partitioning defines both the specificity of the ligand for a single, unique site(s) on the receptor molecule *and* the selectivity of the binding site. Nevertheless, the criteria used to define specificity are somewhat ambiguous because there is no clear crossover between 'specific' and 'non-specific' binding. For example, many proteins and ligands form weak, i.e. low energy, bonds, but bind selectively – that is, they do not bind to other species and compete with other similar molecules for the binding site. The specificity of an interaction can also be linked to higher-order assembly. For example, the weakly binding T-cell adhesion proteins CD2 and LFA3 form specific intercellular 'synapses' through the organized accumulation of protein-protein bonds at cell contact regions (Grakoui *et al*. 1999). By contrast, proteins adsorb strongly and irreversibly, but nonspecifically, to hydrophobic materials. The definition of biological specificity, therefore, ultimately rests on the unique functional manifestations of the interaction *in vivo*.

The selectivity of bio-recognition interactions is defined by the ability of a host molecule such as a protein to distinguish between two closely related species. A protein's selectivity for a particular nucleotide, for example, is quantified in terms of its relative affinities for two different, but similar, nucleotides. With highly selective receptors, small differences in the chemistry of the guest molecule can generate large differences in binding affinities. On the other hand, poor selectivity between two species can be used to inhibit the binding of one ligand by an inhibitor that has a very similar structure and composition. Competition with

https://doi.org/10.1017/S0033583501003687 Published online by Cambridge University Press

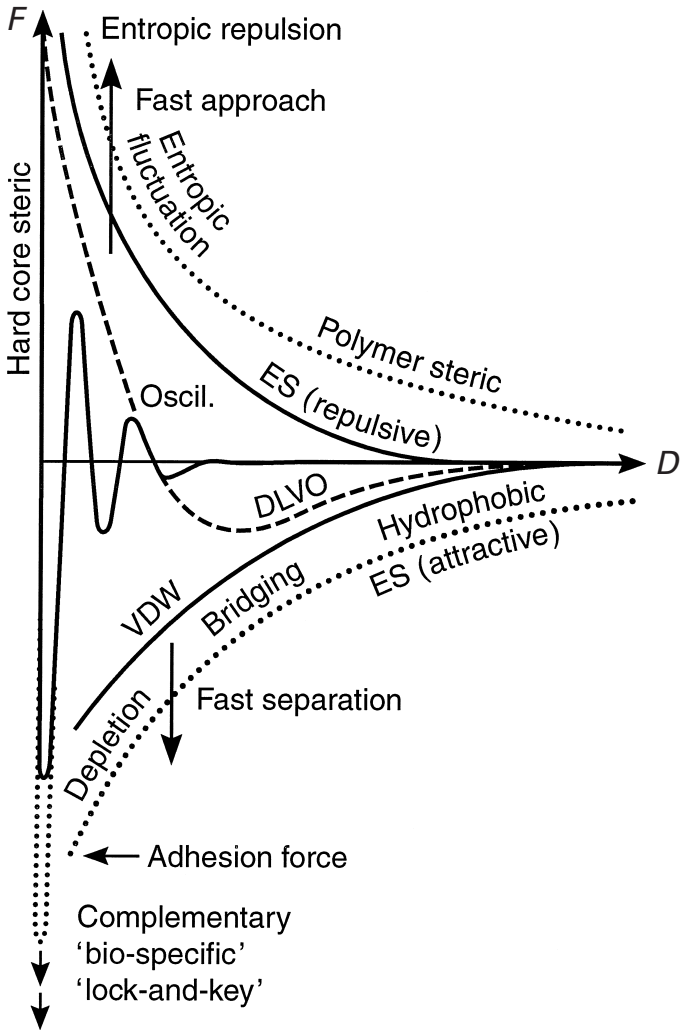


Fig. 15. Generic interaction potentials between two complex macromolecules or biomembrane surfaces. No one system is likely to display all of these interactions at the same time. However, biological molecules and surfaces often interact via four or more of these forces either simultaneously or following on one another.

the inhibitor impedes the binding of the natural ligand. Exploiting the limited ability of receptors to strongly discriminate between two species is a common strategy used in drug design.

Non-specific and site-specific bonds have additional distinguishing features regarding the types of self-assembled structures they give rise to. This is exemplified in Fig. 14, which shows vesicles assembled via both site specific binding and non-specific adhesion forces. In the latter case, all parts of a vesicle's surface can adhere to all parts of another vesicle's surface – causing flattening stresses.

The interactions of biomolecular assemblies such as those shown in Fig. 14 are generally far more complicated than can be described by a simple interaction potential or force function (Fig. 15). The whole process can involve many different forces acting simultaneously or at different locations and at different times and resulting in both normal and lateral

https://doi.org/10.1017/S0033583501003687 Published online by Cambridge University Press

rearrangements of molecules and time-dependent effects. This means that different events can be occurring simultaneously or sequentially in different regions of space, both in the z-direction (away from a surface) and in the x–y plane (at different locations away from the 'center of action').

Biological cells have clearly developed means of controlling different interaction forces over different distance- and time-regimes. For example, a transient change in the *local* pH or calcium ion concentration at a membrane surface could modify the *long-ranged* electrostatic interaction but not the *short-range* LR interaction; or a change in the receptor binding site could alter the short-range force but not the long-range DL force. A change in the local fluidity could alter the diffusion rates of a tethered ligand and thereby prevent or enhance its probability of capture. Changes in membrane fluidity also regulate the opening and relaxation kinetics of ion channels in neurons. Living systems clearly make full use of all of these subtle effects in their control and modulation of complex processes. It should be possible to exert similar controls in the laboratory by carefully changing the processing protocols of drug-delivery vehicles, 'smart' biomaterials, biogels, etc.

1.10 Equilibrium and non-equilibrium forces and interactions

The various force and potential functions so far presented assume equilibrium conditions and are therefore independent of time or the rate of approach or separation of two molecules or surfaces. This is often not the case, especially with biological interactions.

The strength of an isolated bond may be expected to be given by the maximum force it can withstand $F_{\max}$ without rupturing. This should be related to the maximum slope of the potential energy function $E(D)$ by $F_{\max} = (-\mathrm{d}E/\mathrm{d}D)_{\max}$, as illustrated in Fig. 16(*a*). In a classic paper written over 20 years ago, Bell (1978) was one of the first to predict that bond strengths depend not only on the equilibrium energy or force function but also on the temperature and the timescale of the measurement. To appreciate this, we first need to consider exactly what happens when a bond breaks. Consider the simple LR potential in Fig. 16(*b*). In the absence of an external pulling force, due to the ambient thermal energy, there is a finite probability that some receptors and ligands will acquire sufficient energy to diffuse over the activation barrier E_{act} at D_{ts}. The latter can be assumed to correspond with the length of the LR bond. Dissociation will be thermally activated and spontaneous, i.e. occurring in the absence of an external force. The intrinsic bond lifetime τ_0 is given by

$$\tau_0 = \frac{1}{\nu_0} \mathrm{e}^{+E_{\mathrm{act}}/kT}, \tag{25}$$

where ν_0 is the characteristic vibration frequency of the bond, namely the vibration frequency of the ligand in the receptor pocket.[27] For a typical bond $\nu_0 \approx 10^{11}\ \mathrm{s}^{-1}$, so that if the bond

[27] Equation (25) may be understood intuitively by considering the ligand to be oscillating in the potential well at a frequency determined by its mean velocity v and the width w of the bond. The velocity is given by relating the ligand's kinetic energy to the thermal energy: $\frac{1}{2}mv^2 = \frac{1}{2}kT$. For example, for a ligand of MW = 200 Da, its mass is $m = 3{\cdot}3 \times 10^{-25}$ kg. At 37 °C (310 K) its mean velocity is therefore $v = 114\ \mathrm{m\ s}^{-1}$. If the width of the bond is 0·5 nm, then we have $\nu_0 = v/w \approx 2 \times 10^{11}\ \mathrm{s}^{-1}$. Each time the ligand hits the wall of the bond there is a finite probability, given by the Boltzmann factor, that it will escape. This is the basis of Eq. (25). Actually, the real situation is different but results in the same equation: in practice, it is the velocity or kinetic energy of the ligand that is continually changing according to the Boltzmann distribution, until it is high enough to overcome the activation barrier E_{act}.

https://doi.org/10.1017/S0033583501003687 Published online by Cambridge University Press

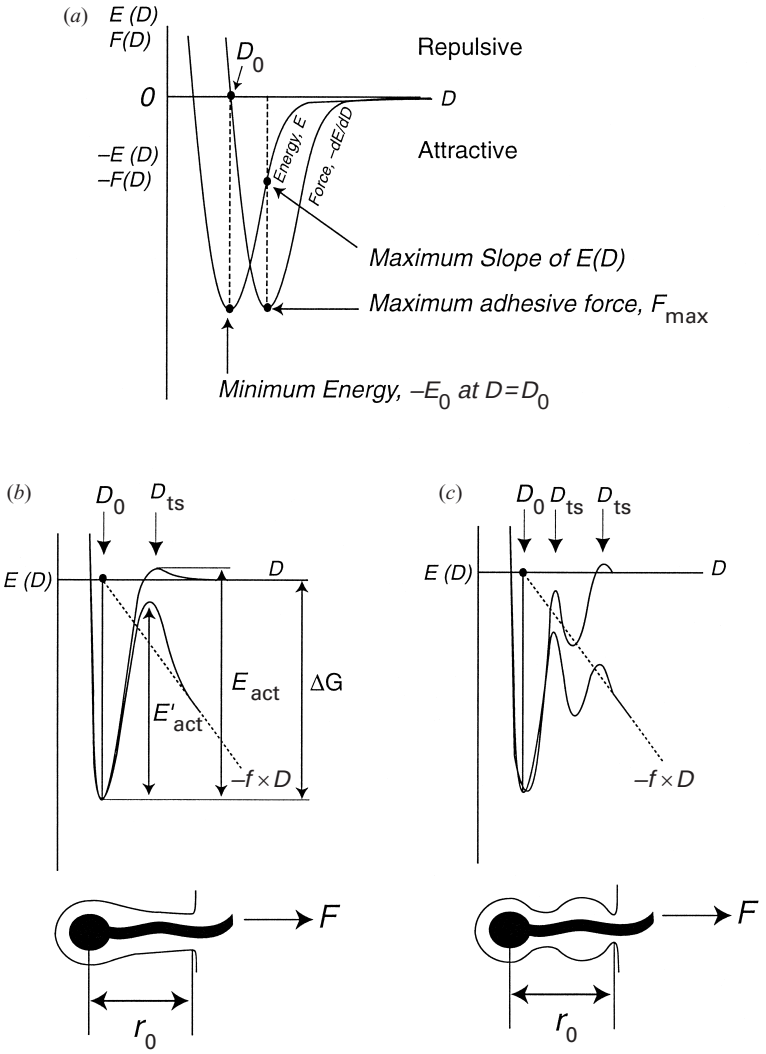


Fig. 16. The effect of an applied mechanical force F on the potential energy surface of an isolated LR bond. (*a*) Equilibrium interaction force and energy profiles. (*b*) Simple intermolecular potential characterized by a single energy minimum and maximum. The mechanical potential $-FD$ tilts the potential and lowers the activation barrier to $E'_{\rm act} = (E_{\rm act} - FD_{\rm ts})$, where $D_{\rm ts}$ is the effective length of the bond at the transition state, ts. Panel (*c*) illustrates the effect of a mechanical force on a more complex potential with multiple energy barriers. As the force increases each of the barriers will emerge in succession as the dominant activation barrier for unbinding. The original Bell Theory (Bell, 1978) considered only the case of an energy minimum, i.e. and did not account for activation barriers along the intermolecular potential. Recent theoretical work (Evans & Ritchie, 1997; Izrailev *et al.* 1997) included the effects of multiple 'activation energy barriers', which can have a large affect on both the on- and off-rates but not on the equilibrium constant of the reaction. Chilkoti *et al.* (1995) confirmed experimentally the importance of the activation energy in unbinding.

energy is $E_{\rm act} = 25\ kT$ the natural lifetime of the bond will be of order $\tau_0 \approx 1$ s. For $E_{\rm act} = 35\ kT$ (40% higher), it will increase by a few orders of magnitude to hours.

The additional potential due to an applied constant force $-F$ along the bond axis will tilt the intermolecular potential by an amount $-FD$. This lowers the activation barrier

https://doi.org/10.1017/S0033583501003687 Published online by Cambridge University Press

to $E_{act} - FD_{ts}$ (Fig. 16(*b*)) such that the lifetime of the bond decreases to the 'Bell Equation'

$$\tau_F = \frac{1}{\nu_0} e^{+(E_{act} - FD_{ts})/kT} = \tau_0 e^{-FD_{ts}/kT}. \tag{26}$$

This simple model predicts that (1) the rate of bond rupture increases with the applied force, (2) all bonds will break when pulled by *any* force if the measuring time is long enough, and (3) the apparent bond strength depends on the time the 'pulling' force is applied: the longer the time, the lower the force needed to break the bond. The bond rupture force is therefore not an equilibrium, or time-independent value, but instead depends on the intrinsic lifetime of the bond, the temperature, and, as we will discuss further in Section 4, the measurement time and loading rate.[28]

The consequences of the above analysis are illustrated using the simple example in Fig. 16(*b*) applied to the biotin–avidin system: assuming a value of 10^{10} s^{-1} for ν_0 and 35 kT for E_{act}, the lifetime of the bond under zero force is therefore $\tau_0 \approx 1{\cdot}6 \times 10^5$ s. The bond will break instantly (in a time of order $1/\nu_0 = 10^{-10}$ s) if we switch on a sufficiently large force given by $F = E_{act}/D_{ts}$ (cf. Eq. (26)) which, for $D_{ts} = 1$ nm (Izrailev *et al.* 1997), is $F = 35(4.2 \times 10^{-21})/(1 \times 10^{-9}) = 150$ pN. This is, in fact, close to the measured avidin–biotin bond strength of 160 ± 20 pN measured with the AFM (Lee *et al.* 1994; Moy *et al.* 1994). However, according to Eq. (26), the apparent strength of the bond would drop to a tenth of this value ($F = 15$ pN) if we were willing to wait for about 1 h.

The Bell model very elegantly captures the underlying physics of forced bond rupture, but it does not treat the kinetics of bond dissociation completely rigorously. In addition, it does not address the rupture of bonds described by complex energy landscapes with multiple barriers (energy maxima) and minima along the binding trajectory (cf. Fig. (16*c*)). Particularly relevant to single bond measurements, bond rupture models need to account for the probabilistic nature of bond failure. Evans & Ritchie (1997) and Israilev *et al.* (1997) addressed these issues by extending the Bell approach in a manner that addresses (1) the stochastic nature of bond rupture, (2) the complex energy landscapes of biomolecular potentials, and (3) the dissipation due to fluid damping and viscous friction within the binding pocket. Evans and Ritchie (1997) used Brownian dynamics simulations and Kramers' theory of reaction rates (Kramers, 1940) to model the detachment of mechanically stressed LR bonds. In contrast to the Bell 'transition-state-like' model, Kramers' theory describes the dynamics of dissociation as a *diffusive* process in which the rate of escape k_{off} from the bound state is determined by a dissipative term (the diffusion coefficient ζ), the width and curvature of the potential well, ℓ_{ts} and ℓ_c, and the height E_{act} of the dominant energy barrier in the intermolecular potential:

$$k_{off} \approx \left(\frac{\zeta}{\ell_c \ell_{ts}} \right) \exp \left[\frac{-(E_{act} - FD)}{kT} \right]. \tag{27}$$

Although this is analogous to the Bell model, there are differences, which are particularly relevant to current single bond measurements in solution. First, Eq. (27) assumes that the

[28] As discussed below, this applies only to bond rupture processes, which determine 'off-rates'. Bond formation, or 'on-rates', are determined by different factors.

https://doi.org/10.1017/S0033583501003687 Published online by Cambridge University Press

activation energy for unbinding E_{act}, not the *equilibrium* bond energy, determines the energy scale for bond rupture. Second, recent theoretical studies (Evans & Ritchie, 1997; Izrailev *et al*. 1997) take into account viscous dissipation due to damping by the surrounding fluid. In both transition state and Kramers' theory, bond rupture is described in terms of the mean passage time for the bonds to diffuse between the bound and dissociated states. Kramer's theory reduces to the transition state theory in the low viscosity limit, when the viscous coupling between the molecules and the solvent bath as well as between the ligand and surface of the binding pocket are low. Although the latter is applicable to gas phase reactions, the inclusion of viscous damping in Kramers' model is a more appropriate description of reactions of complex macromolecules in solution.

Third, Bell's earlier model does not account for the *stochastic* nature of bond rupture. Whereas deterministic models, such as Bell's and Eq. (27) above, predict an average dissociation rate or bond rupture force, they do not account for variations of measured bond strengths due to the distribution of thermal states within a population. Such distributions are typically seen in atomic force microscope (AFM), optical tweezers (OT) and bioforce Probe (BFP) measurements of single and multiple bond-rupture processes, described in Sections 2 and 4. Both Israilev *et al*. (1997) and Evans & Ritchie (1997) derived probability distributions for the measured strengths of isolated bonds subjected to a slowly increasing force. In most bond strength measurements, the applied force F is not instantly switched on, but increases at some finite rate, which is characteristic of the instrument, until the bond breaks. These analyses predict how the pulling rate, the natural bond width and lifetime, and the temperature determine the *most probable* bond rupture force. In addition, Israilev *et al*. (1997) explored how the transducer stiffness K_s would affect the region of the potential probed and, consequently, the pull-off force as measured, for example, with an AFM.

The significance of including viscous dissipation in models of bond failure is apparent when one considers the dynamics or rates of forced bond rupture. Israilev *et al*. (1997) showed that, as the detachment rate approaches or exceeds the natural bond lifetime $1/\nu_0$, the viscous drag on the ligand becomes significant. Under the very fast detachment the timescales in molecular dynamics simulations, the frictional drag on the ligand contributes significantly to the measured force. Thus, the limiting detachment force will not be $F = E_{act}/D_{ts}$. Instead, the force will continue to increase linearly with the pull-off rate. The consequence of this for comparing simulations to experimentally determined bond strengths is discussed in Section 4. By contrast, the dynamic response of current force measurement techniques (except OT) is still on the order of milliseconds, and this is slower than the intrinsic lifetimes of many non-covalent bonds. Currently, viscous drag on the mechanical components of the instruments and inertial effects still poses the greatest limitation to ultrafast single bond detachment measurements (Viani *et al*. 1999a, b).

1.10.1 Multiple bonds in parallel

Despite the attention focused on single bond force measurements, biological interactions, especially those involving membranes, are often not mediated by single high-affinity bonds but by many simultaneous – laterally separated – contacts involving different molecules or chemical groups with widely differing binding energies and kinetics. These may be referred to as 'bonds in parallel', in contrast to 'bonds in series' which is considered next. A good

https://doi.org/10.1017/S0033583501003687 Published online by Cambridge University Press

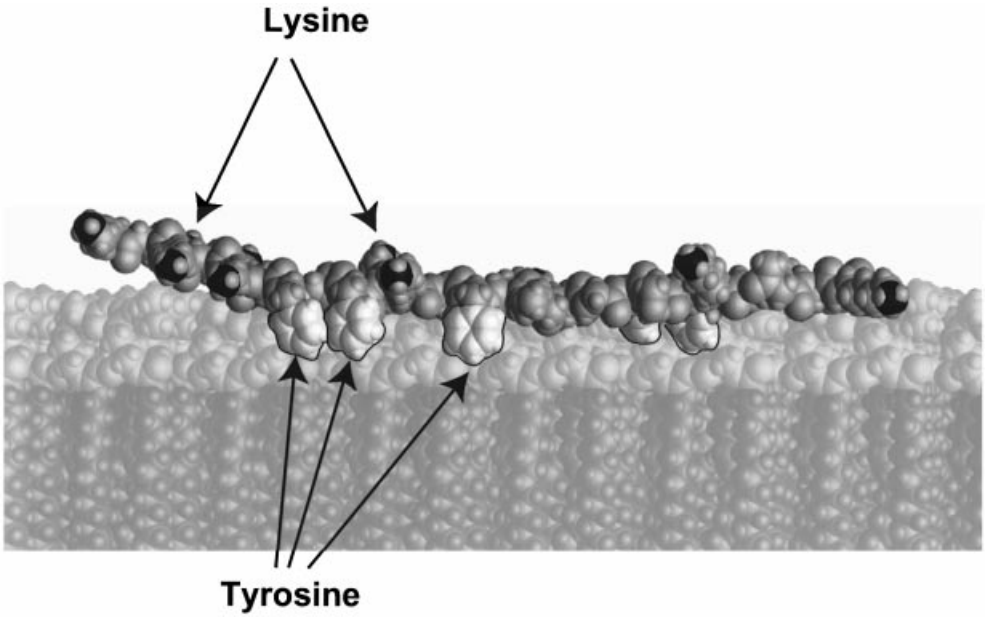


Fig. 17. Association of the MARCKS protein with a negatively charged membrane. The protein associates with the membrane via multiple contacts that involve both electrostatic and hydrophobic interactions. The lysines, which are indicated by the black CPK structures, bind to the negatively charged phospholipid headgroups. Tyrosines insert into the hydrophobic region of the membrane. (Adapted from Arbuzova *et al*. 1998.)

example of parallel bonding occurs in the MARCKS protein (Fig. 17) (Arbuzova *et al*. 1998). This protein is involved in signaling at membrane surfaces. It binds to a membrane via multiple physical bonds that include, for example, hydrophobic contacts, which involve tyrosines, and ionic bonds between lysines and the negatively charged groups on the lipid headgroups. These charged groups may also mediate interactions with membrane proteins. In some instances the binding is further strengthened by myristoylation at the lysine-rich N-terminus (not shown). There are many other examples where multiple, weak RL bonds mediate adhesion. The engagement of multiple bonds ensures strong overall adhesion, or stable binding, while allowing for plasticity at adhesive junctions, the formation of dynamic contacts, and cell motility.

Vijayendran *et al*. (1998) and Seifert (2000) both used theoretical approaches to investigate how the adhesion mediated by multiple bonds in parallel might differ from single bond failure. Vijayendran *et al*. (1998) used the 'adhesive dynamics algorithm' (Chang & Hammer, 1996) to simulate the adhesion between two multiple receptor-linked membrane surfaces in surface force measurements. They found that there is a distribution of bound and free states, so that the *average* bond strength is less than that of an isolated cross-bridge. Although some bonds break, they soon reform since the membranes remain pinned in close proximity by the unbroken neighboring cross-bridges. Because the bonds are constantly breaking and reforming during the detachment process, the tension on each linkage averaged over the time required to break all of the bonds between the surfaces, approaches the rupture force of the individual bonds, only when the intrinsic breakage and reformation rates are faster than the pulling rate.

https://doi.org/10.1017/S0033583501003687 Published online by Cambridge University Press

Seifert (2000) concluded that both the dynamics and the measured (or effective) detachment force of a multiply bonded junction depends on the surface density or number N_0 of cross-bridges and on whether the bonds between the two surfaces are reversible or irreversible. In the case of irreversible bonds, the adhesive force varies as $\log N_0$, but scales as $\sqrt{N_0}$ when bond formation is reversible. Such dynamic bond breakage and reformation undoubtedly occurs in biology. However, this will not be observed in single bond measurements because the surfaces jump out of contact as soon as a (single) cross-bridge fails. The simulations show that this dynamic unbinding and rebinding determines the time-averaged force exerted by the bonds, so that the average bond strength depends in a complicated way on the association rate, the dissociation rate, and the pulling rate.

1.10.2 Multiple bonds in series

Adhesive interactions can also comprise several bonds in series. For example, cell–cell adhesion can involve five or more molecules linked in series, such as string of adhesion proteins, ligands, and membrane anchors. The case of bonds in series is easier to analyze than bonds in parallel. When a linear chain is pulled (unloaded) it will fail at one particular joint (bond) somewhere along the chain. In contrast, the failure of a junction composed of a number of bonds in parallel involves the breakage of all of these bonds. Bonds in parallel can rupture simultaneously, sequentially or in groups, depending in a complicated way on the properties of the individual bonds and on the way they are linked together laterally. The rupture of bonds in series also exhibits interesting subtleties as will be described in Section 4. We might expect that the strength of a chain of cross-bridges will be determined by the weakest link in the chain. Failure would then occur at the bond having the weakest yield *force*, given by $E_{\mathrm{act}}/D_{\mathrm{ts}}$ in Fig. 16.

As an example of this effect, consider the energy E_1 needed to pull a lipid or protein molecule out of a membrane. Since this is the hydrophobic energy of exposing the molecule to the aqueous phase, E_1 is usually on the order of 20–30 kT. However, the effective bond length defined by $D_{\mathrm{ts}} = D_1$ (cf. Fig. 16) is given by the length of the hydrophobic anchor – typically 2–4 nm for lipids or proteins. The yield strength of the membrane–protein 'bond', $F_1 = E_1/D_1$, may therefore be low. In comparison, a RL bond linking the protein (in series) to another molecule or another membrane may have a lower energy, $E_2 < E_1$, but the length of this LR bond D_2 may be significantly shorter than D_1. The yield strength of the LR bond, $F_2 = E_2/D_2$, may therefore be higher than F_1. In this case we will therefore have

$$E_1 > E_2 \quad \text{but} \quad F_2 > F_1.$$

In other words, even though the protein–membrane binding energy is higher than the LR energy, when pulled, failure will occur at the protein–membrane junction.

As we will discuss in Section 4, this is actually an oversimplification because time, temperature, the relative rates of bond failure, and the pulling rates also play a role. Clearly, if no force is applied, spontaneous rupture will occur at the bond with the fastest detachment rate, i.e., the lowest activation barrier E_{act}. This is the situation that applies when bonds form and break spontaneously in solution, and it determines the thermodynamic equilibrium distribution between bound and unbound states. However, the dynamics change completely when the bonds are pulled. As the loading rate is gradually increased from zero (the

https://doi.org/10.1017/S0033583501003687 Published online by Cambridge University Press

thermodynamic state), a point will come where the location of rupture from where the *energy* is lowest to where the *force* is lowest – an intriguing conclusion that could have many important biological consequences for multiple bonds undergoing sequential interactions or bonds under stress.[29] This effect has been studied experimentally by Leckband *et al*. (1995b) and by Evans *et al*. (1992) in model systems involving various lipid–membrane and LR bonds in series subjected to different loading conditions (see Section 4). Under *in vivo* conditions, mechanical stresses can be constant, for example, due to flow, or transient, for example, when the sudden release of Ca^{2+} ions affects the hydrophobic, electrostatic and DL forces (see Sections 3.1 and 3.3). In the laboratory, various kinds of pulling stresses can be applied for measuring such dynamic interactions, as described in Sections 2 and 4.

2. Experimental techniques for measuring forces between biological molecules and surfaces

2.1 Different force-measuring techniques

Different force-measuring techniques often probe different force-regimes (different magnitudes or length scales) or time scales. Some techniques measure the *force*. Others measure the *energy* of an interaction, which provides quite different information. Others may also measure surface deformations, molecular rearrangements or some other conformational or structural change associated with an interaction. Another important distinction is whether a technique measures the true (thermodynamic) equilibrium state or some non-equilibrium interaction: a suspension of vesicles or cells may appear to be stable over a 1 h period but aggregate over a 72 h period. The data collected will therefore be misleading as regards the *equilibrium* state of the vesicles if collected for only 1 h. On the other hand, the data may provide meaningful information on meta-stable conditions, transient effects, and binding kinetics or rates.

Table 4 shows the typical range and strengths of the interaction energies and adhesion forces associated with differently sized biological assemblies or structures. These parameters in turn determines the most suitable experimental technique for studying them. These 'structures' are arbitrarily separated into molecular, nanoscopic, microscopic and macroscopic. The techniques used to study them are listed in the last row of Table 4 and are described in more detail in Table 5. The SFA and AFM techniques are currently the most versatile in that surface forces and separations can be accurately controlled and measured over a large range; the interactions between microscopic particles and cells are best measured using the MPA, BFP, TIRM, RICM, AFM and SFD techniques, while molecular-scale and single-bond interactions are best measured using the OT, AFM, SFD, BFP and MC techniques. One should note that, as yet, all of these techniques are laboratory or *in vitro* methods, although some are closer to mimicking physiological conditions than others.[30]

[29] Theory further predicts that the average strength of a multiple linkage in series should actually be weaker than the weakest bond in the chain (Saterbak & Lauffenburger, 1996). The reason for this is as follows: If the binding probability of each of two different bonds in series is less than unity, then the probability that both bonds will bind simultaneously is the product of the two single-bond probabilities. The overall likelihood of simultaneous binding will then be less than that of either bond.

[30] Protein, vesicle and cell adsorption studies are not covered in this review. These have been traditionally studied by electrical, optical and various labeling techniques (Ramsden, 1993), as well as with the more recent quartz crystal microbalance (QCM) technique (Rodahl *et al*. 1995), which can

https://doi.org/10.1017/S0033583501003687 Published online by Cambridge University Press

Table 4. *Characterizing length scales and typical order of magnitude values for the non-covalent interactions of biomolecules and biomolecular assemblies*

Parameters measured	Bonds, molecules and sub-molecular groups	Nanoscopic surfaces and macromolecules	Microscopic surfaces and small particles	Macroscopic (flat) surfaces and large particles
Typical surface or particle radius, R	0·1 nm	1 nm	1 μm	1 mm
Binding/adhesion energy, $E(0)$*	1 kT	10 kT	1000 kT	10^6 kT 100 mJ m^{-2}
Adhesion force, $F(0)$ or F_a*	10 pN	100 pN	100 nN	100 μN 10^8 N m^{-2}
Effective range of interaction, $E(D)$†	0·2 nm	2 nm	20 nm	50 nm
Suitable experimental techniques‡ (cf. Table 5 for details)	OT, AFM & MC, MPA & BFP	OT, AFM (tip) & MC, MPA & BFP	OT, AFM (bead) & MC, MPA & BFP, TIRM & RICM, SFD	SFA, OP, RICM, SFD

* Typical *maximum* values in aqueous 0·15 M NaCl solutions for particles that remain undeformed (R = constant) during an interaction. Any elastic or other deformations accompanying adhesion tend to increase the binding energy significantly and, to a lesser extent, the adhesion force.

† Since all force functions $F(D)$ vary asymptotically with distance D either as a power law [$F(D) \propto 1/D^n$] or exponentially [$F(D) \propto e^{-D/D_0}$], the force never reaches true zero, i.e. the 'range' of all forces is strictly infinite. As a practical criterion, the range is here defined as the distance D at which the interaction *energy* $E(D)$ is of the same order as the thermal energy $kT \approx 4 \times 10^{-21}$ J at 25 °C. The 'energy range' is different from the 'distance range' that different techniques can measure colloidal forces, given in Table 5, column 4.

‡ AFM & MC (atomic force microscopy & micro cantilever); SFA (surface forces apparatus); OT (optical tweezers or optical trapping); MPA & BFP (micro pipette aspiration & bioforce probe), SFD (shear flow detachment); TIRM & RICM (total internal reflection microscopy & reflectance interference contrast microscopy); OP (osmotic pressure or osmotic stress).

Figure 18 and the inset of Fig. 19 illustrate the major parameters that are typically measured in such experiments. These are[31]: F, D, ΔD, ΔD_0, ΔD_c, ΔD_S, K_S, a, K, T_1 and T_2, including different time intervals and other relevant system parameters and experimental variables. The more of these parameters that can be independently controlled and directly measured in any experiment, the more complete and unambiguous are the data. The most common limitations are: (1) A lack of any *direct* measurement of the absolute surface or interface separation D and layer (e.g. adsorbed protein) thicknesses T_1 and T_2 (Fig. 18, panel (A)). In the case of soft or mobile biological surfaces and interfaces, these are anyway difficult to define. (2) Difficulty in monitoring local surface shape changes and molecular rearrangements, which typically accompany a complex interaction such as the accumulation of adhesion proteins at cell–cell junctions, protein docking, or membrane fusion. (3) The tendency of most techniques to measure some *average* effect involving an unknown number of molecules where the role of, for example, nucleating micro-clusters or transient effects are not easily discernable and yet may be crucial for understanding the overall process. (4)

measure both protein adsorption kinetics (Höök *et al*. 1998) and structural changes of adsorbing vesicles and cells (Fredriksson *et al*. 1998; Keller & Kasemo, 1998).

[31] No technique measures all of these parameters. Indeed, there is no need to do so, because some of these parameters are related, for example, via Eq. (31), and some may not be needed or may be of no interest.

https://doi.org/10.1017/S0033583501003687 Published online by Cambridge University Press

https://doi.org/10.1017/S0033583501003687 Published online by Cambridge University Press

Table 5. *Measured parameters of different force-measuring techniques adapted from* (*Schneider & Tirrell*, 1999).

	Types of measurements made and resolution				
Technique	Typical size or radius R of particles used	Force & time resolution,* $\pm\Delta F$(N) and Δt (s)	$\Delta F/R$ (N m^{-2}), and distance-range,† D_{max} (nm)	Distance resolution,‡ D and $\pm\Delta D$	Special features
Atomic force microscope (AFM) with tip	Nanoscopic 10 nm	$\Delta F = 10^{-11}$ N $\Delta t = 10^{-3}$–10 s	$\Delta F/R = 10^{-3}$ N m^{-2} $D_{max} = 2$ nm	1 nm (est); $\pm$0·1 nm	Gives surface image, contact area and absolute separation distance D must be inferred.
AFM with bead	Microscopic 10 μm	10^{-11} N 10^{-3}–10 s	10^{-6} N m^{-2} $>$ 100 nm	1 nm (est); to $\pm$0·1 nm	Larger distance range than AFM with tip.
AFM, microfiber cantilever (MC)	Single-bond or intermolecular 0·2–1·0 nm	10^{-11} N 10^{-3}–10 s	10^{-2} N m^{-2} 0·2 nm	1 nm (est); $\pm$0·1 nm	Can measure individual bond strengths (adhesion and binding forces) but not inter-molecular force-law $F(D)$.
Surface forces apparatus (SFA)	Macroscopic 10 mm	10^{-8} N 10^{-3} s →	10^{-6} N m^{-2} $>$ 100 nm	0·1 nm (est); $\pm$0·1 nm	Directly measures surface separation, local geometry and contact area *in situ*. Poor lateral resolution.
Reflectance microscopy techniques: TIRM and RICM	Microscopic 10 μm	10^{-14} N 10^{-3} s →	10^{-9} N m^{-2} $>$ 100 nm	1 nm (est); $\pm$1 nm	Very high force sensitivity, restricted to certain systems and only repulsive forces.
Optical tweezers (OT)	Microscopic to molecular 0·1 nm–10 μm	10^{-12} N 10^{-2} s →	10^{-2}–10^{-7} N m^{-2} 0·2–100 nm	— $\pm$5–10 nm	High force sensitivity, good for adhesion/binding forces, but lacks method for measuring absolute separation distances D.
Micropipette aspiration (MPA) and bioforce probe (BFP)	Microscopic to molecular 0·1 nm–10 μm	10^{-13} N 10^{-3} s →	10^{-3}–10^{-8} N m^{-2} 0·2–100 nm	1–5 nm (est); $\pm$1–5 nm	Similar to TIRM and RICM but with added control of particle position. Closely mimics biological conditions, good for adhesion forces.
Shear flow detachment (SFD)	Microscopic 10 μm	10^{-12} N 10^{-2} s →	—	—	Closely mimics biological conditions, good for adhesion and kinetic rate measurements, results difficult to interpret/quantify.
Osmotic pressure (OP)	Macroscopic (planar bilayers)	0·1 mN m^{-2} $>$ 1 h →	25 nm	0·1 nm (est); $\pm$0·1 nm	Molecules or membranes must be assembled into ordered arrays, measures only repulsive forces $F(D)$.

* The lower and upper limits in Δt give the 'dynamic range'. The shortest time gives the fastest (transient) effect that can be measured (which is usually determined by the mechanical resonance frequency of the system); the longest time is usually determined by the ability to control thermal drifts. An arrow → indicates that there is no upper limit, i.e. that measurements can go on indefinitely, in principle.

† As described at the end of Section 2.1, the 'distance range' D_{max} over which a technique can accurately measure attractive or repulsive forces depends not on the force resolution ΔF but on $\Delta F/R$. The more sensitive is $\Delta F/R$ the larger is the distance range.

‡ Gives accuracy in measuring *absolute* distances, D, and *relative* displacements, $\pm\Delta D$. Absolute distances or separations D between two molecules or surfaces are often not directly measurable or known (—) or must be estimated (est), even though the accuracy in measuring *relative* displacements or macromolecular extensions ΔD can be very high (e.g. $\pm$0·1 nm).

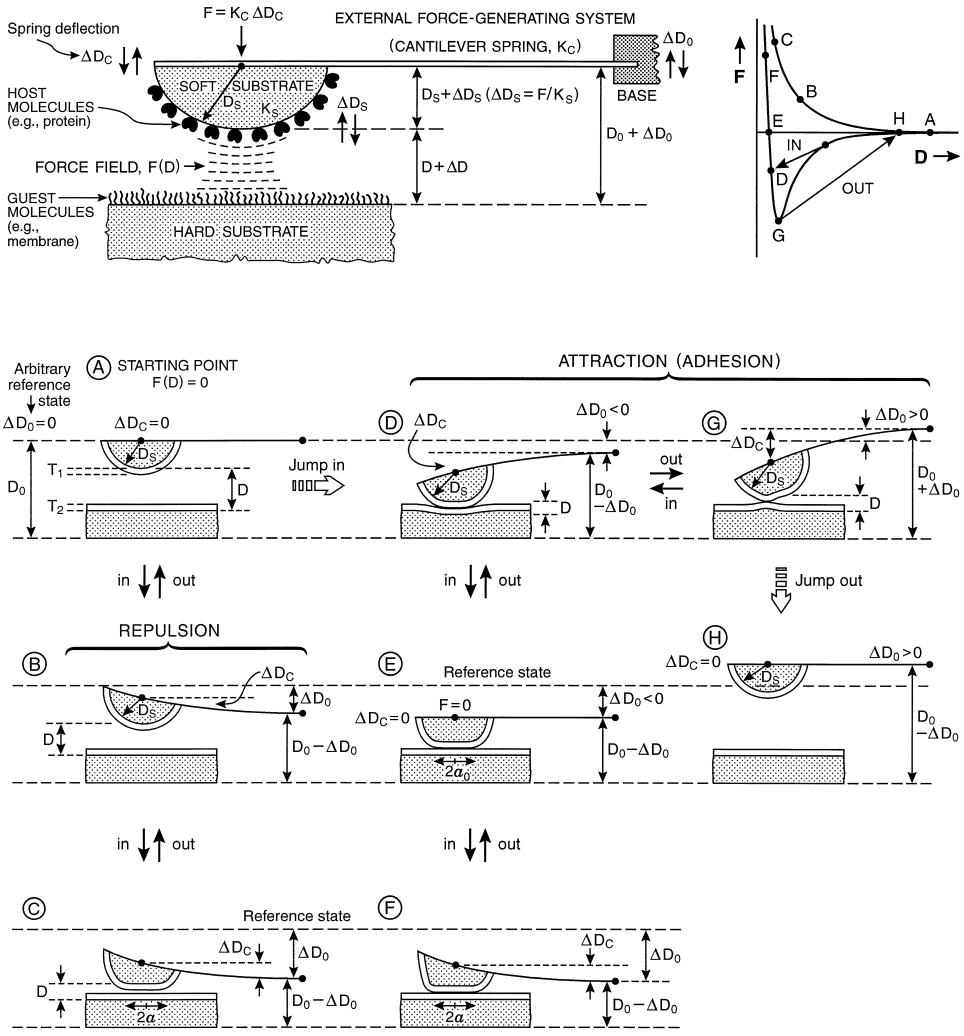


Fig. 18. Generic force-measuring geometry and relevant parameters that must be controlled and/or measured, preferably under both static (equilibrium) and dynamic conditions (when things change with time). *Top*: Interaction geometry of a curved surface or macromolecule interacting with a flat surface, where the intermolecular force between them is shown on the right and where the externally applied force is changed via a simple 'cantilever spring' that supports the top surface. The soft substrate length D_s is usually different from the radius R at the interaction zone, but is shown here to be the same for simplicity. (A) to (H): various stages during the approach, contact, and separation of two surfaces under a repulsive force (*left*) or an attractive force (*right*). Note that, in general, both surfaces deform locally when they interact, adhere or separate, as shown in panels (D) and (G).

Difficulty in combining multiple analytical approaches *in situ*. Most approaches do not combine two or more different techniques, such as force measurements and spectroscopy, that could allow for simultaneous measurements of forces and, for example, accompanying structural changes.

Table 5, column 4, also compares the distance regime or range, 0 to D_{max}, over which different techniques can typically measure attractive or repulsive forces. The *distance* range D_{max} or resolution is related to the *force* sensitivity or resolution, ΔF. For example, consider

https://doi.org/10.1017/S0033583501003687 Published online by Cambridge University Press

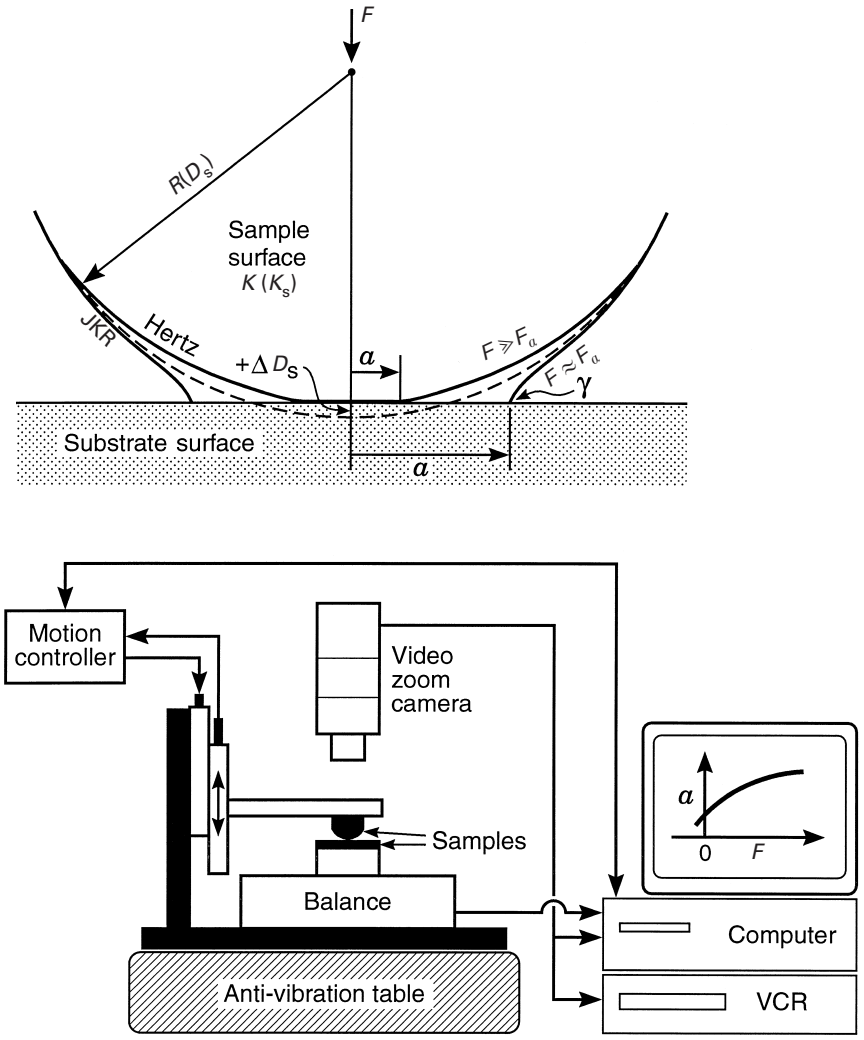


Fig. 19. A JKR apparatus, named after the Johnston–Kendall–Roberts theory of adhesion mechanics (Johnson *et al*. 1971), developed by Tirrell and co-workers (Mangipudi *et al*. 1995; Tirrell, 1996; Tirrell *et al*. 1997) to study the adhesion forces and deformations of macroscopic solids. The device allows for the measurement of the molecular contact radius a as a function of the applied load F, including negative loads. The results can then be used to test theories of adhesion and contact mechanics such as the JKR and Hertz theories. This technique also enables the measurement of surface energies γ via Eq. (35), the effects of different loading and unloading rates, and time-dependent (non-equilibrium or dynamic) adhesion forces that lead to hysteresis and ageing effects. Such non-equilibrium and dynamic effects can be particularly pronounced with viscoelastic materials and biological surfaces.

an AFM with a force resolution of $\Delta F = \pm 10$ pN that is being used to measure the force between a flat surface and a tip of radius $R = 20$ nm. This AFM will therefore be able to reliably measure the VDW attraction, given by $F = -AR/6D^2$, out to $D \approx 1{\cdot}8$ nm (assuming a Hamaker constant of $A = 10^{-20}$ J). In comparison, a technique such as the SFA that is being used measure the force between two cylindrical surfaces of radii $R = 20$ mm to within a much lower force resolution of $\Delta F = \pm 10$ nN will nevertheless be able to measure the same VDW force out to $D \approx 58$ nm. This is ~ 30 times larger than the distance range

https://doi.org/10.1017/S0033583501003687 Published online by Cambridge University Press

of the AFM even though the resolution in measuring the absolute force with the SFA is a factor of 1000 lower (10 nN compared to 10 pN). The range of distances over which a technique can measure forces is determined by $\Delta F/R$ rather than by ΔF.

2.2 Measuring forces between surfaces

The simplest and most direct way to measure the force between two surfaces, such as two particles or a particle and a flat surface, is to suspend one on a spring and measure – from the deflection of that spring – the force needed to bring the surfaces to a certain equilibrium separation D. Externally applied forces can be generated with springs, but also via other means such as fluid flow (viscous drag forces), light pressure, osmotic pressure gradients, and electric and magnetic fields. Figure 18 shows a typical surface force-measuring system using a cantilever spring to generate and/or measure the force between two macroscopic surfaces; the same principles apply to single molecule interactions. For simplicity, we assume that one surface is curved with undeformed local or 'tip' radius R, and that it is supported on a soft, elastically deformable substrate of length D_S and stiffness K_S, defined such that a compressive force F depresses the substrate material by a distance $\Delta D_S = F/K_S$. The opposing surface is assumed to be flat ($R = \infty$) and hard ($K = \infty$), i.e. not deformable. If both surfaces are spherically curved with radii R_1 and R_2, all the equations for the interaction forces apply after replacing R by $R_1R_2/(R_1 + R_2)$, as in Tables 3 and 4. And if both surfaces are soft, all the equations involving surface deformations apply after replacing K_S by $K_1K_2/(K_1 + K_2)$.

Figure 18 (A–H) shows the various stages of interaction on approach and separation of two surfaces when the forces between them are purely repulsive (reversible path A → B → C → B → A) and when they are attractive (irreversible path A → D → E → F → G → H). The surfaces can be brought towards each other or separated by moving the lower substrate surface up or down or, equivalently, moving the base of the cantilever spring up or down by a known amount ΔD_0. In each case, one tries to simultaneously measure the deflection of the cantilever spring ΔD_c, the separation between the surfaces D, the deformation of the substrate ΔD_S, the local radius R, the contact area πa^2, and any other factors that may be associated with the interaction such as protein rearrangements, lateral phase-separation or membrane fusion. Each surface is assumed to consist of a layer of such biological molecules having layer thicknesses T_1 and T_2, respectively, as shown in Fig. 18.

2.3 Measuring force–distance functions, *F(D)*

The full force-law $F(D)$ between two surfaces, that is, the force F as a function of surface separation D, can be measured in a number of ways. The simplest is to start with the surfaces well-separated at D where there is no detectable force between them, i.e. where $F(D) = 0$ at the arbitrary 'reference state' or reference line shown dashed in Fig. 18. The base of the force-measuring spring is now moved by a known amount ΔD_0 to a new position where there is now a detectable force F between the two surfaces which could be attractive or repulsive. This force F is detected because it causes the spring to deflect by $\Delta D_c = F/K_c$. It also causes the substrate and the soft surface layers to compress by $\Delta D_S = F/K_S$. At the same time the surface separation changes by ΔD to the new separation at D. The force F at D is therefore given by

$$F(D) = K_c \Delta D_c, \tag{28}$$

https://doi.org/10.1017/S0033583501003687 Published online by Cambridge University Press

where K_c and ΔD_c are the spring stiffness and deflection, both of which are usually measurable. The force is also given by $F(D) = K_S \Delta D_S$ which can be rearranged to give the substrate deflection

$$\Delta D_S = F(D)/K_S, \tag{29}$$

where K_S is the substrate stiffness, which is usually more difficult to measure. If the surfaces are again moved to a new position, associated with a new spring displacement of $\Delta D_c'$, the force difference $\Delta F'$ between the initial and final separations is given by

$$\Delta F' = F(D) - F(D') = K_c \Delta D_c'. \tag{30}$$

The above simple equations provide the basis for measuring the force, whether attractive or repulsive, at any surface separation D or D' so long as one can directly (i.e. independently) measure D, the cantilever deflection ΔD_c and the cantilever spring stiffness K_c. For example, if a particular force-measuring apparatus can measure D and ΔD_c, then by starting at some large initial separation D where the force is zero ($F = 0$) and measuring the force difference ΔF between this initial reference separation D and $D' = (D - \Delta D)$ using Eq. (28), then working one's way in to smaller separations in increasing increments of ΔD_0, the full force-law $F(D)$ can be constructed over any desired distance regime using Eq. (30).

With some techniques it is not possible to measure all of these parameters directly, especially D, and some alternative or indirect method is then used. The four relevant distances in the system (cf. Fig. 18) are related by $D_0 = D + D_c + D_S$, so that the four displacements, i.e. changes in these distances, are related by

$$\Delta D = \Delta D_0 - \Delta D_c + \Delta D_S. \tag{31}$$

Thus, simultaneous measurement of ΔD_0, ΔD_c and ΔD_S allows determination of the *change* in D, but not in the *absolute* value of D. Even then, ΔD_S is also usually difficult to measure, so that even changes in D may not be directly measurable. The measurement of the absolute separation between two interacting molecules or surfaces remains the most difficult part of any force-measuring technique, and is the most problematic when interpreting the results of force measurements.[32]

Whenever an equilibrium force-law is required, it is always essential to establish that the two surfaces have stopped moving before the equilibrium displacements are measured. When displacements are measured while two surfaces are still in relative motion, one also measures a viscous or frictional contribution to the total force. On the other hand, such dynamic force measurements have enabled the viscosities of liquids near surfaces and in thin films to be measured.

2.4 Relating the forces between different geometries: the 'Derjaguin Approximation'

In practice, it is difficult to measure the forces between two perfectly flat surfaces because of the stringent requirement of perfect flatness *and* perfect alignment at the Ångstrom level. Furthermore, even when two surfaces are in contact in a flat configuration, when they are separated, they usually do this by *peeling* apart from the edges rather than separating in their planar configuration. It is therefore far easier to measure the forces between curved surfaces,

[32] The other problematic issue is the interaction radius a or area at the molecular level, or the number of molecules involved in the interaction, as will be discussed later.

https://doi.org/10.1017/S0033583501003687 Published online by Cambridge University Press

such as between two spheres, a sphere and a flat, or two crossed cylinders. As an added convenience, the total *force* $F_c(D)$ measured between two curved surfaces can be directly related to the *energy* per unit area $E_f(D)$ between two flat surfaces at the same separation, D. This relationship is known as the 'Derjaguin Approximation' (Derjaguin, 1934):[33]

$$F_c(D) = 2\pi\bar{R}E_f(D), \tag{32}$$

where $\bar{R}$ is the radius of the sphere (for a sphere near a flat surface) or the radii of the cylinders (for two identical crossed cylinders). For two different spheres having radii R_1 and R_2 the value of $\bar{R}$ above is replaced by $R_1R_2/(R_1+R_2)$, while for two crossed cylinders $\bar{R}$ is replaced by $\sqrt{R_1R_2}$.

From Eq. (32) it appears that the force functions of flat and curved surfaces are simply related by

$$F_f = -\frac{dE_f}{dD} = -\frac{1}{2\pi\bar{R}}\left(\frac{dF_c}{dD}\right). \tag{33}$$

In other words, two quite different geometries can have similar force profiles – the one being related to the other by a simple differentiation or integration with respect to D. For example, an oscillatory force function or one that exhibits multiple energy maxima and minima between receptor and ligand molecules located on two *planar* surfaces (cf. Fig. 16(*c*)) may remain oscillatory between two macroscopic *curved* surfaces with $R > \sim 1$ μm. This is because the derivative of a sine-function is a cos-function, i.e. a function that is just as oscillatory. The intriguing and non-intuitive aspect of this conclusion is that a curved surface does not necessarily 'smear out' the discrete peaks and valleys in the interaction potential that exists between two molecules or, equivalently, between two flat surfaces exposing these molecules.

But this correspondence in the force curves is not always the case. It depends on the detailed nature of the oscillatory force function. For example, the derivative or integral of an exponentially decaying oscillatory force or energy function having the form $e^{-ax}\cos bx$ or $e^{-ax}\sin bx$ is also an exponentially decaying oscillatory function but with a phase shift. Now consider a different kind of oscillatory interaction – a monotonically decaying energy function that has small ripples on it such that the total energy function $E_f(D)$ never falls to negative values at any separation. In this case, the *force* between the two flat surfaces, $F_f = -dE_f/dD$, will be fully oscillatory, and will cross the $F = 0$ axis between repulsive maxima and adhesive minima (because the *slope* of E_f alternates between positive and negative along the ripples even as the *energy* remains positive at all times). The *force* function F_f will therefore behave or appear like a decaying oscillatory force function, but it is actually very different from an exponentially decaying sine or cos function. Furthermore, by the Derjaguin Approximation, the force function between two curved surfaces F_c will have the same form as the energy function E_f which, as was initially established, is positive at all separations. Overall, we can say that, *in this particular case*, an oscillatory *force* between two *flat* surfaces has given rise to a monotonically repulsive *force* (at all separations) between two *curved* surfaces. In this case, therefore, the curved geometry has indeed smeared out the oscillations in the force profile. Nevertheless, the correlation between the force F_c and the energy E_f hold.

[33] The term 'approximation' was introduced because of the many (unnecessary) assumptions that were made in the original derivation of this equation. Simpler and more direct derivations (Israelachvili, 1991) show that this equation is actually 'exact' so long as the range of the force is much smaller than the radii of the surfaces.

https://doi.org/10.1017/S0033583501003687 Published online by Cambridge University Press

2.5 Adhesion forces and energies

The adhesion or 'pull-off' force F_a needed to separate the two bodies from contact can be obtained from the distance that two surfaces or molecules 'jump' apart when they separate (Fig. 18 (G → H)):

$$F_a = K_c \Delta D_c. \tag{34}$$

This method is applicable even at the microscopic or molecular levels, and it forms the basis of all direct force measuring methods for determining binding and adhesion forces. These forces are in turn related not only to the surface energies of the surfaces but also to their geometry and to the 'mode' of separation, i.e. to the way the surfaces separate,[34] and to the deformations that accompany the separation.

All surfaces deform when they interact regardless of whether the force between them is repulsive or attractive. The most common type of deformation is a simple flattening, as shown in Fig. 18(C) for repulsive forces and Fig. 18 (F → G) for attractive (adhesive) forces. More complex deformations can include a thinning or thickening of the surface layers or membranes (T_1 and T_2 in Fig. 18(A)), the removal or fusion of surface layers, lateral phase separation into domains, pore formation at specific membrane sites within the contact area, etc. Only a few of these cases are currently amenable to direct observation *in situ* or rigorous theoretical analysis, the primary one being the case of the forces and deformations of two elastic spherical surfaces during adhesive contact and separation – an area of materials and biomaterials science known as 'adhesion mechanics' or 'contact mechanics' (Johnson, 1985).

Modern theories of the adhesion mechanics of two contacting solid elastic surfaces are based on the JKR theory (Johnson *et al*. 1971; Pollock *et al*. 1978; Barquins & Maugis, 1982; Johnson, 1985). In the JKR theory two spheres of radii R_1 and R_2, bulk elastic compressibility modulus or Young's modulus K, and surface or interfacial energy γ per unit area, will flatten when in contact. The contact area will increase under an external load or force F, such that at mechanical equilibrium the contact radius a is given by

$$a^3 = \frac{\bar{R}}{K}[F + 6\pi\bar{R}\gamma + \sqrt{12\pi\bar{R}\gamma F + (6\pi\bar{R}\gamma)^2}]. \tag{35}$$

At adhesive equilibrium (under zero load), the contact radius a_0 is therefore given by

$$a_0^3 = \frac{12\pi\bar{R}^2\gamma}{K} \quad \text{at } F = 0, \tag{36}$$

where $\bar{R} = R_1R_2/(R_1 + R_2)$, as before. For a sphere of radius R adhering with a flat surface (cf. inset in Fig. 19) we may replace $\bar{R}$ by R in the above equation. Eq. (35) further shows that the surfaces will spontaneously separate (jump apart as illustrated in Fig. 18 (G → H)) when the contact radius has fallen to $0{\cdot}63a_0$. At this point the force (the 'adhesion', 'detachment', 'separation' or 'pull off' force) is:

$$F_a = -3\pi\bar{R}\gamma. \tag{37}$$

Thus, from a measurement of the adhesion force F_a one may determine the surface or interfacial energy γ (in units of J m^{-2} or N m^{-1}). By definition, γ is related to the total adhesion energy, E_0, by $\gamma = \frac{1}{2}E_0$.

[34] Vertical separation (peeling, rolling) is the most common, but surfaces can also separate by shearing. These are often referred to as 'mode one' and 'mode two' fracture.

https://doi.org/10.1017/S0033583501003687 Published online by Cambridge University Press

It is interesting to note that, according to the JKR theory, a finite elastic modulus, K, while having an effect on the contact radius a or area πa^2, has no effect on the adhesion *force* (cf. Eq. 37) – an interesting and unexpected result that has nevertheless been verified experimentally (Chen *et al*. 1991b). On the other hand, the total adhesion *energy* of two elastically deformable surfaces in contact (at $F = 0$) is given by Johnson (1985)

$$E_0 \approx -\tfrac{4}{3}\pi a_0^2 \gamma \tag{38}$$

which *does* depend on the modulus K of the substrate material via Eq. (36) – the lower the modulus the higher the adhesion energy. As was elaborated on in Section 1.10, the adhesion or binding *force* F_a provides information on the force that must be applied to detach a molecule or cell or from another cell or surface, which is essentially a non-equilibrium process. In contrast, the *energy* E_0 tells us more about the equilibrium state of the system, such as the area of contact, the equilibrium separation between two membranes, and the intrinsic lifetime or off-rate of the adhesive junction or bond in the absence of any external pulling force.

Another important equation of the JKR theory is the elastic deformation or flattening displacement ΔD_S of the surfaces when in adhesive or repulsive contact. This is given by (cf. Fig. 19 inset)

$$\Delta D_S = \frac{a^2}{R}\left[1 - \frac{2}{3}\left(\frac{a_0}{a}\right)^{\frac{3}{2}}\right]. \tag{39}$$

Referring to Figs. 18 and 19, if the substrate geometry is a sphere or a section of a sphere of undeformed radius R, the length D_S can be replaced by R, and the effective stiffness K_S by a function that is related to K, R and γ via Eq. (35). For example, under a large load ($F \gg F_a$) or low adhesion energy ($\gamma \approx 0$) we find that[35]

$$\Delta D_S = \frac{a^2}{R} = \frac{F^{\frac{2}{3}}}{K^{\frac{2}{3}}R^{\frac{1}{3}}} \propto F^{\frac{2}{3}}. \tag{40}$$

At lower and negative loads, the substrate displacement ΔD_S changes from positive to negative as F approaches the pull-off force, $F_a = -3\pi R\gamma$. It is interesting that zero displacement ($\Delta D_S = 0$) occurs not at $F = 0$ but when $F = 0{\cdot}89F_a$ and $a = 0{\cdot}76a_0$, i.e. just before pull-off. On the other hand, at $F = 0$, when the contact diameter is a_0, the surface deformation is $\Delta D_S = a_0^2/3R$. More importantly, it is clear that the effective stiffness of an elastic or 'JKR' junction, defined by K_S such that $\Delta D_S = F/K_S \propto F$, is not a constant independent of the applied force F (cf. Eq. 40).

The Hertzian deformation or 'indentation' of a soft substrate surface or tip behaves like a short-range repulsion (given by Eqs. 39 and 40) that curves upward as the contacting surfaces are pressed further together. Unless one can directly measure the surface separation independently of the deflection of the center of mass of the surfaces or the force-measuring spring, it is not possible to unambiguously distinguish this elastic deformation from the 'real' repulsive force $F(D)$, such as a DL or polymer–steric repulsion, acting between the surfaces across the liquid medium.

[35] Note that this displacement is twice the displacement of a truncated sphere having the same contact area πa^2. Under conditions of high load and/or low surface energy the JKR theory of 'adhesion' mechanics reduces to the Hertz theory of 'contact' mechanics (Hertz, 1881).

https://doi.org/10.1017/S0033583501003687 Published online by Cambridge University Press

Equations (35)–(40) are the basic equations of the JKR theory, which have been verified experimentally (see later) and also found to apply at the nanoscale using a MD simulation (Landman *et al*. 1990; Leuedtke & Landman, 1992; Bhushan *et al*. 1995). The JKR theory provides the framework both for analyzing the measurements of adhesion forces between elastic solids (Fig. 19), and for interpreting the results of load-contact area or load-contact radius measurements (known as JKR plots) in SFA and AFM experiments, especially whenever significant flattening deformations occur (Horn *et al*. 1987; Heuberger *et al*. 1996; Carpick *et al*. 1999; Enachescu *et al*. 1999). For non-adhering surfaces ($\gamma = 0$) as well as for very high loads ($L \gg L_a$) all the equations of the JKR theory reduce to those of the earlier Hertz theory for non-adhering elastic spheres (Hertz, 1881; Johnson, 1985).

2.5.1 An example of the application of adhesion mechanics to biological adhesion

As an example, we consider the case of a soft biological surface of radius $R = 100$ nm (0·1 μm) and with a Young's modulus of $K \approx 10^8$ N m^{-2}.[36] The adhesion energy of this surface with another surface in electrolyte solution will be assumed to be $\gamma = 1{\cdot}0$ mJ m^{-2}, which is typical for the VDW minimum at a contact separation of $D_0 \approx 0{\cdot}4$ nm for surfaces having a Hamaker constant of $A \approx 10^{-20}$ J (cf. Section 1.3). The equilibrium contact radius of the junction under zero external force will be given by Eq. (36) as $a_0 = 15{\cdot}6$ nm (156 Å), and the equilibrium energy of the junction, as given by Eq. (38), will be $E_0 = -3{\cdot}8 \times 10^{-19}$ J or about 100 kT. This may be compared with the adhesion energy of a rigid, undeformable surface (where $K = \infty$) of $-AR/6D_0 = -4{\cdot}2 \times 10^{-19}$ J, which is of similar magnitude, although for progressively softer materials their adhesion energy will be progressively higher than the (fixed) value for rigid bodies. Also at equilibrium, the compressive deformation or flattening of the surface, as given by Eq. (39), will be $\Delta D_s = 0{\cdot}8$ nm (8 Å). On separation, the adhesion force, as given by Eq. (37), will be $F_a = -0{\cdot}94 \times 10^{-9}$ N or about 1 nN, and separation will occur spontaneously when the contact radius has fallen to $0{\cdot}63a_0 = 10$ nm. At this point the deformation displacement is $\Delta D_s = -0{\cdot}3$ nm, i.e. it is *negative* which implies that the surface is under a tensile expansion just before pull-off. In contrast, the adhesion force if the surfaces were rigid ($K = \infty$) would be $4\pi R\gamma = 1{\cdot}25$ nN, which is 25 % higher than the value of 0·94 nN for the soft, deformable surface.

In many cases the above example would be oversimplistic or even totally unrealistic. The adhesion mechanics of biological surfaces can be very different from the system modeled by the JKR or Hertz theories because biological particles and surfaces (for example, two cells or vesicles) cannot always be modeled as purely elastic spheres. Cells or vesicles contain a liquid-like aqueous core that is surrounded by a membrane. It is only the latter that is elastic, while the core, which constitutes the major part of the adhering particle, is liquid-like and can

[36] The Young's modulus of biological materials and tissues cover a range of over seven orders of magnitude between 10^{-3} and 10^{+5} MPa: 0·001–0·1 MPa for cells with a cytoskeleton; 0·1–10 MPa for cells with a stiff cytoskeleton such as muscle and cartilage; 50–200 MPa for lipid bilayers in the fluid and gel states, respectively; 100 MPa for soft, spongy bone; 100–1000 MPa for protein crystals, 1000 MPa for microtubules, and 20 000–50 000 MPa for hard bone and enamel, respectively. These values may be compared with those of non-biological materials such as soft rubber (1–10 MPa), hard rubber (100 MPa), soft polymers such as Nylon, PTFE (Teflon) and polyethylene (500 MPa), and hard polymers such as polymethyl methacrylate (PMMA) and polyvinyl chloride (PVC) (3000 MPa), and metals such as titanium and steel (100 000–200 000 MPa). Some of these materials are commonly used as implant biomaterials.

https://doi.org/10.1017/S0033583501003687 Published online by Cambridge University Press

therefore deform freely so long as its volume remains unchanged (the presence of a rigid cytoskeleton will, of course, alter these conditions, making it much more elastic or 'JKR-like') (see footnote 36). In the case of membrane-bound biological structures, the detachment force is still given by Eq. (37), i.e. it is still independent of the elastic properties of the particle or membrane; but the adhesion energy, which replaces Eq. (38), does depend on the membrane elastic modulus in a complex way (Bailey *et al.* 1990; Israelachvili, 1991). This energy also depends on various other conditions of the system, such as the way the whole structure deforms when it adheres and whether the membrane is permeable to water (which allows its volume to change) and/or ions (which allows its osmotic pressure to change), all of which are important for determining the ultimate equilibrium state (cf. Fig. 14, left panels). For example, if both water and ions can penetrate through a membrane, two initially spherical vesicles will deform on coming into adhesive contact in such a way as to maximize their area of contact. If their membranes' elastic moduli are low,[37] this process will continue until most of the internal solution (water and ions) has been expelled from the vesicles as they collapse onto each other and form flattened myelin-like structures known as cochleate cylinders (Walker & Zasadzinski, 1997), where almost every part of each membrane surface is in adhesive contact with another membrane.

In addition, most theories of adhesion and contact mechanics use continuum theories in their analysis. This could be totally inappropriate when specific molecular-scale interactions determine the adhesion – or example, when hydrophobic pockets open up at specific locations on protein surfaces that in turn bind cooperatively to specific sites on the opposite surface. In this case the local and global deformations would be very different (cf. Fig. 14, right panels), and even the concept of an average surface energy γ to describe the adhesion process may be inappropriate.

Clearly, a simple measurement of only the adhesion force or energy between two surfaces or molecules does not provide the 'complete picture' of what happens during adhesion or separation. Adhesion should be seen more as 'process', involving complex deformations both locally and of the whole system, with effects extending well beyond the adhesion site.

We now proceed with a more detailed description of each force-measuring technique, describing its strengths and weaknesses. Examples of how each has been applied are given in Sections 3 and 4.

2.6 Measuring forces between macroscopic surfaces: the surface forces apparatus (SFA)

One advantage of techniques used for measuring the forces between macroscopic surfaces is that they do not need to have a high absolute sensitivity in order to accurately measure the forces over a large distance regime. This is because the forces between macroscopic surfaces generally scale as their size or radius R (cf. Tables 2 and 3), so that they are much larger between macroscopic than between microscopic surfaces interacting through the same force. Thus, while the SFA and related techniques do not have a high sensitivity in measuring *absolute* forces F (about 1 nN), their sensitivity as regards measuring forces over a large distance range is greater than most other techniques. In mathematical terms, if two techniques measure forces over a similar range of surface separations, say, 100 nm, and if one employs surfaces of large radii, say $R_1 = 1$ mm, while the other employs surfaces of small radii, say $R_2 = 1$ μm, then the force-measuring sensitivity of the second technique will have to be

[37] Biological membranes are believed to possess both a stretch modulus and a bending modulus.

https://doi.org/10.1017/S0033583501003687 Published online by Cambridge University Press

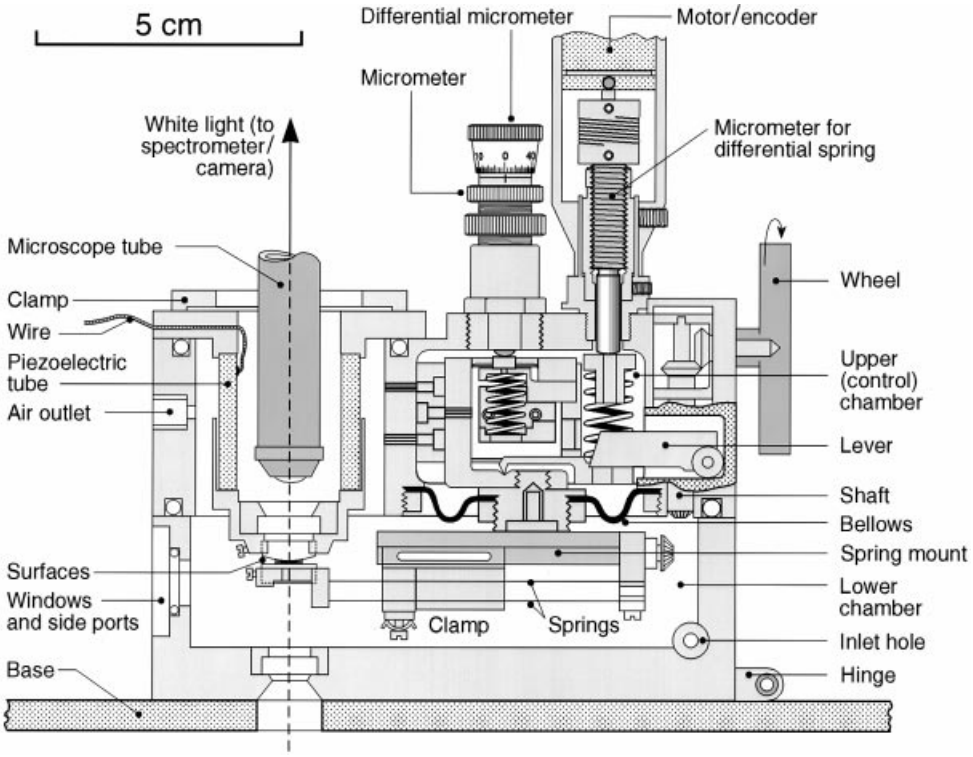


Fig. 20. A SFA where the intermolecular forces (force F *versus* surface separation D) between two macroscopic surfaces of local radius R can be directly measured, and where local or transient surface deformations can be visualized during the interaction (cf. Figs. 21 and 55). The SFA technique allows for the measurement of a very wide range of surface forces and interactions over a large distance regime from ångstroms to microns, including VDW, electrostatic, hydration, hydrophobic, bio-specific (lock-and-key), capillary, adhesion, viscous, lubrication, and even charge-transfer interactions.

$R_1/R_2 = 1000$ times greater than that of the first technique. The same scaling principle applies to measurements of surface or adhesion energies γ, which are also dependent on R via Eq. (37). The sensitivity of a technique as regards the distance range over which it can be applied therefore depends on the factor $\Delta F/R$, rather than ΔF (the force-measuring resolution). In addition, values of F/R rather than F are required for comparing the results of force measurements with theory (cf. Tables 2 and 3), and also when comparing results between different experiments using surfaces of different radii.

The SFA technique (Israelachvili & Adams, 1978; Israelachvili, 1990, 1991) is the only technique that allows for the direct measurement of the force F, the absolute surface separation D, and simultaneous visualization of the interaction zone, i.e. the local geometry, of two interacting *macroscopic* surfaces such as two membranes or protein layers. Surface separations can be quantitatively measured to better than 1 Å (Israelachvili, 1973). Lateral distances can be resolved only to 1 μm and are therefore averaged over this length scale or area. Referring to Fig. 18, the SFA technique can be used to directly measure D, ΔD, ΔD_0, ΔD_S (each to ± 1 Å), a (to ± 1 μm or $\pm 5\%$), and R, K_c, K_S and K (to within 10%). The spring deflection ΔD_c is obtained using Eq. (31).

In a typical SFA, shown schematically in Fig. 20, the sample surfaces are supported on two curved substrates that can be brought towards each other or separated in a controlled fashion

https://doi.org/10.1017/S0033583501003687 Published online by Cambridge University Press

from millimeters to sub-Ångstrom separations. Approach and separation rates can be varied over a range of eight orders of magnitude from 1 mm s^{-1} to 1 Å min^{-1}, or the two surfaces can be brought to a certain distance D from each other and then kept there to see or record what happens. Figure 19 shows a type of SFA designed specifically for adhesion studies, also known as a 'JKR apparatus' or 'adhesion-force SFA'. Surface or substrate radii used in SFA experiments typically vary from $R = 1$ to 20 mm.

Optical visualization of the surfaces using visible white light in SFA experiments usually accompanies the force measurements; this is possible because the *lateral* extent of the interacting surfaces is greater than the wavelength of light, even though the surfaces themselves may be only a few angstroms apart. To resolve lateral distances to 1 μm and surface separations to 1 Å, an optical interference technique is used whereby white light is passed normally through the two surfaces,[38] and the transmitted beam is focused on the entrance slit of a simple grating, spectrometer (Israelachvili, 1973; Heuberger *et al*. 1997). After reflecting off the grating the resulting fringe pattern or 'spectrogram' may be viewed or photographed at the exit port of the spectrometer. The colored fringes are known as fringes of equal chromatic order (FECO) (Tolansky, 1948, 1955; Israelachvili, 1973; Heuberger, 1997).

Figure 21 shows some typical FECO fringes (in black and white, the original being in color) produced by surfaces of different shapes and separations. The shapes and positions of the fringes, as measured in wavelength, can be readily translated into the real shapes and separation of the two surfaces. Indeed, the shapes of the fringes are approximately the same as the shapes of the surfaces or, more correctly, the separation profile between the two surfaces. In addition, the refractive index n of the medium between the two supporting substrate surfaces may also be measured, and this allows for the identification or verification of the material adsorbed on the surfaces, such as a lipid bilayer ($n \approx 1{\cdot}45$), a layer of proteins ($n \approx 1{\cdot}55$), or just a water gap between them ($n = 1{\cdot}33$).

The SFA technique has found applications in many different areas, both biological and non-biological.[39] When applied to biological surfaces, deformations, such as those that accompany membrane compression, adhesion or fusion, can be followed in *real time*, and rapid transient effects such as 'jumps' into or out of adhesive contact can also be monitored and recorded, with a simple video or high-speed camera (recording speeds up to 40000 fps being currently possible). As will be described in Sections 3 and 4, SFA experiments have provided quantitative information on the range and magnitude of the main forces acting between biological surfaces and molecules: VDW, electrostatic, steric, hydration, hydrophobic and LR interactions. Both attractive and repulsive forces can be measured over

[38] Usually thin sheets of transparent material such as mica, silica or sapphire that are partially silvered on their back surfaces to allow for multiple reflections of the light beam as it passes through the mica–liquid–mica 'sandwich'.

[39] For reviews, see Klein (1986); Christenson (1988); Israelachvili (1989); Patel & Tirrell (1989); Horn (1990); Israelachvili (1991); Leckband (1995, 2000); Schneider & Tirrell (1999). Various non-biological surfaces and materials have been successfully used in SFA experiments including mica, silica, bulk polymer films or adsorbed polymer layers, surfactant monolayers and bilayers, and various metal (gold, platinum, silver) and metal oxide (zirconia, alumina, iron oxide) layers or films. The range of non-biological liquids and vapors that have been used as bathing solutions include organic liquids and solvents, polymer melts, molten salts, various petroleum oils and lubricant fluids, and liquid crystals. 'Less common' interactions such as charge-transfer interactions (Horn & Smith, 1992) have also been studied with non-biological materials or surfaces, which hold promise for their application to biological surfaces.

https://doi.org/10.1017/S0033583501003687 Published online by Cambridge University Press

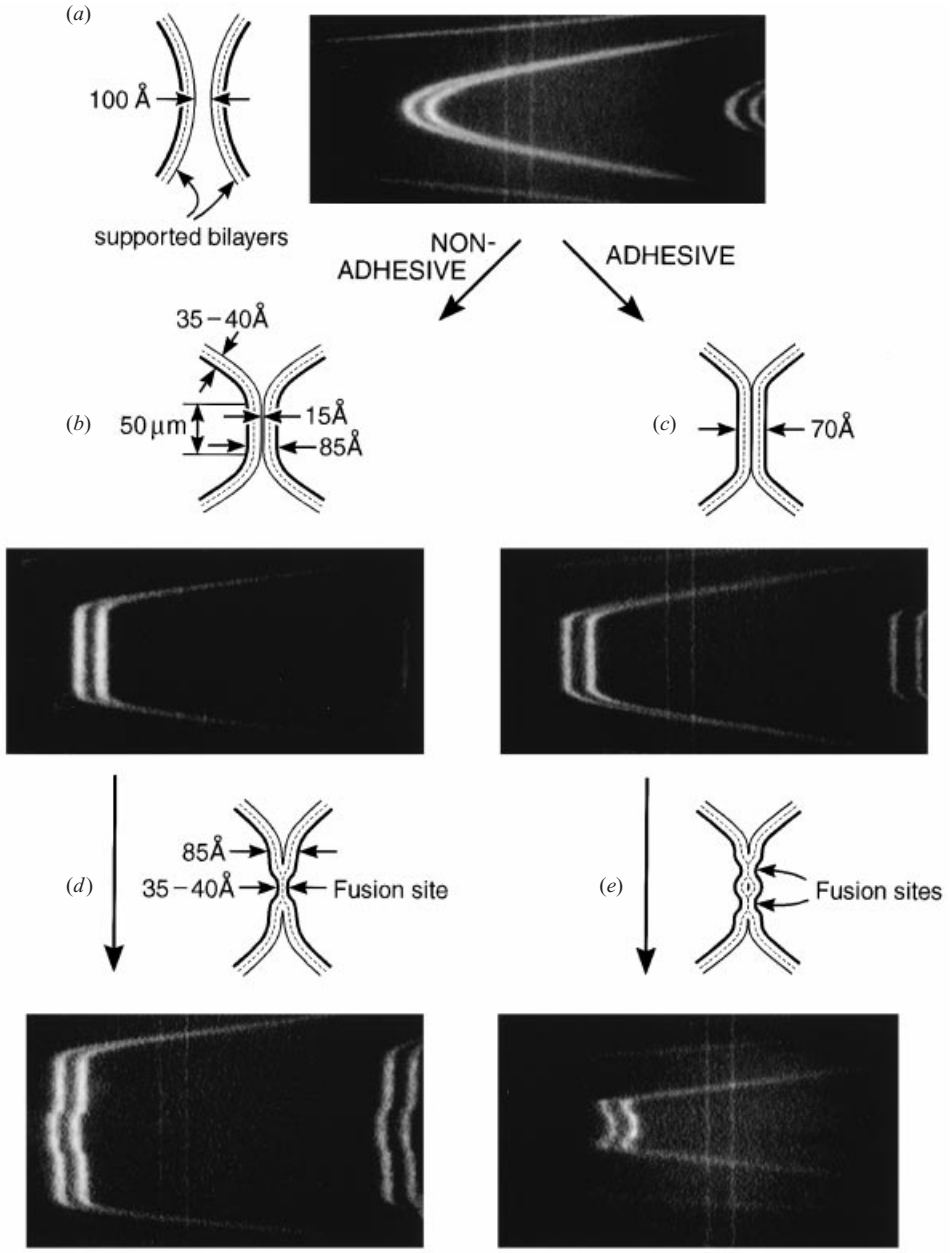


Fig. 21. FECO used to visualize the shapes and distance between two substrate surfaces, which may be supporting a protein or lipid layer, during SFA experiments (cf. Fig. 22). The fringe *shapes* reflect the shapes of the surfaces as illustrated next to each FECO pattern (the fringes appear as doublets if the substrate material is birefringent as is the case with the mica substrates used here). The fringe *positions* along the wavelength axis (i.e., horizontally) reflect the absolute separation D between the two surfaces, which can be measured to ± 1 Å. The refractive index of the intervening liquid or layer can also be measured by this technique. This figure shows the observed deformations of two supported bilayers in the fluid state undergoing hemi-fusion. (*a*) The curved surfaces are well separated by ~ 10 nm in water. (*b*) Non-adhesive 'contact' of bilayers forced together under a compressive pressure of ~ 5 MPa (50 atm) where they flatten but remain separated by a thin layer of water of thickness ~ 1 nm due to the repulsive short-range steric-hydration force between them. (*c*) Adhesive contact of two partially

https://doi.org/10.1017/S0033583501003687 Published online by Cambridge University Press

any distance regime at the Ångstrom resolution level. Various local and global surface deformations that accompany complex biological interactions can be measured and visualized in *real time* (i.e. as they occur) such as the elastic deformations of thin membranes (Chen *et al*. 1991a) or fusion (Fig. 21), as can slow time-evolving interactions such as polymer-mediated interactions that may take a long time (seconds to hours) to fully equilibrate. More recent developments now allow for 'dynamic' force measurements to be made, for example, by moving the surfaces either normally or shearing them laterally past each other. The forces, which now include the viscous, tribological and bio-lubrication forces, between them are measured, and this provides information such as the viscosity and lubricity of water solutions in ultrathin gaps between two surfaces up to pressures as high as 0·5 GPa or 5000 atm (Briscoe & Evans, 1982; Chan & Horn, 1985; Israelachvili, 1986, 1989; Horn *et al*. 1989; Peachey *et al*. 1991; Kuhl *et al*. 1998a).

In a typical SFA experiment, the two sample surfaces are first carefully prepared before they are installed into the SFA chamber, or they can be prepared inside the SFA chamber. In the latter case the two surfaces can be brought into contact first in the absence of any surface-adsorbed species (to measure the fringe positions corresponding to $D = 0$) and then after adsorption of a protein or membrane layer from solution (to measure T_1 and T_2). During subsequent force runs, the two surfaces are made to approach each other at various rates, and the interaction zone is simultaneously 'observed' by monitoring the FECO fringes. This gives the separation D at any instant as well as any deformations of the surfaces, for example, ΔD_s. The displacements ΔD_0, are obtained from the (known) displacements of the micrometer-piezo drives, from which ΔD_c is obtained using Eq. (31). This allows for the force-law $F(D)$ to be determined using Eqs. (28) or (30).

For example, in a particular SFA experiment, starting with the two surfaces at $D = 250$ Å at which $F = 0$, one may expand the piezoelectric tube by 50 Å, i.e. $\Delta D_0 = 50$ Å. If the surfaces come to rest at $D = 205$ Å without deforming (flattening), then $\Delta D_s = 0$ and the change in surface separation ΔD is $250 - 205 = 45$ Å. The spring deflection is therefore $\Delta D_c = 50 - 45 = 5$ Å (5×10^{-10} m). Thus, for $K_c = 100$ N m^{-1} (a typical value), the force at $D = 205$ Å is *repulsive* and equal to $F = 100(\text{N m}^{-1}) \times 5 \times 10^{-10}(\text{m}) = 50$ nN. Further, if $R = 1$ cm, the value of F/R at this separation is $F/R = 50 \times 10^{-9}(\text{N})/10^{-2}(\text{m}) = 5$ μN m^{-1}. On the other hand, if the surfaces had come to rest at $D = 190$ Å, the force at this separation would be *attractive* and equal to $F = -100$ nN, and $F/R = -10$ μN m^{-1}.

A serious limitation of the SFA technique, as currently practiced, is that it measures interactions under nonphysiological conditions, for example, between membranes or proteins adsorbed either directly onto solid substrates or via a lipid group (Marra, 1985; Leckband *et al*. 1993b; Pincet *et al*. 1994). Recent advances in sample preparation techniques are allowing for this limitation to be overcome by using 'softly supported' membranes or

---

depleted bilayers that attract each other via a weak hydrophobic attraction. Note the sharper bifurcation at the edges compared to non-adhering case; this is expected theoretically (cf. JKR *versus* Hertzian contact in Fig. 19 inset) and also shows that the highest stresses occur at the edges. (*d*) Hemi-fusion of non-adhering bilayers, brought about by pressing them together with a pressure in excess of 50 atm. Hemi-fusion occurs at the center, which is the region of highest compressive pressure. After fusion is initiated the fused area grows out rapidly. (*e*) Fusion of adhering bilayers often occurs spontaneously (without the need of an externally applied force) at the *edges*, rather than at the center, because this is where the bilayers are stressed the most (see commentary for panel (*c*)). Vertical lines are spectral lines from a mercury lamp, used for wavelength calibration. FECO fringes from Helm *et al*. (1989).

https://doi.org/10.1017/S0033583501003687 Published online by Cambridge University Press

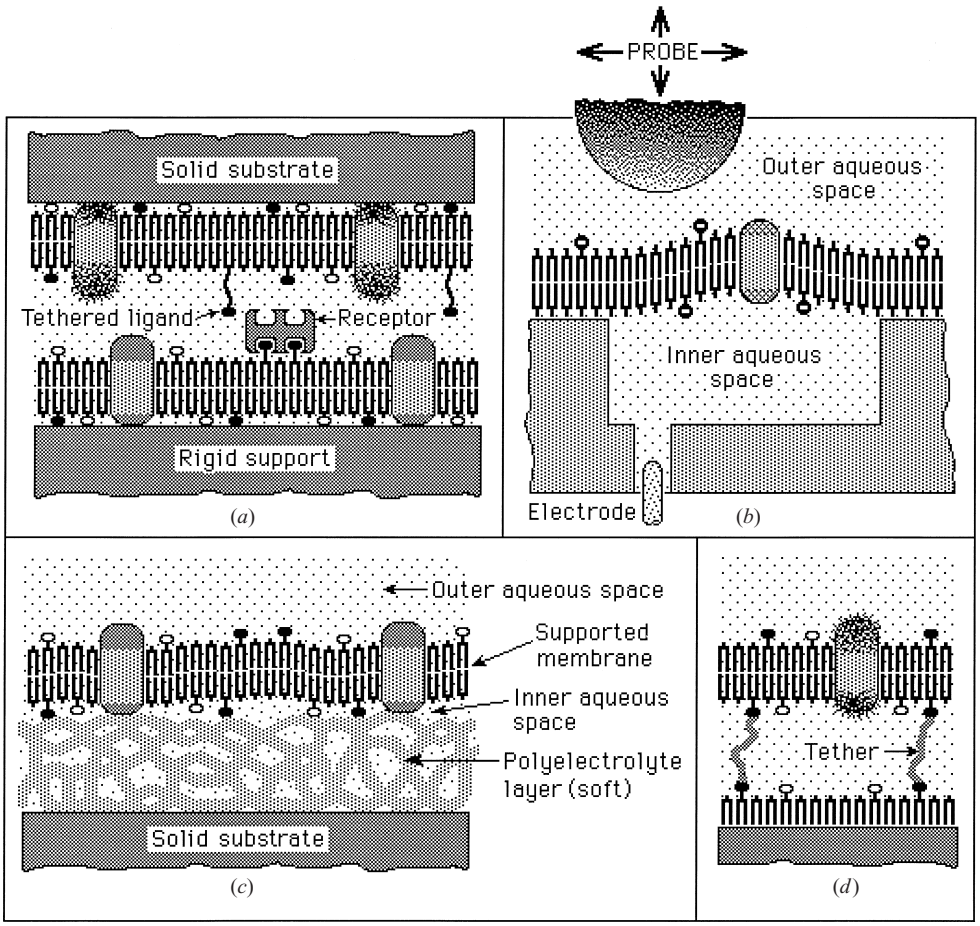


Fig. 22. Hard- and soft-supported membranes. Soft-supports are more suitable for studying the interactions of membranes and biological molecules *in vitro* under controlled conditions that closely mimic physiological conditions (Sackmann, 1996). (*a*) Hard- or 'rigidly supported' membrane: the easiest and, so far, most common method for supporting bilayers and membranes. (*b*) 'Freely supported' or 'hole-spanning' membranes that are 'free' in the sense that there is an aqueous phase on either side of the membrane – the support itself coming from the edges. Such softly supported structures can be used with a number of techniques, including SFA, AFM, fluorescence microscopy and various other optical visualization and spectroscopy techniques. (*c*) 'Polymer-supported' membranes on a layer or 'cushion' of some water-soluble polymer or polyelectrolytes (Wong *et al.*, 1999a, b). (*d*) 'Tethered membranes' or proteins that are attached to a solid surface via inert but hydrophilic polymer chains of PEG or polysaccharides (Seitz *et al.*, 1998, 2000).

macromolecules (Fig. 22). Such soft-supported structures more closely mimic physiological conditions, either of free membranes or proteins in solution, or of membranes supported by a cytoskeleton such as Spectrin in red blood cells. Three types of soft-supports (shown in Fig. 22(*b–d*)) have already produced promising results that are described in Sections 3 and 4. However, no one has yet measured the interaction forces between live cells using the SFA technique.

Another limitation of the SFA technique, as already mentioned, is its low lateral resolution, which is no better than that of an optical microscope, or about 1 μm (cf. the horizontal and vertical distance scales in Fig. 21). In addition, molecular composition and structure (e.g.

https://doi.org/10.1017/S0033583501003687 Published online by Cambridge University Press

molecular orientations) can only be inferred from the FECO fringes and force-measurements rather than directly measured. For these reasons, it is now increasingly common to complement SFA measurements with two or more other techniques that can be used either before, during (*in situ*), or after the SFA experiments, in order to characterize the morphology and composition of the surfaces. These include various optical microscopy and spectroscopy techniques such AFM, electron-microscopy, light absorption spectroscopy, second harmonic generation, sum frequency generation, X-ray and neutron-scattering for analyzing thin-film structure and molecular orientations, and XPS or ESCA for chemical analysis (Idziak *et al*. 1994). One can also compare SFA-measured forces with those obtained using other direct force-measuring techniques (Horn *et al*. 1988). It is even possible to compare SFA measurements with indirect methods for measuring interparticle interactions, such as light scattering (Gee *et al*. 1990). Indeed, excellent agreement was obtained between SFA force measurements between macroscopic surfaces of radius $R \sim 1$ cm with the measured second virial coefficients of suspended colloidal particles of radii ~ 5 nm. Most of these combinations should be applicable to both static and dynamic measurements, i.e. measuring *changes* in structure as they occur during an interaction, but have not been used simultaneously with force measurements in most cases.

2.7 The atomic force microscope (AFM) and microfiber cantilever (MC) techniques

In contrast to the SFA, the AFM (Fig. 23) allows the direct measurement of only ΔD_0, ΔD_c and K_c between a sub-microscopic tip ($R \sim 10$–100 nm) and a flat surface (Binnig *et al*. 1986; Cleveland *et al*. 1993). Larger (microscopic) colloidal particles or 'beads' ($R \sim 0{\cdot}1$–10 μm) can be used to replace the tip (Ducker & Senden, 1992), and smaller (nanoscopic) tips or even individual molecules can also be studied (Florin *et al*. 1994; Moy *et al*. 1994; Wong *et al*. 1998) whose bond strengths can be as small as a few pN (cf. Table 4). To achieve the high resolution in force required for making such delicate measurements, spring stiffnesses as small as $K_c = 0{\cdot}01$ N m^{-1} are used. Thus, to measure a force of 1 pN $= 10^{-12}$ N, and given that spring deflections ΔD_c of order 1 Å $= 10^{-10}$ m can be measured, a spring of stiffness K_c of $10^{-12}/10^{-10} = 0{\cdot}01$ N m^{-1} must be employed. This is currently just possible, and means that the adhesion and short-range colloidal forces between surfaces having molecular dimensions can now be measured with the AFM.

AFM instruments[40] employ a variety of means – mechanical, piezoelectric, optical, capacitance and/or magnetic – for moving/controlling the spring base or substrate surface ΔD_0, and for measuring spring deflections ΔD_c (Fig. 23). AFMs are generally designed to measure ΔD_0 and ΔD_c, but they measure neither the absolute separation D nor the deformations ΔD_s of the surfaces in the interaction zone, at least not directly. The spring stiffness K_c can be calibrated as in the SFA technique, but parameters that depend on the *local* geometry and composition of the surfaces, such as D_s or R, ΔD_s, a, K_s and T (cf. Fig. 18), are not amenable to direct measurement and must be inferred or modeled.

From a knowledge of ΔD_0, ΔD_c and K_c, the changes in the separation ΔD and force ΔF

[40] AFMs come under the more general category of scanning probe microscopes (SPMs) that developed from the original scanning tunneling microscope (STM). Other instruments, such as the friction force microscope (FFM) or lateral force microscope (LFM) are more specialized instruments for measuring both normal and lateral forces.

https://doi.org/10.1017/S0033583501003687 Published online by Cambridge University Press

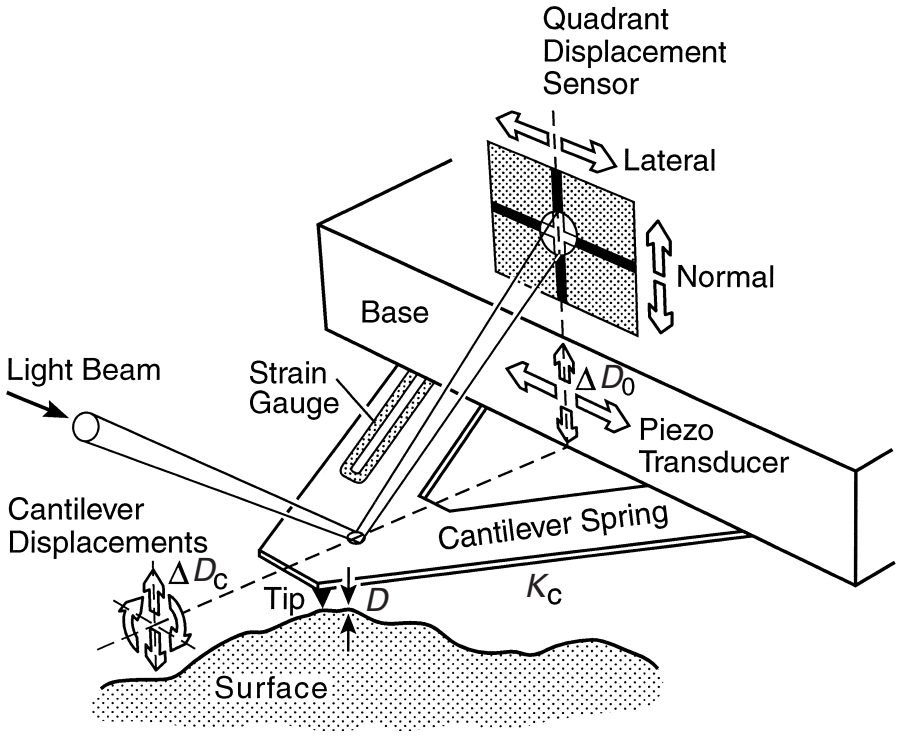


Fig. 23. AFM for imaging the topology of surfaces via the forces experienced by a 'tip' moving normally or laterally across the sample surface. The tip is attached to the end of the cantilever spring whose deflection ΔD_c gives the normal and/or lateral force acting on the tip. These deflections are monitored on a quadrant position sensitive detector (PSD) such as a photodiode array by following the movement of a light beam after it has bounced off the end of the cantilever surface. Movement of the tip relative to the sample surface ΔD_0 is achieved with an XYZ piezoelectric transducer that can act either on the substrate surface or the cantilever spring support. In some AFM instruments the 'beam bouncing' detection method is replaced by resistance strain gauges attached to the cantilever arms, as shown.

from one position to the next are obtained using Eqs (31) and (30), and assuming $\Delta D_s = 0$ (or estimating its value), namely

$$\Delta D = \Delta D_0 - \Delta D_c \tag{41}$$

and

$$\Delta F = K_c \Delta D_c. \tag{42}$$

This limitation in the number of parameters that can be directly measured with the AFM means that D and F/R are never known with certainty. Thus, a change in ΔD_c due to a change in ΔD_0 could be due to a real change in the surface force $F(D)$ at finite separations D. But it could also be due to a change in the deformation ΔD_s of the surfaces[41] that are already in contact, i.e. at $D = 0$. A further limitation of AFM measurements involves non-equilibrium interactions, such as forces that take a long time to equilibrate as often arises with tethered or polymeric systems. This cannot be easily distinguished from thermal drift. Thus,

[41] Such as surface flattening (JKR or Hertzian) or a change in the membrane thickness T due to lipid rearrangements.

https://doi.org/10.1017/S0033583501003687 Published online by Cambridge University Press

a change in the measured force with time arising from a changing ΔD_c *may* be due to a real, non-equilibrium change in F at constant D, although it may also be due to a slow thermal drift in D that takes the system into a different (equilibrium) force regime.

Problems of drift and a lack of direct methods of measuring surface separations, geometry and contact areas present as-yet unsolved difficulties with AFM, especially for soft biomolecules and biomaterials such as fluid membranes or molecules exposing polymer-like tethers such as polysaccharides. Since the AFM technique cannot give unambiguous information on the thickness of adsorbed layers, it offers no means for distinguishing between a contaminant layer, multilayers, or the 'real' layer it is supposed to be measuring.

In view of these limitations, AFM force-curves are usually reliable for measuring equilibrium forces at relatively large separations only, i.e. in the absence of surface deformations, although the absolute surface separation D is only known relative to a model-dependent constant. Adhesion forces F_a can also be measured accurately, especially if these are large, typically > 1 nN, from the measured jumps out ΔD_c from contact, using Eq. (34):

$$F_a = \Delta F = K_c \Delta D_c. \tag{43}$$

Once a force-law or pull-off force is measured, the geometry of the two surfaces (e.g. the local radii R of the surfaces in the interaction zone) must also be measured or estimated before one can use the equations of Tables 3 and 4 to compare the results with theory or with other experiments. In Sections 3 and 4, various AFM force-curves are shown and, where possible, compared with measurements made on similar systems with the SFA and other force-measuring techniques. As with the SFA technique, there is a trend to combine AFM with other interaction-associated techniques in the same experiment, such as electric, magnetic or various optical spectroscopy techniques. These should provide valuable additional insights into complex biological interaction processes at both the molecular and collective levels.

As a result of some of the limitations described above, the majority of AFM investigations of biological interactions or the properties of single molecules focus on determinations of the force to break bonds or stretch molecules, rather than on measurements of force laws. Due to the potential to shear the surfaces (Stuart & Hlady, 1995) (cf. Fig. 23) or to compress soft biomolecules and cells, the molecules of interest are generally sparsely immobilized on soft, polymeric supports. Receptors are immobilized on the tip, which is often also coated with a soft material such as an adsorbed protein or polymer matrix (Florin *et al*. 1994; Lee *et al*. 1994; Moy *et al*. 1994). As the 'receptor-derivatized' cantilever tip presses into the polymer matrix containing bound ligands, bonds form between the surfaces. The receptors and ligands are generally sufficiently sparsely distributed that only a few bonds can form, and bond rupture is then detected as abrupt discrete jumps in the force as the tip is pulled out of the matrix. The small force jumps will then correspond to a small, integral numbers of bonds, the average value of which can be determined from autocorrelation analyses of the distribution of the measured forces (Florin *et al*. 1994). Optimally, the rupture forces would correspond to single bond rupture events.

Recent reports (Mehta *et al*. 1999) suggest that the mechanical properties of single molecules can also be determined from measurements of the relative extensions of large macromolecules. Again, these measurements are done by pressing the tip into an adsorbed macromolecular film, and then pulling it away from the surface. If the macromolecules bind or adsorb to the probe, occasional, characteristic signatures in the force traces are attributed to the unfolding or stretching of single molecules. However, as we will discuss in Section

https://doi.org/10.1017/S0033583501003687 Published online by Cambridge University Press

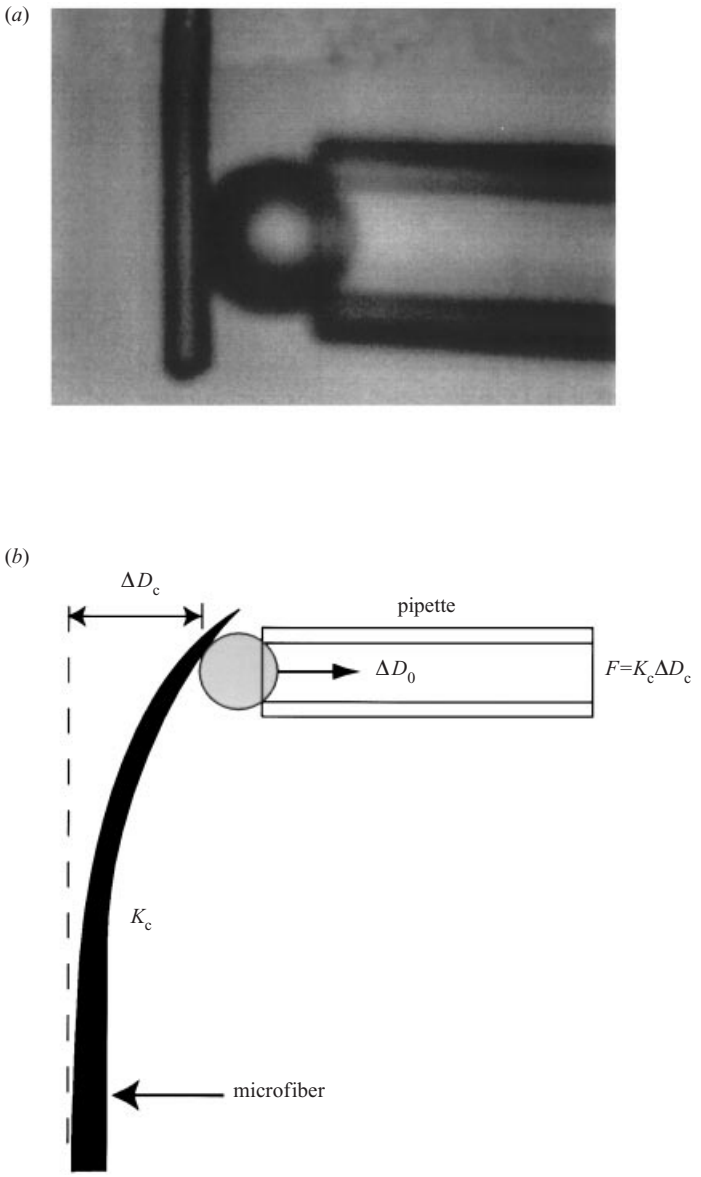


Fig. 24. Microfiber cantilever. The upper panel (*a*) shows a glass fiber in contact with a small, functionalized bead supported on a movable pipette. The lower panel (*b*) shows the fiber deflection as the adhering bead is retracted. At pull-off, the fiber springs back by ΔD_c to its original, vertical position.

4.10, since the absolute positions of the ends of the molecules are unknown, the molecular extensions can only be determined from fits of the data to theories describing polymer extension.

The *microfiber cantilever* (Fig. 24) operates on a similar principle to the AFM where the thin glass fiber is analogous to the cantilever spring and probe tip of the AFM. The fiber is usually derivatized with a ligand or receptor of interest, and is brought into contact with a bead modified with complementary molecules as illustrated in Fig. 24(*a*). The bead is then retracted, and the fiber deflects in proportion to the force exerted by the bead. As in the AFM

https://doi.org/10.1017/S0033583501003687 Published online by Cambridge University Press

measurements, the adhesion force is determined from the deflection (jump distance) of the fiber ΔD_c when the bond breaks according to Eq. (43). The fiber's spring constant K_c is calibrated in an independent measurement.

The glass fiber cantilever or glass micro-needle has a force sensitivity of 10^{-11} N or 10 pN (Essavaz-Roulet *et al*. 1997; Schmitz *et al*. 2000), which is similar to that of the AFM (Table 5). It differs from both the AFM and the SFA in that the location of the fiber relative to the bead is visualized by optical microscopy, but neither the absolute intersurface distance D nor the local geometry of the contact site R can be determined. For this reason, measurements of biological adhesion focus on single bond measurements with coated fibers and probe surfaces that are only sparsely coated with receptors and ligands. Sparsely coated fibers ensure that no more than one or two bonds will form in the contact zone at any one time, so that the measured adhesion forces will be simple multiples of the individual bond strength. This approach is therefore restricted to sensitive measurements of forces in the 1–100 pN regime that are nevertheless large enough to generate deflections of the fiber that can be observed by optical microscopy (resolution $\sim 1\ \mu$m). This requires extremely low fiber stiffness of the order of $K_c \approx 10^{-11}/10^{-6} = 10^{-5}$ N m^{-1}.

As described in Sections 3 and 4, the microfiber technique has been used to measure single bond strengths and the traction forces exerted by migrating cells when they run into the fibers (Yoneda, 1960). The technique can also be used for making 'dynamic' force measurements (Tees *et al*. 2001). For example, variations in the pulling rate from between 200 and 5000 pN s^{-1} (Tees *et al*. 2001) allows one to investigate the dynamics of RL bond failure and associated energetics, as discussed in Section 1.10.

2.8 Micropipette aspiration (MPA) and the bioforce probe (BFP)

The MPA and the BFP techniques are used to measure the forces (1) between a cell or giant vesicle and another cell or vesicle, and (2) between a functionalized bead and a cell, vesicle, or material surface (Evans, 1987, 1988; Evans *et al*. 1992, 1995; Noppl-Simson & Needham, 1996; Evans & Ritchie, 1997; Chelsea *et al*. 1998). In the latter case, the bead can be used to probe interactions between materials bound to the bead surface and any arbitrary 'test material', such as a cell or polymer. The experimental setup is shown in Fig. 25. The force transducer is an elastically deformable red blood cell (RBC) membrane or giant vesicle, which is held by suction at the tip of a glass micropipette (Evans, 1988). In some cases, a functionalized bead is attached to the red blood cell via biospecific bonds. The use of attached beads, as opposed to cells or giant vesicles, allows for more versatility in the molecules that can be studied with this approach (Evans *et al*. 1995). The latter configuration is shown in the upper left box (A) in Fig. 25B. In the simplest case, without the bead, the red blood cell interacts with a second membrane, and both membranes deform elastically in response to the net attractive or repulsive force between them and to the applied suction. The mechanical equilibrium between these two deformable membranes determines their final shapes, which are recorded as shown in Fig. 25. The intersurface force, membrane tension, and total interaction energy are then obtained from the micromechanical analysis of the (measured) global shapes of the deformed membranes (Evans, 1987, 1988; Evans & Needham, 1988; Evans & Rawics, 1990; Evans *et al*. 1992; Noppl-Simson & Needham, 1996; Chelsea *et al*. 1998). As in the case of other adhering surfaces (cf. Section 2.5), if the two membranes adhere, they will distend as the micropipette is retracted. When the bonds fail, the membranes recoil

https://doi.org/10.1017/S0033583501003687 Published online by Cambridge University Press

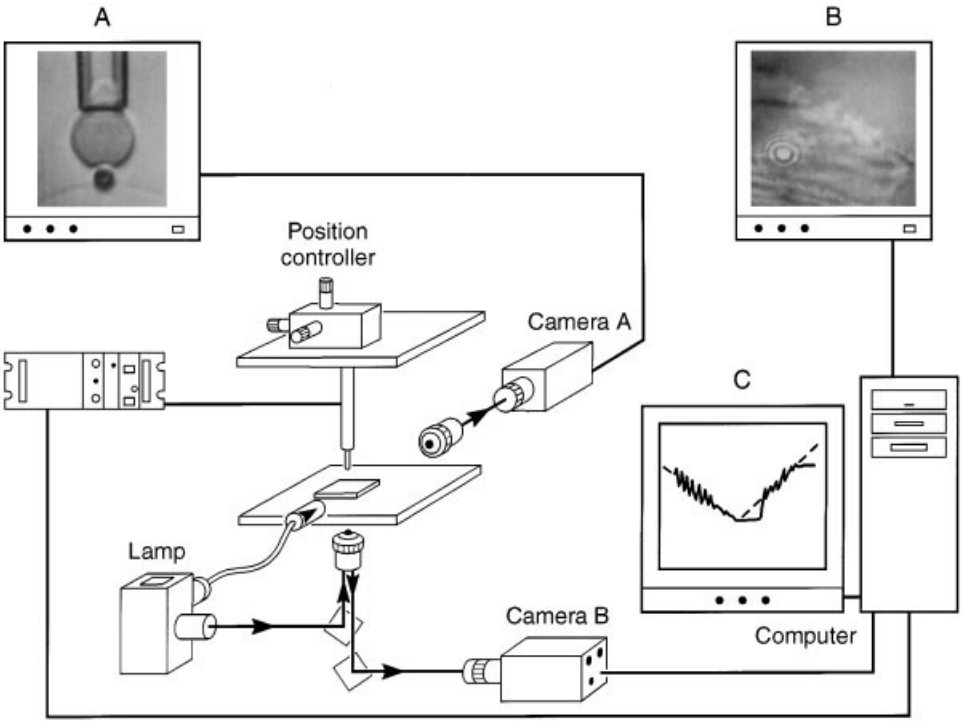


Fig. 25. Schematic of the MPA and BFP techniques. The upper left panel (A) shows the bead attached to the membrane force transducer. The red blood cell is held by suction at the end of the glass micropipette. The central stage is surrounded by two orthogonal microscopes. The microscope perpendicular to the micropipette monitors the movement of the bead towards or away from the glass substrate on the microscope stage. The inverted microscope records the interference pattern (B) and feeds it to a computer (C) that coverts the recorded images into the separation distance D between the bead and glass surface.

back to their undistorted, spherical shapes. With beads attached to the blood cell transducer (Fig. 25A), the adhesion between the bead and any arbitrary material will cause similar shape distortions in the RBC that depend on the bead adhesion (Evans *et al.* 1995).

This instrument uses the soft membrane material, rather than a mechanical spring, as the force transducer. Membrane tension, which controls the stiffness of the RBC, can be adjusted by aspirating different amounts of the membrane into the pipette by the application of different hydrostatic pressures. This allows the tension to be varied over a wide range of values to yield effective spring constants K_c between 10^{-6} and 10^{-2} N m^{-1} (Evans, 1988; Evans *et al.* 1995; Chelsea & Zhu, 1996). With the additional capability of detecting small distortions in the membrane shape, forces can be measured from 0·1 to 1000 pN. This is the widest range of force sensitivity currently accessible with any of the instruments described in this review (cf. Table 5).

Earlier measurements with the prototype MPA were generally between cell membranes and a second membrane. More recently, functionalized beads were attached to the membrane transducer by biospecific glues, such as lectins, to expand the repertoire of biological molecules that can be studied with this approach (Evans *et al.* 1995). The use of beads also makes it possible to determine the distances between the materials. This cannot be done when only membranes are used. In this more recent configuration, known as the BFP, reflectance

https://doi.org/10.1017/S0033583501003687 Published online by Cambridge University Press

interference contrast microscopy (Albersdörfer *et al*. 1997, 1998) is used to quantify the distance between the bead and test material, e.g. cell on a glass coverslip, with 5 nm resolution (Fig. 25B) (Evans *et al*. 1995). The glass slide beneath the bead in Fig. 25 is coated with a magnesium fluoride (MgF_2) film on which test materials are deposited. The interference patterns generated by the multiple reflections of light between the bead and layered surface (Fig. 25B) are then converted into bead–surface distances, D. The 5 nm resolution is much poorer than attainable with the SFA, AFM and some other techniques (described below). For this reason, accurate force–distance *profiles*, $F(D)$, cannot be measured, but the *magnitudes* of the net attractive or repulsive force at contact can be accurately determined.

With the BFP, one can also access a wide dynamic range of loading and unloading rates. Increasing the suction on the membrane increases the membrane tension. In adhesion measurements, this amounts to pulling materials apart (unloading them) by increasing the tension rather than separating them by retracting a spring. One can vary the rate of unloading over seven orders of magnitude from 0·1 to 10^6 pN s^{-1} (Evans *et al*. 1995; Evans 1999; Merkel *et al*. 1999). Because the membrane deformations are visualized by video imaging, the upper bound is set by the video framing speed. The slow thermal drifts of the instrument set the lower limit. It may be possible to achieve faster pulling rates with the AFM. However, for single bond measurements, the BFP can access the widest dynamic range. Examples of how this can be used to map intermolecular potentials are given in Section 4.

2.9 Osmotic stress (OS) and osmotic pressure (OP) techniques

In the OS technique (Fig. 26) forces or, more strictly, pressures are measured between bilayers, membranes, biocolloidal particles (Homola & Robertson, 1976; LeNeveu *et al*. 1976; Parsegian *et al*. 1979; Lyle & Tiddy, 1986; Rand & Parsegian, 1989; McIntosh *et al*. 1992a, b; McIntosh & Simon, 1994), or biological macromolecules such as viruses and DNA that form ordered colloidal structures or 'arrays' in solution (Onsager, 1949; Parsegian & Brenner, 1976; Rau *et al*. 1984; Podgornik, 1989; Leikin *et al*. 1993). The structure of these ordered phases can be studied using X-ray and neutron scattering techniques (Parsegian *et al*. 1979; Caffrey & Bilderback, 1983; Wiener & White, 1992). This provides the mean separation between the particle surfaces as well as additional information such as the extent of membranes undulations, or DNA bending motion, due to thermal effects. Ordered structures can be stacked sheets ('lamellar phases' as occur with lipid bilayers and membranes), arrays of rods ('hexagonal phases' as occur with DNA and some virus particles), and various other three-dimensional structures.

Both repulsive forces and attractive forces between macromolecules can give rise to such ordered structures, depending on the magnitude and range of the forces and on the concentration of molecules or particles in the solution. The case of an attractive force giving rise to an ordered assembly is easy to understand. The case of repulsive forces leading to ordering may be understood by considering that if dissolved particles or membrane sheets want to get well away from each other, they can do this most effectively by assembling into a lattice where each particle sits as far away from its neighbors as possible. Any movement away from each 'lattice site', for example, if the lattice 'melts' and the particles start to move freely in the solution, will bring the particles closer together *on average*. Their mean separation will therefore decrease which, because the force between them is repulsive, will cause an (unfavorable) increase in the potential or interaction energy of the system. This however is

https://doi.org/10.1017/S0033583501003687 Published online by Cambridge University Press

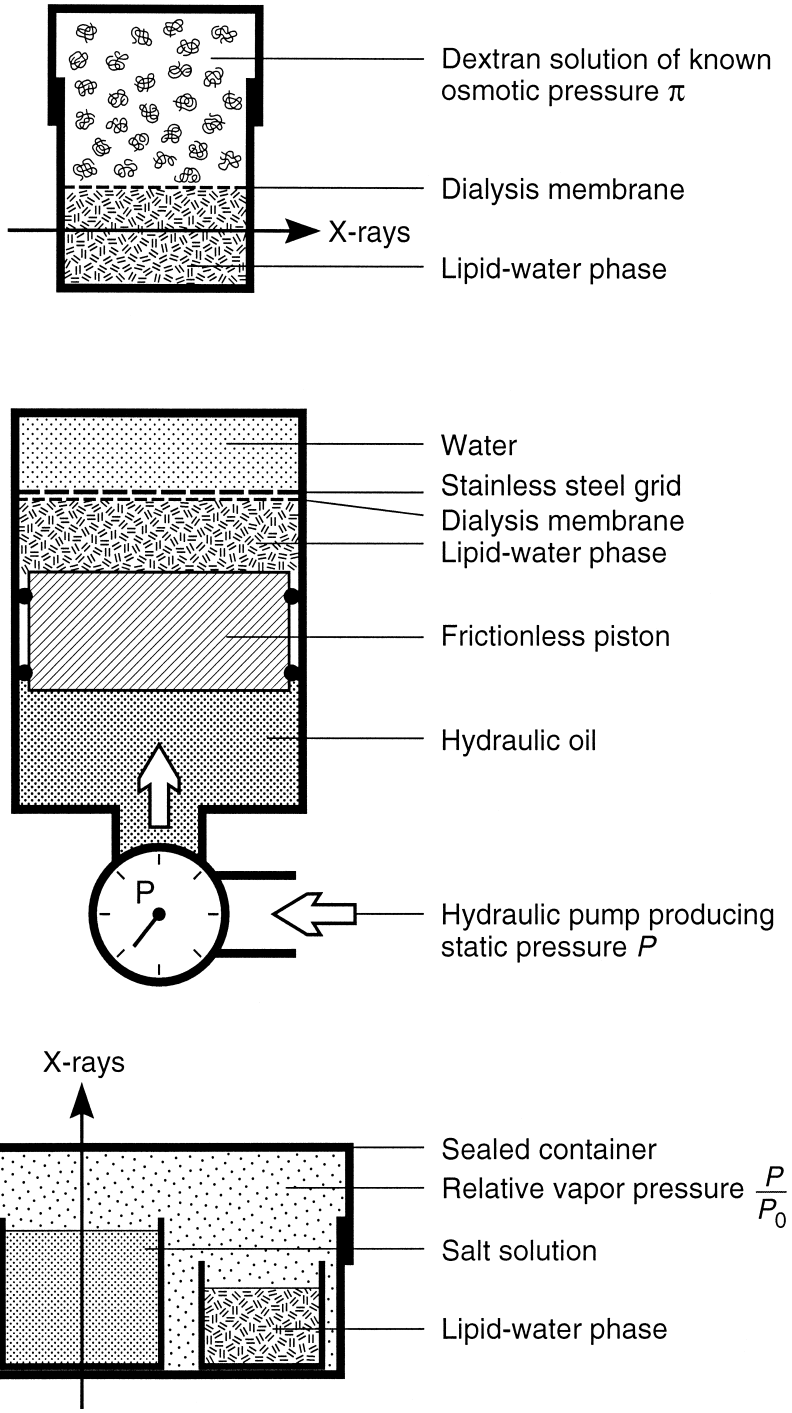


Fig. 26. OS or OP techniques: three methods commonly used for varying the osmotic pressure of a colloidal or biocolloidal dispersion while monitoring the structures in the solution and their separation using X-rays and/or neutron scattering (Wiener & White, 1992). (Adapted from Parsegian *et al.* 1979.)

https://doi.org/10.1017/S0033583501003687 Published online by Cambridge University Press

offset by the (favorable) increased entropy of the particles, which, together with the potential energy determines the total free energy and hence the OP of the solution. For this reason it is not a simple matter to extract the interaction potential $E(D)$ or force-law $F(D)$ between the particles from the measured OP $P(D)$ of the solution which also includes these entropic contributions. Entropic contributions can be large; for example, for a solution containing *non-interacting* solute molecules their OP is given by $P = \rho RT$ where ρ is the solute number density. This repulsive pressure is large even for dilute solutions and yet arises from purely entropic effects, i.e. when there is no actual force – attractive or repulsive – between the suspended particles (Israelachvili & Wennerström, 1992).

In the OP techniques, the X-ray measurement of the mean interparticle separation D is accompanied by a measurement of the osmotic pressure P of the solution using one of three techniques shown in Fig. 26 whose suitability depend on the range of pressures under investigation. In some cases, especially when measuring the pressure between bilayers, different values are obtained depending on which method is used. This has been attributed to the slow relaxation times that are needed for these systems to equilibrate or re-equilibrate after a change in the solution conditions, which requires the slow diffusion of water and ions in or out a stack of semi-permeable bilayers. Equilibrium values can be obtained only after long equilibration times (Katsaras, 1998), giving the OP P as a function of the interbilayer separation D or the distance between linear macromolecules such as DNA. Only repulsive forces can be measured using the OP technique. In Sections 3 and 4 we compare some measurements of forces between phospholipid bilayers and between proteins using the OP and SFA technique – the two most common techniques for studying the interactions of macroscopic surfaces (Table 5).

2.10 Optical trapping and the optical tweezers (OT)

The use of optical traps to manipulate small particles was first demonstrated in 1986 (Chu *et al*. 1986). Since the initial demonstration, several trap designs have led to an explosion in the number of uses of these tools to probe the miniscule forces in biological systems. Several excellent reviews describe the variety of studies of biological interactions using OT (Block, 1992; Svoboda & Block, 1994; Sterba & Sheetz, 1998).

OT developed as a natural application of the trapping of atoms using cold lasers. Optical trapping results from the use of radiation pressure and optical gradients to generate restoring forces, which prevent dielectric spheres from diffusing away from the center of a focused laser beam (Ashkin *et al*. 1986, 1987; Chu *et al*. 1986; Ashkin, 1992, 1997). For particles much larger than the diffraction limit ($R \gg \lambda$), the forces acting on a particle can be understood using simple ray optics (Fig. 27). When a laser beam is focused onto a dielectric sphere, the rays incident on the particle are reflected and refracted at the surface. As a result, the electromagnetic waves entering the sphere are bent and undergo a change in transverse momentum. By conservation of momentum, the reaction force (gray arrows, Fig. 27) exerted on the particle balances this momentum change. Figure 27 shows the change in momentum and the resultant force vectors. If the ray intensities on both sides of the particle are identical, as shown in Fig. 27 (left), the net reaction forces along the x-axis normal to the incident light on the left and right sides of the sphere balance each other, and the net lateral force on the particle will be zero. This also shows that a particle that moves away from the center (or high-intensity region) of the beam will experience a restoring force that pulls it back into the

https://doi.org/10.1017/S0033583501003687 Published online by Cambridge University Press

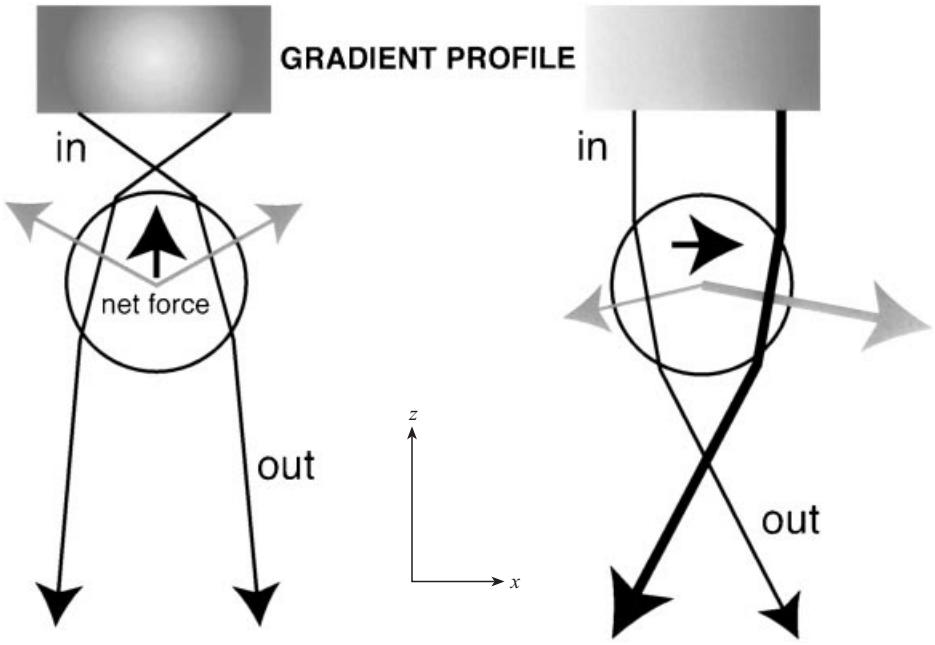


Fig. 27. Ray optics diagrams illustrating the origins of optical forces exerted on dielectric spheres. *Left*: When a laser beam is focused slightly above the particle, there is no net lateral force on the particle, due to the radial symmetry in the intensity of the light impinging on the bead. However, by focusing the beam just above the particle, the gradient along the z-axis exerts a normal (as opposed to lateral) force on a bead that tends to pull the particle up into the trap. *Right*: asymmetric force on a particle generated by a light gradient. In this instance, the intensity of the incident light beam increases from left to right across the bead. The rays on each side of the bead are refracted by the particle. However, because of the differences in the intensities and corresponding differences in the transverse optical pressure of the refracted rays, there is a difference in the net force in the x-direction exerted on the bead (black arrow, bead center). (Adapted from Svoboda & Block, 1994.)

center. Furthermore, the equilibrium position of a bead in a laser trap is slightly above the focal plane (in an inverted microscope), so that the restoring force is proportional to the displacement from the equilibrium position, which is different from the laser beam focus. If instead of a uniform beam, where the intensity distribution is radially symmetric, there is an intensity gradient within the beam, as exhibited by the different thicknesses of the rays in Fig. 27 (right), then the reaction forces are not balanced across the sphere. As a result, there will be a net lateral force in the x-direction.

3D light intensity gradients are thus used to manipulate the position of a particle or to pull or push it against another particle. In this way, the traction force of a motor protein, for example, can be directly measured. The OT used to position particles are generated by 3D optical gradients, which are present in any focused light beam. Increasing or decreasing the beam focus can tune the sharpness of the gradient. In practice, laser tweezers require relatively steep gradients to ensure that the gradient force exceeds the scattering force. In addition, the force exerted on the particle is also proportional to the laser intensity.

While the accessible applied forces can range, in principle, from tens to hundreds of piconewtons, a limiting factor is sample heating at high energy fluxes. Ashkin (1987) used near infrared light to minimize heating in aqueous samples, and laser traps for biological

https://doi.org/10.1017/S0033583501003687 Published online by Cambridge University Press

investigations typically use near-infrared light sources. Intense laser power nevertheless damages biological samples and kills cells, so that the forces accessible for studies of biological materials are typically limited to tens of piconewtons. Despite this limitation, such weak forces are nevertheless relevant to many biological interactions. For example, the force required to stall kinesin translocation along microtubules is ~ 10 pN (Block, 1995; Kuo & Sheetz, 1993; Visscher *et al*. 1999). Similarly, the power stroke of bacterial flagellum exerts a force of about 1 pN (Ashkin, 1997).

Most small biological molecules are not sufficiently refractile to trap. For this reason, biological molecules are attached to carrier particles, known as 'optical handles', such as transparent polystyrene beads (Svoboda & Block, 1994; Ashkin, 1997; Sterba & Sheetz, 1998). The refractive indices of 'handles' typically in use are well-suited for laser trapping. Although the wavelength of the light λ determines the efficiency of the grasp of a trap, but is possible to manipulate particles much larger than the wavelength. To visualize very small particles, trap designs can be interfaced with a variety of optical tools such as bright field, differential interference contrast, fluorescence, phase contrast, and confocal microscopy. In some cases, these imaging methods allow determination of changes in the particle position with submicron resolution (Visscher *et al*. 1996; Gijs *et al*. 2000). However, Svoboda *et al*. (1993) incorporated a dual beam laser-spot interferometer developed by Xu *et al*. (1995) that is capable of achieving nanometer resolution in particle displacements ΔD_0 (Visscher *et al*. 1996). Although single molecules are difficult to trap directly, this important development made it possible to accurately measure the single 8 nm steps in the progression of kinesin along microtubules (Svoboda *et al*. 1993). More recent designs (Visscher *et al*. 1996; Dai & Sheetz, 1999; Gijs *et al*. 2000) monitor the position of a laser beam scattered off the particle, similar to the approach used in AFM measurements (cf. Fig. 23) where 1 nm displacements can be measured. These methods for achieving nanometer-level resolution in position sensitive detection are essential for measurements of, for example, the force-extension profiles of single, extensible molecules such as titin and DNA, as well as monitoring the displacements of molecular motors (Kuo & Sheetz, 1993; Svoboda *et al*. 1993; Bustamante *et al*. 1994; Block, 1995; Kellermayer *et al*. 1997; Visscher *et al*. 1999; Gijs *et al*. 2000).

The small beads or particles used in these studies undergo Brownian motion, which can limit the resolution in position measurements. Unrestrained beads undergo even larger fluctuations. The thermal noise can be reduced or damped by exerting a restraining force on the particle. This does not eliminate the noise completely, but it improves the resolution of the displacement measurements to about 0·5 nm. On the other hand, the Brownian noise can also be used to determine the force on the particle: the power spectrum of the particle fluctuations depends both on both the applied load and the interparticle force, so that analysis of the amplitude and frequency of 'bead fluctuations' can be used to determine the mean force on the particle (Visscher *et al*. 1996). A similar approach is used in both the TIRM and RICM experiments described below to map particle-surface potentials.

A distinct advantage of optical trapping techniques is the degree of control over the applied force. Optical forces can be rapidly increased or abruptly terminated, and loading or unloading rates can be easily changed. The latter approach has been used in investigations of the activation barriers to unbinding. For example, Tskhovrebova *et al*. (1997) varied the rate of titin stretching and demonstrated that the apparent differences in the force-extension profiles measured by AFM and OT were due to the different pulling rates. More recently, the introduction of a feedback loop enabled Wang *et al*. (1998) to vary the load exerted on

https://doi.org/10.1017/S0033583501003687 Published online by Cambridge University Press

molecules probed by a trap. By gradually increasing the restraining load on kinesin, they were able to determine the precise stalling force for both kinesin movement (Visscher *et al*. 1999) and RNA polymerization (Wang *et al*. 1998). The ability to rapidly increase or suddenly switch off the load gives the tweezers perhaps the best time-dependent control of forces applied to single molecules.

2.11 Other optical microscopy techniques: TIRM and RICM

Prieve and co-workers (see recent extensive review by Prieve (1999)) introduced a new method for measuring the minute forces between an individual colloidal particle and a surface, which is typically a glass slide, in aqueous solutions (Prieve & Alexander, 1986; Prieve & Frej, 1990). A colloidal particle, if it is heavier than water, will slowly sink towards the surface. The gravitational force is opposed by radiation pressure exerted by a laser beam focused on the particle from below, and by any repulsive intermolecular forces between the particle and surface. The balance of the gravitational force, radiation pressure, and particle-surface forces determines the equilibrium height of the particle above the glass slide. The radiation pressure and the gravitational force on the particle determine the sensitivity of the technique. If the particle is too light, it will not settle, but if it is too heavy, the radiation power required to levitate the bead will cause excessive sample heating. This approach was recently reviewed by Prieve (1999).

The TIRM technique uses the intensity of an evanescent beam scattered off the particle or bead to determine the height at which a bead of typical radius $R \sim 10\,\mu$m hovers over a surface (Fig. 28) (Prieve, 1999). From the intensity of the scattered beam one can measure small *changes* in the separation with an accuracy of ~ 5 nm, but the absolute separation D is difficult to determine. Since the levitated particle is sitting at the bottom of a shallow potential energy well, its Brownian motion causes it to sample positions both smaller and larger than the mean value, D_0. By analyzing how the reflected light intensity varies with space and time, the time-averaged spatial distribution function $\rho(D)$, which gives the distances sampled on either side of the equilibrium distance, is obtained.[42] From the distribution function, one can determine the interaction potential $E(D)$ or force-law $F(D)$.

In a variation of the TIRM approach, Albersdörfer *et al*. (1997) used RICM to quantify the spatial variation in the distance between the surface of a particle and the supporting surface. With RICM, the substrate on which the particle settles is a MgF_2-coated glass coverslip (Fig. 29(*a*)). The added MgF_2 layer shifts the intensity *versus* distance profile $I(D)$ to where small changes in D cause large changes in I, and this significantly enhances the ability to measure D accurately. The reflections generate a series of interference fringes (Fig. 29(*b*)), so that one can map the particle-substrate distance from the fringe patterns (Fig. 29(*b*)). The distance resolution depends on the reflectivity of both the particle and substrate, but reports range from 0·3 nm to 5 nm.

The RICM technique is similar to the BFP, and both have been used to quantify the forces between membranes and various substrate surfaces, membrane adhesion energies, the shape of the contact line between a membrane and a substrate, and membrane bending moduli

[42] As illustrated in Fig. 28, there is really no such thing as an 'equilibrium distance' when the Brownian motion of a particle or macromolecule causes it to sample regions of space far from the mean position. In quantitative terms, this occurs when the width of the particle's potential well, in units of kT, is greater than a few Ångstroms or nanometers.

https://doi.org/10.1017/S0033583501003687 Published online by Cambridge University Press

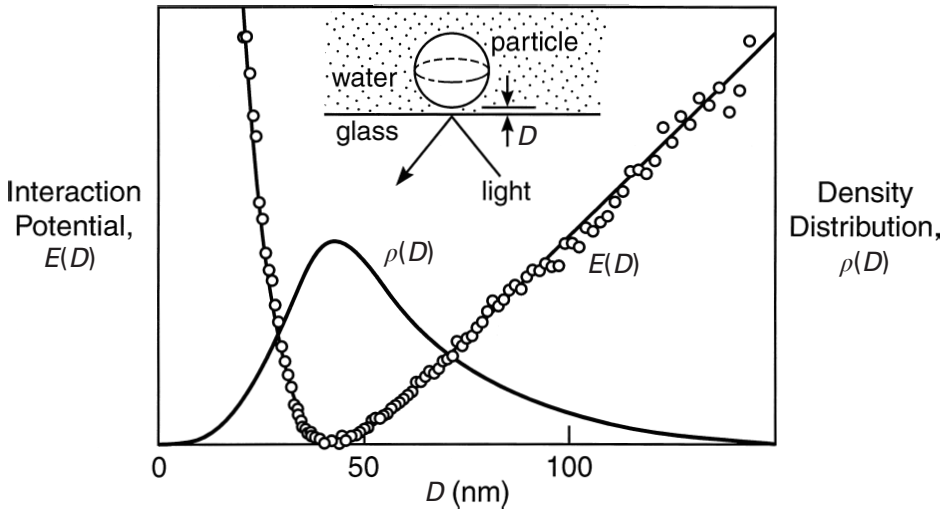


Fig. 28. Measuring repulsive colloidal forces with the TIRM technique. Measured density distribution $\rho(D)$ and corresponding potential energy profile $E(D)$ for 10 μm polystyrene sphere near a glass surface in a 1 mM NaCl solution (Prieve & Frej, 1990). The steep repulsion close in is due to the DL interaction, the linear attraction farther out is due to the gravitational potential. Note that there is no *equilibrium separation* between the sphere and the surface, only a distribution of distances about the mean distance, D_0. This 'distribution' defines the thermodynamic equilibrium *state* of the particle.

(Rädler & Sackmann, 1992; Zilker *et al*. 1992; Albersdörfer *et al*. 1997, 1998). As an example of this, Fig. 29(*a*) shows a giant vesicle that has been allowed to settle on a glass substrate. The vesicle has spread and deformed until mechanical equilibrium has been reached. The latter is determined by the balance of forces between the spreading pressure generated by the intersurface attraction, the gravitational force that promotes further spreading, and the tension exerted by the membrane which prevents spreading. This determines the *global* equilibrium shape, including the macroscopic contact angle θ, which is determined by the Young–Dupre equation:

$$\tau(1-\cos\theta) = E_0. \tag{44a}$$

Here, E_0 is the adhesion energy per area as before, τ is the membrane tension, and θ is the contact angle, defined in Fig. 29(*a*).[43] The *local* shape, which is determined by the bending modulus of the membrane, is determined from the interference fringes shown in Fig. 29(*b*). Importantly, in contrast to adhesion force measurements that determine adhesion energies by forcing materials apart – an inherently non-equilbrium process – this approach quantifies the *equilibrium* adhesion energy. For two adhering vesicles as in Fig. 14, instead of a vesicle in a flat surface as in Fig. 29, Eq. (44a) become replaced by (see Servuss & Helfrich, 1989):

$$2\tau(1-\cos\theta) = E_0. \tag{44b}$$

[43] E_0 is the same as the $-E(D)$ at the equilibrium mean separation $D = D_0$ between the membrane and substrate surface, where D_0 could be finite (Fig. 16) or zero (in the case of molecular contact). The contact angle θ is usually defined *inside* the droplet, in which case $\cos\theta \to -\cos\theta$ in Eq. (44). The membrane tension τ is not the same as the surface or intefacial tension γ of a liquid–vapor or liquid–liquid interface – a quantity that is independent of the surface area (but it has the same units of N m^{-1}). The tension of a membrane arises from its elastic stretching force, given by $\tau = k_a \Delta a/a_0$, where k_a is the area stretch or compressibility modulus (in units of N m^{-1}), $\Delta a = (a - a_0)$ is the change in area, and a_0 is the original area. The elastic energy itself is given by $\frac{1}{2}k_a \Delta a^2/a_0$.

https://doi.org/10.1017/S0033583501003687 Published online by Cambridge University Press

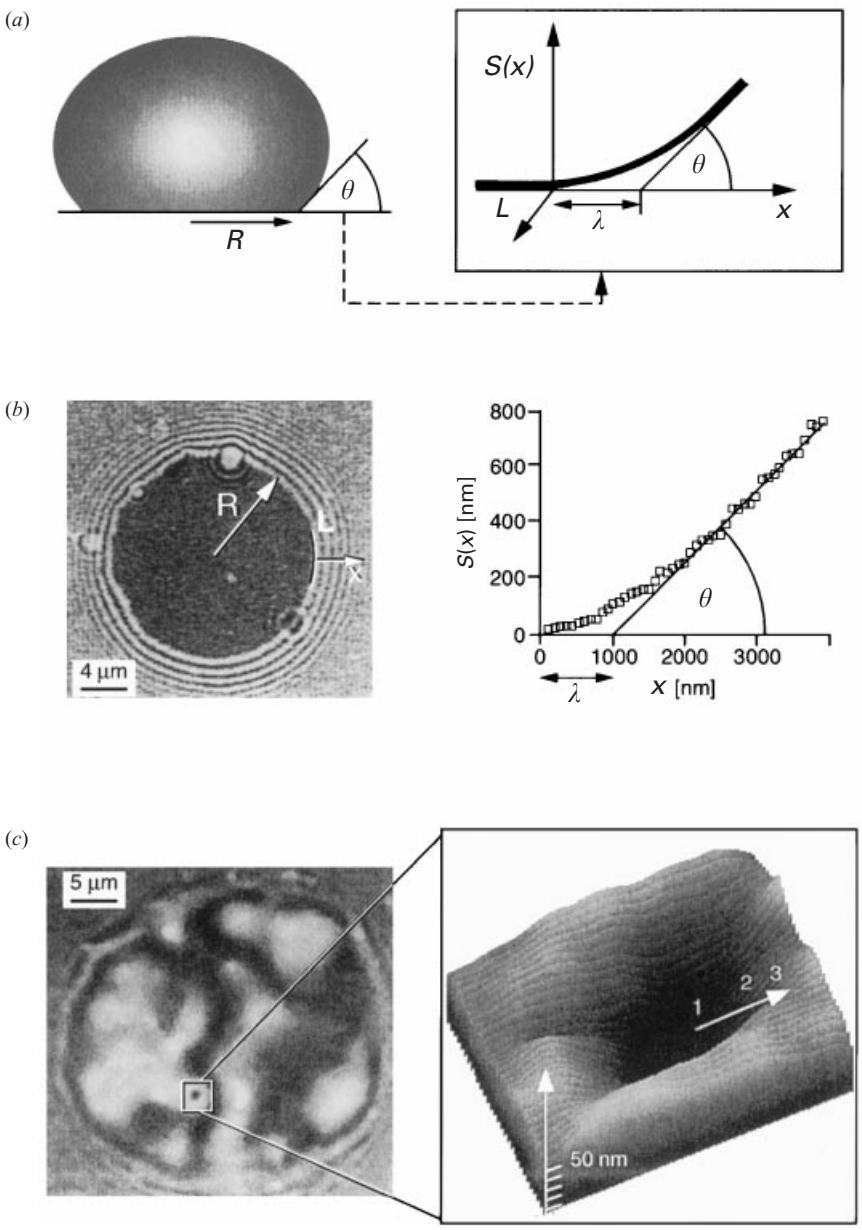


Fig. 29. RICM. (*a*) Hypothetical membrane 'droplet' adhering to a substrate. The right panel shows the shape of the contact line where u and x are the radial distances from the center of the adhering droplet, $S(x)$ is the surface contour away from the substrate, L defines the contact line or boundary, λ is the range over which bending elasticity determines the curvature, and θ is the macroscopic contact angle. Analysis of the measured interference pattern between the adhering vesicle and substrate (*b*, left) yields the vesicle contour $S(x)$ at the edge of the contact region (*b*, right). Note the waviness of the surface, which is typical of soft membrane surfaces: the smooth contour $S(x)$ shown in (*a*) is a time-averaged function. The instantaneous profile can be highly rippled. In (*c*), bonds between biotin on the vesicle and streptavidin on the substrate mediate vesicle–substrate adhesion. Dark regions are adhesion sites, where 2D crystalline patches of streptavidin have bound to the vesicle. Bright regions correspond to unbound membrane. The measured topography near one attachment point, indicated by the small box on the left, is shown on the right of (*c*). (Adapted from Albersdörfer *et al.* 1997.)

https://doi.org/10.1017/S0033583501003687 Published online by Cambridge University Press

For sufficiently large vesicles, the whole area of contact between the membrane and surface can be imaged in real time. For uniform materials this can reveal the thermal fluctuations (Brownian motion) of the surfaces (Zilker *et al*. 1992). With RL-bonded surfaces, where receptors and ligands on the opposing surfaces can diffuse laterally and cluster, local variations in the adhesion can be monitored. These may appear as differences in the local contact angle and curvature near the pinning sites (Fig. 29(*c*)). In cases of phase separation or the formation of large clusters, the contact area contains dark regions that reflect pinning sites, and light regions exposing blisters or bulges where the membrane is unbound (Fig. 29(*c*)). Nardi *et al*. (1997) used this technique to detect phase separation and blistering of fluid membranes composed of a mixture of charged and neural lipids, and Albersdörfer *et al*. (1997) observed the formation of clusters of RL cross-bridges between membranes.

In other studies, membrane fluctuations were detected from the flickering in the fringe intensities within and just outside the membrane-surface contact region. The amplitudes of the fluctuations depend on the bending modulus of the membranes, so that analyses of the undulations of the membrane adjacent to the supporting surface enabled Zilker *et al*. (1992) to determine the bending moduli k_b of cell membranes.

2.12 Shear flow detachment (SFD) measurements

In addition to force balance approaches, which allow the direct measurement of isolated bond strengths, bond strengths can be inferred from the hydrodynamic fluid shear force required to detach molecularly bound beads or cells from surfaces (Bongrand *et al*. 1988; Kaplanski *et al*. 1993; Tees *et al*. 1993; Alon *et al*. 1995; Pierres *et al*. 1995, 1996; Kwong *et al*. 1996; Tees & Goldsmith, 1996; Brunk & Hammer, 1997; Swift *et al*. 1998). In this approach, receptors are fixed to a surface, and beads or live cells in the fluid displaying complementary ligands become attached to the surface via specific bonds. The fluid flows through the chamber at a given velocity, and the fluid shear stress at the wall determines the net torque exerted on the bound particle or cell (Fig. 30). According to the force balance diagram shown in Fig. 30, the force on the bonds anchoring the particle is determined from the balance of normal F_n and tangential forces. At some critical force, the bonds will rupture, and the bead (or cell) will be swept downstream at a velocity equal to the velocity of the fluid. The force per bond F_b can be determined from the net force on the particle at the time of rupture, averaged over the contact area, and the number of bonds per area (Lindermann & Lanfferburger, 1993). Because the latter approach assumes the geometry of the contact region and a uniform stress distribution within the adhesive junction, one can only estimate the bond strength using this approach. This difficulty was in part addressed by Chang & Hammer (1996) whose adhesive dynamics simulation algorithm was used to track (1) the stress distribution throughout the contact zone, (2) the force on the individual proteins, and (3) the dynamics of individual bond formation and rupture.

There are several variants of the shear detachment assay that are used to measure bond strengths. Generally, because the magnitudes of the shear stresses are determined by the fluid velocity profiles, the different experimental configurations all involve simple geometries with well-defined flow characteristics. One of the more common designs involves fluid flow between two parallel or tapered plates (Kaplanski *et al*. 1993; Alon *et al*. 1995). In a variation of this method, a rod coated with receptors or ligands is drawn through a slender tube coated with the complementary molecules (Tees *et al*. 1993). In yet another example, aggregated

https://doi.org/10.1017/S0033583501003687 Published online by Cambridge University Press

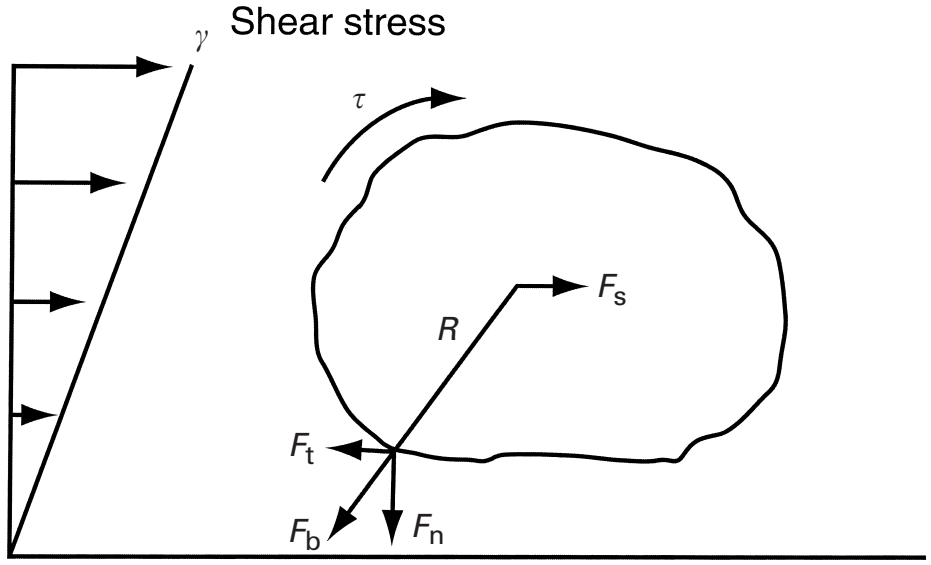


Fig. 30. Force balance on cells or particles in the SFD assay. This illustrates the force on a single bond formed between a particle and a substrate. The particle radius is R, D is the distance between the bead and substrate, L is the bond length, and F_n and F_t are the normal and tangential, respectively, components of the bond force F_b. T is the tension on the bond, N is the non-specific force on the bead due to colloidal forces. The applied external shear force is F_s, and the torque on the particle is τ. (Reprinted with permission from Alon *et al*. 1995.)

particles are subjected to shear stress by a counter-rotating 'cone on plate' rheometer (Kwong *et al*. 1996; Tees & Goldsmith, 1996). The parameters measured can also vary. For example, in a parallel plate flow chamber, cells might be allowed to settle on the substrate, and the fluid velocity would then be increased until 50% of the cells detach. Alternatively, dynamic measurements of the rates of bond formation and rupture can be determined from the motion of beads or cells as they flow by, roll, or attach firmly to the substrate (Kaplanski *et al*. 1993; Pierres *et al*. 1995, 1996). In all cases, the particles or cells adhere to a second surface, and are subjected to hydrodynamic shear. This approach can be used with cells (Kaplanski *et al*. 1993; Alon *et al*. 1995; Swift *et al*. 1998), or cell-free systems, such as receptor-coated beads (Pierres *et al*. 1995, 1996; Brunk & Hammer, 1997).

In the more common parallel-plate flow chamber, bond kinetics and rupture forces are extracted by modeling the particle trajectories over the surface and the duration of arrests when the particles attach (Kaplanski *et al*. 1993; Alon *et al*. 1995). At low ligand densities, measurements of both the kinetics and strengths of single bonds are possible (Pierres *et al*. 1996). At higher densities where adhesion can involve multiple bonds, the rupture forces are estimated from the average bond strength or by comparing the adhesive behavior with simulations. The latter can be difficult to interpret rigorously because little is known about the cell surface roughness and the bond distribution between the surfaces. Single bond events are easier to interpret, but must be done at relatively low (pN) forces exerted on the particles. As the fluid velocity increases, it becomes difficult to observe arrests by single bonds, so that only multiple bond events are detected. The lower limit of detectable adhesion forces is on the order of 1 pN, and the maximum velocity at which the particle trajectories can be tracked determines the upper limit.

https://doi.org/10.1017/S0033583501003687 Published online by Cambridge University Press

In contrast to the force probes, the force on the bonds in the flow cell is switched on almost as soon as the bond forms and the cell movement stops. This is an advantage, since the loading rate in the flow chamber is essentially constant in a first approximation. This makes determination of the dissociation rate at a given force more straightforward. In contrast, with the other force measuring techniques, the measured bond strengths, as well as estimated dissociation rates, vary between research groups on account of differences in the rates at which the unloading forces are applied in the particular experiment. The nearly instantaneous application of the hydrodynamic force makes it possible to determine the dissociation rate as a function of the applied load (cf. Section 4.3). Moreover, the time resolution of rate constant measurements is on the order of 20 ms, and dissociation rates as rapid as $\sim 8\ s^{-1}$ have been measured (Pierres *et al.* 1996).

In SFD studies with cells, other membrane processes can also contribute to the measured detachment force. The excess membrane on and inside cells serves as a reservoir to buffer changes in membrane tension (Raucher & Sheetz, 1999), and the membrane can deform in response to the tension exerted on the intersurface bonds. Earlier OT and MPA studies found that the work to pull out membrane tethers – that is, long narrow, presumably hollow tubes of membrane lacking cytoskeletal components – was relatively low (Hwang & Waugh, 1997; Dai & Sheetz, 1999; Raucher & Sheetz, 1999). In recent studies of rolling neutrophils, Schmidtke & Diamond (2000) directly observed tether formation between the cell membrane and ligand-coated substrate. Those findings clearly showed that the apparent bond rupture forces determined with cells in SFD studies may include both the force to deform and pull out such tethers and the force to rupture the bonds. As a result, the bond rupture strengths determined in cell-free SFD studies with rigid beads and/or nondeformable substrates may differ from those measured with real cells.

Another interesting possible consequence of using shear to quantify bond strengths concerns the directionality of the applied force. Bond rupture forces obtained from SFD measurements are predicted to be somewhat lower than those determined with the force probe methods on account of the differences in the direction of the applied loads. The force probes apply tension parallel to the bond axis, whereas the hydrodynamic shear force is tangential to the molecular bond (F_t in Fig. 30). Chang & Hammer (1996) showed that the tangential force needed to rupture bonds can be more than 50 times lower than rupture forces exerted parallel to the bond axis. Thus, the apparent bond strength may also depend on the direction of the applied force relative to the bond axis, in addition to the dynamic variables discussed in Section 1.10. This prediction has not yet been directly tested, however.

2.13 Cell locomotion on elastically deformable substrates

In RICM measurements, the cell or membrane-substrate adhesion energy can be determined from the deformations of the soft membrane surrounding the cell or vesicle. On the other hand, the force exerted on the substrate by the cell can be determined by monitoring the induced deformations in elastically deformable substrates over which the cells move. The use of isotropic, elastically deformable materials to determine the tension exerted by adhesive or locomoting cells was recognized several years ago (Harris *et al.* 1980).

The principle behind this approach is straighforward: The tension exerted by cells adhering to the substrate causes the soft materials to wrinkle or deform. If the elastic constant of the material K_s is known, the force exerted can be quantified from the magnitude of the

https://doi.org/10.1017/S0033583501003687 Published online by Cambridge University Press

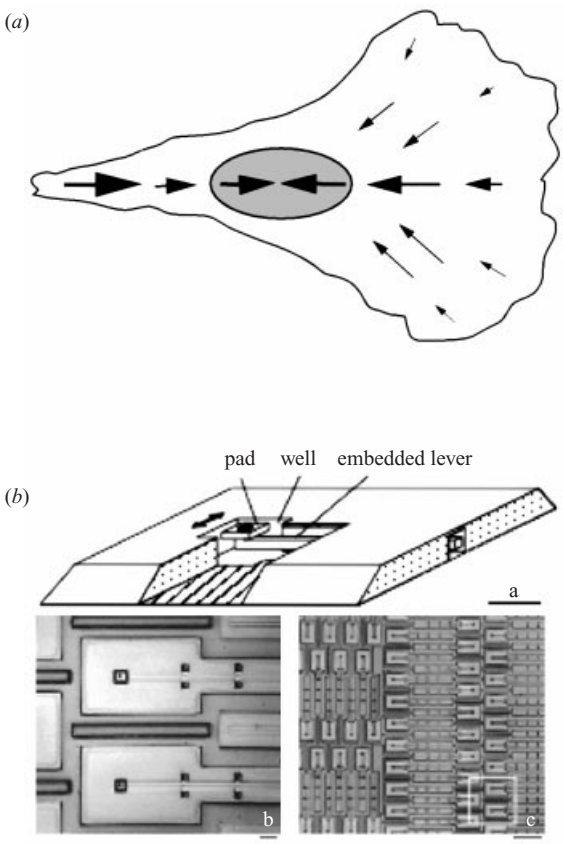


Fig. 31. Determination of the force exerted by locomoting cells on elastic substrates. (*a*) This shows the spatial distribution of measured force vectors and their corresponding relative magnitudes and directions exerted at different positions of the cell during migration. (*b*) Schematic of a micromachined device used to determine the force exerted at different locations of a locomoting cell.

surface deformations ΔD_s. The substrates used are generally silicone rubber or polyacrylamide gels (Pelham & Wang, 1997). Because changing the amount of bis-acrylamide cross-linker can vary the stiffness of the polyacrylamide gel, the latter material is more versatile. The extent of the local deformations is visualized with small particles embedded in the gel (Dembo & Wang, 1999). The bead displacement correlates with the degree of substrate deformation, and the analysis of the particle movement gives the force exerted by the cell (Dembo & Wang, 1999). Additionally, forces exerted by locomoting cells can be determined from the real-time measurements of substrate deformations. The spatial resolution is also sufficiently high that one can determine the distribution of forces exerted at different positions of the cell (Fig. 31 (*a*)).

A micromachined device consisting of an array of cantilevers embedded in a silicone matrix is a more sophisticated apparatus for conducting similar measurements of forces exerted by locomoting cells (Galbraith & Sheetz, 1997). The device, shown in Figure 31 *b*, consists of microcantilevers etched in silicon substrates. Pads of 4–25 μm^2 are positioned on the ends of the cantilevers. Cells contacting the pads deflect the hidden beams. From analyses of the images of the cells on the devices, obtained with polarized reflection optics, the deflections

https://doi.org/10.1017/S0033583501003687 Published online by Cambridge University Press

are determined with $\pm 0{\cdot}02$ μm resolution. Since the spring constant is ~ 76 nN mm^{-1}, the force resolution is ~ 1 pN.

3. Measurements of equilibrium (time-independent) biological interactions

3.1 Long-range VDW and electrostatic forces (the two DLVO forces) between biosurfaces

The DLVO interaction, composed of the VDW and electrostatic 'DL' forces (described in Sections 1.3 and 1.4), is the 'generic' interaction that exists to greater or lesser extent between all biosurfaces (e.g. cells, membranes) in water and aqueous electrolyte solutions such as normal saline, cytoplasmic fluid and sea-water. As was illustrated schematically in Fig. 6, the net DLVO interaction can be attractive or repulsive at all separations, or it can be attractive then repulsive then attractive again, or some other combination,[44] depending on the dielectric properties and charged states of the surfaces.

Figure 32 shows DLVO force-distance curves measured between (1) two negatively charged di-hexadecyl phosphate (DHP^-) bilayers adsorbed on mica surfaces in various NaCl solutions and at different pH values using the SFA technique, and (2) between a silica bead and a silica surface using the AFM technique. Both types of measurements agree with each other and with the DLVO theory (see below) except at small separations, below about 2 nm, where additional monotonically repulsive steric–hydration forces sometimes dominate over the VDW attractive forces. In Fig. 32(*a*) these repulsive forces (dashed line) dominate only at high ionic strength and high pH because only then do hydrated Na^+ ions bind to the negatively charged phosphate headgroups, imparting an additional short-range steric–hydration force. In Fig. 32(*b*) they dominate under all solution conditions because of the intrinsic hydration of silica surfaces (Vigil *et al.* 1994).

As an example of the quantitative implications of the forces shown in Fig. 32, we may analyze the long-range repulsive DL force between the two DHP bilayers in 10^{-3} M NaCl, shown in Fig. 32(*a*), which is well-fitted by the exponential force function: $F(D)/R = 2 \times 10^{-3}\, e^{-D(\mathrm{nm})/8{\cdot}5}$ N m^{-1}. This is of the same form as the theoretical curve: $F/R = \kappa Z e^{-\kappa D}$ given in Table 3 for this geometry. The measured exponential decay length of 8·5 nm may be compared with the theoretical Debye length, given by Eq. (7), of 9·5 nm at this concentration. The pre-exponential factor, 2×10^{-3} N m^{-1}, implies that $Z = 1{\cdot}7 \times 10^{-11}$ J m^{-1} which from Eqs. (10) and (8) further imply that the surface potential and charge density are, respectively, $\psi_0 = -49$ mV and $\sigma = -3{\cdot}8 \times 10^{-3}$ C m^{-2}. The latter corresponds to one electronic charge per 42 nm^2 (one per 4200 Å^2).

This charge density means that only a small fraction, of order 1%, of the phosphate headgroups are charged (ionized). If the headgroups were fully ionized, the surface charge density would be about 1 electronic charge per 0·64 nm^2, corresponding to $\sigma = 0{\cdot}25$ C m^{-2}, and the surface potential would then be ~ 250 mV. Such high surface potentials and charge densities are rarely encountered on biological surfaces, even though they have the potential of reaching such high values. The low charge density of amphiphilic surfaces is believed to

[44] Between two identical surfaces the long-range DL force is always repulsive and the VDW force is always attractive. However, both of these forces can have the opposite sign between dissimilar surfaces, as often arises in biological systems.

https://doi.org/10.1017/S0033583501003687 Published online by Cambridge University Press

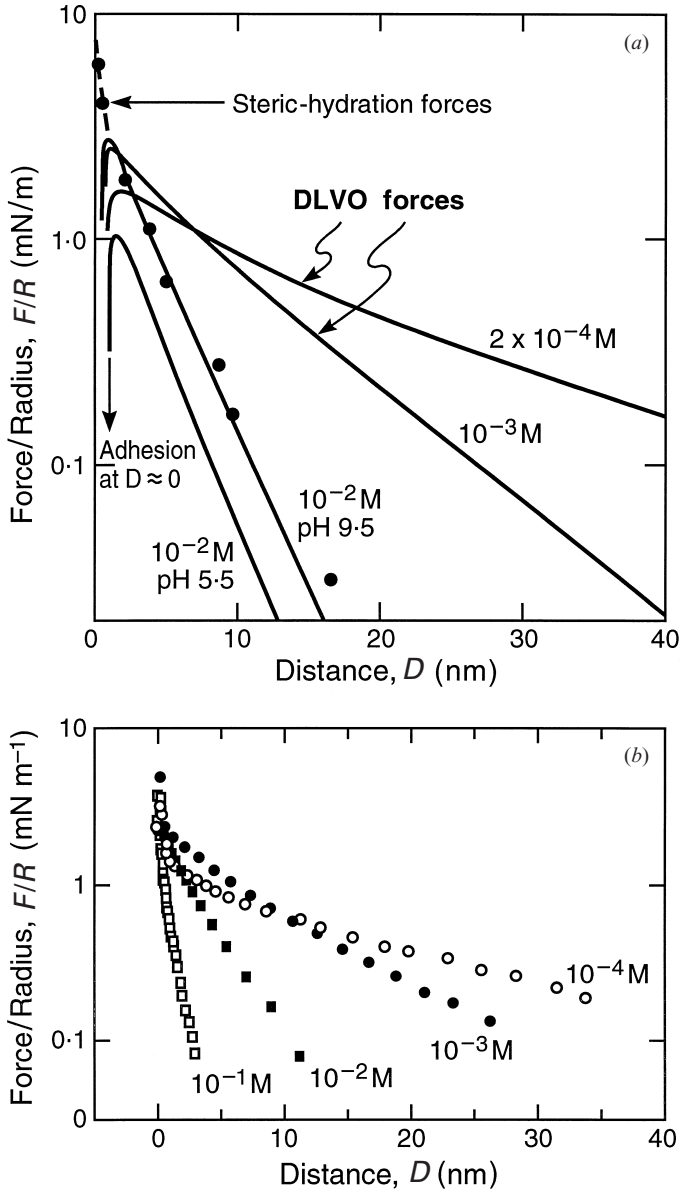


Fig. 32. DLVO force-distance curves measured between (*a*) two DHP^- surfactant bilayers using the SFA technique (adapted from Claesson & Kurihara, 1989), and (*b*) between two glass surfaces using an AFM (adapted from Ducker & Senden, 1992). Both types of measurements agree with each other and with the DLVO theory (cf. theoretical solid lines in (*a*)), except at small separations (cf. dashed line in (*a*)). In (*a*) $D = 0$ corresponds to the position of the adhesive minimum; in (*b*) the absolute value of D is not known.

be due to the low dielectric constant environment of the bilayer or membrane interior just below the headgroups, composed of hydrocarbon chains with a dielectric constant of $\epsilon \approx 2$. This makes it energetically very unfavorable for the headgroups to dissociate. In contrast, surfactant and lipid headgroups in small micelles and isolated molecules are much more

https://doi.org/10.1017/S0033583501003687 Published online by Cambridge University Press

exposed to the aqueous solution ($\epsilon \approx 80$). They are much more likely to be dissociated, with the ionized fraction being typically 25% in small micelles and close to 100% for isolated molecules in solution.[45]

Further analysis of the DL forces in Fig. 32(*a*) shows that the system behaves like a 'constant potential' one, i.e. the surface potential ψ_o (rather than the charge σ) remains roughly constant as the ionic strength increases. However, as might be expected, with a lowering of the pH from 9·5 to 5·5 at the *same* ionic strength, the potential falls. A constant potential system means that, even though the DL force decays more rapidly at higher ionic strengths, the short-range repulsion *increases* with increasing ionic strength. This is clearly illustrated in Fig. 32, and is expressed quantitatively by the equations for the DL forces between various geometries (see Table 3) that are all proportional to a purely geometric factor multiplied by $\kappa Z e^{-\kappa D}$ or $\kappa^2 Z e^{-\kappa D}$ or $\kappa^{\frac{3}{2}} Z e^{-\kappa D}$, where Z is a function of ψ_0 only. Thus, at constant potential, with increasing ionic strength (increasing κ), the DL forces *increase* in magnitude as $D \to 0$ even as the ionic 'screening' of the electrostatic field increases.

Finally, Fig. 32 shows that in 10^{-3} M NaCl there is a force maximum at $D \approx 1{\cdot}2$ nm. Application of the appropriate equation for the VDW force from Table 2: $F/R = -A/6D^2$ to the fitted DL force, $F/R = +2 \times 10^{-3}\, e^{-D(\mathrm{nm})/8{\cdot}5}$, shows that the Hamaker constant must be approximately 1×10^{-21} J for the net interaction to peak at 1·2 nm, but this is a somewhat crude way of measuring Hamaker constants.[46] The magnitudes of the *adhesion* forces at $D \approx 0$ are discussed in Section 3.3.

From Fig. 32 we may conclude that at separations above about 2 nm, or 8 molecular diameters of water, the continuum Lifshitz theory of VDW forces and the continuum (PB) equations of DL forces are valid, at least for monovalent ions such as NaCl. This in turn implies that the equations listed in Tables 2 and 3 should be valid down to such separations. Similar conclusions have been obtained from measurements on smooth, non-biological surfaces, such as mica and silica (Israelachvili & Adams, 1978; Israelachvili, 1991; Vigil *et al.* 1994) and similar results have been obtained with other liquids where, in general, for films thicker than 5–10 molecular diameters, their continuum properties, both as regards their interactions and other properties such as viscosity, are already manifest (Israelachvili & Adams, 1978; Chan & Horn, 1985; Horn *et al.* 1989; Israelachvili, 1991; Vigil *et al.* 1994; Israelachvili & Wennerström, 1996). The implications of these findings mean that water films as thin as 1–2 nm may be expected to exhibit their bulk continuum properties, at least as far as their interaction forces are concerned. Whenever deviations do occur at small, or even large, separations it is more likely that some other force is also operating rather than that the DLVO theory has broken down.[47]

[45] Geometric factors also play a role. The electric field outside a curved charged surface decays faster than from a planar charged surface, so that the counterions around a cylinder (e.g. DNA) or a small sphere (e.g. a micelle or small hydrophilic protein) have a weaker electrostatic force pulling them back onto the surfaces. All things being equal, the surface charge density or degree of ionization usually follows the following order: spheres > cylinders > planar surfaces (Manning, 1969; Shklovskii, 1999, and references therein).

[46] Differentiating the full force-law and setting it equal to zero gives: $A = 3(2 \times 10^{-3}/8{\cdot}5 \times 10^{-9}) D^3 e^{-D(\mathrm{nm})/8{\cdot}5} = 1{\cdot}1 \times 10^{-21}$ J on inserting $D = 1{\cdot}2$ nm. The real VDW Hamaker constant is actually significantly higher than the value estimated here because adhesive contact at $D = 0$ actually occurs at a larger from the 'dehydrated bilayers' due to the short-range repulsive steric–hydration forces between them, discussed in Section 3.2. The hydrated layer is typically $\sim 1{\cdot}0$ nm thick, which would imply that the real Hamaker constant is closer to 10^{-20} J.

[47] The intriguing case of divalent and multivalent ions is discussed in Section 3.3.

https://doi.org/10.1017/S0033583501003687 Published online by Cambridge University Press

Figure 33 shows the DLVO forces in a more complex and biologically more relevant system – an 'asymmetric' system, where the two interacting surfaces are different, display different charged groups, and, in addition, bind via a complementary RL bond (Leckband *et al*. 1994). This is the streptavidin–biotin LR system, which has been used as a model to study and characterize LR interactions in general. As shown in the inset of Fig. 33, streptavidin and biotin–lipid have different pI and pK values, respectively. At pH < 4 both surfaces are positive, while at pH $> 6{\cdot}5$ both are negative; either of these conditions results in a long-range repulsion, such as shown in Fig. 33 at pH 7·2. At pH values between ~ 4 and $\sim 5{\cdot}5$ the surfaces have opposite net charge, and the long-range DL force is *attractive*, as shown in Fig. 33 at pH 5·0. At very small separations, below 1 nm, the steeply attractive force and subsequent strong adhesion is due to the biotin–streptavidin LR bond whose strength is largely independent of the ionic strength and pH of the solution. The theoretical strength of the purely VDW force contribution to the total adhesion force is also shown (dash line) to illustrate its relative weakness, by a factor of about 100, compared to the adhesion mediated by the multiple, strong streptavidin–biotin bonds (Leckband, 1994).

The results of Fig. 33 provide a nice example of how a cell–surface receptor system could qualitatively alter the long-range interaction between the cell surface and another membrane or macromolecule via a local or transient change in pH.[48] The lowering of the pH also lowers the long-range electrostatic energy barrier, transforming it into an attraction, which pulls the two surfaces closer together. This allows the ligands and receptors on them to bind. The pH-dependent or metal ion-dependent membrane adhesion and fusion events *in vivo* are generally attributed to triggered conformational changes in such proteins as hemagglutinin A (Rosenthal *et al*. 1998) or SNAREs (Sutton *et al*. 1998). Changes in the long-range repulsion undoubtedly reduce the work required by the proteins to pull the membranes together and induce fusion.

The principles illustrated above apply to any two amphoteric surfaces where each has a different pH of zero charge (pzc). However, proteins have complex structures, and the charges are distributed unevenly over their surfaces so as create non-uniform electrostatic potential fields surrounding the molecules (cf. Section 1.4). One consequence of this is that one face of the protein might have a net positive charge, even though the overall protein has a net negative charge. A negatively charged ligand would then be attracted to one face but repelled by others (Klapper *et al*. 1986; Leckband *et al*. 1995a) (cf. Fig. 7).

In the SFA measurements (Fig. 33), the oriented streptavidin exposed only its binding face, which has a charge distribution that differs from that of the overall molecule. To determine how the local surface properties differed from the overall electrostatics of the molecule, Sivasankar *et al*. (1998) measured the electrostatic DL force between identical streptavidin monolayers, or between a streptavidin monolayer and a surface of known charge density, as a function of pH. The charge density of the streptavidin surface was then determined by

[48] A change in the pH of two units from 7·0 to 5·0 corresponds to a change in the H^+ ion concentration of about 10^{-5} M, or 6×10^{21} ions m^{-3}. If this change occurs locally between two membranes of area 100 nm $\times$ 100 nm that are 10 nm apart, the number of ions that need to be injected into the aqueous space (of volume 10^5 $nm^3 = 10^{-22}$ m^3) to achieve this pH change is about 1.

[49] The plane of charge was assumed to lie at the outer VDW surface of the streptavidin, so that the fitted electrostatic properties of the protein monolayer gave the effective charge density in a plane tangent to the outermost residues of the oriented streptavidin molecule. For this reason, the values reported do not correspond to the actual number of positive and negative charges on the exposed protein surface.

https://doi.org/10.1017/S0033583501003687 Published online by Cambridge University Press

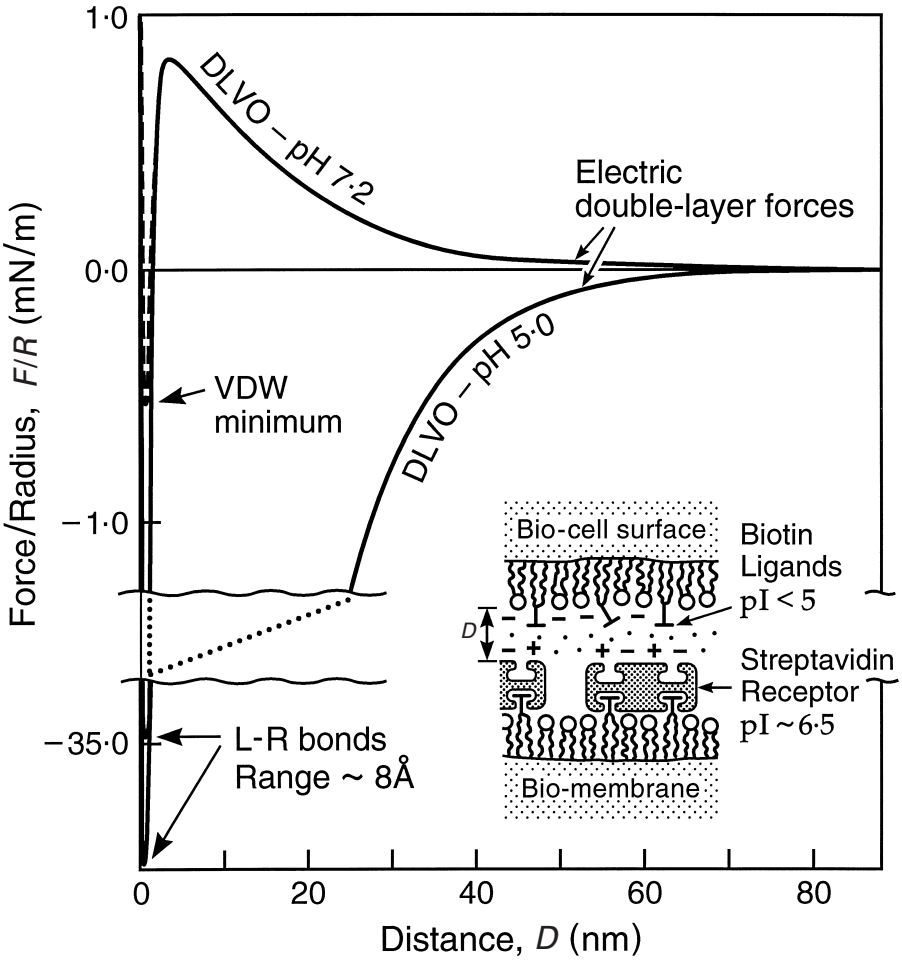


Fig. 33. DLVO force–distance curve between streptavidin and biotin at pH 5·0 and 7·2 showing how the long-range electrostatic 'DL' force between two surfaces with different pI values can be repulsive or attractive, depending on the pH. In contrast, the short-range binding force or energy remains largely unaffected by pH. (Adapted from Leckband *et al.* 1994.)

fitting the measured force profiles to the DLVO force at the different pH values. At pH 7·6, for example, the fitted charge density of the streptavidin monolayer was -12 ± 1 mC m^{-2}, or $-2{\cdot}1 \pm 0{\cdot}2$ e/streptavidin; this value dropped to $-0{\cdot}7 \pm 0{\cdot}2$ e/streptavidin at pH 6,[49] where e is the electronic charge ($e = 1{\cdot}602 \times 10^{-19}$ C). The pzc of the streptavidin monolayer was determined to be pH 5, which differed from the pI of 6·5 measured for the soluble protein. The results suggested that the composition of the outer, exposed protein surface significantly influenced the measured surface potential of the protein monolayer at the ionic strengths used in the study (Sivasankar *et al.* 1998). They further suggested that SFA measurements could be used to map the relative differences in the charge densities on different faces of a protein, and thereby determine how the distribution of charges might play a role in molecular recognition.

Sivasankar *et al.* (1998) tested this by comparing the measured values with the electrostatic charge densities adjacent to the identical surface of streptavidin calculated using the PB

https://doi.org/10.1017/S0033583501003687 Published online by Cambridge University Press

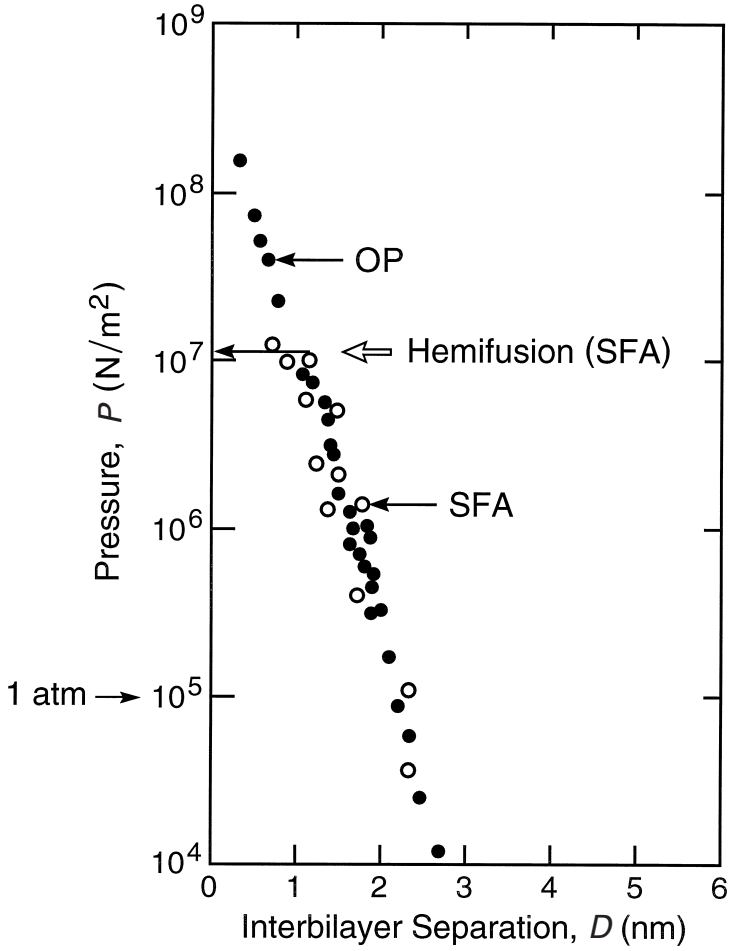


Fig. 34. Comparison of force curves between egg-PC bilayers as measured by the SFA and OP techniques. This also shows the difference between systems having a reservoir (as in the SFA chamber) and no reservoir (as in the OP cell). In the OP technique there is no separate lipid reservoir so that all parts of the system are the same, i.e. a continuous stack of bilayers (Fig. 26). In the SFA, and most other force-measuring techniques, the interacting surfaces meet at a certain point within an infinite reservoir of non-interacting molecules in solution; this allows for *localized* hemi-fusion or full fusion of membranes to occur in which the lipids from the fusion site are ejected to the reservoir. It is interesting to note that when fusion occurs, there is no prior indication in the steadily increasing repulsive force that something drastic is about to happen. This suggests that fusion may be likened to a first-order phase transition. Further aspects of bilayers and membrane fusion are discussed in Section 3.4. (Figure adapted from Helm *et al*. 1992; Horn *et al*. 1988.)

equation (Madura *et al*. 1995). The calculated pzc of $\sim 5{\cdot}3$ agreed quantitatively with the measured value. Their results showed that (1) when the Debye length is close to or smaller than the protein dimensions, the measured electrostatic surface potentials of oriented monolayers reflect the local composition of the exposed protein surface rather than the overall charge on the molecule, and (2) direct force measurements can detect subtle differences in the electrostatic potentials of protein surfaces due to the heterogeneous distribution of surface charges.

Surface force measurements were similarly used to show that local charge clusters can also

https://doi.org/10.1017/S0033583501003687 Published online by Cambridge University Press

generate locally attractive DL forces, which can steer oppositely charged ligands to protein binding sites and thereby enhance association rates. This was illustrated by measurements of the interactions between fluorescein-derivatized membranes and oriented Fab′ fragments of an anti-fluorescein monoclonal antibody (Leckband *et al*. 1995a). A ring of positively charged amino acids surrounding the binding site of the antibody was thought to electrostatically guide the negatively charged fluorescein into the binding pocket (Herron *et al*. 1989). At pH 7·2, where both the Fab′ (pI = 6·8) and the fluorescein-lipids (pK ∼ 3) are net negatively charged,[50] the measured force–distance profile between the protein and ligand surfaces was attractive at all separations. The long-ranged ($D > 1$ nm) part of the force profile was described by DLVO theory, and fits of the DLVO force profile to the data gave an electrostatic potential for the protein monolayer of +5 mV (0·2 e/Fab′). To demonstrate that the positive charge was due to the charge cluster near the exposed binding site of the folded protein, experiments were also conducted with the thermally denatured Fab′ (Leckband *et al*. 1995a). The negative electrostatic charge density of -1 e/Fab′ thus measured was as expected for a disordered polyeletrolyte with the amino acid composition of the Fab′. The positive electrostatic potential of the Fab′ monolayer is therefore primarily due to the cluster of positively charged amino acids on the outer, exposed face of the protein. This positive electrostatic potential likely plays a functional role by steering the negatively charged fluorescein to the binding pocket (Herron *et al*. 1989; Bedzyk *et al*. 1990; Leckband *et al*. 1995a).

These direct measurements showed that DLVO forces also operate on a local scale between patches on heterogeneous macromolecular surfaces. The influence of local charges on one protein face will, however, depend on the ionic strength and the distance between charges relative to the Debye length. Cytochrome b5 mutants, which could be immobilized on surfaces in different orientations (Stayton *et al*. 1992; Yeung *et al*. 1999), made it possible to control the different surface regions of cytochrome b5 exposed. Direct force measurements and equilibrium binding studies together showed that the local variations in the charge density were effectively smeared out at low ionic strength where the Debye length of 40 Å exceeded the 35 Å protein length (Yeung & Leckband, 1997; Yeung *et al*. 1999). As a result, the charged ligand bound to two different exposed surfaces of cytochrome b5 seemingly equally well at low salt concentrations. However, at high ionic strength, where the Debye length was 12 Å, the local surface variations in steric and electrostatic properties became more apparent. This generated ionic-strength-dependent differences in the interaction energies between the ligand and the different exposed cytochrome b5 surfaces and, at the higher ionic strength, this resulted in a higher ligand affinity for the surface exposing the actual binding site (Yeung *et al*. 1999). Thus, the ability of local charge variations to influence RL interactions depends on both the charge distribution and the Debye length.

3.2 Repulsive short-range steric–hydration forces

In Section 1 various non-DLVO forces were described. In this section we consider the short-range monotonically repulsive forces that arise between fluid-like hydrophilic surfaces or surfaces containing mobile surface groups such as lipid headgroups, polysaccharide chains or

[50] The differences between the pK, pI and pzc of a surface or protein are as follows: the pK applies to a single acid or basic group such as $-COO^{-}H^{+}$, whereas the pI and pzc apply to a surface or protein consisting of different acid and basic groups whose point of zero charge (pzc), when averaged over the surface or particle, occurs at a pH known as the isoelectric point (pI).

https://doi.org/10.1017/S0033583501003687 Published online by Cambridge University Press

polyelectrolyte tethers. Steric–hydration forces come under the general category of thermal-fluctuation forces that were described in Section 1.7. These forces are due to the direct interaction between the surface or surface groups. They should be distinguished from the structural–solvation forces, described in Section 1.5, that are due to interactions mediated purely by the *solvent*, and whose experimental measurements and biological manifestations are discussed in Section 3.6.

Figure 34 shows the steric-hydration force between egg-lecithin bilayers, as measured independently by the SFA and OP techniques. These bilayers are electrostatically neutral (uncharged) and the force between them is essentially made up of the VDW attraction at long-range (see Fig. 41) and the stabilizing, steric–hydration repulsion at short-range, shown in Fig. 34. The agreement between these two quite different techniques is remarkably good, considering that in the SFA technique the bilayers are supported on solid surfaces of mica, while in the OP technique they are 'semi-free' in solution (but restrained by the other bilayers in the compressed stack).

The measured repulsion is roughly exponential and can be fitted by the following force function per unit area, or pressure: $P(D) = 3 \times 10^8 \, e^{-D/\lambda_0}$ N m^{-2}, where $\lambda_0 \approx 0{\cdot}25$ nm is the decay length. This may be compared with the theoretically predicted expression for the protrusion force (Eq. 23): $P(D) = 3(\Gamma kT/\lambda_0)e^{-D/\lambda_0}$, or the expression for the repulsion between polymer brush layers (Eq. 16): $P(D) = 32(\Gamma kT/s)e^{-D/L}$. In each case Γ is the surface coverage of the lipid molecules which, at an area of $a \sim 0{\cdot}70$ nm^2 per lecithin molecule, implies that $\Gamma = 1/a = 1{\cdot}4 \times 10^{18}$ m^{-2}. We also have $s = 1/\Gamma^{\frac{1}{2}} = 8{\cdot}3 \times 10^{-10}$ m, and $kT = 4{\cdot}2 \times 10^{-21}$ J. Thus, theoretically, in the case of the protrusion force, we expect the pre-exponential factor to be $3(\Gamma kT/\lambda_0) \approx 0{\cdot}7 \times 10^8$ N m^{-2}, while in the case of the polymer brush force we expect it to be $32(\Gamma kT/s) \approx 2{\cdot}3 \times 10^8$ N m^{-2}. These values may be compared with the measured pre-exponential factor of $\sim 3 \times 10^8$ N m^{-2} for egg-lecithin bilayers. Concerning the decay lengths of these forces, various theories, equations, and simulations have been presented to account for the roughly exponential decay of the protruding headgroups of fluid-like bilayers. These are usually in very good agreement with measured values (Granfeldt *et al*. 1991; Israelachvili & Wennerström, 1992).

The measured forces are often larger than theoretically predicted because of the finite excluded volume of the protruding hydrophilic groups, which are hydrated by a layer of water (the primary hydration shell). This increases the OP in the same way that the finite sizes of atoms and molecules increase the pressure of a VDW gas by a factor $RT/(V-b)$ where $b = \frac{2}{3}\pi\sigma^3$ is the VDW coefficient that accounts for the finite sizes of molecules of diameter σ. The role of a primary hydration shell was discussed in Section 1.5, and illustrated in Figs. 9 and 10.

Experiments on a variety of amphiphilic systems show that the steric-hydration force can vary tremendously from system to system, and that it is also temperature dependent (Parsegian *et al*. 1979; Lis *et al*. 1982; Marra, 1985; Lyle & Tiddy, 1986; McIntosh & Simon, 1986; Marsh, 1989; Rand & Parsegian, 1989). Measured decay lengths λ_0 range from below 0·1 nm to above 0·6 nm, and the pre-exponential factors also exhibit large variations (cf. Fig. 35(*b*) with Fig. 34). As might be expected, these forces decrease as the temperature falls, with abrupt changes occurring at phase transitions. Detailed analyses, both theoretical and experimental (Israelachvili & Wennerström, 1992), show that steric forces in general are not purely exponential, but that they increase much more steeply as $D \to 0$. The existence of a short-range steric–hydration force also prevents the membranes from coming closer than 0·4

https://doi.org/10.1017/S0033583501003687 Published online by Cambridge University Press

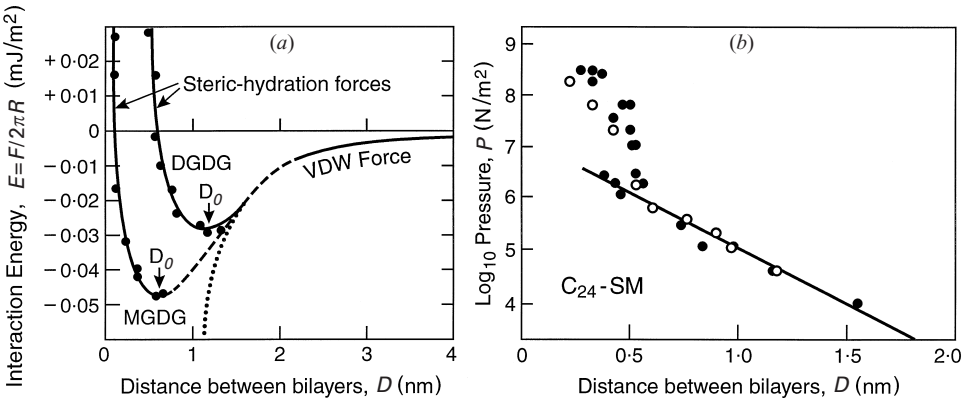


Fig. 35. Short-range steric–hydration forces between (*a*) solid-supported bilayers of di-galactosyl-diglyceride (DGDG) and mono-galactosyl-diglyceride (MGDG) using the SFA technique (Marra, 1985, 1986b) and (*b*) quasi-free bilayers of C_{24}-SM in multi-bilayer stacks using the OP technique (McIntosh *et al*. 1992b). In (*b*) the steric–hydration pressure is roughly exponential in the range $D = 0{\cdot}5$–$1{\cdot}5$ nm and is well fitted by: $P(D) = 0{\cdot}15 \times 10^8 e^{-D/\lambda_0}$ N m^{-2}, with $\lambda_0 = 0{\cdot}2$ nm (solid line). Note the 20-fold lower pre-exponential factor for these bilayers compared to the factor for lecithin of 3×10^8 N m^{-2} (Fig. 34).

to 2·0 nm under passive conditions, i.e. when not subjected to an active external force or OS. As discussed in more detail in the following section, this implies that their adhesion force or energy is much reduced compared to true contact adhesion. Both of these effects are illustrated in Fig. 35, which shows the full interaction force (1) between neutral DGDG and MGDG bilayers containing sugar headgroups, as measured with the SFA (Fig. 35(*a*)) and (2) between bilayers of sphingomyelin as measured with the OP technique (Fig. 35(*b*)). We may note the effect of the repulsion on diminishing the strength of the VDW adhesion force in the case of the sugar lipids, and the steeper repulsion at separations below 0·5 nm in the case of the sphingomyelin bilayers.

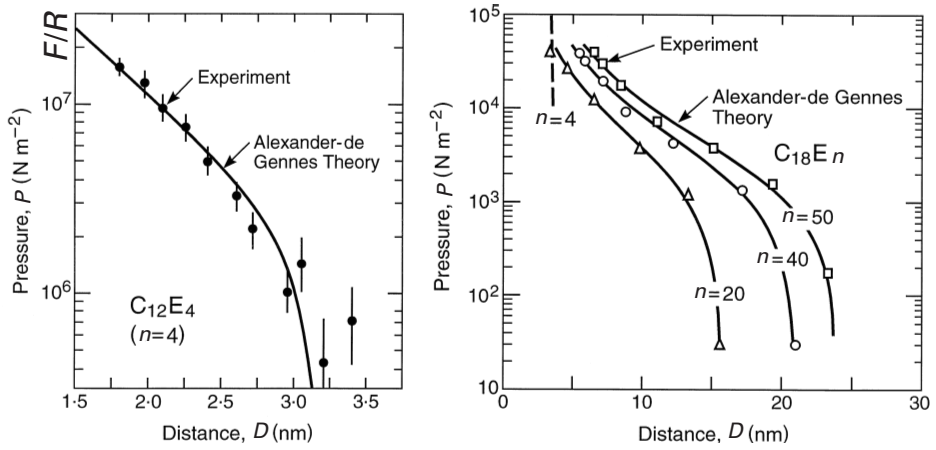
The case of bilayers or membranes exposing longer chained hydrophilic groups or tethers is illustrated in Fig. 36. In both cases the protruding chains are polyethylene oxide (PEO) or polyethylene glycol (PEG)[51] with from 4 to 50 PEO groups per chain. In all cases the Alexander–de Gennes theory of interacting brush layers (Section 1.6) appears to provide a satisfactory quantitative description of the measured forces.

More SFA recent work (Kuhl *et al*. 1994, 1995, 1996, 1998a, b) on the interactions between lipids with PEO headgroups (also known as PEGylated lipids) of higher MW, as well as with different surface coverages from 'mushrooms' to 'brushes' (see Section 1.6), again indicate good agreement with polymer theory for these systems. In all cases the forces are monotonically repulsive.

Short-chained oligoethylene-coated surfaces appear to be biologically inert, in that they do not illicit immunological responses *in vivo*, and the PEO degradation products are nontoxic (Harris, 1992). PEO-protected surfaces, which use longer polymer chains, are the basis of Stealth Liposomes™ and various other coatings used to produce biocompatible surfaces and drug-delivery vehicles. Direct force measurements (Sheth *et al*. 2000) and other experimental evidence show that interactions with other neutral, hydrophilic surfaces are repulsive due to

[51] Polyethylene oxide (PEO) is $-[-CH_2-CH_2-O-]_n-$; polyoxy ethylene (POE) is $-[-CH_2-O-CH_2-]_n-$. Polyethylene glycol (PEG) is $-[CH_2-CH_2-O-]_n-CH_2-CH_2-OH$ where the terminal group is specifically $-OH$ rather than $-CH_3$ which is the other possibility (see also footnote 17).

https://doi.org/10.1017/S0033583501003687 Published online by Cambridge University Press



(*a*) (*b*)

Fig. 36. Measured forces between adsorbed monolayers or bilayers in water of the polyethylene-oxide headgroup surfactant C_mE_n where m refers to the number of carbons in the hydrocarbon chain and n refers to the number of ethylene-oxide groups. The solid lines are fits to the full Alexander–de Gennes equation (see footnote 18) for the steric repulsion between the overlapping headgroups which are modelled as polymer 'brush' layers. (*a*) Bilayers of $C_{12}E_4$ in water (Lyle & Tiddy, 1986) and corresponding theoretical curve (solid line) using $L = 1{\cdot}6$ nm (0·4 nm per EO group), $s = 0{\cdot}93$ nm, and $T = 25$ °C. (*b*) Adsorbed monolayers of $C_{18}E_n$ in water (Homola & Robertson, 1976) and corresponding theoretical fits (solid lines) using $L = 7{\cdot}8$ nm for $n = 20$, $L = 10{\cdot}5$ nm for $n = 40$, and $L = 12$ nm for $n = 50$ (all fitted for $s = 13$ nm).

the steric-hydration force. Moreover, the polymer carries no charge so that neither positively nor negatively charged groups are attracted to them. The segments appear to H-bond mainly to water. In many ways, EO groups 'look like' water to other molecules,[52] and this may be the reason for their biological inertness, their resistance to protein adsorption, non-toxicity, and their lack of immunogenicity (Abuchowski & Davis, 1981; Harris, 1992). However, this does not mean that PEO will repel all materials, including proteins, in aqueous media. PEO is amphiphilic and does adsorb as a monolayer at the air–water interface and at hydrophobic surfaces in water (Kuzmenka & Granick, 1988a, b; Cao & Kim, 1994; Kuhl *et al*. 1994, 1995; Baekmark *et al*. 1995; Majewski *et al*. 1998; Sheth *et al*. 2000). Furthermore, direct force measurements demonstrated that PEO chains weakly bind proteins (Sheth & Leckband, 1997). Thus, many properties of PEO (and other polymers) can be described by steric repulsion models, but the chemical properties of the polymer backbone can generate deviations from predicted behavior. Direct force measurements made it possible to test assumptions underlying these theories directly, and to identify circumstances where more realistic descriptions of the polymer are warranted.

3.3 Adhesion due to VDW forces and electrostatic complementarity

As discussed in Section 1.3, the VDW force between biological molecules or surfaces is usually weak due to the low Hamaker constant A that is typically of order 10^{-20} J or less for biological surfaces interacting in salt solutions. The existence of a primary hydration layer

[52] However, the two methyl groups in each PEO segment, when suitably oriented, impart a degree of hydrophobicity to PEO which makes it behave like a surfactant or amphiphile in certain circumstances.

https://doi.org/10.1017/S0033583501003687 Published online by Cambridge University Press

and/or a short-range repulsive steric–hydration force implies that most biological surfaces cannot come closer than 0·4 to 2·0 nm, which further lowers the adhesion energy from what it would be at true (dehydrated) molecular contact, as illustrated in Fig. 35(a) for glycolipids and Figs. 36 and 40 for other uncharged lipids. For example, for two lecithin bilayers in adhesive 'contact' at $D = D_0 \approx 2{\cdot}0$ nm, typically measured adhesion forces and energies are, respectively, $F_a/R \approx -0{\cdot}5$ mN m^{-1} (see Figs. 41 and 43), and $E_0 = F_a/2\pi R \approx -0{\cdot}08$ mJ m^{-2}. The measured Hamaker constant for this type of system is $A \approx 1 \times 10^{-20}$ J (see Section 1.3) which, at $D = D_0 \approx 2{\cdot}0$ nm, is expected to contribute $A/12\pi D_0^2 \approx -0{\cdot}07$ mJ m^{-2} to the adhesion energy. It is clear that in this case, the VDW force can account for the observed adhesion. On the other hand, the adhesion energy of MGDG bilayers (Fig. 35(*a*)) is weaker than expected from the estimated strength of the VDW force at the equilibrium separation D_0. Other examples are listed in Table 6 where an assessment is also made of whether or not the measured adhesion energies can be accounted for by the VDW interaction alone.

Another way of measuring the adhesion of bilayers and membranes is to study the aggregation of cells or vesicles in solution. Figure 14 (left) shows a freeze fracture electron micrograph of aggregated microscopic vesicles in solution. From the deformed shapes of the vesicles, especially the 'contact angle' at the bifurcation, one can determine the adhesion energy E_0 using Eq. (44). For example, Bailey *et al.* (1990) obtained values in the range $E_0 = -0{\cdot}3$ mJ m^{-2} for swollen (osmotically stressed) lecithin vesicles of radii ~ 30 μm in aqueous solution, but much lower values, of order $E_0 = -0{\cdot}002$ mJ m^{-2} for unswollen (unstressed) vesicles. These values are in reasonably good agreement with values measured by Evans & Metcalfe (1984), Servuss & Helfrich (1989), and others on giant vesicles or supported bilayers using different techniques such as the pipette aspiration technique (Fig. 25), the RICM technique (Fig. 29), and the AFM technique (see inset in Fig. 41). The decreasing adhesion energy E_0 with decreasing tension τ on the bilayers is believed to arise from the increased repulsive undulation force associated with unstressed membranes (Helfrich, 1978).

It is interesting to note that the strength of an adhesive junction is often not due to the strength (magnitude and range) of the *attractive* force alone, but also depends on the *repulsive* force. The reason for this is nicely illustrated in Fig. 35(*a*) and also in Fig. 37. In the case of the monosaccharide and disaccharide lipids, MGDG and DGDG, of Fig. 35(*a*), the Hamaker constants of both lipids are essentially the same. Their different adhesion energies therefore arise from their different steric–hydration forces because these determine the equilibrium separation D_0, which in turn determines the energy minimum E_0 and the adhesion force F_a.

Figure 37 illustrates another, but still controversial, example of this effect. Here we see the changing adhesion forces between two surfaces exposing short PEO groups as a function of the *temperature*. The increased attraction between such partially hydrophobic groups with a change in the temperature is responsible for the 'Lower Consolute Temperature'[53] of many surfactant and lipid micelles containing headgroups of PEO or its analogs, and this effect has long been attributed to the entropic nature of the hydrophobic interaction. Figure 37, however, shows that the adhesion can be quantitatively accounted for by the (unchanging)

[53] On increasing the temperature of a micellar solution, at the LCT the one-phase system becomes a two-phase system due to the onset of aggregation or a structural change, usually from small micelles to larger structures. This is in contrast to 'normal' solutions that usually go from a two-phase to a one-phase system with increasing T at the 'Upper Consolute Temperature'.

https://doi.org/10.1017/S0033583501003687 Published online by Cambridge University Press

Table 6. *Adhesion energies measured between various surfaces divided into VDW dominated adhesion forces and other, stronger, forces*

System and solution conditions Monovalent (e.g. NaCl): 1–150 mM. Divalent (e.g. $CaCl_2$): 10 μm–10 mM.	Method of measurement and system*	Adhesion (in the primary minimum) Measured adhesion energy E_0 (mJ m^{-2}) or force F_a (pN) at D_0.†	Distance of energy min at D_0 relative to 'dehydrated' contact which defines $D = 0$.‡	Is the measured adhesion energy accountable for by the VDW force at D_0?§
Adhesion determined by balance of attractive VDW force and repulsive steric–hydration force				
Solid-supported lecithin bilayers in monovalent (NaCl) solutions above or below the chain melting temperature, T_c	SFA[1]	$T > T_c$: 0·10 mJ m^{-2}	2·4 nm	Yes
	DMPC, DLPC	$T < T_c$: 0·15 mJ m^{-2}	2·1 nm	Yes
	DMPC, DPPC DPPE	$T < T_c$: 0·80 mJ m^{-2}	1·2 nm	Yes
Free bilayers in solution under decreasing stress, τ, which lowers E_0 (cf. inset in Fig. 41)	Vesicle adhesion[2]	0·3–0·002 mJ m^{-2}	Not measured	Probably yes, after subtracting the T-dept undulation repulsion
	MPA, BFP[3]	0·015 mJ m^{-2}	Not measured	
	Bilayer adhesion[4]	< 0·001 mJ m^{-2}	Not measured	
Unstressed, softly-supported DMPC bilayers separating from a hemi-fused state	SFA[5]	0·02 mJ m^{-2}	Not Applicable ($D < 0$)	—
MGDG and DGDG bilayers	SFA[6], MPA[6]	0·03–0·05 mJ m^{-2}	0·6–1·2 nm	Somewhat weaker
Glycine bilayers, first contact	JKR apparatus	0·14 mJ m^{-2}	Not measured	Yes
$C_{12}E_5$ monolayers in water at different temperatures[9]	SFA[7]	0·03 mJ m^{-2} (20 °C)	~ 3 nm	Yes
		0·13 mJ m^{-2} (37 °C)	~ 1 nm	Yes
Rigid $DSPG^-$ and fluid $DMPG^-$ bilayers in NaCl	SFA[8]	No adhesion measured, and none expected: the double-layer repulsion between these charged bilayers dominates at small separations.		
$DSPG^-$ and $DMPG^-$ bilayers in $CaCl_2$ above and below T_c	SFA[8]	0·5–1·0 mJ m^{-2}	0·2 ± 0·2 nm (0–2 water layers)	Yes (or somewhat stronger)
Adhesion in water or salt solutions determined by stronger, non-VDW forces				
Mica surfaces in water and dilute NaCl, KCl solutions	SFA[11]	~ 10 mJ m^{-2} in first (primary) minimum	~ 0·2 nm (in first oscillatory minimum)	Yes or stronger ($A = 2{\cdot}2 \times 10^{-20}$ J)
Mica surfaces at low pH and in $CaCl_2$ solutions	SFA[12]	21 mJ m^{-2} at pH 2·7	0–0·2 nm	Yes or stronger
		40–50 mJ m^{-2} in $CaCl_2$	0–0·2 nm	Stronger (salt bridges)
Glycine headgroup bilayers	JKR apparatus[8]	16 mJ m^{-2}	Not measured	Stronger (H-bonds)
Hydrophilic surfaces in humid air	SFA[13]	~ 144 mJ m^{-2}	0·5–1·0 nm	Stronger (due to capillary forces)
	Large beads[14]	~ 144 mJ m^{-2}	Not measured	
Stressed or depleted bilayers, partially or fully hydrophobic	SFA[10]	0·1 → 100 mJ m^{-2}	2 nm → 0 nm	Stronger (due to hydrophobic interaction)
	Contact angles	Up to 100 mJ m^{-2}	0 nm	
Complementary surfaces, complementary H-bonds, or LR pairs	SFA/JKR app[8,15]	> 6–16 mJ m^{-2}	< 1 nm	Generally stronger than ~ 40 pN (due to complementary interactions)
	AFM[16]	90–400 pN	Not measured	
	OT[17]	0·7–55 pN	Not measured	
	SFD[18]	1–120 pN	Not measured	
	RICM[19]	0·6–22 μJ m^{-2}	Not measured	
	MPA[20]	5–1000 pN	Not measured	

* AFM & MC (Atomic force microscopy & micro cantilever); SFA (surface forces apparatus, including JKR adhesion apparatus); OT (optical tweezers or optical trapping); MPA & BFP (micro pipette aspiration & bioforce probe), SFD (shear flow detachment); TIRM & RICM (total internal reflection microscopy & reflectance interference contrast microscopy); Vesicle adhesion (imaging of adhering structures in solution using freeze-fracture or cryo-electron microscopy).

† Based on $E_0 = F_a/2\pi R$ or $E_0 = 2F_a/3\pi R$ when determined from pull-off force measurements. Also, $E_0 = 2\gamma_i$ by definition, where γ_i is the interfacial energy. For LR interactions, E_0 is the effective binding energy per bond (in units of J) defined by Eq. (45). The reported bond rupture forces reflect the measured strengths of isolated RL bonds.

‡ In the case of lipid bilayers, especially in the fluid state, the hydrated headgroup region swells in water and extends, on average, about 0·5 nm further out *per surface* compared to the pure 'dehydrated' crystalline state, which defines $D = 0$. The energy minimum can range from $D_0 = 0{\cdot}2$ nm to $D_0 = 2{\cdot}5$ nm depending on the temperature, the phase state of the bilayers, and other factors (Marra & Israelachvili, 1985).

§ Within 33 %, calculated using $E_0 = -A/12\pi D_{VDW}^2$ for two surfaces and $E_0 \approx 40$ pN as a typical value for two atoms or small molecular groups (Section 1.3). For hydrated lipid bilayers surfaces, the planes of origin of the VDW and DL forces (which define $D_{VDW} = 0$ and $D_{ES} = 0$, respectively, in equations for these interactions) can be as much as 1 nm smaller than D_0 due to swelling of the hydrated headgroups. When so defined, the Hamaker Constants A of lipid bilayers are typically $(6–10) \times 10^{-21}$ J (Marra, 1985, 1986a, b; Marra & Israelachvili, 1985; Israelachvili, 1994). Note that the plane of origin of the electrostatic interaction, also known as the Outer Helmholtz Plane (OHP), is not generally located at the same place as the VDW plane both for lipid bilayers (Marra & Israelachvili, 1985; Marra, 1986b) and colloidal surfaces (Frens & Overbeek, 1972; Shubin & Kékicheff, 1993; Vigil *et al.*

https://doi.org/10.1017/S0033583501003687 Published online by Cambridge University Press

VDW force (dotted line in Fig. 37), with the main effect of increasing the temperature being a reduction in the range of the repulsive steric–hydration force. This could also be due to the 'dehydration' of the PEO groups at higher temperature – a well-known effect (Bekiranov *et al*. 1997; Kjellander & Florin, 1981) that would reduce the excluded volume of each PEO group and, hence, the steric repulsion between them.

More generally, since Hamaker constants do not normally differ by more than a factor of about 4 between different biological materials, it is likely that in many cases the much larger variations seen in bioadhesion forces and energies are due to differences in the magnitude and range of the stabilizing *repulsive* forces, rather than the *attractive* VDW forces. Of course, other types of attractive forces can enhance the attraction significantly, sometimes by many orders of magnitude, and also result in dramatic structural changes of membranes and proteins such as the formation of inter-membrane channels or pores, tight junctions and fusion sites. Recent studies on some of these other forces will now be described.

Figure 38 shows the measured DLVO forces between solid-supported bilayers of dipalmitoyl-phosphatidyl glycerol ($DPPG^-$) in different electrolyte solutions. In monovalent electrolyte (NaCl) the measured force curves are well described by the DLVO theory (solid lines) at all separations and ionic strengths.[54] The forces in divalent $CaCl_2$ solutions are also well-described by theory (but note the dramatic reduction in the DL repulsion already at micromolar concentrations of Ca^{2+}, an effect known as Manning condensation) except at separations below 3 nm where the attraction is significantly greater than the theoretically expected VDW force. In this short-distance regime the measured force profiles in $CaCl_2$ solutions are shown by the dashed lines where the force maxima at J – from where the 1994).

References for Table 6

[1] See Figs. 41–43, and Marra (1985, 1986a,b) and Marra & Israelachvili (1985).
[2] See Figs. 14 and 41, and Bailey *et al*. (1990).
[3] See Fig. 25, and Evans (1987, 1988).
[4] Servuss & Helfrich, 1989.
[5] See Seitz *et al*. (1998, 2000); Wong *et al*. (1999a, b).
[6] See Fig. 35(*a*) and Marra (1985, 1986b).
[7] See Fig. 37, and Claesson *et al*. (1986).
[8] See Fig. 38, and Marra (1986b). NaCl and $CaCl_2$ have antagonistic effects: addition of NaCl to a $CaCl_2$ solution tends to lower the adhesion energy (Leckband, 1992).
[9] Schneider *et al*. (1998).
[10] See inset of Fig. 41, and Chen *et al*. (1991b, 1992); Helm (1992).
[11] McGuiggan & Israelachvili (1990); Shubin & Kékicheff (1993). Oscillatory force with multiple (up to 4) adhesion minima at discrete water layer separations.
[12] Israelachvili (unpublished results).
[13] See Fisher & Israelachvili (1981).
[14] See McFarlane & Tabor (1950).
[15] See Fig. 33, and Leckband *et al*. (1995a, b); Sivasankar *et al*. (1999).
[16] See Chilkoti *et al*. (1995).
[17] See Block (1995); Svoboda *et al*. (1993); Svoboda & Block (1994)
[18] See Bongrand *et al*. (1988); Kaplanski *et al*. (1993).
[19] Measurements with live cells or soft beads (Kloboucek *et al*. 1999; Moy *et al*. 1999; Simson *et al*. 1998).
[20] See Evans (1995).

---

[54] The nonlinearity in the curves at small separations arises from the 'exact' solution to the PB equation for the DL force. The purely exponential equations given in Section 1.4 and Table 3 are 'approximate' and strictly valid only at separations greater than the Debye length.

https://doi.org/10.1017/S0033583501003687 Published online by Cambridge University Press

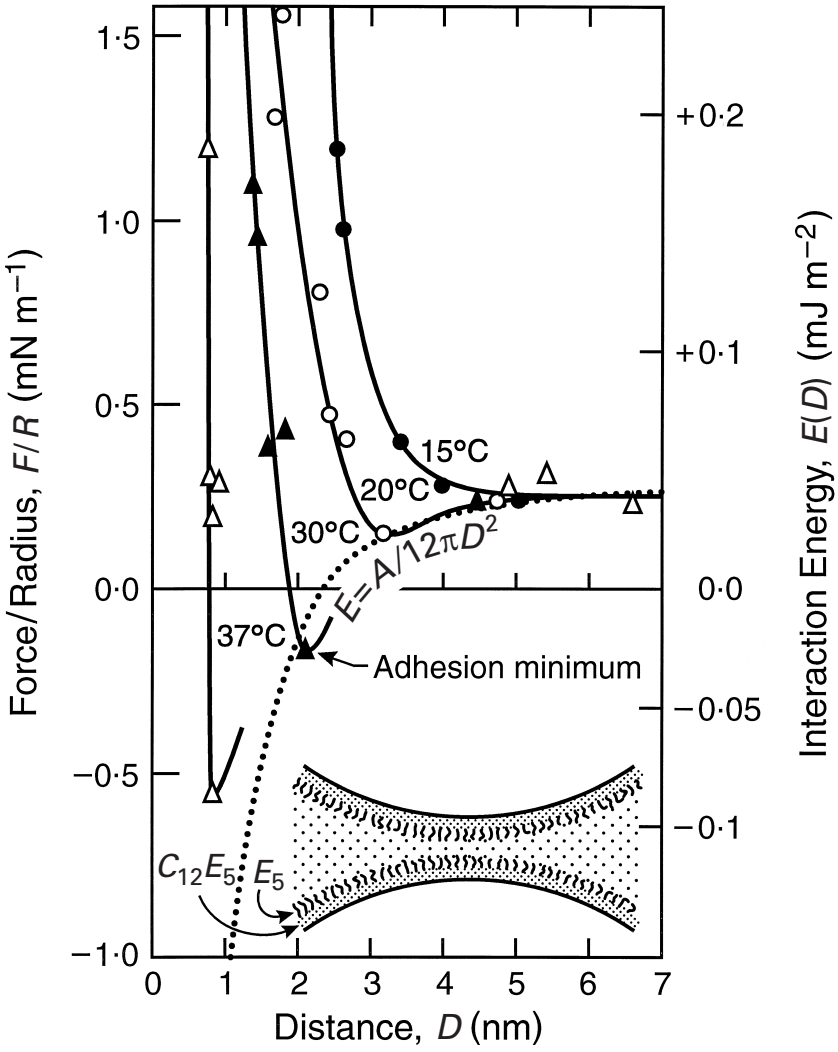


Fig. 37. Measured forces between adsorbed monolayers of the nonionic surfactant $C_{12}E_5$ in water at different temperatures. The dotted line shows the expected VDW force contribution $F/R = -A/6D^2$ (or $E = F/2\pi R = -A/12\pi D^2$ using the Derjaguin Approximation) based on a Hamaker constant of $A = 10^{-20}$ J. (Adapted from Claesson *et al*. 1986.)

surfaces jump into strongly adhesive contact at $D \approx 0$ – are significantly farther out than predicted by the DLVO theory (solid lines). This additional short-range attraction is due to the 'ion correlation' force that was mentioned in Section 1.4. This force may be thought of as the VDW force between the mobile and highly polarizable counterions at each surface. This ionic contribution to the net VDW force is not included in the Lifshitz theory.

But the effects of divalent ions on short-range adhesion forces are even more dramatic: the bidirectional stoichiometry of Ca^{2+} and Mg^{2+} ions allows them to *bridge* two negatively charged ions together – a mechanism that is denied to monovalent cations. The combination of ion-correlation effects, Manning condensation and ionic bridging (or electrostatic complementarity) results in the much greater adhesion that is typically measured between

https://doi.org/10.1017/S0033583501003687 Published online by Cambridge University Press

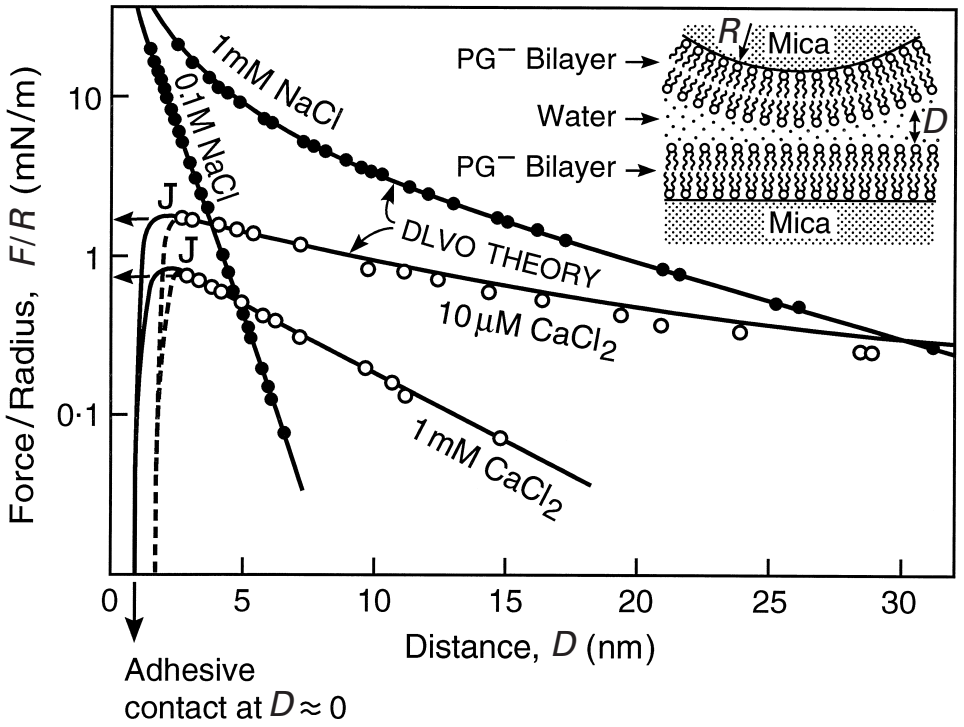


Fig. 38. Measured DLVO forces between solid-supported bilayers of the negatively charged lipid dipalmitoyl-phosphatidyl glycerol ($DPPG^-$) in different electrolyte solutions. Agreement with theory is excellent except in the presence of divalent counterions (Ca^{2+}) at small separations due to attractive 'ion-correlation' forces. (Adapted from Marra & Israelachvili, 1985; Marra, 1986b).

negatively charged surfaces even in quite low concentrations of calcium. In many cases, the two surfaces come into true nonhydrated molecular contact at ($D_0 < 0{\cdot}25$ nm) and the resulting adhesion force is significantly higher than could be expected from the VDW force at D_0 due to these electrostatic complementarity effects (see Table 6). This is in contrast to the situation in monovalent solutions such as NaCl or KCl where the adhesion occurs farther out (at $D_0 > 0{\cdot}4$ nm), is much weaker, and, in most cases, *is* well-accounted for by the VDW force.

Table 6 shows some measured adhesion energies and contact separations[55] between various surfaces and molecules in air and in monovalent and divalent electrolyte solutions. Both biological and non-biological surfaces are included to illustrate the generality of the effects described above. It is clear from this table that, in the absence of other attractive interactions, the VDW force – which is always present – appears to adequately describe the adhesion, but only if the stabilizing repulsive steric-hydration force is also taken into consideration. These VDW-dominated forces are listed in the first part of Table 6 and they can usually be quantitatively described by theoretical equations. Much stronger adhesion forces are encountered in the presence of divalent ions (for the reasons discussed above), as well as between hydrophobic or partially hydrophobic surfaces, and between surfaces carrying complementary ligands and receptors. In those cases the adhesion force or binding

[55] In the 'primary minimum'. The adhesion in the 'secondary minimum' is usually substantially smaller. (See Fig. 6.)

https://doi.org/10.1017/S0033583501003687 Published online by Cambridge University Press

energy can be 100 times greater than the VDW contribution. These forces are listed in the second part of Table 6; only some of them, for example, the hydrophobic interaction, can be quantitatively described by theoretical equations, as discussed in the following section.

In the case of complementary interactions, these should not be strictly expressed in terms of energy or force *per unit area* (in units of J m^{-2}) but in terms of the energy per intersurface bond, or

$$\frac{\text{energy per area}}{\text{accessible surface area displaying receptors or ligands}}\ \text{mJ m}^{-2}. \tag{45}$$

However, this should only be done with the knowledge that the 'accessible area' depends on the surface density of the receptor and ligand molecules, and this value can change by lateral diffusion, clustering, or the smoothing out of rough surfaces. For example, in the case of the streptavidin–biotin interaction, each streptavidin molecule occupies an area of about 20 nm^2 and exposes two biotin binding sites, each of binding energy 35 kT. Let the receptor molecules occupy 25% of the membrane surface (the other 75% being inert lipid and protein), and let the biotin density on the opposite surface be one per 100 nm^2 (again, the rest being occupied by inert lipid). In this case the 'effective site-binding surface energy' would be $2 \times 35 \times (4{\cdot}2 \times 10^{-21})/100 \times 10^{-18} = 2{\cdot}9$ mJ m^{-2}, because every biotin (which occupies an area of 100 nm^2) can access a streptavidin binding site (which occupies a lower area of 40 nm^2). In this case the limiting factor is the low surface density of the biotin ligands.

A more realistic model must take into account the ability of both the ligand and receptor molecules to move both laterally and vertically within their respective membranes so as to increase the probability of capture and thereby increase the local binding energy per unit area. In the above example, this could be achieved if the streptavidin and biotin molecules concentrated in one spot, or gradually diffused to this spot, to form a much stronger adhesion junction. The maximum effective surface energy of this junction would now be limited by the large size of the streptavidin receptors, which at close packing, expose one binding site per 10 nm^2. It is assumed that much smaller biotin-derivatized molecules can easily collect together at this density. The '*maximum* effective site-binding surface energy' of this system is therefore $35 \times (4.2 \times 10^{-21})/10 \times 10^{-18} = 15$ mJ m^{-2}, which is five times higher than before the molecules were 'allowed' to redistribute. Such a redistribution is energetically and thermodynamically favorable, but is rate-limited depending on the diffusion coefficients of the molecules in the membranes (or supported on substrate surfaces) in relation to the collision time of the two surfaces. Such time effects on measured adhesion forces are explored further in Section 4. In Table 6, the quoted values for the measured surface adhesion energies of LR interactions (see last few rows) may be ambiguous because the effects of time, which can be crucially important, were usually not measured.

Examples of geometric and electrostatic complementarity are often difficult to identify or distinguish from non-specific VDW or weakly specific, such as electrostatic or H-bonding, interactions. Weak, short-range interactions such as hydrogen bonding can be difficult to quantify for similar reasons. Measurements of short-range H-bond interactions between complementary nucleotide bases illustrate the challenges involved. The adhesion between individual nucleotide bases was studied with both the AFM and SFA. In measurements with the SFA (Pincet *et al.* 1994), the interactions were measured between membranes of double-chain surfactants in which nucleotides were covalently bound to the headgroups. Alternatively, Boland & Ratner (1995) physisorbed the bases directly to both a gold-coated

https://doi.org/10.1017/S0033583501003687 Published online by Cambridge University Press

AFM probe tip and a gold substrate. The SFA measurements exhibited both a large, short-ranged attraction and a long-ranged attraction. The latter was similar to the nonspecific attraction between hydrophobic surfaces in water (see Section 3.4), and may have arisen as a result of the low packing density of the lipids in the membranes. The relative differences in the intermembrane adhesion were as expected for complementary nucleotide base-pair formation, but the large, nonspecific background forces prevented Pincet *et al*. (1994) from quantifying the *adhesion energy* per base pair. A combination of nonspecific forces and the high surface density of bases similarly made it difficult to quantify the single base pair interactions with the AFM (Boland & Ratner, 1995). By estimating the number of bonds contributing to the short-ranged attraction between multiple base pairs, Boland & Ratner (1995) estimated the *rupture force* of the A–T bond to be ~ 54 pN. However, the need for a relatively high bond density, on account of the weak H-bond interaction in water, together with the relatively large nonspecific forces acting in both systems contributed to the difficulty in quantifying H-bond strengths. A different system, which we discuss in Section 4.1, was able to overcome many of these difficulties.

Electrostatic docking interactions that involve the complementary charges on two molecules also mediate binding between protein receptors and ligands. The electrostatically mediated binding between cytochrome c and cytochrome b5 was investigated by surface force measurements. The force profiles were measured between a monolayer of cytochrome c and a monolayer of cytochrome b5 (see Fig. 8) (Yeung *et al*. 1999). The proteins were immobilized so that their binding sites were uniformly presented to the opposing membrane. The proteins were bound to slightly negatively charged lipid bilayers, so that a repulsive electrostatic DL force dominated the long-range interaction between the proteins. However, at short distances, the proteins were able to dock via the salt-bridges shown in Fig. 8. The measured attraction F_{attr} in Fig. 39 is attributed to the specific recognition interaction between the two proteins, and is due largely to electrostatic and hydrophobic contacts between the binding pockets.

In the examples discussed above, the adhesion energy reflects the energy change upon the formation of the multiple bonds that contribute to the strong, short-range binding interactions. Often this binding energy results in the formation of a stable, i.e. long-lived bond with a slow dissociation rate, as in the case of many antibody–antigen interactions. In other instances, the bond energy is coupled to large conformational changes in one or both of the associating molecules. The energy released upon binding then reduces the configurational entropy in one of the molecules or induces torsional bond strain so as to favor a different, active (or inactive) conformation of one (or both) of the molecules. One example of this 'induced fit' behavior is the large conformational change in DNA induced by the binding of the high mobility group (HMG) proteins (Fig. 40). HMG is a nonhistone DNA binding protein, which modulates the structure of chromatin, and thereby activates such processes as recombination and transcription (Dow *et al*. 2000). In this example, the binding energy is used to bend the DNA into an energetically unfavorable configuration (Fig. 40(*c*)) that in turn activates other biological processes (Murphy *et al*. 1999). In other examples, the structure of either the protein or both molecules change. In the case of double stranded DNA, hydrophobic interactions between successive base pairs on the DNA ladder induce the helical twist in the double-stranded DNA configuration (Saenger, 1984). Although some of the contributing bonds may be electrostatic, such induced fits involve several, different bonds typical of molecular recognition.

https://doi.org/10.1017/S0033583501003687 Published online by Cambridge University Press

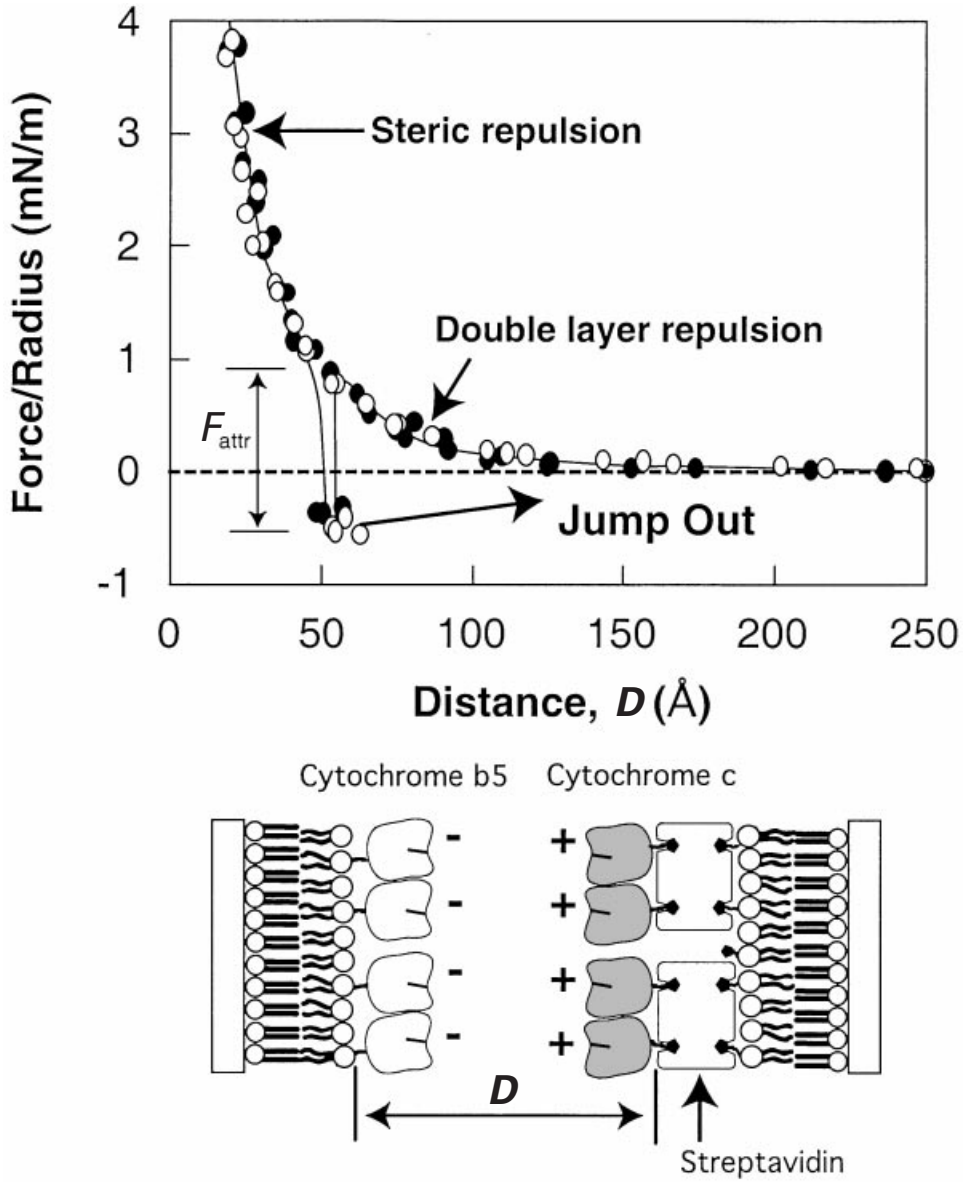


Fig. 39. Charge complementarity generates the short-range adhesion between cytochrome c and cytochrome b5. In these measurements, cytochrome b5 was bound directly to the membrane, and biotinylated cytochrome c was immobilized to an oriented streptavidin monolayer bound to a lipid membrane (lower panel). At large distances, the interaction between the cytochrome monolayers is dominated by the long-ranged, DL repulsion between the negatively charged membranes beneath the proteins. However, the proteins form an adhesive complex at a membrane separation of $D = 60$ Å, which is the distance where the proteins' binding sites come into contact. The docking interaction is mediated, in part, by the formation of short-range electrostatic bonds between the molecules (see Fig. 8) (Rodgers *et al*. 1988). The electrostatic bonds and hydrophobic contacts give rise to the measured short-ranged attraction. (Adapted from Yeung *et al*. 1999.)

https://doi.org/10.1017/S0033583501003687 Published online by Cambridge University Press

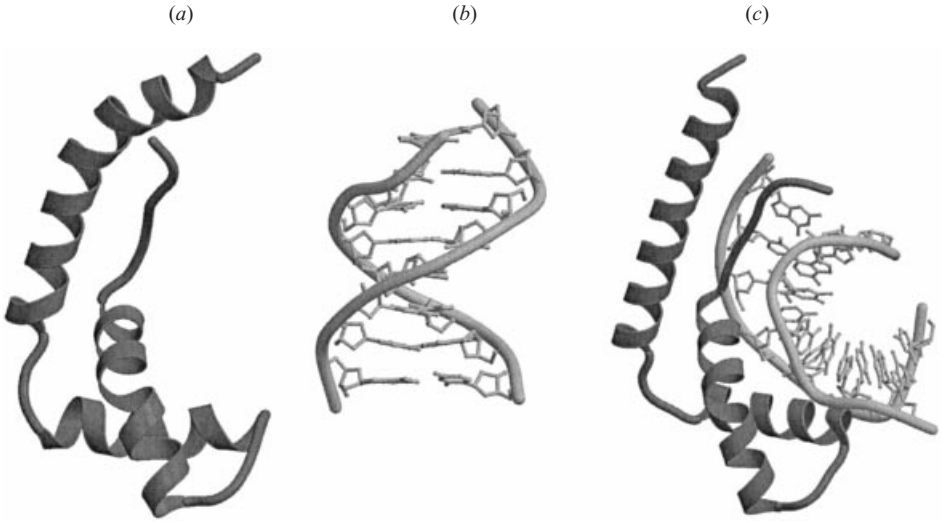


Fig. 40. Illustration of the induced fit upon the binding of the high mobility group (HMG) protein to DNA. The protein structure in the absence of DNA is shown in (*a*) and the unperturbed DNA is shown in (*b*). (*c*) Shows the large conformational changes in the DNA, upon binding to the HMG protein. (Figure adapted from Jones *et al*. 1994; Shatzky-Schwartz *et al*. 1997; Murphy *et al*. 1999.)

Force–distance profiles associated with induced fit interactions have not been studied by any of the force measuring instruments described in this review. The information obtained would, however, be particularly rich since the force profiles would embed both molecular recognition and folding interactions.

3.4 Attractive forces between surfaces due to hydrophobic interactions: membrane adhesion and fusion

Since the pioneering work of Kauzman (1959) the hydrophobic interaction and force (see footnote 15) have been known to be stronger than the VDW force and of entropic origin. It is only more recently that direct measurements of this force have shown it to be of long-range, at least between macroscopic surfaces (Christenson & Claesson, 2001). As discussed in Section 1·5, the broader implications of these measurements for biomolecular interactions and protein folding are still largely unexplored. Indeed, the physical origin of this important interaction itself is still very controversial.

Helm *et al*. (1992) measured the forces between 'depleted' lecithin bilayers in water as a function of increasing hydrophobicity of the two outer monolayers. This was achieved by progressively increasing (stressing) the amphiphilic molecules by depleting the lipids from the aqueous reservoir, thereby increasing their headgroup area and exposing more of the hydrocarbon chains to the aqueous phase. The results (Fig. 41) showed that with increasing hydrophobic area per molecule: (1) the attractive forces, which were initially VDW, became stronger and longer ranged, (2) the repulsive short-range steric–hydration force decreased in magnitude or range, and (3) the adhesion increased, eventually reaching $\sim$ 1000 times the original value. These results showed how the overall force curve changes continuously as an initially hydrophilic surface becomes progressively more hydrophobic.

In the experiments summarized in Fig. 41, the hydrophobicity was induced by depleting

https://doi.org/10.1017/S0033583501003687 Published online by Cambridge University Press

the bathing solution of lipid. Other ways of inducing hydrophobicity in membranes is to stress them mechanically, electrically or osmotically so that they are forced to thin and/or stretch. As shown in the inset of Fig. 41, even a small applied stress τ can cause a significant increase in the adhesion force due to the progressive 'turning on' of the hydrophobic force. A number of different experiments have shown that to a good approximation, the hydrophobic adhesion energy between partially hydrophobic bilayers is simply proportional to the applied stress τ according to

$$E_0 \approx -\tau \quad \text{N m}^{-1} \text{ or mJ m}^{-2}. \tag{46}$$

In other words, an applied lateral stress or tension in translated into a normal attractive force of about the same magnitude.

Equation (46) may be expressed more generally in terms of the full hydrophobic potential function (cf. Eq. 13)

$$E(D) \approx -\tau e^{-D/\lambda_0} \tag{47}$$

which reduces to Eq. (46) at $D = 0$. The increased hydrophobic interaction may also be expressed in terms of the increased area of a stretched membrane. Using the stress–strain relationship (stress/strain = membrane elastic modulus) we can express the area strain as

$$\frac{a - a_0}{a} = \frac{\Delta a}{a} = \frac{\tau}{k_a}, \tag{48}$$

where a is the expanded or stressed area per molecule and a_0 is the equilibrium, unstressed area (the optimum area); k_a is the area expansion modulus of the membrane which for bilayers and membranes in the fluid state is typically of order 150–200 N m^{-1}, or about $4\gamma_i$ (Kwok & Evans, 1981; Marsh, 1989; Evans & Rawics, 1990). This is for *bilayers*; for *monolayers* or individual surface layers k_a is half of this value, i.e. $k_a \approx 2\gamma_i$. With this substitution the full hydrophobic interaction, Eq. (47), may be written as

$$E(D) = -\frac{2\gamma_i \Delta a}{a} e^{-D/\lambda_0} \quad \text{per unit area}, \tag{49}$$

where $\Delta a = (a - a_0)$. Equation (49) basically states that any exposed hydrophobic area over and above the equilibrium, unstressed area contributes its full hydrophobic potential in direct proportion to the additionally exposed area. Thus, for an unstressed membrane the hydrophobic contribution is zero. For a highly stressed membrane where $a \gg a_0$, we have $\Delta a/a = 1$, and the adhesion energy at $D = 0$ is $E(0) = E_0 = 2\gamma_i$ which is the same as for two fully hydrophobic surfaces. Most interesting, for an area expansion of only 1% above the unstressed area ($\Delta a/a = 0{\cdot}01$), the hydrophobic contribution to the adhesion energy is $2\gamma_i/100 = 1$ mJ m^{-2}. This is already *significantly* higher than the VDW contribution (cf. Fig. 41). Indeed, it is worth recalling that the hydrophobic force is probably the strongest of all the physical interaction forces operating between biological surfaces and molecules, both specific and non-specific (Table 6). It is surpassed only by chemical bonds. Clearly, even small lateral stresses and local stress-gradients can produce large changes in the normal attractive force between surfaces composed of conformationally adaptable amphiphilic molecules such as fluid lipids or flexible proteins. These changes can be local or extend over a large area of a membrane. Thus, hydrophobic adhesion in one place could be triggered by a membrane stress generated far from the adhesion site.

https://doi.org/10.1017/S0033583501003687 Published online by Cambridge University Press

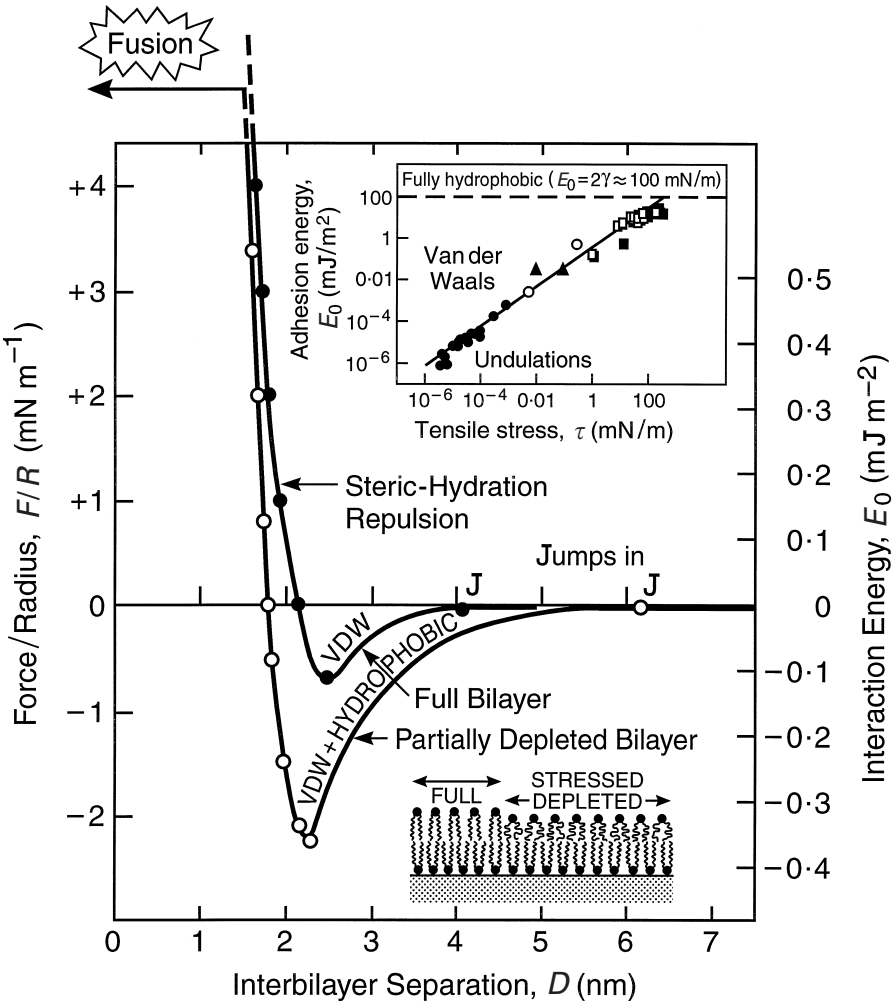


Fig. 41. VDW and hydrophobic forces measured between fully hydrophilic, partially hydrophobic bilayers. Full bilayers are in the unstressed state where their hydrocarbon chains are shielded from the aqueous phase by the hydrophilic headgroups; the equilibrium area occupied per lipid headgroup is known as the 'optimum area' and is typically $a_0 = 0{\cdot}65$ nm² for bilayers in the fluid state. Partially hydrophobic (stressed or depleted) bilayers are under tension so that the area per headgroup a is larger than a_0. Such bilayers expose additional, 'unshielded' hydrophobic groups to the aqueous phase that results in an additional hydrophobic contribution to the force. The enhanced adhesion force or surface energy E_0 has been found to be proportional to the applied stress τ (see inset), which in turn is proportional to the additional hydrophobic area exposed at the bilayer-water interface. Thus, for a fully depleted bilayer, i.e. an inverted monolayer, the interfacial energy approaches $2\gamma_i = 100$ mN m^{-1} (mJ m^{-2}) – the value for a pure hydrocarbon–water interface. The inset shows values obtained by different authors using different experimental techniques. (Figure and inset adapted from Evans & Metcalfe, 1984; Servuss & Helfrich, 1989; Bailey *et al.* 1990; Helm *et al.* 1992.)

3.4.1 Hydrophobic interactions at the nano- and sub-molecular levels

Still unanswered is the crucial question of whether the hydrophobic interaction is long-ranged even between small molecules and sub-molecular groups, such as hydrocarbon chains or hydrophobic amino-acid residues. As discussed in Section 1·5, this is important for

https://doi.org/10.1017/S0033583501003687 Published online by Cambridge University Press

knowing whether long-range attractions are involved in, for example, molecular recognition and protein folding. Direct AFM force measurements between micron-sized hydrophobic spheres (Ducker *et al*. 1994; Yoon *et al*. 1997) have found that the interaction is long-ranged (for a recent review see Christenson & Claesson, 2001), and analysis of the aggregation forces and kinetics of hydrophobic colloidal particles having microscopic dimensions further support the existence of long-ranged hydrophobic forces (Xu & Yoon, 1989a, b; Christenson & Claesson, 2000). But these microscopic particles, having radii of order 1–10 μm, are still essentially macroscopic, so that these results do not answer the crucial question. As explained in Section 2, there are no techniques that can directly measure long-range forces between individual atoms or small molecules. The MC and OT techniques come closest to being able to do this (see Table 5), but so far there have been no reports of any measurements of hydrophobic forces as a function of intermolecular separation using any of these methods.

However, there is *indirect* evidence, which suggests that the hydrophobic interaction remains long-ranged even at the nano-scale. First, as was mentioned in Section 1·5, the magnitudes of the adhesion forces between hydrocarbon chains and even small spherical molecules such as methane in water are quantitatively well-described by the same equations that apply to macroscopic surfaces. Of course, this tells us something about the adhesion forces of molecules in contact (at $D = 0$), but not the range of the forces. On the other hand, the long-range forces measured between depleted or stressed bilayers do appear to imply that very small hydrophobic patches give rise to a long-range attraction. Thus, when the stressed area is only 1–2% above the equilibrium area, the exposed hydrophobic patches on the surfaces must be laterally separated from each other by, on average, ten times their diameter, which implies that they are acting as *individual* or *discrete* hydrophobic patches. Further, these patches must have submolecular dimensions (of order 1 $Å^2$ per lipid molecule of equilibrium area 65 $Å^2$). Consequently, the measured long-ranged forces between two such surfaces must represent the accumulated contributions from discrete submolecular patches. This reasoning may be faulty: hydrophobic interactions 'work in subtle ways' (see following paragraph) and their exact mode of action is still a mystery. However, if the interaction is indeed of long-range even between individual molecular groups, the implications are far-reaching. For example, a long-range attractive force between hydrophobic side chains could favor certain protein folding pathways over others, and thereby enhance folding rates. Current *ab initio* calculations of protein folding do not include long-range attraction between nonpolar groups in water. Although measured and calculated folding rates agree roughly within a factor of two, a long-range attraction between different chemical groups could significantly alter the calculated values and lead to a reevaluation of the interactions and pathways that dictate folding. In addition, long-range attractive forces between very small hydrophobic defects in bilayers would facilitate membrane fusion without having to invoke other mechanisms for overcoming the repulsive hydration barrier (discussed further below).

3.4.2 Hydrophobic interactions and membrane fusion

Experiments on macroscopic surfaces have shown that the mode of action of hydrophobic forces is often much more subtle than a simple bringing together of two surfaces or molecules. The interaction is usually triggered or accompanied by a rearrangement of the molecular configurations at or near the adhesion 'site', and this sometimes leads to fusion. For example, the parting of the hydrophilic headgroups on the surface of a lipid bilayer

https://doi.org/10.1017/S0033583501003687 Published online by Cambridge University Press

exposes a hydrophobic patch to the outside aqueous medium. When this occurs on two bilayers that face each other (see Fig. 21), the exposed hydrophobic chains jump across the water gap towards each other and meet at the center. This constitutes the first (hemi-fusion) stage of a fusion event.

The opening up or exposure of hydrophobic groups can be triggered by a number of stress-inducing effects such as protein aggregation, a local curvature change, calcium ion changes on one side of the membrane, trans-membrane electric fields, flow stresses, and changes in the trans-membrane OP. Moreover, not all of these changes have to occur at the adhesion or fusion site; for example, an OP change triggered in one region of a cell may alter the tension of the entire cell membrane, and thereby cause it to fuse with vesicles in a completely different place. The converse of this has in fact been detected experimentally. Endocytotic events altered the membrane tension measured by OT at a site distal to the vesicle fusion sites (Dai & Sheetz, 1999; Raucher & Sheetz, 1999).

An example of how hydrophobic and electrostatic interactions between mixed lipid bilayers can work together to induce fusion is illustrated in Fig. 42. The top half shows the structure and inter-membrane forces in monovalent electrolyte. The effects of Ca^{2+} on mixed lipid bilayers are quite different from those induced on the pure, single-component DLPC or $DLPG^-$ bilayers. With mixed bilayers, lateral phase separation or clustering occurs where Ca^{2+} binding induces the condensation of PG^- lipids. The condensed PG–calcium domains result in a tensile stress on the remaining PC-rich regions, which become more hydrophobic and thereby act as adhesion and/or fusion sites (Leckband *et al*. 1992a; Evert *et al*. 1994). In this system, fusion would not occur unless a number of favorable factors were present simultaneously: mixed rather than single-component bilayers, divalent counterions on one side of the bathing solution, and fluid membranes that allow molecular rearrangements to occur. Note, too, that with this type of fusion mechanism, the fusion can occur at a different location from the calcium binding sites.

The role of calcium, protons, and to a lesser extent magnesium, in triggering membrane fusion is generally thought to occur more commonly via structural changes in fusion *proteins*, which causes them to expose hydrophobic domains (Rosenthal *et al*. 1998; Skehel & Wiley, 1998), rather than by directly inducing structural changes in the *lipids*. The reason for this undoubtedly lies in the specificity, control, and rapid fusion kinetics that the proteins provide. For example, crystal structures of hemagglutinin A from the influenza virus showed that pH changes induce large, rapid conformational changes in the protein that exposes a hydrophobic helix, which may induce fusion by penetrating the opposing membrane (Rosenthal *et al*. 1998; Skehel & Wiley 1998). Nevertheless, the accompanying reduction in intermembrane repulsion by metal ion binding is also expected to lower the electrostatic energy barriers to allow these protein-mediated processes to occur.

3.5 Attractive depletion forces

As described in Sections 1·5 and 1·6, attractive forces can also arise both from the oscillatory structural force between surfaces in a solvent due to the finite size of the solvent and, additionally, from any dissolved solute molecules or particles, especially when these do not adsorb or are repelled from the surfaces. We first consider the latter case. Figure 43 shows the measured force-distance curves between two hydrophilic lecithin bilayers in various PEO solutions. Unlike the previous cases considered in Sections 1·6 and 1·7 where the PEO was

https://doi.org/10.1017/S0033583501003687 Published online by Cambridge University Press

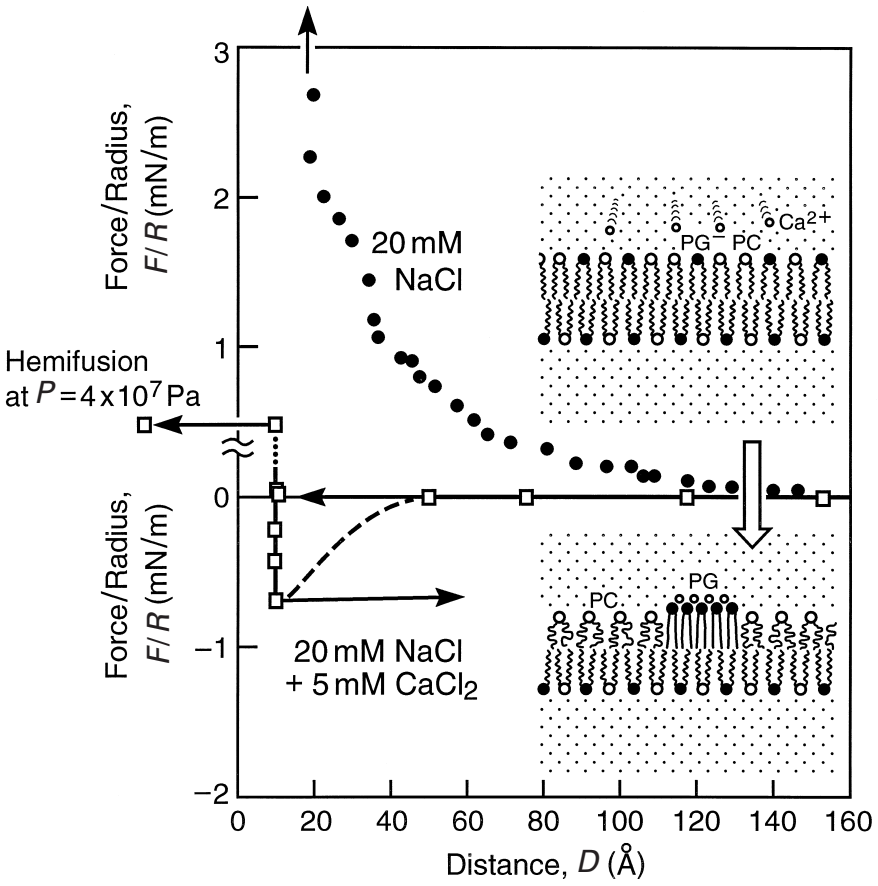


Fig. 42. Measured forces between mixed anionic/uncharged 25% $DLPG^-$ + 75% DLPC bilayers in 20 mM NaCl with and without added 5 mM $CaCl_2$ at pH 5·6 and 25 °C. The force in NaCl solution (without calcium) is dominated by the DL repulsion and is similar to the force between pure anionic bilayers. In contrast, the force in the presence of calcium is completely different from the force between either pure DLPC or pure $DLPG^-$ bilayers (Fig. 38). With the mixed lipid bilayers, calcium-induced phase separation (clustering) of the negatively charged lipids separates the charged from the uncharged lipids as shown in the lower inset. (Figure adapted from Leckband *et al.* 1992a.)

chemically attached to the surfaces, here the PEO is 'non-adsorbing', i.e. free in solution. And since PEO is not attracted to lecithin bilayers in water, its contribution to the force between the two bilayers – the 'depletion' force – is purely entropic (proportional to kT), attractive, and theoretically given in Section 1·6 by Eq. (20):

$$E(D) \approx -\rho kT(R_g - D) \quad \text{per unit area,} \tag{20}$$

which gives the adhesion energy and pressure at contact ($D = 0$) as $E_0 = -\rho kTR_g$ and $P(0) = -\rho kT$, where ρ is the concentration or *activity*, and where R_g is the average size of the solute particles or dissolved polymer molecules in the solution. For dilute polymer solutions in an indifferent solvent (a 'theta' solvent) R_g is the radius of gyration; in a 'good' solvent it becomes replaced by the larger Flory radius, R_F, while for concentrated solutions R_g corresponds to twice the polymer correlation length 2ξ in the solution, and ρ must be replaced by the activity. The results of Fig. 43 for 10 kDa PEO ($R_F = 9{\cdot}1$ nm, $2\xi = 4{\cdot}2$ nm)

https://doi.org/10.1017/S0033583501003687 Published online by Cambridge University Press

bear out the theoretical predictions very well: the attraction has a range of about 2ξ, and the extra adhesion scales with the concentration or activity ρ as predicted by Eq. (20). For example, at a concentration of 5% ($\rho = 0{\cdot}05 \times 6{\cdot}02 \times 10^{29}/10\,000 = 3{\cdot}0 \times 10^{24}$ m^{-3}), the predicted increase in the adhesion energy is $E_0 = (3{\cdot}0 \times 10^{24}) \times (4{\cdot}2 \times 10^{-21}) \times (4{\cdot}2 \times 10^{-9}) = 0{\cdot}053$ mJ m^{-2}. This may be compared with the measured value (cf. Fig. 43) of $F/R \approx -1{\cdot}2$ mN m^{-1},[56] which translates to a surface energy of $E_0 = 2F/3\pi R = -0{\cdot}25$ mJ m^{-2}, which is over four times the theoretical value. However, as previously mentioned, it is strictly the *activity* ρ' that should be used for the concentration in Eq. (20), rather than the number density. For PEO solutions at 5 wt% $\rho' \approx 4\rho$, which modifies the theoretical prediction to $E_0 = -0{\cdot}21$ mJ m^{-2}, in much better agreement with the measured value of $-0{\cdot}25$ mJ m^{-2}.

Depletion forces were first measured between giant vesicles using the MPA technique (Evans & Needhan, 1988), where good agreement was obtained between theory and experiment for the strength of the depletion-induced adhesion force. They have also been measured between surfaces in micellar solutions where the charged, repelling micelles act as non-interacting particles (Richetti & Kekicheff, 1992).

Depletion forces can cause cells, vesicles and supported bilayers to fuse, and with PEO it is most effective at molecular weights in the region of 10 kDa and at concentrations above 5 wt% (Poste & Nicholson, 1978; Boni *et al*. 1981, 1984; Arnold *et al*. 1983, 1985, 1988; de Gennes, 1988; Hui *et al*. 1999). Just as in the case of calcium-induced fusion of mixed lipid bilayers, PEO-induced fusion (cf. Fig. 43) is probably also associated with the opening of hydrophobic patches on opposing membranes that have been first brought together by the attractive depletion force (Kuhl *et al*. 1996, 1998a).

3.6 Solvation (hydration) forces in water: forces associated with water structure

As was discussed in Sections 1·5 and 1·6, the depletion attraction is related to the oscillatory solvation (hydration) force that exists between two surfaces in *pure* solvent, i.e. even without dissolved solutes. In the absence of dissolved solutes the (smaller) solvent molecules simply behave like a highly concentrated solution of solute molecules, and the expression for the primary adhesion energy, Eq. (20), is essentially the same. However, these forces arise only between hard, solid, crystalline surfaces whose roughness is smaller than the size or diameter σ of the solvent molecules.[57] In the case of water ($\sigma \approx 0{\cdot}25$ nm) such forces and interactions have been measured between surfaces of mica and between a few other smooth, crystalline surfaces (Caffrey & Bilderback, 1983; Israelachvili, 1983, 1991).

Figure 44 shows the measured forces between two mica surfaces in various KCl and KNO_3 solutions, where at small separation, below 1·5–2·0 nm or about 6–8 water molecule diameters, a rapidly decaying oscillatory force is superimposed on the DLVO force. It is still not clear whether this type of short-range, non-DLVO, force is purely oscillatory or whether there is also an additional monotonic component (Pashley & Israelachvili, 1984). What is

[56] When deducing the attractive contribution to adhesion energies from experimental force curves that involve more than one type of force acting at the same time, as in Fig. 42, one must subtract the minimum energy from the maximum energy at the equilibrium separation. In this system, one must also subtract the attractive VDW contribution to get the pure depletion contribution.

[57] Likewise, if the surfaces are rougher than the size of the dissolved solute particles, the depletion force will be smeared out or eliminated.

https://doi.org/10.1017/S0033583501003687 Published online by Cambridge University Press

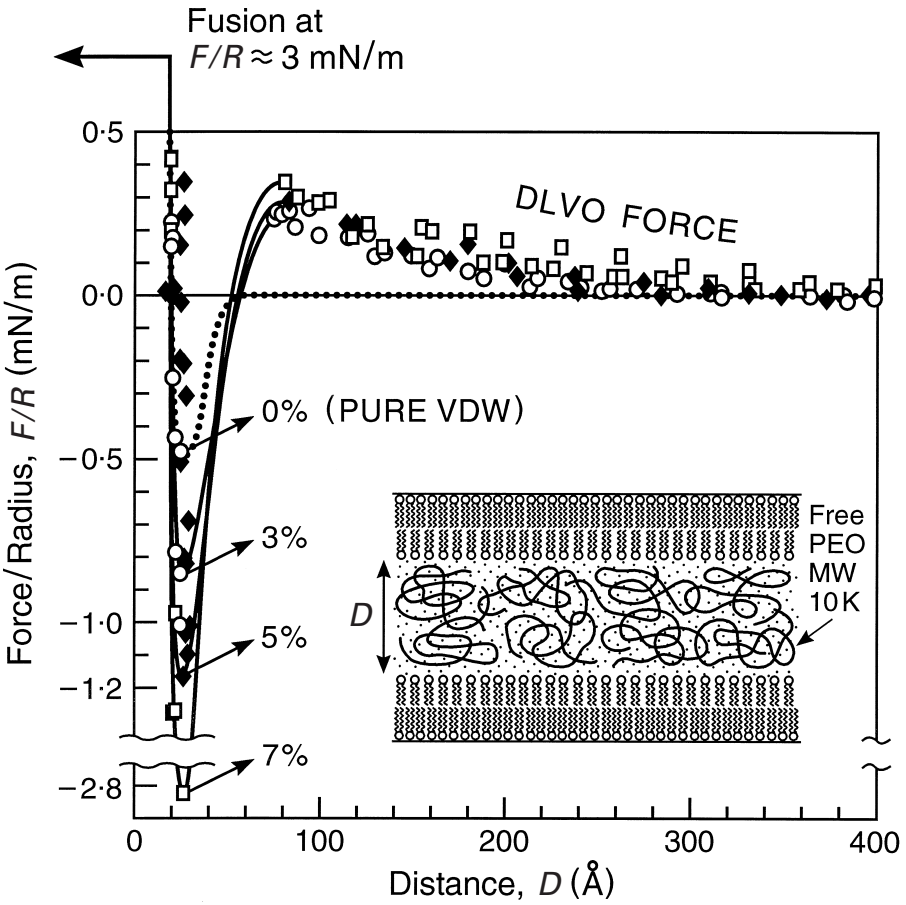


Fig. 43. PEO-induced depletion attraction and resulting fusion. Depletion force between two lecithin bilayers mediated by free PEO (actually PEG) of MW = 10 kDa in concentrated aqueous solutions (Kuhl *et al*. 1996, 1998a). The attractive force in the absence of PEO is the VDW force, which is enhanced with increasing PEO concentration. The enhanced adhesion at contact ($D = 0$) is well-described by theory (Eq. 20) if the bulk concentration ρ is replaced by the *activity* of PEO in aqueous solution at this concentration. The long-range repulsion is due to a weak DL force and/or to the long-range repulsive tail of the depletion force.

clear, however, is that such additional forces prevent two surfaces from approaching closer than 1–2 nm, and for this reason they are often confused with the steric–hydration force that has a similar magnitude and range. However, unlike the monotonic steric–hydration (or thermal fluctuation) force that arises between *fluid-like* interfaces and that involves direct collisions of mobile surface groups, this type of hydration (or solvation) force occurs between hydrophilic surfaces that order the water molecules between them, and operates indirectly through the solvent.[58] These forces can be modulated by changing the pH or ionic composition of the solution – the more hydrated the bound ions on the surface or

[58] A nice example showing the very different water structure associated with these two interactions was given by Caffrey & Bilderback (1983) who used X-ray diffraction to show that bilayers swell or dehydrate continuously, i.e. monotonically, in water, whereas clay surfaces do this discontinuously in steps of discrete water layers.

https://doi.org/10.1017/S0033583501003687 Published online by Cambridge University Press

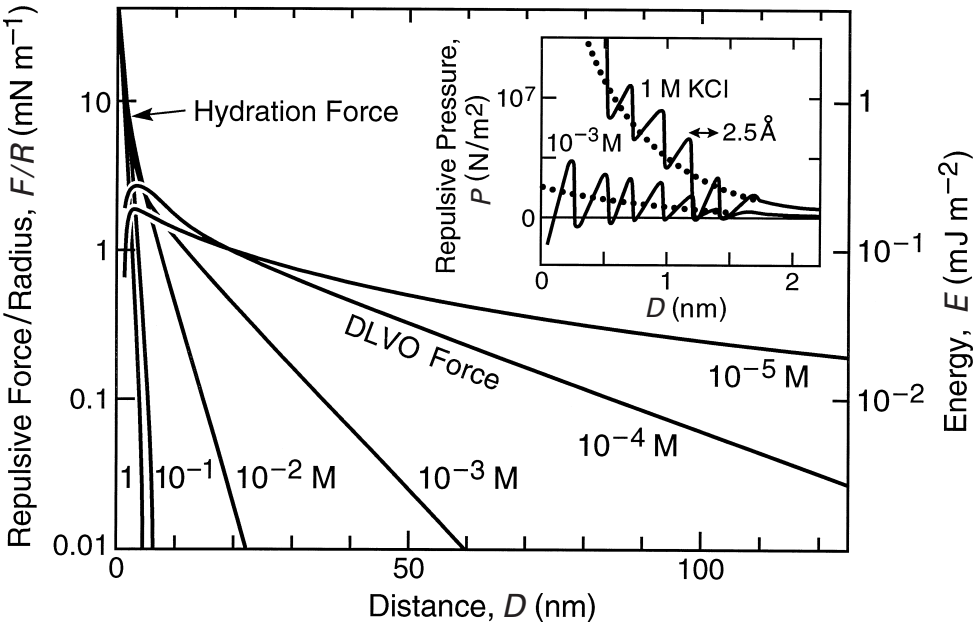


Fig. 44. Long-range DLVO and short-range oscillatory hydration forces in aqueous KCl solutions due to water-structuring between two solid, rigid surfaces of mica, an alumino-silicate clay mineral that exhibits 'perfect cleavage' at its basal plane. Mica surfaces are often used in studies where inert, molecularly smooth surfaces are required. The mica basal plane has a pI of about 2·5 and is ion-exchangeable, allowing for different ions and protons to adsorb and replace each other by altering the solution conditions. Various surfactant and lipid bilayers, as well as proteins, polymers and polyelectrolytes, can be adsorbed on mica and used in model experiments. (Adapted from Pashley & Israelachvili, 1984.) Similar forces have been measured between aligned clay sheets using other techniques such as the OS technique (Del Pennino *et al*. 1981; Viani *et al*. 1983).

macromolecule, the greater the hydration repulsion. For example, since magnesium is more hydrated than calcium, the adhesion of negatively charged surfaces in $MgCl_2$ solutions is generally weaker than in $CaCl_2$ solutions, and magnesium is usually less effective in promoting membrane adhesion or fusion than calcium. Likewise, at high concentrations the more hydrated lithium ions are generally more effective at dispersing colloid particles than sodium or potassium ions. These repulsive forces also act *laterally*, for example, between adjacent headgroups on the same membrane surface (see Israelachvili, 1991, for a review of these different effects).

Examples of repulsive hydration forces due to the binding of hydrated ions are given in Fig. 44 for mica and in Fig. 32(*a*) for lipid bilayers. In both cases at low ionic strengths the forces are well described by the DLVO theory, but at high ionic strengths and high pH, where the hydrated cations bind to the negatively charged surfaces, there is an additional repulsion that is not accounted for by theory. This repulsion effectively eliminates the adhesion in the primary minimum and, in colloidal systems, results in the dispersal of colloidal particles. Similar effects have been found to occur in the interactions of soluble proteins. Thus, Petsev *et al*. (2000) and Petsev & Vekilov (2000) used the OP technique and found that certain proteins in aqueous solution experience an 'unexpected' additional repulsion in high salt, similar to that previously observed between certain colloidal particles

https://doi.org/10.1017/S0033583501003687 Published online by Cambridge University Press

and lipid bilayers. As in the previous studies, the action of these hydration forces was found to depend strongly on the adsorption of hydrated counterions. They further found that the second virial coefficients of the protein solutions vary in a way that is consistent with the short-range hydration forces previously measured with the SFA between surfaces that exhibit similar behavior. It is apparent that these solvent-mediated hydration forces act between individual molecular groups or discrete hydration sites on surfaces, and that the net interaction between two surfaces is simply the sum of the individual pair interactions.

Such hydration forces can also affect the recognition of small, surface-immobilized ligands by receptors. The latter will be especially evident when the range of the hydration force is close to the range of the attractive RL interaction. In SFA measurements of specific binding between immobilized, monoclonal anti-fluorescein Fab′ fragments and membrane-tethered fluorescein, the 18 Å fluorescein tether was just long enough to permit the Fab′ to fully bind the immobilized ligand. Binding would, therefore, be unimpeded in the absence of any additional steric barriers near the membrane that could impede the protein's access to the fluorescein. By using tethers as molecular rulers, Leckband *et al*. (1995a) demonstrated that the specific intersurface adhesion decreased in proportion to the directly measured steric thickness of the hydration layer on the ligand-functionalized membrane. In 1 mM Na_2HPO_4, the hydration layer thickness was 4 Å, and the measured adhesion energy was 4·3 mJ m^{-2}. However, increasing the Na_2HPO_4 concentration to 30 mM increased the measured hydration layer thickness to 7 Å, and correspondingly reduced the RL adhesion to 2·7 mJ m^{-2}. The RL interaction in solution is independent of the buffer concentration, so that the changes were attributed solely to changes in the hydration forces. As in the case of membrane interactions described above, the observed behavior results from a delicate balance between the short-range RL attraction and the equally short-ranged hydration repulsion (Leckband *et al*. 1995a). A similar balance occurs between attractive depletion forces and repulsive steric-hydration forces in the interactions between lecithin bilayers in PEO solutions (Kuhl *et al*. 1996, 1998a).

3.7 Forces between 'soft-supported' membranes and proteins

Figures 22 and 45(*a*) show some of the constructs that are currently being developed for supporting bilayers, membranes, tethered proteins, ligands and receptors, etc., to allow for their interactions to be measured *in vitro* but under near-physiological conditions. Such soft-supported systems can be used with almost any one of the force-measuring techniques described in Section 2, as well as with other, non force-measuring, techniques such as electro-physiological, patch-clamp, fluorescence microscopy, etc. Here we review a few of the recent results obtained using these constructs.

Figure 45 shows results of force measurements between lecithin bilayers supported on a soft polyelectrolyte cushion of polyethylene imine (PEI), a weakly charged cationic water-soluble polymer that acts as a soft bridge between the negatively charged substrate surface (mica) and the negatively charged phosphate groups on the lecithin headgroups (see Fig. 45(*a*)). These measurements show how the long-range forces, short-range adhesion forces, and fusion barriers are different for rigidly supported and softly supported bilayers. As expected, softly supported membranes experience additional repulsive thermal fluctuation (undulation) forces that contribute a weak long-range repulsion that decreases or eliminates the VDW adhesion energy minimum. But the repulsive barriers to hemi-fusion and full-

https://doi.org/10.1017/S0033583501003687 Published online by Cambridge University Press

fusion are also lowered, in spite of the stronger repulsion, probably because of the greater ease with which the more mobile and fluid membranes can develop local defects or 'fusion pores' that act as nucleation sites for fusion.

3.8 Equilibrium energies between biological surfaces

Although the majority of force or energy measurement techniques involve pulling and following a 'jump' out from adhesive contact – an inherently non-equilibrium processes – there are some approaches with which one can measure the equilibrium interfacial energies between biological materials. In these cases, a soft material is placed on a hard surface or on a second soft material, and the soft material deforms and spreads over the second surface. The interfacial contact area will increase until mechanical equilibrium is established (cf. Fig. 29). The subsequent analysis of the material shape, contact angle, or the size of the contact area gives the interfacial energy γ or the adhesion energy per unit area. As discussed in Section 2.5, this macroscopic parameter reflects the molecular interactions between the two surfaces, and will vary with the density and type of intersurface bonds. However, because the measurements do not require pulling, the adhesion energy per area reflects the equilibrium value, and does not depend on the dynamic response of the instrument or the pulling or pushing rate.

In a variation of the JKR approach, Moy *et al*. (1999) used the RICM technique to quantify the contact area between a soft agarose bead, decorated with biotin, bound to an avidin-functionalized, glass (hard) substrate. Instead of mechanically deforming the beads, they allowed them to settle onto the glass, and to deform as the receptors and ligands bound. The receptors and ligands were not laterally mobile. Using the JKR theory and the measured elastic constant K_s of the soft bead, the measured surface energy or adhesion energy density between the streptavidin-coated particles and the streptavidin–functionalized substrate was $\gamma = 0{\cdot}17\ \mathrm{mJ\ m^{-2}}$. This is much lower than the adhesion energy between streptavidin and biotin–lipid membranes measured with the SFA (Leckband *et al*. 1994). However, these RICM results are not easily compared with other measurements since the estimated density of RL bonds was not reported.

Under the equilibrium conditions of the RICM measurement, Moy *et al*. (1999) did demonstrate that the adhesion energy density varies with the equilibrium binding constant for the RL pair, and hence with the binding *free energy*. By contrast, the adhesive strength of the streptavidin–biotin bond, measured with the AFM, scales with the activation *enthalpy* for unbinding (Chilkoti *et al*. 1995). The RICM data demonstrate an important point regarding the relevant energies that scale the 'strength' of a particular interaction. As discussed in Section 1.10 (also in Section 4), the bond *strength*, when determined by pulling, is a kinetic parameter that scales with the activation energy for dissociation (unbinding). However, it also depends on the rate of pulling relative to the intrinsic dissociation rate. In contrast, under the equilibrium conditions of the RICM measurements, the strength of the interaction, as quantified by the adhesion energy density, is time-independent and was found to increase with the *equilibrium* bond energy. The free energy, not the bond rupture force, determines such parameters as the equilibrium intersurface separation and contact area (Lindermann & Lauffenburger, 1993). The RICM results further demonstrate that the relevant parameters such as force or energy, which govern the 'strength' of a biological interaction, will depend

https://doi.org/10.1017/S0033583501003687 Published online by Cambridge University Press

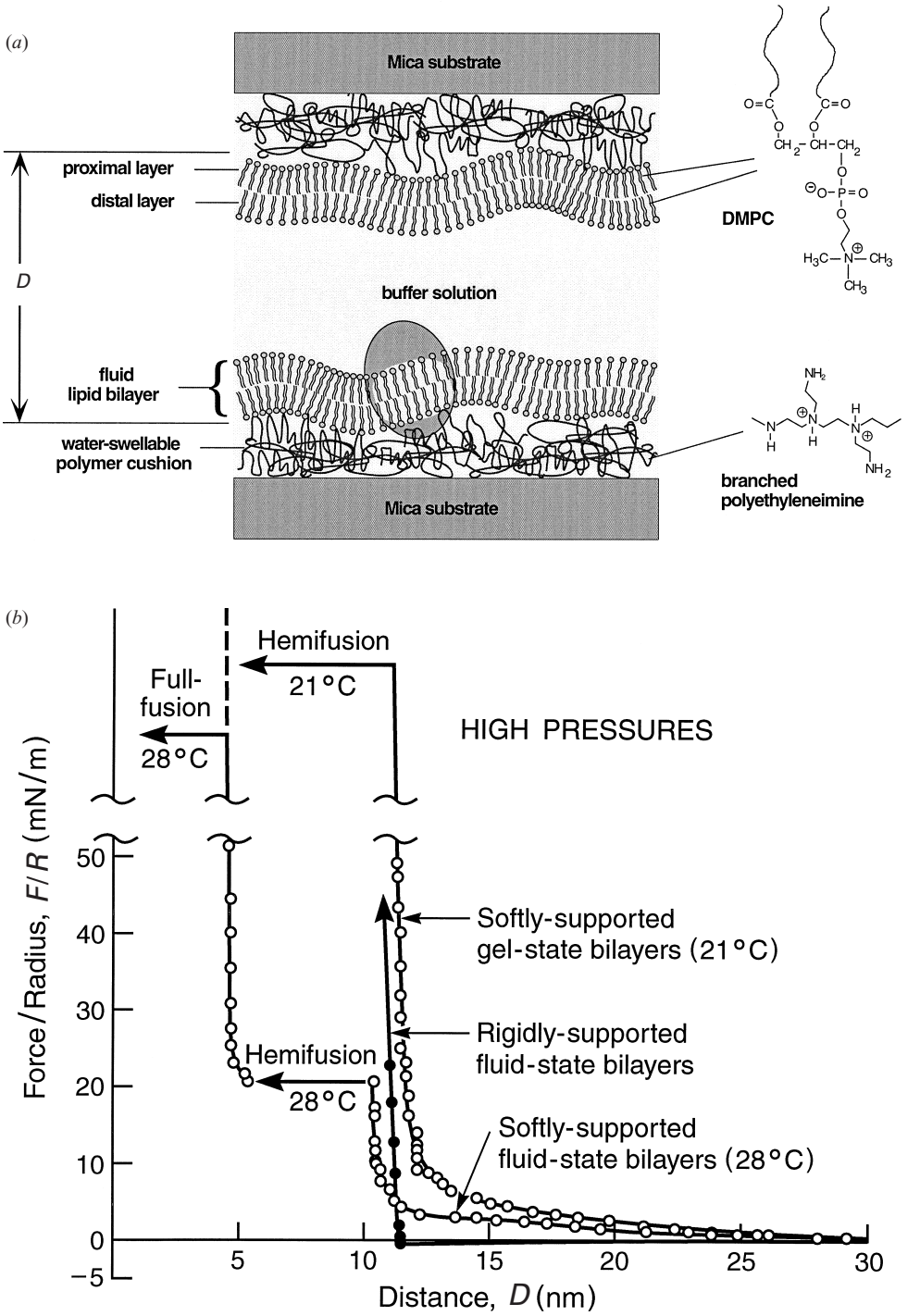


Fig. 45. Forces between softly supported bilayers. (*a*) Typical construct of polymer-supported membrane. The measured forces, shown in (*b*), are between two pure DMPC bilayers (with no protein) supported on a 1·5 nm thick PEI film. White circles: soft-supported bilayers in the fluid ($T = 28$ °C) and solid ($T = 21$ °C) state. The chain melting temperature of DMPC is 24 °C. Black circles: previous results for rigidly supported bilayers on mica. The separation distance D is defined in (*a*). (Figure adapted from Seitz *et al.* 1998, 2000; Wong *et al.* 1999a, b.)

https://doi.org/10.1017/S0033583501003687 Published online by Cambridge University Press

on the biological context, and whether, for example, the bonds are being pulled or whether the system is in a quasi-equilibrium[59] state.

To compare measured bond or intersurface energies obtained with different techniques or with different systems requires some knowledge of the effective contact area (cf. Eq. (45)), and the number of receptors and ligands forming cross-bridges between the surfaces. In another study with streptavidin and biotin, Albersdörfer *et al*. (1997) determined the adhesion energy per area between dense clusters of streptavidin on a supported bilayer and biotin-displaying giant vesicles. In the latter case, the local adhesion energy determined at membrane pinning sites was on the order of only 0·01 mJ m^{-2}, which is much smaller than the value determined by Moy *et al*. (1999) with the agarose beads. This difference is likely due to the fact that the streptavidin clusters at the pinning sites are rigid 2D crystals which prevented the accumulation of cross-bridges at sites of membrane tension such as occurs at cell–cell junctions. Because of the low levels of biotin on the attached vesicles, the density of actual cross-bridges within the streptavidin domains may not have been particularly high, and this may account in part for the low average adhesion energy per streptavidin determined by Albersdörfer *et al*. (1997). The modified JKR and RICM approaches are both powerful methods for investigating receptor-mediated adhesion under equilibrium conditions. However, to compare the bond strengths or energies determined under these conditions with bond strengths obtained by other methods requires more information regarding the number of bonds that mediate adhesion in each case.

Differences in adhesion energies or membrane bending moduli measured by equilibrium methods are also being used to monitor changes in the membrane composition and cytoskeletal properties of living cells. RICM was used to investigate the adhesion of living cells on biologically active surfaces. The adhesion energies of both wild-type and mutant *Dictyostelium discoideium* were determined from the deformations of cell membranes near adhesive contacts (Simson *et al*. 1998). This group also quantified differences in the membrane bending moduli on the basis of the membrane shape near the cell–substrate contact line. Measured differences between the bending moduli of the wild-type and mutant cells were attributed to the perturbations in the mechanical properties of the cytoskeleton, that is, to the absence or presence of the cytoskeletal proteins in mutant cell lines. The analysis of the 3D shape of the cell membrane near the contact region also gave the local adhesion energy. However, as will be discussed in Section 4, the membranes of living cells are dynamic and constantly restructuring, so that the adhesion energies measured most likely reflect a snapshot of a changing system rather than true equilibrium.

4. Non-equilibrium and time-dependent interactions: sequential events that evolve in space and time

4.1 Equilibrium and non-equilibrium time-dependent interactions

Biological systems are not at equilibrium, and are, consequently, either undergoing dynamic changes in response to stimuli or being maintained at a steady state by the input of energy.

[59] Biological systems are rarely at true equilibrium. However, locally, the system may achieve the lowest free energy configuration given the constraints imposed by, for example, the surrounding tissues or the organization of the cytoskeleton. This is often referred to as ‘restricted equilibrium’, ‘metastable

https://doi.org/10.1017/S0033583501003687 Published online by Cambridge University Press

In addition, as discussed in Section 1.10, some parameters that determine the strengths and other characteristics of biological interactions depend on the rate at which the bodies are pulled apart or brought into contact. The experimental challenge is to determine the physico-chemical principles that underlie time-dependent changes in biological interactions, and how dynamic parameters such as the rate of approach or separation in turn determine how two biomolecules or biosurfaces interact.

It is important to consider both the context in which dynamic or time-dependent interactions play a role in biology and the time scales of interactions investigated with force measurement techniques. In living systems, time-dependent changes can occur by active mechanisms such as directed cytoskeletal rearrangements following changes in the cell. Alternatively, the system may change passively as it evolves towards some equilibrium state. In a very general sense, the relevant time-scales vary widely, by over 10 orders of magnitude: some systems change relatively slowly, such as the adhesion and assembly of protein or bacterial layers on a surface,[60] while others occur rapidly (microseconds) as in neurotransmitter release at a synapse. In these cases, the dynamics of the interaction are determined by the system and are not a consequence of the measurement technique. In other cases, however, the measurement itself perturbs the system, and the response (i.e. what is actually measured) will depend both on the rate or time-scale of the measurement and on the relaxation time of the molecules or materials. For this reason, it is important to consider how the instrument dynamics affect the measured parameters, and to evaluate the relevance of the measurements to the interactions *in vivo*. Bearing this in mind, one can more clearly identify the most appropriate methods for investigating a particular system or interaction, and interpret the results within the biological context.

Most of the force-measurements described in Section 3 involved macroscopic or microscopic surfaces composed of many molecules and having long relaxation times, so that dynamic changes are slow on the timescale of the measurements. The techniques used, mainly SFA, AFM, MPA and OP, are particularly suited for studying such interactions. In contrast, when small particles, individual molecular pairs, or a small number of molecules are involved, the dynamics of the interactions tend to be much faster and more statistical in character. However, in order to fully understand the behavior of an entire population and how single molecule behavior affects macroscopic properties, or 'many body' interactions, requires some subtle averaging over both space and time. The appropriate techniques for the latter studies are the MC, OT, MPA, AFM, TIRM, and SFD techniques, which can measure the weak forces and very rapid changes that are characteristic of such interactions (see Tables 4 and 5).

A non-equilibrium, time-varying interaction that is slowly evolving towards the equilibrium state should be clearly distinguished from the very different 'statistical' or 'stochastic' process that involves random fluctuations about the equilibrium configuration. In the former, the system is slowly changing *in a certain direction*, and the slowness usually implies that the activation barriers are high or, equivalently, that the multiple potential energy

---

equilibrium' or 'kinetically trapped equilibrium'. For example, the cytoskeleton could (temporarily but effectively) prevent a cell from spreading on an adhesive substrate, but receptors and ligands could still accumulate in the contact area and maximize the adhesion energy under conditions of limited membrane deformation.

[60] In these cases, the rearrangements may be slower than the time-scale of the measurement, so that the system may still be evolving during the measurement.

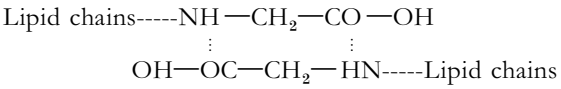
https://doi.org/10.1017/S0033583501003687 Published online by Cambridge University Press

minima are deep. In the latter case, the system is in rapid thermal (Brownian) motion but is always in the equilibrium state.[61] Here the energy barriers or potential wells are usually shallow. It is ironic that an interaction that is not changing in time may be far from equilibrium, but one that is rapidly fluctuating may be in the equilibrium state.

For both types of time-dependent interactions, i.e. both those that are near and far from equilibrium, the adhesion and binding forces generally depend on the loading or unloading rates, and in both cases the measured forces and dynamics are different for macroscopic (many, cooperative) systems versus single bonds. At the molecular level we find single-bond interaction energies that can range from 0·001 to 35 kT (in solution) as we go from weak VDW binding to strong RL binding (covalent bonds are not included in this review). The lifetimes of such bonds can also range from picoseconds to days. At the macroscopic level we find interfacial adhesion energies that range from below 0·01 to 100 mJ m^{-2} (see Table 6), and dynamics that are substantially slower. In Section 1.10, it was explained how the *measured* values of adhesion can be very different from the *equilibrium* energy and force profiles, depending on the pulling or pushing rates and on the 'measurement' or 'observation' time. Such non-equilibrium effects lead to hysteresis, irreversibility, transient effects, discontinuous or sudden changes, diffusion-limited interactions and, in particular, important differences between local *versus* global effects.

4.2 Adhesion energy hysteresis

The adhesion of surfaces that are soft or fluid-like are often highly hysteretic: the adhesion energy on loading being less than the energy on unloading. A good example of this phenomenon, which also illustrates many other aspects of non-equilibrium bio-interactions, is shown in Fig. 46, which shows the loading and unloading JKR curves for two bilayer surfaces containing 'complementary' peptide amphiphiles terminated by glycine groups



The long-range forces between these surfaces depended on the pH. At pH 8·2 the surfaces were negatively charged (about 30 % dissociated) and the force was dominated by the double-layer and steric–hydration repulsion at all separations, as in Fig. 32(*a*) at high pH. There was no adhesion, and the loading and unloading curves are reversible and follow the Hertz equation for non-adhering surfaces ($\gamma = 0$).

As the pH was lowered to 5·6–6·8 the glycine groups became progressively less charged, and the surfaces could now come close enough for adhesive contact to occur between the nearly uncharged glycine groups on each surface, as in Fig. 32(*a*) at low pH. These bonds consist of weak VDW bonds as well as two strong hydrogen-bonds per glycine–glycine pair (see sketch above). On loading at pH 6·8, the two surfaces initially adhere only via the VDW force between them, which acts instantaneously as the two surfaces come together. Thus, on loading or 'advancing', the measured surface energy is $E_A = 2\gamma_A = 0{\cdot}14$ mJ m^{-2}, which is

[61] Actually, in both cases, the systems may be approaching or fluctuating about some local energy minimum rather than the 'global' minimum.

https://doi.org/10.1017/S0033583501003687 Published online by Cambridge University Press

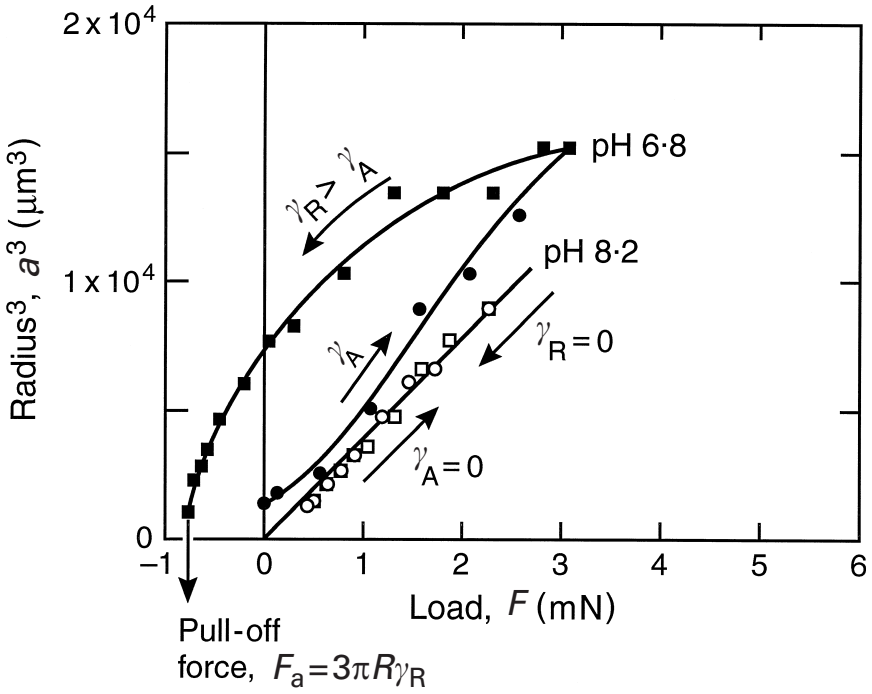


Fig. 46. Adhesion hysteresis of supported bilayers composed of glycine-functionalized lipids in various aqueous solutions as measured with a 'JKR apparatus' (Fig. 19). JKR plots of contact radius *a versus* applied load F give the adhesion energy $E_0 = 2\gamma_i$ on loading or 'advancing', $E_A = 2\gamma_A$, and unloading or 'receding', $E_R = 2\gamma_R$, via Eq. (35). This type of adhesion hysteresis loop is qualitatively similar to that observed with many other surfaces, both biological and non-biological, as described in the text. At high pH (~8·2) the adhesion is weak or zero and the loading and unloading curves are the same, i.e. the adhesion is reversible and there is no hysteresis. At low pH (5·6–6·8), the loading curve corresponds to an adhesion energy of $E_A = 2\gamma_A = 0{\cdot}14$ mJ m^{-2}, which is typical for the VDW adhesion force between uncharged or weakly charged but unfunctionalized bilayers in water (see Table 6). However, unlike unfunctionalized bilayers that interact only via (reversible) VDW forces, the unloading curve here is very different – following a much higher adhesion energy of $E_R = 2\gamma_R = 16$ mJ m^{-2}, which also determines the pull-off force $F_a = 3\pi R\gamma_R$ where $R = 1{\cdot}5$ cm in this case. (Adapted from Schneider *et al.* 1998.)

typical for VDW contacts (cf. bilayer adhesion values in Table 6). After a short time in contact, the glycine groups on the opposite surfaces diffuse and mutually orient so as to form hydrogen-bonding junctions of the type found in β-pleated sheets in the anti-parallel configuration.[62] Thus, on unloading, the adhesion is much greater because both H-bonds and VDW bonds have to be broken. In the present example shown in Fig. 46, the unloading or 'receding' energy E_R as determined from the unloading JKR curve and/or the pull-off force F_a is $E_R = 2\gamma_R \approx 16$ mJ m^{-2}, which is more than two orders of magnitude higher than the loading energy E_A. This is much stronger than any possible VDW contribution between bilayers (see Table 6) and corresponds to $1{\cdot}5\,kT$ per Gly–Gly bond. This high adhesion energy is, however, only a *lower bound* for the H-bonding contribution, for it was found that on separating the two surfaces from adhesive contact, failure occurred via lipid pull-out rather

[62] Schneider *et al.* (1998) established that the terminal hydroxyl group (−OH) was not involved in the H-bonding, and that no strong bond formed in the absence of the glycine $-NH-CH_2-CO-$ group.

https://doi.org/10.1017/S0033583501003687 Published online by Cambridge University Press

than by the breaking of the hydrogen-bonds. The reason for this was previously explained in Section 1.10 and illustrates one of a number of subtle aspects associated with non-equilibrium interactions: namely, that bond breakage – when it is done quickly – occurs where the *force* is weakest, not where the *energy* is lowest. In this case, the higher energy of lipid pull-out, because it acts over a large distance given by the length of the hydrocarbon chains, implies a lower *force* than is needed to break the energetically weaker but much shorter hydrogen bonds. A similar effect was observed in the adhesion of avidin- and biotin-functionalized lipid bilayers (Leckband *et al*. 1995b) (cf. Fig. 33). On the other hand, one predicts that, if the pulling rate is decreased (pulling-time increased), then the failure would become energy-controlled rather than force-controlled, and breakage would eventually occur where the binding energy is lowest. However, as we will discuss in Section 4.7, one cannot simply extrapolate all aspects of single bond behavior to the failure of adhesive junctions that involve many bonds either in series or in parallel.

Such large hysteresis effects are not uncommon, even for non-specific interactions. For example, between inert, non-polar polymer surfaces where significant segment interdigitation can occur across the interface after contact (which effectively increases the molecular contact area), adhesion forces on separation can reach 10^3–10^4 times of the values expected from the equilibrium adhesion energies γ_0, namely from the VDW forces acting between two *flat* surfaces (Kendall, 1994; Luengo *et al*. 1998). This is the reason why polymers make such good adhesives, in spite of their intrinsically low surface energies. When the adhesion hysteresis is large so that $E_R \gg E_A$ or, equivalently, $\gamma_R \gg \gamma_A$, the hysteresis, which is commonly defined by $\Delta\gamma = (\gamma_R - \gamma_A)$, is essentially the same as the pull-off value γ_R. Therefore, we may write $\Delta\gamma \approx \gamma_R$, where γ_R can be very much higher than the equilibrium adhesion energy, γ_0.

A number of experiments on a variety of biological and non-biological surfaces, that involve both specific and non-specific interactions, have investigated the subtle effects of adhesion hysteresis. These studies have included polymer surfaces (Mangipudi *et al*. 1995; Tirrell, 1996; Falsafi *et al*. 1997; Luengo *et al*. 1998), surfactant and lipid monolayer surfaces (Chen *et al*. 1991b). More recently, these studies include biological surfaces such as S-layer proteins that interact via non-specific hydrophobic interactions (Leckband *et al*. 1993) and ligands, which bind to their complementary receptors (Evans *et al*. 1985; Berndt *et al*. 1995; Dori *et al*. 2000).

In the case of soft polymer surfaces, the large adhesion observed on separation is due to both molecular-scale interdigitation and macroscopic flow effects; these cause the two separating surfaces to undergo dramatic shape deformations both at the molecular and macroscopic levels (Baljon & Robbins 1996; Luengo *et al*. 1998). The deformations are manifested by long thin filamentous bridges or 'strings' that continue to hold the surfaces together before they finally detach as each string snaps in turn. In some cases, only a single bridge occurs, usually at the center, while in others, a number of bridges form within the original contact area. Such effects have been observed between macroscopic polymer surfaces with the SFA (Luengo *et al*. 1998) and between microscopic surfaces with the AFM (Portigliatti *et al*. 2000). Different manifestations of this complex effect are variously referred to as 'sintering', 'stringing', 'tack', 'crazing' or 'cavitation'. There is evidence, discussed later, that some biological cell surfaces may also pull apart from an adhering surface or particle via similar mechanisms (Hwang & Waugh, 1997; Dai & Sheetz, 1999; Raucher & Sheetz, 1999; Schmidtke & Diamond, 2000).

In general, the adhesion hysteresis depends on the loading and unloading rates, on the

https://doi.org/10.1017/S0033583501003687 Published online by Cambridge University Press

contact time (the 'resting' time between loading and unloading), on the applied load or pressure during contact (the resting pressure), and on the temperature, which determines various diffusion rates. For example, in the case of specific LR interactions, the more fluid the bilayers that carry the receptor and ligand molecules, the more rapid is the binding, and the faster the adhesion reaches the maximum value. Also, if the surfaces are kept together for a fixed time before being separated, the more fluid membranes exhibit higher adhesion energy. Both of these effects are temperature-dependent. In some cases, the system can change dramatically due to only a small temperature change, for example, when T passes though the fluid-to-solid phase transition temperature of the membrane, which drastically alters the lateral diffusion coefficients of the membrane components (Leckband *et al*. 1994). These effects are discussed in more detail in Section 4.8.

The effect of loading–unloading rates and temperature can be very dramatic and are particularly interesting: if a loading-unloading process is considered as a cycle taking a finite time τ_m, which may be the 'measurement' or 'observation' time of an externally controlled process, or the 'collision' or 'contact' time of a natural dynamic interaction. We can further define the natural relaxation time or lifetime of the system or interaction by τ_r, which is generally diffusion- and thus temperature-controlled. These two times allow us to define a dimensionless number known as the Deborah Number, De,

$$\mathrm{De} = \frac{\text{measurement time}}{\text{relaxation time}} = \frac{\tau_m}{\tau_r}. \tag{50}$$

In many different systems it has been found that maximum hysteresis occurs when De is close to 1, and there are good theoretical reasons for this general observation (Israelachvili & Berman, 1995). The degree of hysteresis is also a measure of the efficiency of trapping energy or of the energy lost or dissipated in a cycle.[63] Maximum dissipation (maximum thermodynamic irreversibility) occurs when all the energy inputted is absorbed by the system or process.[64] For example, if the natural lifetime of an unstressed ligand in a receptor pocket is $\tau_r = 10^{-3}$ s, then the maximum likelihood of capture will occur when De $\approx$ 1, i.e. when the collision or contact time τ_m is also about 1 ms. If the dimension of the receptor site is 1 nm and the ligand passes close to the receptor, the optimum capture efficiency should therefore occur at a flow rate of $10^{-9}/10^{-3} = 1\ \mu\mathrm{m\ s^{-1}}$. At faster flow rates the ligand travels too fast to be captured, while at slower flow rates there is now more than enough time for the thermal energy to unbind the ligand. Fortunately, the exact numbers are not particularly critical because the efficiency varies with the logarithm of the time, the flow rate or speed.

4.3 Dynamic forces between biomolecules and biomolecular aggregates

Several of the force balance techniques described in Section 2 are sufficiently sensitive for studying the behavior of single noncovalent, intermolecular bonds. These techniques have been used to quantify the strengths of single bonds; to map the energy landscapes of specific,

[63] One must remember that by the First Law of Thermodynamics the total energy is always conserved. Thus when one talks about energy being dissipated or lost one really means that it has been *transferred*, either to a different form (e.g. heat from mechanical energy) or to a different place (the solvent or colliding particle).

[64] Cf. the Carnot Cycle or any other thermodynamic cycle where the efficiency is defined in terms of the work input and output as $(W_{out} - W_{in})/W_{in}$.

https://doi.org/10.1017/S0033583501003687 Published online by Cambridge University Press

noncovalent bonds; to probe the mechanical properties of extensible biomolecules such as DNA and titin; and to investigate the stochastic and time-dependent nature of single molecule interactions. In these measurements force is used to induce chemical transformations, which are linked to the disruption of stabilizing bonds. The intitial studies of single bonds focused primarily on measurements of bond strengths. However, more recent studies have addressed (1) the effect of mechanical forces on intermolecular potentials and bond rupture rates, (2) the dependence of bond strength on the measurement dynamics, and (3) the relationship between rupture forces and bond chemistry.

4.3.1 Strengths of isolated, noncovalent bonds

To understand what the measured bond strengths reveal about the intrinsic bond chemistry and the intermolecular potential, it is necessary first to consider the interrelationships between the applied force and the chemistry, thermodynamic properties, and bond rupture kinetics. One of the predictions of the Bell model (Eq. 26) is that mechanical loads on intermolecular bonds will lower the energy barriers for dissociation and thereby increase the kinetics of bond failure. To test this required the ability to quantify bond dissociation rates as a function of the applied load.

The SFD assay (Fig. 30) is perhaps the best method for testing Bell's prediction. This is primarily because, in contrast to all of the other methods described, the force on the bond is switched on as soon as the bond forms. Since the particles or cells are in a flowing fluid, bond formation arrests the particle, and the shear force exerted on the particle or cell is instantly transmitted to the bond tethering the cell or bead. The applied force is also relatively constant at constant fluid flow rates, and depends in a well-defined way on the fluid velocity and the particle size (Kaplanski *et al*. 1993; Lindermann & Lauffenburger, 1993; Alon *et al*. 1995; Pierres *et al*. 1995, 1996). In all of the other techniques, the applied force is increased slowly or rapidly until the bond fails. In all SFD studies, the rate at which the load on the bond is switched on is essentially the same, so that measurements from different laboratories should be comparable and unaffected by variations in the dynamic properties of the measurement technique. In addition, this is one of the few techniques with which it is possible to measure the rates of bond formation and dissociation between two surfaces.

Both Alon *et al*. (1995) and Pierres *et al*. (1996) used SFD measurements to demonstrate that the bond dissociation rate increases with the applied load, as predicted by Eq. (26). Alon *et al*. (1995) determined the dependence of bond rupture rates on the applied load by measuring the dynamic adhesion between P-selectin and the carbohydrate sialyl Lewis^x. In their studies, the P-selectin was incorporated into supported membranes on glass substrates, and the carbohydrate was displayed on the surfaces of neutrophils transported in the fluid stream above the membrane. By modeling the trajectories of neutrophils as they rolled over the P-selectin monolayer, these authors determined both the bond formation and bond rupture rates as a function of the fluid velocity – that is, as a function of the tensile force on the bond. The measurements revealed a modest, but definite, increase in the dissociation rate with increasing shear stress. The dissociation rate increased $\sim$ threefold, from 1 to 3·5 s^{-1} when the force on the bonds increased $\sim$ fivefold from 20 to 110 pN. The generality of this behavior was further demonstrated by Pierres *et al*. (1996), who also used SFD to study the lifetimes of bonds between receptor-coated beads and ligand-coated substrates in a cell-free

https://doi.org/10.1017/S0033583501003687 Published online by Cambridge University Press

system. Such cell-free assays are less vulnerable to complications due to the pull-out of membrane tethers, as discussed in Section 2.13. Increasing the fluid shear stress, and hence the force on the bond, also increased the dissociation rates of both antibody–antigen and CD2–CD48 (T-cell adhesion protein) interactions. With the low affinity CD2–CD48 interaction ($K_a \approx 10^4$ M^{-1}), the bond dissociation rates increased from 7·8 to 15 s^{-1} when the shear stress increased from 11 to 22 pN (Pierres *et al*. 1996). The different response to increasing force by the CD2–CD48 bond *versus* that of the selectin-carbohydrate bond is likely due to the different activation barriers to unbinding. In addition, by reducing the density of receptors and ligands on one or both surfaces, Pierres *et al*. (1996) reduced the number of bonds formed to very low levels. As a result, their measurements reflected the dynamic behavior of isolated RL bonds. Both Alon *et al*. (1995) and Pierres *et al*. (1996) focused on the *rates* of bond failure, rather than on the *forces* associated with bond rupture. This is because the bonds did eventually break at each applied load, but the rupture kinetics, and hence the lifetimes of the bonds, varied with the fluid shear stress.

With other force measurement techniques, the objective has been to determine single bond rupture forces. As was discussed in Section 1.10, the force required to break a bond depends on how long one is willing to wait. However, in contrast to the SFD measurements, the other techniques described in this review do not switch on the force instantaneously, but gradually increase the load at a particular rate R_F that is determined by the dynamic response of the instrument. At some point in this process the bond fails, but the force at which the bond breaks now depends on both the magnitude of the force and the time it takes to achieve a certain load. The situation is now more complicated because both the dynamics of loading and of spontaneous bond rupture determine the most probable rupture force. To address bond failure under these conditions, Evans & Ritchie (1997) considered how the interplay of loading dynamics and bond rupture kinetics affect the bond rupture measurements. Intuitively, one would predict that there would be three different dynamic response regimes in plots of the most probable bond rupture force F *versus* the loading rate R_F. In the very slow loading regime, the intrinsic dissociation rate of the bond is much faster than the rate at which the force reaches any appreciable level, and the apparent bond strength tends to zero. In this regime, bond dissociation is thermally activated, so that detachment is primarily determined by the activation energy E_{act}, and is only weakly dependent of R_F. At the opposite extreme of ultrafast loading rates, the applied load reaches the critical rupture force $F = E_{act}/r_0$ much faster than bond dissociation rate. In this forced unbinding regime, one quickly reaches the maximum bond rupture force, and the measured bond strength is not expected to increase further with the loading rate.[65] In the intermediate regime, the loading rate R_F is comparable to the force-activated dissociation rate, so that the apparent bond strength will depend strongly on the loading dynamics, as described in Section 1.10. This is actually the regime within which most of the instruments described in this review operate.

Measurements of the strengths of isolated bonds, done with the AFM and with the BFP (Section 2.8) confirmed the prediction that the measured strengths of bonds are loading-rate dependent (Fig. 47). In early AFM measurements with streptavidin and biotin, the force was applied to the streptavidin–biotin bond at a rate of 10^5 pN s^{-1}. Under those conditions, the measured streptavidin–biotin bond strength was $\sim$ 200–300 pN (Lee *et al*. 1994; Moy *et*

[65] Strictly speaking this is not the case, since friction and inertia also contribute to the measured force in this regime. Above the critical bond rupture force, the measured force will continue to increase linearly since the frictional contribution is proportional to the loading rate (Izrailev *et al*. 1997).

https://doi.org/10.1017/S0033583501003687 Published online by Cambridge University Press

al. 1994). The avidin–biotin interaction, measured under essentially identical conditions, was somewhat weaker at ~ 160 pN (Moy *et al*. 1994). By contrast, with the BFP, using both avidin and streptavidin, Merkel *et al*. (1999) found that, at very slow pulling rates of $\sim 10^{-2}$ pN s^{-1}, the apparent streptavidin (avidin)–biotin bond strength could be as low as ~ 5 pN. To demonstrate this, they varied the pulling rates over 7 orders of magnitude from 10^{-2} to 10^{5} pN s^{-1} (Fig. 47). As predicted, at very low pulling velocities, where the time to reach even tiny forces is slower than the time it takes for the bond to break spontaneously, the bond strength tends to zero. The streptavidin measurements show that this is even the case for bonds with very high affinities that are usually considered to be very strong.

The predicted bond strength should, in principle, vanish at loading rates much less than ν_0^{-1}. It should, therefore, be possible to estimate the intrinsic bond lifetime by extrapolating the slope of the F *versus* log R_F curve along the branch corresponding to the lowest rates ($R_F < 10$ pN s^{-1}, Fig. 47) back to zero force. The estimated intrinsic biotin–avidin dissociation rate, determined with this approach, was ~ 1 h^{-1}. This is, however, 50 times faster than the dissociation rate measured in solution. This result suggests that there may be some unidentified mechanism that enhances the biotin dissociation rate in these measurements, but the origins of this discrepancy have so far not been accounted for. One reason may be the large error associated with extrapolating the nearly flat curve back to $F = 0$. Even a small error in the slope could translate into a large error in the point at which the extrapolated line crosses the R_F axis.

By measuring the tension on a RL bond under conditions of mechanical equilibrium, it is also possible to determine the bond strength at 'zero loading rate'. Under these circumstances, once a system achieves equilibrium, a relatively constant (time-independent) force is exerted on the bonds by the deformed mechanical components of the system, e.g. a membrane or deformable bead. Using the RICM approach (Section 2.10) Albersdörfer *et al*. (1997) calculated the strength of streptavidin–biotin bonds between two adhering membranes at mechanical equilibrium. A biotinylated membrane vesicle was placed on a dilute monolayer of streptavidin, and the vesicle became pinned by discrete streptavidin–biotin links that distorted the membrane locally. The surface density of streptavidin molecules was sufficiently small that each of the pinning sites represented a single streptavidin–biotin cross-bridge. By analyzing the local membrane distortion, Albersdörfer *et al*. (1997) calculated the force required to create membrane pinning centers, and concluded that the streptavidin–biotin bonds exert ~ 7 pN of force on the membrane. This is more than an order of magnitude lower than the detachment forces determined with the AFM, but compares well with the BFP measurements at extremely low pulling rates. The significance of this finding is that these conditions of mechanical equilibrium are similar to those found in many cells and tissues where the exerted forces are relatively constant. The RICM studies show that the bond strengths determined under these conditions will likely be substantially weaker than those determined at more rapid loading rates. They further suggest that, in order to relate measured bond strengths to behavior *in vivo*, one must first consider the conditions under which the molecules function and the relevance of the force measurement parameters to the latter.

4.3.2 The strengths of isolated bonds depend on the activation energy for unbinding

The experimental results described above show clearly that the apparent bond strength depends on the measurement time or pulling rate. However, to understand the relationship

https://doi.org/10.1017/S0033583501003687 Published online by Cambridge University Press

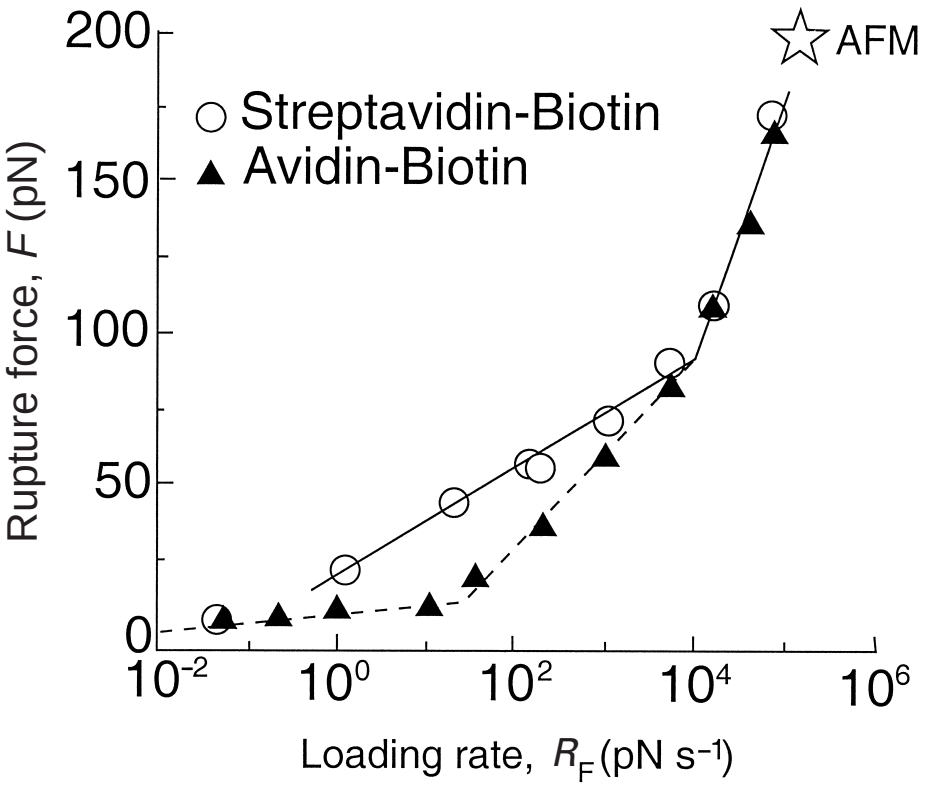


Fig. 47. Dependence of bond strength (rupture force) on the loading rates for streptavidin–biotin and avidin–biotin. The avidin bond strength exhibits three distinct regimes with three different slopes that map the positions of three different energy barriers along the unbinding trajectory, as described in the text. Streptavidin exhibits only two such regimes. (Adapted from Evans & Ritchie, 1997.)

between bond chemistry and bond strength, we also need to consider the appropriate thermodynamic parameter that determines the magnitude of the rupture force. The models of Evans & Ritchie (1997) and of Israilev *et al*. (1997) both predicted that the bond strength increases linearly with the activation energy for unbinding $E_{\rm act}$ (Fig. 16(*b*)), whereas Bell's initial model assumed that the binding free energy ΔG is the relevant energy scale (Fig. 16(*b*)). Dembo *et al*. (1988) similarly predicted that the rupture force would vary linearly with ΔG, and therefore with the logarithm of the affinity constant.

To test the prediction of Dembo *et al*. (1988), Kuo & Lauffenburger (1993) used the SFD technique to measure the dependence of antibody–antigen rupture forces on the RL affinity. Indeed, the strengths of antibody–antigen bonds determined by shear flow detachment varied linearly with the logarithm of the affinity, that is, with ΔG. On the other hand, AFM measurements of the strengths of bonds between avidin and different biotin analogues varied linearly with the equilibrium binding enthalpy ΔH, but not with the binding free energy ΔG (Florin *et al*. 1994). This apparent contradiction was resolved by Chilkoti *et al*. (1995) who genetically engineered streptavidin mutants that exhibited variations in both their kinetic and equilibrium binding characteristics. Differences in affinities reflected differences in ΔG, whereas differences in kinetic rate constants reflected differences in $E_{\rm act}$. By engineering

https://doi.org/10.1017/S0033583501003687 Published online by Cambridge University Press

streptavidin mutants that differed in H_{act}[66] but had the same affinities – that is, the same ΔG values – they showed unambiguously that the streptavidin–biotin bond rupture force increased with H_{act}. These findings were consistent with the predictions of Evans & Ritchie (1997) and of Izrailev *et al.* (1997). However, kinetic rate theory (Section 1.10) predicts that the rate processes scale with E_{act}, so that the dependence on H_{act} is likely because of the negligible entropic contribution to streptavidin–biotin binding. The activation entropy S_{act} is related to the width of the potential and the distribution of bound states (Jencks, 1969). Although S_{act} apparently contributes little to the dissociation kinetics of streptavidin–biotin bonds, it could contribute to bond rupture forces in other systems.

The relationship between the detachment force and E_{act} further suggests the possibility of using force measurements to investigate the potential energy surfaces of intermolecular bonds. With a single barrier, one could estimate the activation energy from the force measured at rapid pulling rates and the determined bond length r_0 since, in the rapid loading limit, $F = E_{act}/r_0$ (Fig. 16). This is, however, difficult to achieve due to the limited dynamic and spatial resolution of most instruments, and the contribution of dissipative forces at loading rates that approach intermolecular dissociation rates. Recent analyses (Evans & Ritchie, 1997; Evans, 1999; Merkel *et al.* 1999) suggest that it may nevertheless be possible to map the positions of the energy barriers along the unbinding trajectory by measuring the detachment force over a range of different pulling rates.

If the unbinding trajectory is characterized by a single barrier, as shown in Fig. 16(*b*), then the characteristic dissociation rate is given by Eq. (25) (using E_{act} instead of ΔG) or by Eq. (27). The dissociation rate will then increase linearly with the logarithm of the applied force. If the force is gradually increased, however, as in most force measurements, then the force on the bond and the RL dissociation rate continue to increase with time. Under these conditions, Evans & Ritchie (1997) showed that the most probable rupture force F varies with the loading rate according to:

$$F = \frac{kT}{r_0} \ln \left(\frac{R_F r_0}{kT \tau_0} \right), \tag{51}$$

where τ_0 is the intrinsic lifetime of the unperturbed bond. This simple relationship predicts that the slope of the plot of the rupture force F *versus* the natural logarithm of the loading rate $\ln R_F$ is kT/r_0. According to this model, the position of the activation barrier r_0 can be determined from the slope of the F *versus* $\ln R_F$ curve.

As shown in Fig. 16(c), however, kinetic processes that involve complex molecules such as proteins and nucleic acids may exhibit multiple local maxima and minima along the reaction coordinate. In such cases, by extending the analysis described above, it can be shown that plots of F *versus* $\ln R_F$ should exhibit a sequence of lines with different slopes, each one mapping the position of a particular energy barrier in the unbinding path (Evans & Ritchie, 1997; Evans, 1999; Merkel *et al.* 1999). The intercepts of the different linear segments of the curves, when extrapolated to $F = 0$ (cf. Fig. 47), will then differ by an amount that is related to the relative differences in the magnitudes of the energy barriers $\Delta E_{act} = E_{act,1} - E_{act,0}$. Because one must assume certain properties of the bond, however, the absolute values of the differences in activation barriers cannot be calculated directly by this method.

[66] At constant temperature and pressure E_{act} is equivalent to the activation free energy G_{act}. The corresponding activation enthalpy H_{act} and activation entropy S_{act} can be determined from the temperature dependence of the kinetic rate constants (Jencks, 1969).

https://doi.org/10.1017/S0033583501003687 Published online by Cambridge University Press

The logarithmic dependence of the most probable rupture force on R_F was demonstrated in BFP measurements with streptavidin, avidin, and P-selectin. In each of these cases, the force F *versus* ln R_F curves exhibited a sequence of linear regimes with different slopes. In particular, the avidin–biotin bond rupture data in Fig. 47 exhibit three distinct slopes. The prediction is that these different slopes should correspond to the positions of three different energy barriers along the streptavidin–biotin unbinding trajectory. The positions of the barriers thus determined were 0·12, 0·5, and 3 nm (Merkel *et al*. 1999). As will be discussed in Section 4.4, the three putative energy maxima had been identified in prior molecular dynamics simulations (Izrailev *et al*. 1997). The calculated and measured values of the positions of the two inner maxima were in surprisingly good agreement, as can be seen from the simulation data in Fig. 48.

On account of the weak logarithmic dependence of the force F on R_F, dynamic force measurements must be carried out over a wide range of pulling rates R_F. For example, the detection of all three barriers with the BFP required measurements at loading rates that spanned 7 orders of magnitude! The dynamic range accessible with the BFP may, however, be difficult to achieve with other force probe instruments. Two limitations, for example, are the resonant frequency of the force transducer, and viscous dissipation, as the cantilever is rapidly moved through liquid. These limit the timescales accessible in such dynamic measurements. Fluid drainage from between the macroscopic, extended surfaces also limits the dynamic range of SFA measurements (Chan & Horn, 1985). If the oscillation frequency of the AFM probe exceeds the resonant frequency of the cantilever, or if there is substantial viscous damping, then the cantilever deflection will not reflect the true tip-sample interaction (Chan & Horn, 1985; Viani *et al*. 1999a, b). A recent AFM study showed that hysteresis in the force-extension profiles of the muscle protein titin depends on the velocity of the piezo movement that drives the cantilever motion (Viani *et al*. 1999a, b). The latter was attributed both to fluid damping and to the finite resonant response of the cantilever. To circumvent these limitations, smaller cantilevers have been developed with the same stiffness but smaller dimensions (Viani *et al*. 1999b). The smaller cantilevers increase the sensitivity of the force transducer, expand the frequency bandwidth accessible in the measurements, and minimize viscous damping. By contrast, similar limitations do not affect OT or TIRM measurements since those instruments lack the bulky mechanical components of the AFM and SFA.

4.4 Simulations of forced chemical transformations

Despite the sensitivity with which biological systems can be studied with these force probes, the measurements do not tell us anything about the chemistry responsible for the determined forces. To address this question requires additional experimental and theoretical tools that can reveal the specific chemical contacts and interactions that contribute to the energy barriers in the induced transformations. K. Schulten's group has developed a SMD simulation technique both to map the force on a ligand as it is pulled out of the binding site and to identify the physical bonds between different chemical groups that presumably determine the activation barriers to force-induced unbinding or unfolding (Izrailev *et al*. 1997, 1998).

The SMD simulations reproduce the AFM or OT measurements by attaching a stretched 'pseudo spring' to the end of the ligand or biomolecule. Rather than increasing the force by pulling one surface away from the second, the simulations increase the spring stiffness K_S with time, and then follow the consequent changes in the positions and energies of the molecules

https://doi.org/10.1017/S0033583501003687 Published online by Cambridge University Press

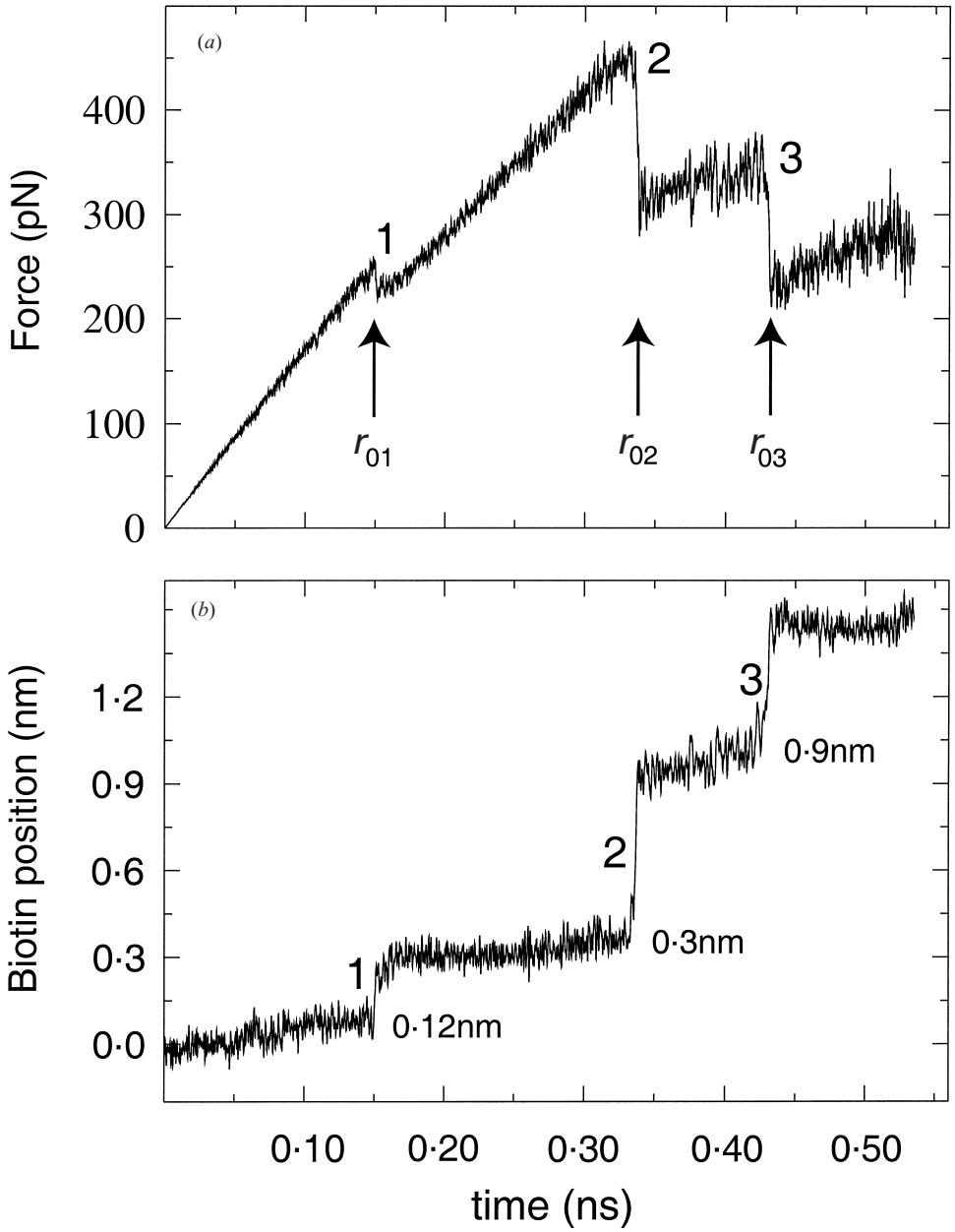


Fig. 48. Energy *versus* distance of biotin–streptavidin interactions. These plots show steered molecular dynamics (SMD) simulations of (*a*) the force on the bond, and (*b*) the biotin position, both *versus* the simulation time. In these simulations, the spring constant increased at a given rate, thus forcing the biotin out of the streptavidin binding pocket. The force on the biotin at different time points, corresponding to increasing applied loads, is shown in (*a*). The abrupt drops in force are due to the successive barrier crossings along the trajectory. The elemental bonds ruptured at those points in the simulation generate the observed activation barriers. The lower panel (*b*) shows the biotin position *versus* time. Here the abrupt jumps in position also correspond to barrier crossings and the accompanying abrupt reductions in force. (Adapted from Israilev *et al*. 1997.)

https://doi.org/10.1017/S0033583501003687 Published online by Cambridge University Press

(Israilev *et al*. 1998). One can thereby follow the force and ligand position as a function of time. For example, in simulations of the avidin–biotin detachment shown in Fig. 48, biotin extraction from the binding pocket was achieved by increasing the stiffness of the 'pseudo-spring' tethering the bound ligand (biotin). The maximum forces exerted on the biotin as it moves out of the binding pocket coincided with the positions of the sharp discontinuities observed in the measured plots of the biotin position versus time (Izrailev *et al*. 1997). The first two positions of the three barriers detected in the experimental BFP results (Merkel *et al*. 1999) agree quantitatively with the positions of the abrupt jumps at $\sim$ 0·12 nm and 0·3 nm evident in Fig. 48. The third calculated and measured barrier at 0·9 and 3 nm, respectively, were in poorer agreement. A comparison of the force and position traces with the physical interactions between chemical moieties on the biotin scaffold and amino acid side-chains in the avidin binding site identified the physical chemical interactions responsible for each of the force maxima in the simulated trajectory. In particular, the energy barriers appeared to be due primarily to the rupture of hydrogen bonds between the biotin and streptavidin in the unbinding trajectory (cf. Fig. 13) (Izrailev *et al*. 1997). Interestingly, site-directed mutations in the streptavidin binding pocket showed that tryptophans, which contribute significantly to the equilibrium binding free energy, do not appear to significantly impact the rupture force (Chilkoti & Stayton, 1995). The different roles played by tyrosine further suggest that there are physical chemical differences between the interactions that contribute to the bond *energy versus* those that determine the bond *strength*. While the single molecule force measurements alone can not identify the chemistry underlying the bond rupture or molecular extensions, the SMD results show that a combination of MD simulations and force probe studies can provide important insights into (1) the potential energy surfaces of noncovalent bonds, and (2) the fundamental chemistry that determines the bond failure and the mechanical properties of biomolecules. Finally, conclusions concerning the likely governing chemistry can be directly tested with site-directed mutagenesis.

While such MD simulations appear to account for the *qualitative* features of single molecule force measurements, there remain substantial technical obstacles to *quantitatively* mapping the potential energy surfaces of intermolecular bonds on the basis of bond rupture data. This is mainly on account of the very different timescales of simulated and experimentally induced bond rupture. The nanosecond timescales used in MD simulations are too fast relative to both intrinsic bond lifetimes and experimentally induced bond rupture rates, which occur on timescales of milliseconds to minutes. In the simulations, extremely large forces are applied very rapidly to overcome all the potential barriers within a few nanoseconds (cf. Fig. 48b). Under these conditions, Balsera *et al*. (1997) showed that the frictional contribution to the rupture force is large relative to the applied load. Moreover, since the frictional term scales roughly with the detachment velocity, the simulations significantly overestimate the experimental values. The simulations are therefore in error with respect to the measurements, by an amount that scales linearly with the irreversible work done during the simulated forced unbinding (Balsera *et al*. 1997). For example, at the AFM pulling rate of 200 pN s^{-1}, the measured streptavidin–biotin bond strength was $\sim$ 300 pN (Chilkoti *et al*. 1995). By contrast, the simulated pull-off force was $\sim$ 450 pN at a loading rate of 10^8 pN s^{-1} (Izrailev *et al*. 1997). This difference is attributed primarily to the large frictional contribution to the simulated rupture force.

Thus, a quantitative link between simulations and force measurements is still missing. Put in another way, the energy landscapes of RL bonds cannot at present be reconstructed

https://doi.org/10.1017/S0033583501003687 Published online by Cambridge University Press

quantitatively from force probe measurements. Some recent theoretical developments suggest that it may be possible to bridge the gap between experiment and theory by constructing the *potential of mean force* (see footnote 1) from the simulated force detachment data (Gullingsrud *et al*. 1999). The latter could then be used to interpret or predict *experimental* force measurements. The potential of mean force for the unbinding path can be computed through a time series analysis of the positions and applied force data obtained from the calculated SMD trajectories. This analysis should quantitatively reflect the free energy surface sampled by the ligand as it is pulled through the binding site. The activation energies thus determined would then correspond to the same values that determine experimentally measured pull off forces.

4.5 Forced extensions of biological macromolecules

In addition to measurements of bond strengths, force probes have also been used to investigate the mechanical properties of biological macromolecules. The main objective of these studies is to determine how the molecular structure and intramolecular bonds determine the mechanical stability of biomaterials at the molecular level. Studies include investigations of protein unfolding, DNA stretching, carbohydrate extension, and chromatin and DNA unraveling (Kellermayer *et al*. 1997; Tskhovrebova *et al*. 1997; Rief *et al*. 1997a, b, 1998, 1999; Carrion-Vazquez *et al*. 1999).

These measurements are typically done by adsorbing a protein or DNA film on a substrate or a small sphere or bead. The probe tip is then pushed into the relatively thick ($\sim$ micron) film, and molecules in the film adhere to the probe. As the tip is pulled from the biomolecular film, the force is measured as a function of the relative displacement of the tip from the surface. Typically the substrates are coated with a high density of molecules in uncontrolled orientations. As a result, the probability of (1) forming multiple adhesive contacts between the two surfaces, (2) attaching polymer segments of different lengths, and (3) pulling at different angles, is high so that the force–distance profiles measured during the pull-off are complicated by these different factors. As a result, most of the force–distance information is impossible to interpret in terms of single molecule mechanics.

However, on rare occasions, a small number of molecules may remain bound. As tension is exerted on those last few molecules, particular signatures are observed in the force–distance profiles suggestive of mechanical deformations of isolated macromolecules. To interpret the force–extension profiles in terms of molecular details of bond rupture and the loss of secondary structure requires subnanometer distance resolution. Force–extension measurements on single molecules have therefore been done with the AFM and OT since these instruments have the requisite distance resolution and force sensitivity.

The force–extension measurements of the muscle protein titin were the first that used force probes to investigate the mechanical response of this highly extensible molecule to an applied force (Kellermayer *et al*. 1997; Rief *et al*. 1997a). Proteins are stabilized by multiple, noncovalent physical interactions, and the disruption of these bonds by either mechanical or chemical means can induce unfolding. Titin is a scaffold for the formation of thick filaments in muscle, and it determines the elasticity of relaxed, striated muscle. The protein structure consists of multiple, tandem repeats of immunoglobulin (Ig)-like and fibronectin type III (Fn3)-like domains. With the AFM and OT, two groups independently measured the

https://doi.org/10.1017/S0033583501003687 Published online by Cambridge University Press

force–extension profiles of this protein. The distinguishing feature in the AFM curves was the sawtooth profile shown in Fig. 49(*c*) (Rief *et al*. 1997a; Fisher, 1999). The regular periodicity of the peaks, which averaged 28 nm, was attributed to the successive unfolding and extension of different domains along the protein backbone, and the peaks were attributed to the activation steps in the unfolding path. The precipitous fall in the force at each peak suggested that each protein domain unfolds cooperatively via a two-state process – that is, from a folded, intact state directly to an unfolded, random coil state, as illustrated in Fig. 49(*b*).

In these, as well as in force–extension measurements with other biopolymers, although one achieves subnanometer distance resolution in the *relative* movement of the probe, the locations of the *ends* of the polymer are not known. As a result, the absolute molecular extension cannot be directly determined. To determine the length of the fully extended, unfolded polymer domains, or the contour length L_c^0, the data were fitted to the worm-like chain (WLC) model of polymer elasticity (Bustamante *et al*. 1994; Rief *et al*. 1997a), shown in Fig. 49(*a*). This WLC model describes the energy penalty associated with straightening a random coil polymer that behaves like an entropic spring. In the case of the putative unfolding of the individual titin domains, based on the known length of the protein backbone within each domain, the distance between successive peaks indicates that the unfolded protein domains can be extended to nearly their full contour length L_c^0. This is manifested by the steeply rising parts of the curves in Fig. 49 (Rief *et al*. 1997a, 1998; Carrion-Vazquez *et al*. 1999; Fisher *et al*. 1999). The peaks in the curves are attributed to the disruption of an additional Ig domain, so that the contour length increases by L_c^1. The difference $L_c^1 - L_c^0$ should correspond to $L_c = Na$ where N is the number of amino acids per domain multiplied by the peptide bond length a. However, because high forces are required to fully stretch the chains, other domains unfold before the former occurs. For example, at a separation rate of 1 μm s^{-1}, the peaks in the profile occur at forces of 150–300 pN (Rief *et al*. 1997a), which is comparable to the measured streptavidin–biotin bond strength (Lee *et al*. 1994; Moy *et al*. 1994). Much higher forces would be required to fully stretch the coils. Thus, fits of the force extension profiles to the WLC model (Fig. 49(*c*), thin solid lines) give the contour length. In these fits, the two adjustable parameters are the persistence length, which corresponds to the length of the peptide bond, and L_c. Importantly, L_c only counts the load-bearing amino acids, since they are the only ones that contribute to the restoring force, i.e. the elasticity. In the titin stretching experiments, the increase in the contour lengths due to the unfolding of Ig-type domains was $L = 28{\cdot}7 \pm 0{\cdot}2$ nm (Carrion-Vazquez *et al*. 1999), and the persistence length was 0·4 nm (Rief *et al*. 1997a). The former compares reasonably well with the calculated length of 30 nm, based on the length of the peptide bond (0·4 nm) and number of monomers per Ig domain.

The force–extension profiles do not always conform to the WLC profiles, but the deviations can provide insights into the underlying chemistry of the polymer. For example, in Fig. 49, the amplitudes of successive peaks in the titin profiles increase. This suggests that (1) the Ig domains of titin are heterogeneous, and (2) the weakest domains unfold first. Measurements with engineered proteins, which contained either identical, tandemly repeated domains or multiple repeats of two different domain types exhibited only one and two peak heights, respectively (Carrion-Vazquez *et al*. 1999). Similarly, altering the lengths of the polypeptide linkers between successive Ig domains of engineered polyproteins with five glycines altered the fitted contour lengths by 2 nm, which agrees with the predicted increase

https://doi.org/10.1017/S0033583501003687 Published online by Cambridge University Press

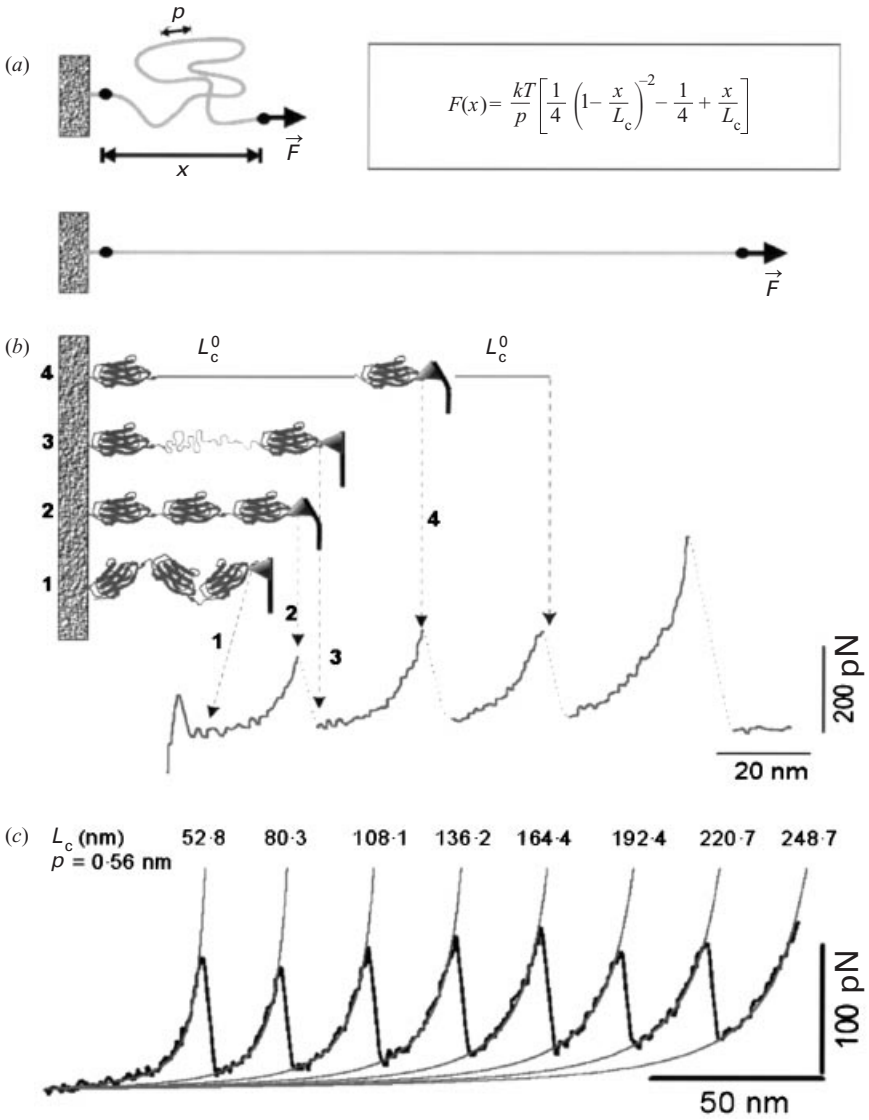


Fig. 49. Force-induced protein unfolding. Panel (*a*) shows the forced extension of a structureless polymer coil. The equation for the force–extension curve, based on the WLC model (Bustamante *et al*. 1994) is on the right. Panel (*b*) shows the measured force–extension profile and the corresponding changes in the protein structure that generate the different features in the curves. Panel (*c*) shows the fits of the WLC model to the regions of the force–extension curves between the force maxima. In these regimes, the extension of the unfolded protein initially follows that of an elastic material. The spacing between successive peaks is roughly constant with a mean value of 28–29 nm, which appears to exclude other possible detachment mechanisms such as 'tack' – the breaking of multiple laterally separated strings – described in Section 4.2. (Adapted from figure 2 in Fisher *et al*. 1999.)

in the extended polypeptide length (Carrion-Vazquez *et al*. 1999). It is interesting that, in the case of tandem repeats of identical Ig-type domains, the molecular extensions between peaks are fairly uniform. One also expects to see stochastic variations in the unfolding force, as has been observed in bond rupture measurements. In addition, with multiple bonds in series (cf.

https://doi.org/10.1017/S0033583501003687 Published online by Cambridge University Press

Section 4.6), there is a finite probability that two domains could fail simultaneously, and thereby double the change in the contour length. The latter has not been observed in any reports to date.

Stretching measurements have also been done with other biological polymers such as DNA, chromatin and polysaccharides (Rief *et al*. 1997a; Baumann *et al*. 2000; Claussen-Schaumann *et al*. 2000; Katrich *et al*. 2000). In an AFM study of the extension of dextran, which was covalently bound to a modified gold surface, deviations in the force–extension profiles from the WLC model at high forces were attributed to the conversion between the shorter chair conformation of the sugar rings to the more extended boat conformation (Rief *et al*. 1997a). Similarly, changes in DNA force–extension curves under different salt concentrations and nucleic acid compositions have been interpreted in terms of salt-induced changes in free energies of double-helix melting and base pairing (Baumann *et al*. 2000; Claussen-Schaumann *et al*. 2000).

In the case of the titin extension studies, the unambiguous determination of the physical chemistry underlying the observed features in the force–extension profiles of proteins required a combination of site-directed mutagenesis and theoretical modeling (Marszalek *et al*. 1999). SMD simulations of forced protein unfolding suggested that the peaks in the sawtooth profiles of stretched titin are due to the force needed to rupture hydrogen bonds between two antiparallel strands of the beta sheet of the Ig-domains (Lu *et al*. 1998). In addition to the WLC-like force–extension profiles, in some cases, the domain unfolding traces also exhibit a small hump just before the primary unfolding event. The SMD simulations suggested that the small hump peak is due to the rupture of a small cluster of hydrogen bonds that in turn results in a small 6 Å extension of the protein prior to the main unfolding event. The disruption of these bonds by site-directed mutagenesis abolished the small hump, and shifted the protein extension corresponding to the primary unfolding event further out by 15 Å (Marszalek *et al*. 1999).

Despite the agreement between AFM measurements and simulations, which occur on fast timescales, not all force–extension measurements of identical molecules yield identical profiles. As discussed in Section 1.10, the force measurements should depend on the unfolding kinetics relative to the extension rate. The differences between the titin force–extension profiles obtained with the AFM and with OT indicated that the qualitative features of the force–extension profiles depend on both the unfolding chemistry and the dynamic response of the instrument (Kellermayer *et al*. 1997; Rief *et al*. 1997a). Whereas the AFM curves displayed a sequence of periodically spaced peaks (Rief *et al*. 1997a), one set of OT data exhibited a broad, extensible region that was attributed to titin unfolding (Kellermayer *et al*. 1997). Evans & Ritchie (1999), using a similar analysis to their description of bond rupture dynamics (Evans & Ritchie, 1997), rationalized these observations in terms of the relative rates of titin domain unfolding and the different pulling rates used in the two studies. In other words, the rate of pulling in the OT measurements (Kellermayer *et al*. 1997) were slow relative to the intrinsic unfolding rate of the Ig domains so that discrete domain unfolding events were not as distinct as in the AFM measurements, which were done at much faster loading rates (Rief *et al*. 1997a). In agreement with this interpretation, a second OT study of titin stretching, done at more rapid extension rates, also exhibited the sawtooth pattern seen in the AFM studies (Tskhovrebova *et al*. 1997). The qualitatively similar features in the AFM traces and in the MD simulations presumably arise because the unfolding is conducted at timescales that are much faster than the intrinsic unfolding rates.

https://doi.org/10.1017/S0033583501003687 Published online by Cambridge University Press

Dynamic force measurements have also been used to investigate the transition states that determine the force required to extend and separate double-stranded DNA. Dynamic AFM measurements (Strunz *et al*. 1999) showed that the force F *versus* ln R_F curve is actually a straight line with a single slope, and hence a single energy barrier. By varying the DNA length, they found that both the apparent distance of the energy barrier from the minimum in the potential r_0 and the logarithm of the DNA dissociation rate were proportional to the number of base pairs. These data suggest that a single activation barrier governs DNA denaturation, but that the apparent displacement r_0 of the activation barrier depends on the polymer length. However, as we discuss in the Section 4.6, the correspondence between denaturation pathways induced by pulling *versus* temperature is by no mean straightforward (as was discussed in Section 4.3, the reaction coordinate defined on the basis of a length r_0 having a definite direction may differ in important ways from a reaction profile based on an order parameter that is linked to the 3D free-energy landscape of the complex).

4.6 Force-induced *versus* thermally induced chemical transformations

An assumption, which is either implied or stated directly regarding measurements of force-induced chemical transformations, is that the energy landscape sampled in force measurements is the same as that probed under different experimental conditions, e.g. in equilibrium in solution at different temperatures. Along this line of reasoning, it is assumed that force or length is an appropriate parameter by which to characterize the actual reaction coordinate or free energy surface for force-induced changes such as bond rupture or protein unfolding. For example, do the same activation barriers that determine the force maxima in bond rupture experiments also determine the rates of spontaneous bond dissociation and association in solution? We already saw in Section 1.10 that the rupture of a multiply bonded junction when a force is applied may be different from the spontaneous dissociation of the junction – the former is determined by the path of least *force*, the latter by the path of lowest *energy*.

Socci *et al*. (1999) first addressed this issue with respect to force-induced protein unfolding and its relationship to the energy landscapes that dictate protein folding and unfolding in solution. They suggested that it is misleading to assume that the force-induced protein extension is a direct map of the reaction coordinate for unfolding since applying a mechanical force to a protein alters the energy landscape that controls protein unfolding in a different way than, for example, denaturants or temperature. Socci *et al*. (1999) proposed that protein folding (unfolding) proceeds down (up) an energy funnel, characterized by a multidimensional (rather than 1D) energy surface, such as shown in Fig. 50. Parameters such as temperature are scalars, and are rotationally invariant. As a result, they do not intrinsically bias any of the potential routes out of the funnel in Fig. 50. Because force is a vector, the application of a mechanical force along a certain direction polarizes the molecule in an unnatural way (Socci *et al*. 1999). It can thereby bias the unfolding trajectory, so that a reaction coordinate determined from changes in the geometric length of the molecule would in fact differ from that defined by an order parameter related to the native 3D structure.

Using a lattice simulation, Socci *et al*. (1999) tested these ideas by comparing the simulated unfolding reaction coordinate of a stressed chain with that of an unstressed polymer. In the former case, they calculated the free energy of the chain as a function of the molecular extension. Their results showed that stretching the protein by pulling on its ends initially shifts the activation barrier towards a slightly more compact state, which precedes the major

https://doi.org/10.1017/S0033583501003687 Published online by Cambridge University Press

unfolding event. In the lattice model simulations of the unfolding of the unstressed chain, they similarly observed that a small shift to a more compact state preceded the unfolding transition. These findings suggested that the two unfolding pathways may follow similar trajectories. However, on account of the vectorial nature of the perturbation (force), it is also reasonable to expect that the similarities between the unfolding transitions will depend on the direction of the applied force with respect to the protein axes. In the simulations, the protein was pulled from the ends. Pulling the protein along different axes from different positions in the backbone should generate different reaction coordinates, which may or may not correlate with the reaction path(s) adopted under unstressed conditions.

MD simulations of the stretching of all β-sheet and all α-helix proteins confirmed that applied forces may indeed bias the unfolding pathway to favor different intermediate states than those that occur in solution (Paci & Karplus, 2000). Simulations of the unfolding of spectrin (all α-helix) and Ig domains (all β-sheet) used temperature and applied force to induce structural changes in the peptides. Proteins unfolded by each of these perturbations exhibited significant differences in the unfolding intermediates and in their final unfolded configurations. In addition, the energies of the unfolded states were much higher in the forced unfolding simulations than in simulations of thermal denaturation (Paci & Karplus, 2000). For example, in the case of thermal denaturation, the final protein adopts a random coil, whereas, in the case of force-induced unfolding, the protein is extended. Both these simulations and those of Socci *et al*. (1999) therefore show clearly that any interpretation of forced protein stretching in terms of the native energy landscape that control unfolding in solution must be done with caution.

The biological relevance of some of these experiments also needs to be taken into account. In some cases, these molecular stretching measurements do measure molecular extensions in a biologically relevant manner. For example, during the extension and contraction of muscle fibers, titin is pulled and released from the ends as in the AFM measurements (Rief *et al*. 1997a, 1998). Similarly, spectrin provides a mechanical scaffold for the cell membrane, and may experience tension along the axes of the α helices in response to membrane deformations similar to those exerted in AFM studies (Rief *et al*. 1999). However, in other cases, biological macromolecules may never be stressed in this way *in vivo*. Thus, the forced extension measurements should be interpreted cautiously, and considered within the functional context of the protein or macromolecule under investigation.

A recent study (Carrion-Vazquez *et al*. 1999) provided promising evidence that, in some cases, forced unfolding favors similar pathways as induced by other methods. To do this, they took advantage of the dependence of bond rupture kinetics on loading rates, and then compared force curves obtained at different pulling rates with MC simulations of force–induced unfolding. They then determined the unfolding rate as a function of pulling velocity, and extrapolated the values to zero velocity. The quantitative agreement between the unfolding rate thus determined and the measured unfolding rate in solution strongly suggests that the activation barriers for both processes are the same for the Ig polyproteins used in their study.

4.7 The rupture of bonds in series and in parallel

In general, adhesive interactions in biological systems do not involve single bonds. They almost always involve multiple 'elemental' interactions, which exhibit different individual

https://doi.org/10.1017/S0033583501003687 Published online by Cambridge University Press

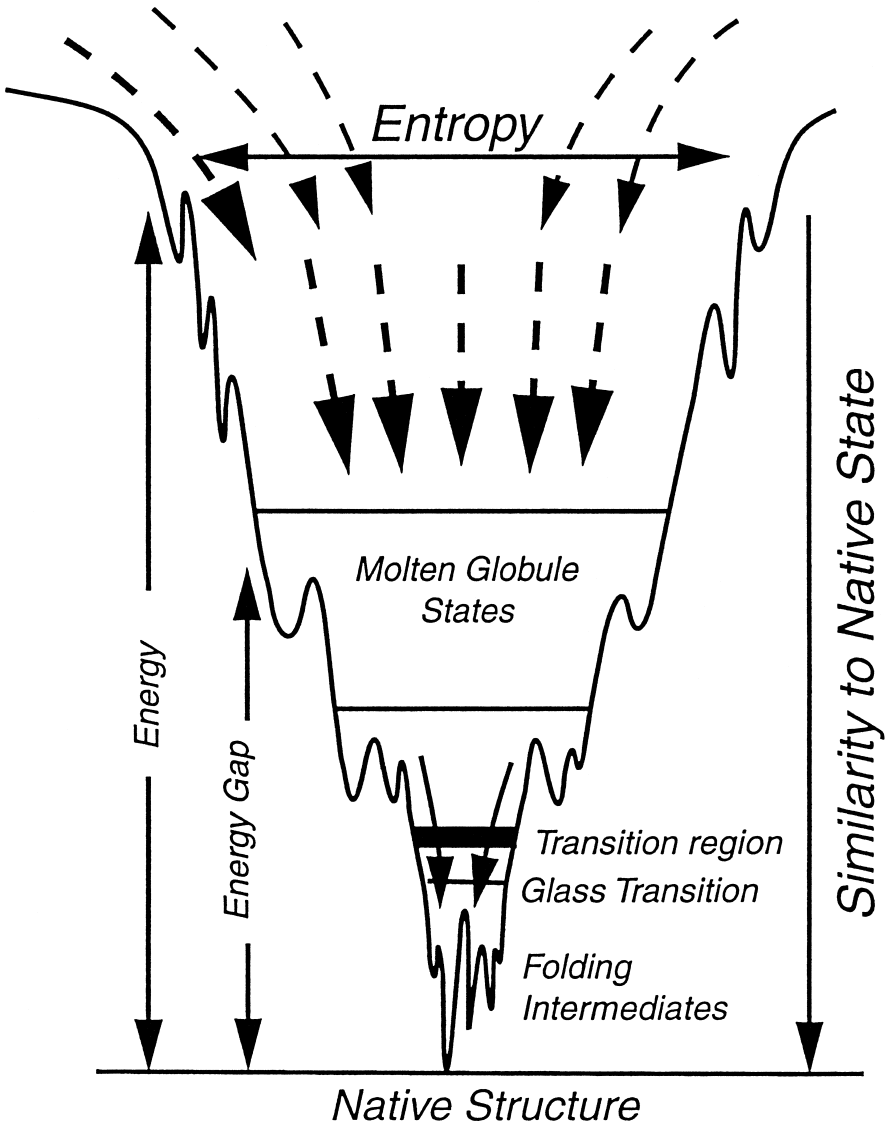


Fig. 50. Schematic of the energy landscape for protein folding, showing a cross section of the 3D energy surface through which the protein structure is funneled from a random coil configuration to the folded state. The latter is characterized by the energy minimum. This picture of protein folding does not involve any preferred pathway, so that the precise energy surface down which the protein structure is funneled (in space and time) will vary depending on the starting position, the temperature, and on random thermal fluctuations during the folding process. However, the final state will be the same in all cases. (Adapted from Onuchic *et al*. 1995.)

bond energies and kinetics. Here we will discuss two different scenarios: namely, multiple bonds in series and multiple bonds in parallel. As an example of multiple bonds in series, many cell–cell linkages involve, in addition to the RL bond, transmembrane segments and attachments to the cytoskeleton. If both receptor and ligand are transmembrane, cytoskeletally bound proteins, then the entire intercellular chain would involve five links in series. Each of these would be a potential candidate for rupture when the system or junction is subjected to

https://doi.org/10.1017/S0033583501003687 Published online by Cambridge University Press

a pulling force. On the other hand, sites of adhesion between extended surfaces such as cell membranes are generally held together by many bonds in parallel. The different bonds can further have different bond energies and exhibit different binding and unbinding rates. In each case, both the parameters that determine the bond strengths and the dynamics of the failure of the adhesive junction will differ from those observed in single bond measurements.

4.7.1 Bonds in series

Consider the case where a chain of N bonds in series links two adhering cells. Probabilistic arguments predict that, when pulled, the strength of the chain will be less than any of the individual links (Saterbak & Lauffenburger, 1996). The argument for this is that, if the probability that the nth bond remains intact after a certain time is X_n (where $X_n < 1$), then the probability that all bonds will exist simultaneously is the product of their individual probabilities, $X_1X_2X_3 \ldots X_N$. This is lower than any of the X_n values. Thus, the overall likelihood of simultaneous binding, and hence the apparent strength of the intact cross-bridge, will be less than that of any of the individual bonds, including the weakest.

This hypothesis was confirmed by SFD assays (Saterbak & Lauffenburger, 1996). The shear assays were used to determine the strength of linkages formed between two different immobilized antibodies joined by a common antigen. One antibody (A) was immobilized on beads and the other (B) was bound to a flat substrate. Antibody A and antibody B were cross-linked by a mutual antigen, which bound to each of the two antibodies with different affinities K_A and K_B. Thus, each bead–surface cross-bridge comprised two low affinity antibody–antigen bonds in series. In agreement with the predicted behavior, they found that the average cross-bridge rupture force was 2–10 times smaller than the strength of the weakest bond in the chain.

In contrast to a stressed chain, for an intact chain that is free (unstressed) in solution, we expect the *energetically* weakest individual bond – that is, the one with the lowest activation energy E_{act} and fastest dissociation rate – to break first, and to thereby determine the 'effective strength' of the chain. Accordingly, one would expect that, with increasing stress, the strength of the chain will go from being determined by the links with the lowest energy to those with the lowest tensile strength.

Surface force measurements were used to test the physical parameters that determine how bonds in series fail (Leckband *et al*. 1995b). The SFA experiments measured the strength of the adhesion forces, and identified the failure mechanism upon separation of two lipid bilayers linked by streptavidin–biotin bonds. In this study, two membranes containing biotin–lipid conjugates were cross-linked by streptavidin. Since streptavidin is twofold symmetric, each side of the protein bound two biotins on each of the opposed membranes (cf. Fig. 33, inset). In this system, when the membranes are separated, adhesive failure can occur either at the streptavidin–biotin bonds on either side of the protein or via lipid pull-out from the membranes (Fig. 51(*d*, *e*)). The SFA measurements done with a series of biotin analogues with different streptavidin affinities showed that the bond with the lowest rupture *force*, estimated from $\Delta G/r_0$, failed first. The force–extension curves of titin suggest similarly that the domains unravel in the order of increasing unfolding force.

This hierarchy of effective bond strengths depends on the relative activation energies of the two bonds, their effective bond lengths and, as discussed in Section 1.10, how fast the chain is pulled. At very slow pulling rates, bond dissociation is thermally activated, so that the bond

https://doi.org/10.1017/S0033583501003687 Published online by Cambridge University Press

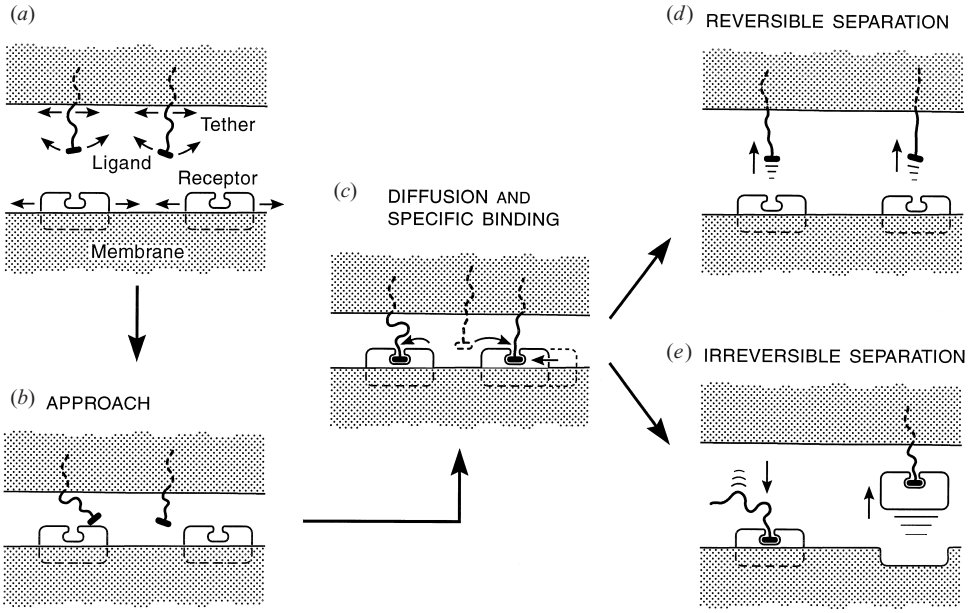


Fig. 51. Effect of temperature and approach/separation rates on binding and unbinding mechanisms of two adhering membranes exposing mobile ligand and receptor groups. A surface with flexible ligands approaches a surface with receptors (*a*). Upon approach, the bulky ligands may initially bump into the receptor surfaces (*b*), but lateral mobility allows the ligand and receptor to bind after a certain period of time (*c*). Upon separation, bond rupture can occur at either the LR bond (*d*) or the lipid–membrane or the protein–membrane attachment sites, depending on the relative values of the LR bond energies and bond lengths. Both the force profile measured during approach ($a \rightarrow c$) and the mode of detachment are influenced by the tether length, the temperature, the fluidity of the membrane lipids, and the detachment rate.

with the lowest activation energy E_{act} in the series will break first. On the other hand, at rapid pulling rates, the bond with the smallest rupture force $F \sim -E_{\mathrm{act}}/r_0$ will fail first. Recall that the slope of the F *versus* $\ln R_{\mathrm{F}}$ curve is kT/r_0. If the slopes for two bonds in series differ, then the force *versus* loading rate curves will cross (Fig. 52) at a pulling force given by Evans (1999)

$$f_{\otimes} \approx \frac{\Delta E_{\mathrm{act}} + kT \ln(r_{01}/r_{02})}{\Delta r_0}. \tag{52}$$

Here, $\Delta E_{\mathrm{act}} = E_{\mathrm{act},2} - E_{\mathrm{act},1}$ and $\Delta r_0 = (r_{02} - r_{01})$ are the differences in the activation energies and bond lengths, r_{01} and r_{02}, along their unbinding paths, respectively. This is best illustrated graphically (Fig. 52). To the left of the crossover point, the upper curve (higher rupture force) corresponds to the 'stronger bond' and the lower curve to the 'weaker bond' with the lowest activation energy. To the right of the crossover point, the hierarchy is reversed: the supposedly stronger bond becomes the weakest, and the 'weaker bond' exhibits the higher rupture force.

The data in Fig. 52 were acquired with P-selectin (PSGL-1), which is membrane-anchored via a lipid tail, and sialyl Lewis$^{\mathrm{x}}$ on the surface of neutrophils. The activation energy E_{act} for selectin–carbohydrate bond rupture is lower than that for lipid pull-out ($\sim 30kT$). Thus, at low loading rates, where bond rupture is largely thermally activated, the selectin bond (lower

https://doi.org/10.1017/S0033583501003687 Published online by Cambridge University Press

curve) breaks easily and appears to have no strength relative to the lipid 'bond' (upper curve). However, the effective length of the lipid–membrane bond r_{0L} ($\sim$ 1·4 nm) is larger than that of the selectin bond r_{0S} ($\sim$ 0·5–1 nm) so that, in the dynamic BFP measurements, the slope of the *F versus* ln R_F curve for lipid pull-out was shallower than that for the rupture of the selectin bond. From the slope of the *F versus* ln R_F curve for the extraction of di-stearoyl phosphatidyl ethanolamine (DSPE) from a stearoyl oleoyl phosphatidyl choline (SOPC) membrane, r_{0L} was found to be $\sim$ 1·2 nm. By contrast, there were three slopes in the *F versus* ln R_F curve for the selectin bond rupture, and these mapped to putative energy barriers at $\sim$ 0·06, 0·3, and 1·2 nm (Evans, 1999). At pulling rates > 100 pN s^{-1}, the crossover point, the selectin bond becomes stronger, since the bond rupture *forces* dictate the relative bond strengths. Now the shorter selectin bond is stronger than the longer lipid–membrane 'bond' . If we now reconsider the similar streptavidin–biotin lipid rupture measurements done with the SFA (Leckband *et al*. 1995b), a comparison of the curve for lipid anchor pull-out with that of streptavidin–biotin bond rupture suggests that the effective loading rates in the surface force measurements were > 200 pN s^{-1}.

The dynamic force measurements therefore confirm that the apparent hierarchy of the strengths of bonds in series will depend on the activation energies for unbinding, the bond lengths, and the loading velocity. This can have interesting consequences for adhesion and detachment in biological systems. Cell–cell adhesion junctions, for example, are often not mediated by single RL interactions, but by several different proteins and ligands. This heterogeneity may provide the flexibility that cells and tissues require in order to respond to a variety of locally and globally exerted forces over the lifetime of the organism. Receptors with low affinities and fast dissociation rates may have evolved to withstand slowly increasing forces, but other proteins may form linkages that are better suited for resisting, for example, abrupt impact. The importance of these different molecules in cell adhesion will, however, depend on the dynamics of the particular force stimulus, which, in a biological context, could be generated by flow, kinesin locomotion, cytoskeletal pressure, the action of chaperone proteins, ion binding, lateral phase separation, or some long-range force.

4.7.2 Bonds in parallel

When multiple bonds act in parallel to mediate adhesion between extended surfaces such as occurs in cell–cell adhesion, the parameters that determine how the membranes interact differ from single bond behavior in many important ways. The rupture of a chain occurs when the first link is broken, whereas the rupture of an adhesive junction comprising many links in parallel occurs when the last link is broken. The rupture of such junctions is further complicated by the fact that individual bonds in parallel can reform after they break, i.e. before the whole junction detaches. The analysis of Evans & Ritchie (1997) did not allow for such rebinding to occur, but theoretical considerations and simulations (Vijayendran *et al*. 1998; Seifert, 2000) have shown that when parallel cross-bridges are involved, although some bonds may break, the surfaces remain pinned by the unbroken neighboring cross-bridges. This allows the detached bonds to reform.

A second difference is the larger adhesion energy and longer lifetime of a multiply bonded junction (compared to a chain having the same number of links). Because adhesion between extended surfaces is determined by the dynamic equilibrium of multiple bonds, surface detachment is not determined by a single kinetic event – that is, single bond dissociation. We

https://doi.org/10.1017/S0033583501003687 Published online by Cambridge University Press

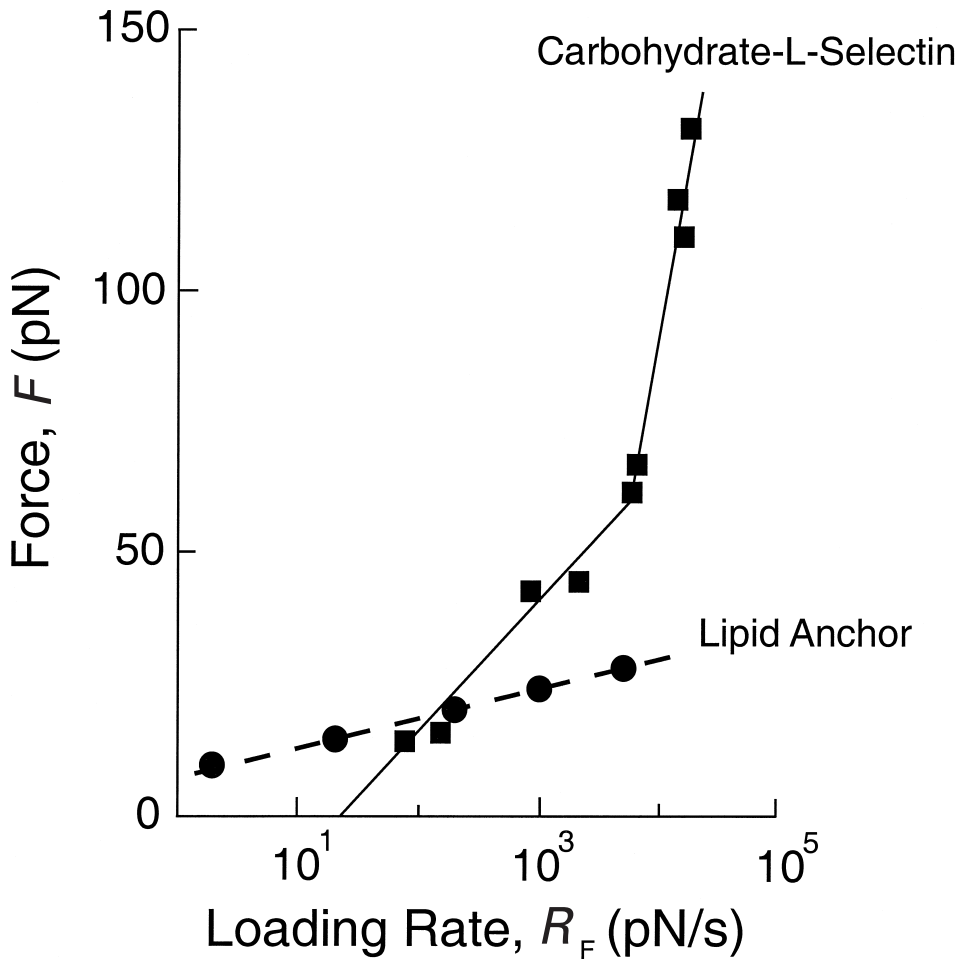


Fig. 52. Force *versus* loading rate curves for selectin–carbohydrate and lipid–membrane bonds. The force to break selectin–carbohydrate bonds and the force to pull lipids out of a membrane were both measured with the BFP as a function of the pulling rate R_F. The differences in the two slopes differ on account of the different bond lengths r_0 in each case. The positions at which each of the curves cross the R_F axis also differ by an amount that is proportional to the difference in the magnitude of the activation energies. The two curves cross each other at a force defined by Eq. (52). When the bonds are in series, the selectin bond of lower activation energy will fail first at low loading rates (below the crossover point). At higher pulling rates, the lipid becomes the weakest link and fails first. (Adapted from Evans, 1999.)

therefore anticipate that the relevant energy scale that determines the intersurface adhesion will also differ from, and greatly exceed that of, single bond behavior. When macroscopic surfaces are pulled apart slowly on the timescale of the relaxation time of the interacting materials, the work of adhesion should scale with the depth of the interaction potential or the surface energy per unit area γ_i (Israelachvili, 1991) rather than with the activation energy for unbinding E_{act}. This is because two surfaces generally separate by peeling (i.e. curving away from each other) along a line or circle rather than as two flat surfaces.[67] For biological

[67] That the adhesion force between two surfaces arises from their peeling apart at their common boundary is an underlying assumption in the JKR theory, described in Section 2.5 and assumed in almost all adhesion force measurements.

https://doi.org/10.1017/S0033583501003687 Published online by Cambridge University Press

surfaces, especially when mobile surface receptor and ligand groups are involved that preclude a simple definition for γ_i, this much more complicated scenario has only been studied with simple theoretical models (Vijayendran *et al*. 1998; Seifert, 2000), and has not been systematically addressed by experiments. As a result, these issues have yet to be resolved.

Vijayendran *et al*. (1998) used the adhesive dynamics algorithm to simulate the adhesion between receptor-linked surfaces in surface force measurements. At equilibrium, the *average* bond strength is less than that of the isolated cross-bridges because of the equilibrium distribution of bound and free states between the surfaces. This means that the behavior of multiple bonds in parallel cannot be simply extrapolated from single bond measurements. An ensemble of bonds is in dynamic equilibrium, so that dynamic breakage and reformation also occurs during detachment. As a result, the time-averaged tension on each linkage during the junction rupture approaches the critical rupture force of the individual bonds. The probability of rebinding depends on the surface detachment rate relative to the binding kinetics, so that the adhesion will depend on the surface separation rate. Thus, with multiple contacts in parallel, the strength of an adhesion junction depends on the bond dissociation rates, the pulling rates, *and* the association kinetics.

Other proteins such as fibronectin may bind more than one ligand simultaneously, or have multiple binding sites for a unique ligand. Additionally, most cell adhesion molecules have large, multidomain extracellular regions, and some exhibit multiple contacts with their corresponding ligands. While multiple interactions may contribute to binding, their implications for protein-mediated adhesion have not been explored.

A recent study identified one possible consequence of multiple, sequential interactions. The extracellular domain of an adhesion protein cadherin comprises five homologous domains in tandem. Cadherin binds to identical proteins on opposing cell surfaces. Using the surface force apparatus, Sivasankar *et al*. (1999, 2001) found that cadherin extracellular domains bind in at least three antiparallel configurations (Fig. 53). By controlling the distance between two cadherin monolayers, they identified three discrete sequential protein separations at which the proteins adhere. The force–distance profile generated during protein detachment suggests that the sequential rupture of these bonds may hinder the abrupt failure of cadherin junctions under a force.

4.8 Dynamic interactions between membrane surfaces

As already discussed and now illustrated schematically in Fig. 51, both the adhesion and detachment of biological surfaces can occur via a number of different mechanisms or 'pathways' that depend not only on the nature of the elemental bonds (whether specific or non-specific, in series or in parallel), but also on the temperature, the fluidity and deformability of the supporting membrane or surface, the approach and separation rate, and other factors that can arise in biological (but not always in laboratory) situations.

4.8.1 Lateral mobility on membrane surfaces

The fluidity of biological surfaces allows for lateral rearrangements of proteins and lipids on membrane surfaces that can alter the local composition and in turn change the intersurface forces over time. In some cases, active processes in the cell may drive receptors to accumulate

https://doi.org/10.1017/S0033583501003687 Published online by Cambridge University Press

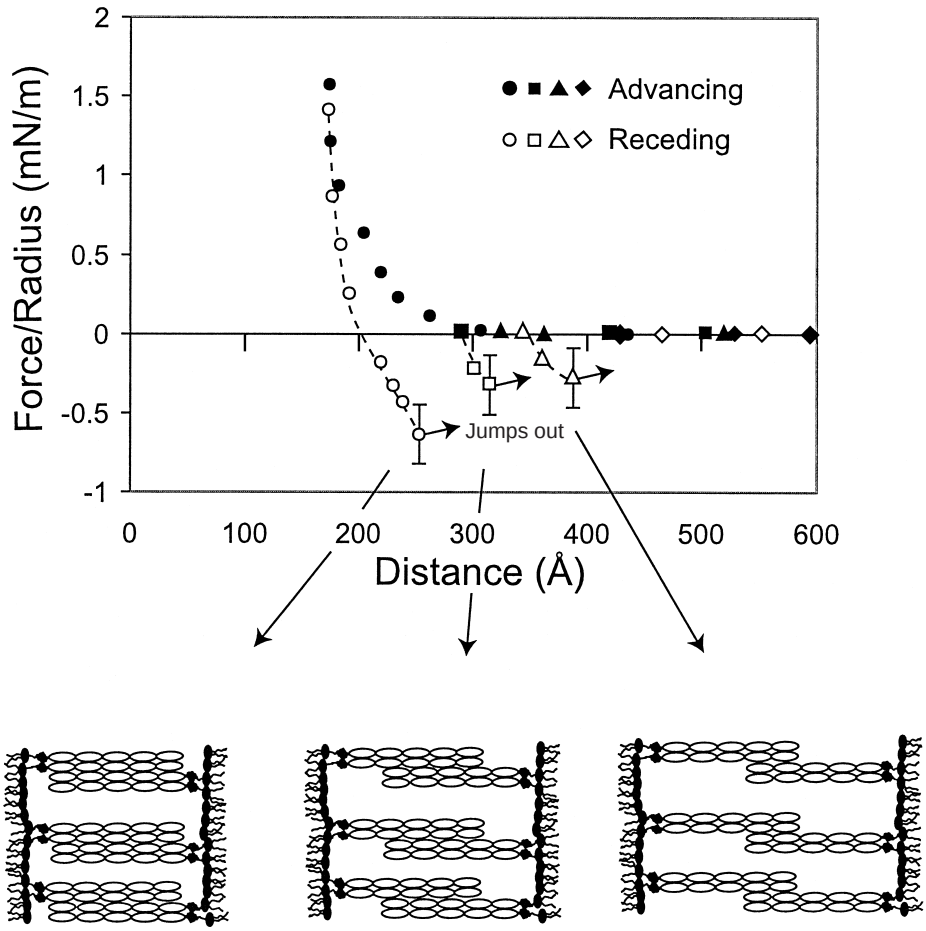


Fig. 53. Energy-distance profile for the interaction between identical cadherin extracellular domains. The proteins bind in three different alignments, which are indicated by the three force minima. The strongest bond is between the fully interdigitated protein monolayers at 250 Å, and there are two additional bonds that form at 320 Å and 400 Å. Once the first bond fails, the proteins are caught in the second and third minima as the proteins slide past each other. Video recordings of the time-dependent motion of the interference fringes were used to quantify the detachment velocity as a function of D. These measurements demonstrated that the additional attractive minima slow the detachment of the cadherin monolayers. (Reproduced with permission from Sivasankar *et al*. 2001.)

at specific membrane sites. For example, the clustering of weakly binding adhesion molecules at contacts between T-cells and target cells collectively generate the 'immunological' synapse shown in Fig. 54. In this case, individual proteins randomly dispersed over the membranes do not bind molecules on the opposing cell sufficiently strongly to aggregate the cells. However, upon formation of an initially weak adhesive contact, laterally mobile receptors diffuse into the contact zone, bind to their complements on the opposite cell, and accumulate in the contact zone. This forms an adhesion junction that is strong enough to maintain cell–cell contact for a sufficient period to trigger an immune response.

Such dynamic changes, which result in adhesion strengthening, are well known in biology, and several approaches have been used to study the effects of active and passive dynamic

https://doi.org/10.1017/S0033583501003687 Published online by Cambridge University Press

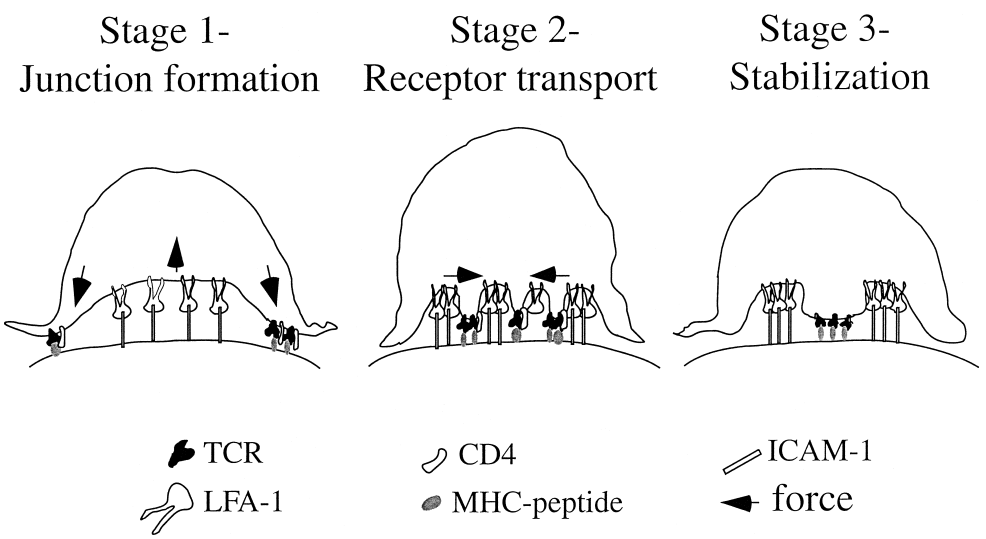


Fig. 54. Adhesion strengthening at cell–cell junctions due to the lateral diffusion of cell surface adhesion molecules in membranes. The adhesion between T-cells and target cells involve a sequence of steps involving the accumulation of adhesion receptors and intercellular bonds at the adhesive junction. Stage 1 involves the initial junction formation, which is mediated by the formation of a sparse number of bonds between the surfaces. In Stage 2, stresses within the contact region convect the receptors into local clusters. These may segregate according to the sizes and bond lengths between the membranes. In the final Stage 3, receptor clustering and segregation is complete, and this results in a substantially stronger, more stable adhesive junction than at Stage 1. (Adapted from Grakoui *et al*. 1999.)

changes on cell adhesion. Because these changes involve the collective reorganization of many species, single molecule measurements are not informative. For this reason, the BFP, SFD, SFA and RICM techniques are more suited for investigating the interactions between extended surfaces such as cell membranes or biomaterials.

The redistribution of receptors at cell junctions in response to stresses in the contact region was shown by (Evans *et al*. 1992), who used the earlier version of the BFP – the MPA technique. Fluorescently labeled lectins were used to cross-link red blood cells. They observed, after membrane separation, that the receptors within the contact region had been convected to the perimeter of the region where the tensile forces on the bonds were greatest.

Both receptors and ligands outside the contact region can diffuse to and accumulate at an adhesion site. In some cases active, i.e. energy-requiring, processes in the cell may drive receptor accumulation. However, MPA studies with fluorescently labeled streptavidin- and biotin-coated giant vesicles demonstrated that this can also occur via passive processes (Noppl-Simson & Needham, 1996). Fluorescence images of the vesicle–vesicle contact region showed that streptavidin rapidly accumulates at the vesicle junction. The latter occurred by natural diffusion without the input of energy as the system evolved toward the equilibrium distribution between bound ligands and receptors in the contact zone and free species outside the region.

To demonstrate the influence of lateral diffusion on receptor-mediated adhesion, Leckband *et al*. (1994) used the SFA to measure directly the streptavidin-mediated adhesion between biotin–lipid-containing membranes. The membrane fluidity, and hence the lateral biotin

https://doi.org/10.1017/S0033583501003687 Published online by Cambridge University Press

(ligand) mobility, was controlled by raising or lowering the experimental temperature above or below the chain melting temperature T_m of the membrane lipids. When the streptavidin- and biotin-coated membranes were initially brought into contact, on account of the statistical distribution of receptors and ligands on both surfaces, not all of the protein binding sites and ligands were initially in register. At 25 °C ($T < T_m$) the free molecules could not diffuse to their binding partners on the opposite surface, so that the number of bonds formed was low. The measured adhesion force F/R was only 4 mN m^{-1}, which corresponds to $E_0 = F/2\pi R \approx 0{\cdot}6$ mJ m^{-2} (Fig. 55(*b*)). In contrast, when the temperature was increased above T_m, the molecules could diffuse laterally on the fluid membranes and bind to their corresponding cognate receptor on the opposite surface. Under the latter conditions, the measured adhesion force F/R increased by an order of magnitude to 36 mN m^{-1}, which corresponds to $E_0 = F/2\pi R \approx 6$ mJ m^{-2}.

Using RICM, Albersdörfor *et al.* (1997) followed time-dependent changes in the adhesion sites between biotin-decorated giant vesicles and streptavidin on supported lipid bilayers. The vesicles also contained lipid–PEO conjugates to mimic the repulsive intermembrane interactions due to the glycocalyx. Changes in the membrane height profile away from the substrate revealed regions of strong adhesive contact. Measurements of the sizes of these pinning sites showed that they continued to grow in size as streptavidin and biotin accumulated in the existing contacts. Polymer lipids with bulky PEO headgroups were, however, gradually squeezed out of the tight adhesive junctions into segregated domains or 'blisters'. In the latter domains, the polymer–surface repulsion forced the membrane surfaces apart. Although this was a model system, these measurements nicely demonstrate how attractive and repulsive forces between different membrane components that can diffuse in the plane of the membrane can produce laterally segregated domains that have different normal and lateral forces (with potentially different properties and functions).

4.8.2 Intersurface forces depend on the rate of approach and separation

Not only do the forces between membranes vary due to the dynamics of lateral molecular rearrangements on the surfaces, but they also depend on the rate of intersurface approach and separation relative to the various relaxation times of the molecules or tethered ligands mediating the interactions (cf. arrows in Fig. 51(*a*)). The dependence of intersurface forces on the rate of approach was demonstrated by SFA measurements of interactions between streptavidin monolayers and biotin–lipid membranes (Fig. 55). As discussed above, the streptavidin binding pockets and biotins are not initially in register on two opposed membranes, but they will diffuse to their binding partners if the membrane is fluid. However, if the membranes are brought into contact faster than the biotin ligands can diffuse to a receptor site on the opposite surface, then the biotins will simply collide with the streptavidin surface rather than lock into a binding site. This results in an initial short-range steric repulsion as shown in the inset in Fig. 55(*a*). If the ligands are free to diffuse, i.e. if $T > T_m$, then they will eventually find a binding site, and the repulsive force will collapse as the receptors and ligands bind. The time for this may be less than a microsecond to many seconds, depending on the fluidity or diffusivity of the species and on the surface density of receptors and ligands (as well as on the tether length, discussed below). On the other hand, if the membranes are brought into contact sufficiently slowly, the molecules have time to align and no repulsive steric barrier is observed. The surfaces then come smoothly into adhesive contact

https://doi.org/10.1017/S0033583501003687 Published online by Cambridge University Press

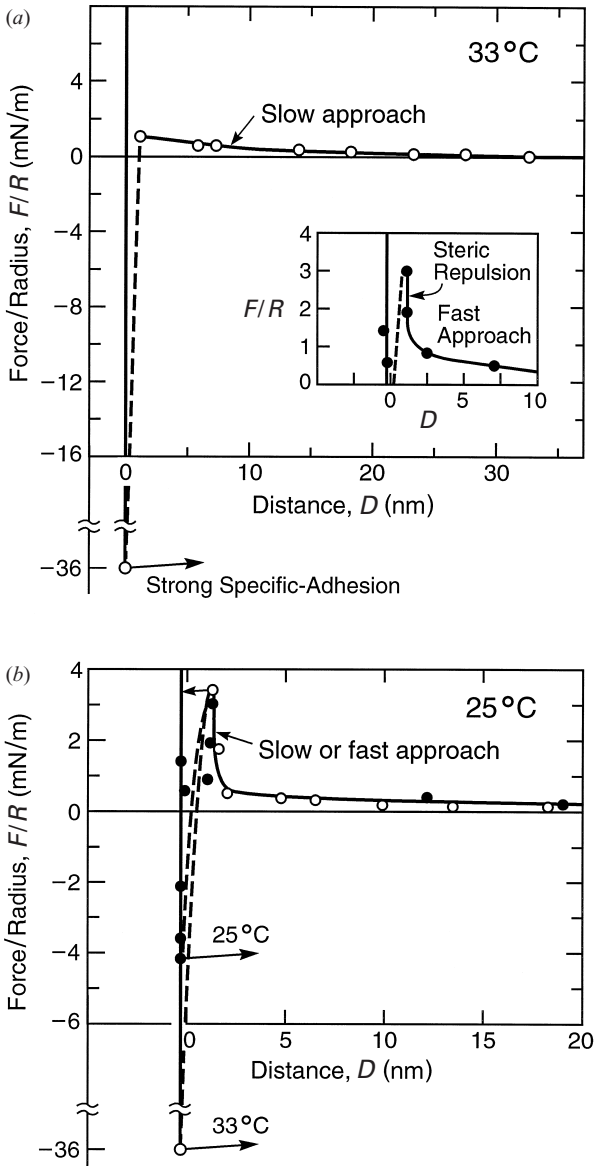


Fig. 55. Examples of effect of the rate of approach and temperature on the long- and short-range forces in LR interactions. Interaction force between a surface exposing streptavidin receptors and a surface exposing biotin ligands attached to short tethers (cf. Fig. 51). Panel (*a*) at 33 °C ($T > T_m$): the long-range force (solid line) is the equilibrium repulsive electrostatic DL force (cf. Fig. 33). The shorter-ranged attractive force is due to the LR bond. On fast approach (inset) the additional short-range force barrier results from the steric repulsion between the tethered ligand and protein surfaces (cf. Fig. 51(*b*) because the ligand does not have time to find the binding site until some finite time after the surfaces have been close together (Fig. 51(*c*)). On separation, depending on the relative bond energies, bond lengths, time in contact, and the rate of separation, the LR bond may break, or lipid molecules may be pulled out of the membrane, or the receptor molecules may be pulled out (cf. Fig. 51(*d*) and (*e*)). In this example, separation occurred by lipid pull-out. The case of biotin attached to long tethers is shown in Fig. 56. Panel (*b*) at 25 °C ($T < T_m$): slow and fast approaches now follow similar force paths, and similar to the fast approach at 33 °C. The adhesion at 25 °C is significantly lower than at 33 °C. (Reprinted with permission from Leckband *et al*. 1994.)

https://doi.org/10.1017/S0033583501003687 Published online by Cambridge University Press

as shown in Fig. 55(*a*).[68] The qualitative features of the interaction potentials therefore depend on the rate of approach relative to the timescales of molecular rearrangements and redistributions on the approaching surfaces.

The scenario described above illustrates that several dynamic variables, including the lateral diffusivity, tether dynamics, and RL binding (and unbinding) kinetics together determine the adhesion between materials as a function of their approach (or separation) rate. Chelsea *et al*. (1998) recently developed a method based on the MPA technique for determining the kinetics of RL association and dissociation between two cells, on the basis of dynamic adhesion measurements. This approach involves inducing transient contacts between cells. The adhesion measurements are then compared with the calculated probability that an encounter will occur in the same timeframe, given the receptor and ligand densities, their lateral mobility, their association and dissociation rates, and the contact area. This approach takes advantage of the dependence of adhesion on the dynamics of molecular diffusion and reaction in order to quantify the governing parameters.

While the mechanisms of detaching biomolecules and separating surfaces have already been studied in great detail, much less work has been done on approaching surfaces or molecules. The former studies give insights into off-rates, the latter into on-rates; but both types of studies are important for understanding other biological processes such as adhesion, fusion, endocytosis, pore opening, and various transport processes such as those illustrated in Fig. 1. It is more difficult to experimentally study or 'observe' approaching molecules and surfaces, because this usually requires greater absolute distance and time resolution than measurements that involve separating surfaces.

Using the SFA, Wong *et al*. (1997) and Jeppesen *et al*. (2001) studied the approach and binding of a 'tethered LR' system, i.e. one in which the ligand is attached to the end of a long flexible tether (Fig. 56). In this type of system, which is common in biology, the ligand does not have to diffuse in the plane of the membrane in order to find the receptor pocket on the opposite surface. It can diffuse in the solution, sampling a large volume of space around the anchoring site, and constrained only by the fully extended length of the tether. The relevant time and distance scales for this type of RL interaction now become determined by the tether length and the tether dynamics in solution, rather than by the lateral diffusion rates of the membrane components. Wong *et al*. (1997) found, somewhat surprisingly, that binding was triggered when the two surfaces were only slightly closer than the fully extended lengths of the tethers L, rather than at the radius of gyration R_g of the tethers. R_g gives the *average* tether extension and is much smaller than L.

Jeppesen *et al*. (2001) extended these studies both theoretically and experimentally to other tether lengths and different approach times. They concluded that given the time-scales for tethers to sample the space around them (the Zimm time), a small fraction of tethers will actually extend close to L over a period of a few milliseconds. This allows for the first binding or 'trap' to occur, which is quickly followed by others. The binding mechanism, time and energetics of tethered ligands are therefore seen to be determined by the dynamic properties of the *tethers* in addition to the direct LR binding energy and kinetics. This effect is analogous to the role of tethers in *unbinding* processes, as was discussed earlier and illustrated in Fig. 49.

[68] If the surfaces are pressed together rapidly under a large force, it is possible to trap the otherwise mobile species and 'freeze' them in place even at $T > T_m$. Under such conditions, the binding will take even longer than under a slow approach.

https://doi.org/10.1017/S0033583501003687 Published online by Cambridge University Press

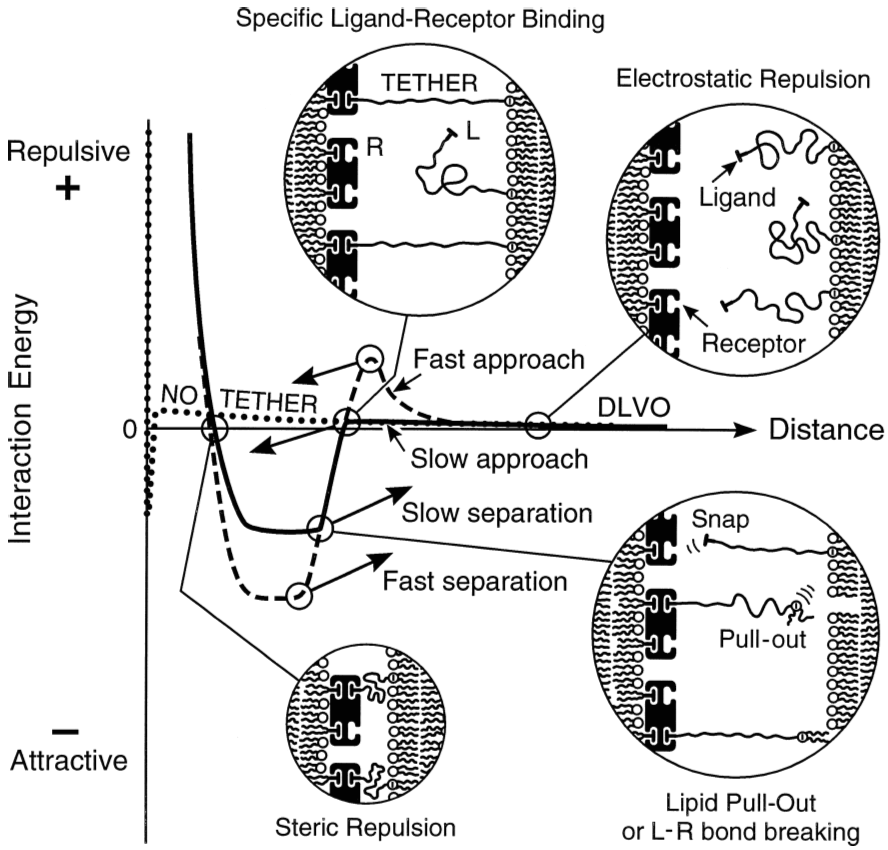


Fig. 56. Tethered LR interaction curves, showing the different interaction potentials measured on approach and separation for a biotin ligand attached to the end of a flexible tether interacting with a streptavidin receptor surface. The very different interaction curve for *untethered* ligands is shown by the dotted curve (cf. Fig. 55(*a*)). Note how the presence of a tether greatly extends the range of binding of the ligand, in addition to changing the interaction potential and timescale of the whole process. The circled diagrams show the different processes occurring at each stage of the approach and separation. (Adapted from Wong *et al*. 1997.)

The examples described so far, focus on measured changes between local regions of contact between membranes and surfaces. Motile cells, on the other hand, constantly change the positions and strengths of cell–surface contacts, and the different forces exerted at various locations are correlated; for example, the front of a locomoting cell advances at the same time the rear of the cell retracts. To quantify the traction exerted at different positions of the cell during migration required the design of the spatially addressable force transducers described in Section 2 (Fig. 31).

With elastically deformable polyacrylamide gels in which fluorescent particles were embedded as displacement detectors, Dembo & Wang (1999) mapped the spatial distribution of traction forces exerted in real time by a migrating fibroblast. From the extent of the substrate deformations, visualized by bead imaging, they determined the force exerted by the cells. During migration, the cells extend filopodia, and there is extensive ruffling at the leading edge. On soft substrates, the cells exert high stresses along the front edge on the order of 5–10 kPa. These high stress regions extend around the leading edge of the cell to about the

https://doi.org/10.1017/S0033583501003687 Published online by Cambridge University Press

position of the nucleus. The investigators further demonstrated the large degree of heterogeneity in both the location and magnitude of the tension exerted in this region. The forces exerted at the rear of the cell, by contrast, were weaker at *ca*. 1–2 kPa.

In another variation of the elastic substrate approach, Galbraith & Sheetz (1997) used an array of buried silcone micro-cantilevers (cf. Fig. 31) to map the forces exerted by locomoting chicken fibroblasts on micropad arrays. By following the cantilever displacements as the cells migrated over these cantilevers, they determined the distribution of tension exerted by the cells on the substrate. The physical principles are the same as the elastic substrate approach used by Dembo & Wang (1999), but the nature of the transducer and quantification of the forces exerted differed. Nevertheless, the results obtained with both methods are very similar. The micro-machined device revealed that the force exerted against the pad is always oriented against the direction of the cell's membrane extension, and that there is a reversal in the direction of the traction forces exerted at the center of the cell near the nucleus. The authors also observed fluctuations in the tension exerted. These fluctuations presumably reflect the stochastic nature of the local cell–substrate contacts.

By comparing the traction measurements of locomoting cells on responsive substrates with changes in the cytoskeletal components, these groups proposed qualitative models for how a cell propels itself forward. The concerted changes in several different interactions, including the adhesive cell–substrate contacts and the cytoskeletal organization, together generate the forces required for cell locomotion. Here, the essential information needed to probe the basis of this dynamic behavior is not provided by measurements of single bond strengths or equilibrium force profiles. Instead, the dynamics of the entire cell surface as well as biochemical information concerning the temporal and spatial changes in the cytoskeletal organization, and interior signaling processes, are required. Together, these provide a comprehensive picture of the principles described in this review: namely, that cell processes involve complex sequences of spatially and temporally directed changes.

Finally two approaching biomolecules or surfaces may not only adhere but also fuse. This is illustrated in Fig. 57 for two bilayers. Fusion (including hemi-fusion) should be distinguished from adhesion, however strong. In the case of adhesion, two molecules or surfaces are 'happy' once they are in contact; in the case of fusion, the molecular or membrane *interiors* must come together and mix – the adhesion stage being merely one of the steps on the way to fusion. The critical step, shown in Fig. 57(*b*, *c*), involves the local separation of hydrophilic groups on the surfaces and exposure or opening of hydrophobic pockets on opposite sites; this generates a strong medium- to long-range hydrophobic force that rapidly brings the hydrophobic *interiors* of the two surfaces together – the 'breakthrough' step. The various stages shown in Fig. 57 leading to complete fusion appear to be generic, with minor variations, for all bilayer fusion events so far studied (Chernomordik *et al*. 1987). And the same scenario may well apply, albeit in a much more complex way, to protein-induced membrane fusion. This is suggested by the observation that most proteins involved in fusion are thought to expose hydrophobic regions, which may insert into and destabilize membranes (Rosenthal *et al*. 1998; Skehel & Wiley 1998; Sutton *et al*. 1998).

4.9 Concluding remarks

The main purpose of this review has been to demonstrate how recent experimental and theoretical advances have revealed how the structure and composition of biological

https://doi.org/10.1017/S0033583501003687 Published online by Cambridge University Press

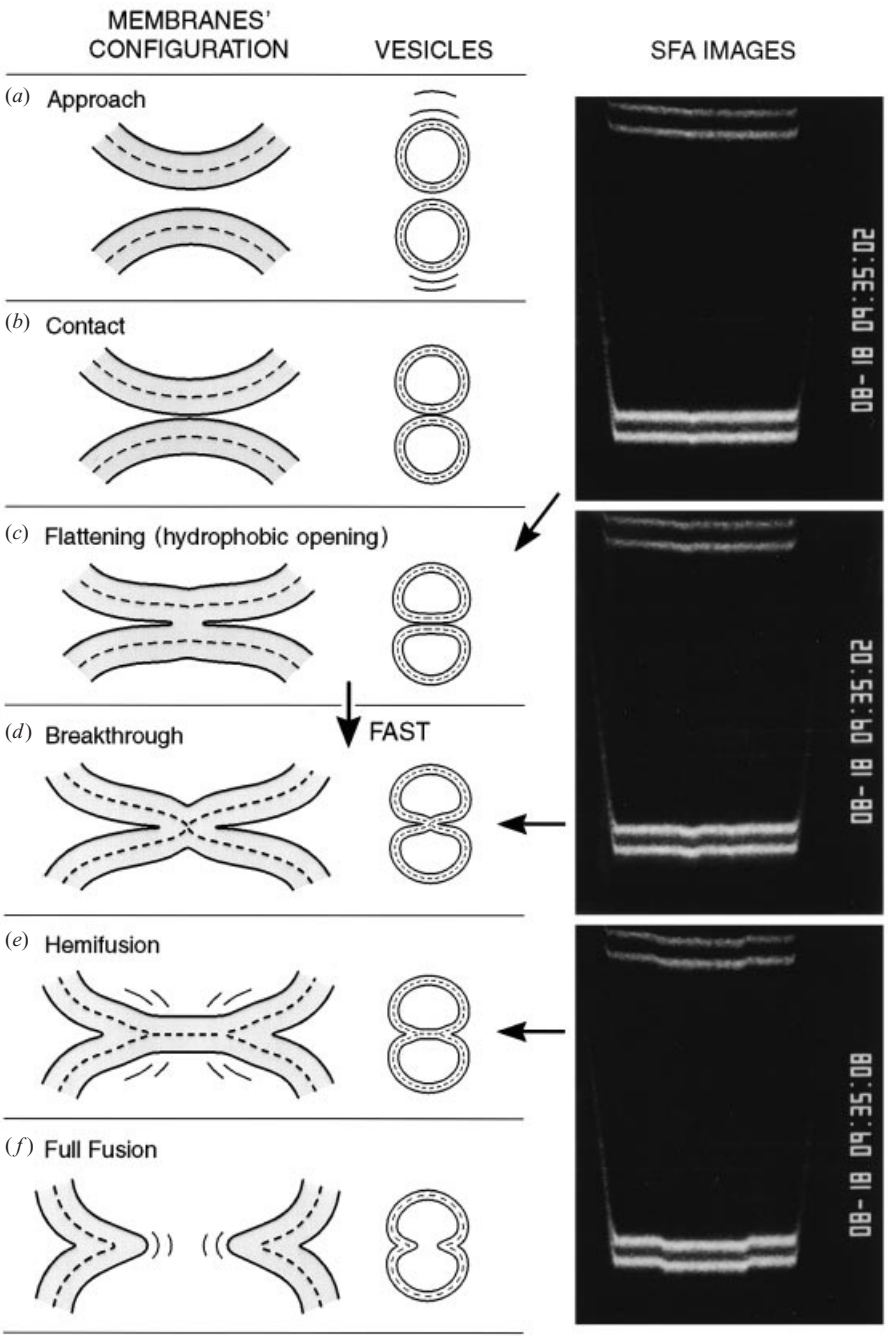


Fig. 57. Bilayer fusion mechanisms (left) as imaged or visualized in SFA experiments employing optical interference fringes (right, cf. Fig. 21). (Adapted from Horn, 1984 and Helm *et al*. 1989, 1992.)

molecules, surfaces and biomaterials determine, for example, the mechanical properties of proteins as well as protein interactions with other molecules and surfaces both *in vivo* and in the laboratory. An important consequence of investigations with these force probes is that they also demonstrated that biological interactions cannot be simply understood in terms of

https://doi.org/10.1017/S0033583501003687 Published online by Cambridge University Press

static interaction potentials, except at the most elementary level. Each interaction – and by this we mean a whole 'process' or 'event', such as LR binding, membrane fusion, signaling processes, or locomotion along a microtubule or surface – consists of a number of separate 'elemental interactions'. However, it is the differences in ranges over which they act, the different strengths of the interactions, and the different timescales on which they occur that gives rise to the rich variety of behavior exhibited by living systems. Often the net effect is totally different from what would be predicted by simply summing or averaging the individual elemental interaction potentials or force functions. The experimental techniques described in this review made possible investigations of these interactions at an unprecedented level of detail. However, this field is relatively young. The continuing rapid developments in force measurement instruments, as well as the explosion in knowledge and molecular biology tools resulting from the 'genomics revolution', promises to yield new challenges and research opportunities for several years to come.

5. Acknowledgements

We gratefully acknowledge the very helpful comments and critiques by, as well as discussions with Pierre Bongrand, Taekjip Ha, Todd Martinez, Martin Gruebele, Dennis Prieve, Evan Evans and Scott Diamond. We thank Klaus Schulten, Daniel Hammer, David Tees, Julio Fernandez, Michael Sheetz, Cathy Galbraith, Stuart McLaughlin, Ana Arbuzova, Steve White, Mair Churchill, and Mathew Tirrell for contributing figures for this manuscript. This work was supported by NIH [GM51338-05 (D. E. L.), GM-47334 (J. N. I.), NSF, and ONR.

References

Abuchowski, A. & Davis, F. F. (1981). Enzymes in drugs. In *Enzymes in Drugs* (eds. J. Holsenberg & J. Roberts), pp. 367. New York: Wiley.

Albersdörfer, A., Bruinsma, R. & Sackmann, E. (1998). Force spectroscopy on adhesive vesicles. *Europhys. Lett.* **42**, 227–231.

Albersdörfer, A., Feder, T. & Sackmann, E. (1997). Adhesion-induced domain formation by interplay of long-range repulsion and short-range attraction force: a model membrane study. *Biophys. J.* **73**, 245–257.

Alon, R., Hammer, D. A. & Springer, T. A. (1995). Lifetime of the P-selectin–carbohydrate bond and its response to tensile force in hydrodynamic flow. *Nature* **374**, 539–542.

Arbuzova, A., Murray, D. & McLaughlin, S. (1998). MARCKS, membranes, and calmodulin: kinetics of their interaction. *Biochim. biophys. Acta* **1376**, 369–379.

Arnold, K., Hermann, A., Gawrisch, E. & Pratsch, L. (1985). The dielectric properties of aqueous solutions of poly(ethylene glycol) and their influence on membrane structure. *Biochim. biophys. Acta* **815**, 515–518.

Arnold, K., Pratsch, L. & Gawrisch, K. (1983). Effect of poly(ethylene glycol) on phospholipid hydration and polarity of the external phase. *Biochim. biophys. Acta* **728**, 121–128.

Arnold, K., Zschornig, O., Pratsch, L., Donath, E., Barthel, D. & Herrmann, A. (1988). Exclusion of PEG from membrane surfaces and aggregation of liposomes and lipoproteins. *Stud. Biophys.* **127**, 113–120.

Asakura, S. & Oosawa, F. (1954). On interaction between two bodies immersed in a solution of macromolecules. *J. chem. Phys.* **22**, 1255–1256.

Asakura, S. & Oosawa, F. (1958). Interaction between particles suspended in solutions of macromolecules. *J. Polymer Sci.* **33**, 183–192.

Ashkin, A. (1992). Forces of a single-beam gradient laser trap on a dielectric sphere in the ray optics regime. *Biophys. J.* **61**, 569–582.

Ashkin, A. (1997). Optical trapping and manipulation of neutral particles using lasers. *Proc. natn. Acad. Sci. USA* **94**, 4853–4860.

https://doi.org/10.1017/S0033583501003687 Published online by Cambridge University Press

Ashkin, A., Dziedzic, J. M., Bjorkholm, J. E. & Chu, S. (1986). Observation of a single-beam gradient force optical trap for dielectric particles. *Optics Lett.* **11**, 288–290.

Ashkin, A., Dziedzic, J. M. & Yamane, T. (1987). Optical trapping and manipulation of single cells using infrared laser beams. *Nature* **330**, 769–771.

Baekmark, T. R., Elender, G., Lasic, D. D. & Sackmann, E. (1995). Conformational transitions of mixed monolayers of phospholipids and poly(ethylene oxide) lipopolymers and interaction forces with solid-surfaces. *Langmuir* **11**, 3975–3987.

Bailey, S. M., Chiruvolu, S., Israelachvili, J. N. & Zasadzinski, J. A. N. (1990). Measurements of forces involved in vesicle adhesion using freeze-fracture electron microscopy. *Langmuir* **6**, 1326–1329.

Baljon, A. & Robbins, M. O. (1996). Energy dissipation during rupture of adhesive bonds. *Science* **271**, 482–484.

Balsera, M., Stepaniants, S., Izrailev, S., Oono, Y. & Schulten, K. (1997). Reconstructing potential energy functions from simulated force-induced unbinding processes. *Biophys. J.* **73**, 1281–1287.

Barquins, M. & Maugis, D. (1982). Adhesive contact of axisymmetric punches on an elastic half-space: the modified Hertz-Herber's stress tensor for contacting spheres. *J. Méc. Théor. Appl.* **1**, 331–357.

Baumann, C., Bloomfield, V. A., Smith, S. B., Bustamante, C., Wang, M. D. & Block, S. B. (2000). Stretching of single collapsed DNA. *Biophys. J.* **78**, 1965–1978.

Bedzyk, W., Herron, J. N., Edmundson, A. B. & Voss, E. W. (1990). Active site structure and antigen binding properties of idiotypically cross-reactive anti-fluorescein monoclonal antibodies. *J. biol. Chem.* **265**, 133–138.

Bekiranov, S., Bruinsma, R. & Pincus, P. (1997). Solution behavior of polyethylene oxide in water as a function of temperature and pressure. *Phys. Rev. E* **55**, 577–585.

Bell, G. I. (1978). Models for the specific adhesion of cells to cells. *Science* **200**, 618–627.

Berndt, P., Fields, G. B. & Tirrell, M. (1995). Synthetic lipidation of peptides and amino acids – monolayer structure and properties. *J. Am. chem. Soc.* **117**, 9515–9522.

Bhushan, B., Israelachvili, J. N. & Landman, U. (1995). Nanotribology: friction, wear and lubrication at the atomic scale. *Nature* **374**, 607–616.

Binnig, G., Quate, C. F. & Gerber, C. (1986). Atomic Force Microscopy. *Phys. Rev. Lett.* **56**, 930–933.

Block, S. (1995). Nanometres and piconewtons: the macromolecular mechanics of kinesin. *Trends cell. Biol.* **5**, 169–175.

Block, S. M. (1992). Making light work with optical tweezers. *Nature* **360**, 493–495.

Boland, T. & Ratner, B. D. (1995). Direct measurement of hydrogen bonding in DNA nucleotide bases by atomic force microscopy. *Proc. natn. Acad. Sci. USA* **92**, 5297–5301.

Bongrand, P., Capo, C., Mege, J.-L. & Benoliel, A.-M. (1988) Use of hydrodynamic flows to study cell adhesion. In *Physical Basis of Cell Adhesion* (eds. Bongrand), pp. 125–156. Boca Raton: CRC Press

Boni, L. T., Hah, J. S., Hui, S. W., Mukherjee, P., Ho, J. T. & Jung, C. Y. (1984). Aggregation and fusion of unilamellar vesicles by poly(ethylene glycol). *Biochim. biophys. Acta* **775**, 409–418.

Boni, L. T., Stewart, T. P., Alderfer, J. L. & Hui, S. W. (1981). Lipid–polyethylene glycol interactions 1. Induction of fusion between liposomes. *J. Membrane Biol.* **62**, 65–70.

Bratko, D., Curtis, R. A., Blanch, H. W. & Prausnitz, J. M. (2001). Interaction between hydrophobic surfaces with metastable intervening liquid. *J. chem. Phys.* **115**, 3873–3877.

Briscoe, B. J. & Evans, D. C. (1982). The shear properties of Langmuir Blodgett layers. *Proc. R. Soc. Lond.* **A380**, 389–407.

Brunk, D. K. & Hammer, D. A. (1997). Quantifying rolling adhesion with a cell-free assay: E-selectin and its carbohydrate ligands. *Biophys. J.* **72**, 2820–2833.

Bustamante, C., Marko, J. & Siggia, E. (1994). Entropic elasticity of *l* phage DNA. *Science* **265**, 1599–1600.

Caffrey, M. B. & Bilderback, D. H. (1983). Real-time X-ray diffraction using synchrotron radiation: system characterization and applications. *Nucl. Instrum. Meth.* **208**, 495–510.

Cantor, C. & Schimmel, P. (1980). *Biophysical Chemistry*. New York: Freeman.

Cao, B. & Kim, M. W. (1994). Molecular weight dependence of the surface tension of aqueous poly-(ethylene oxide) solutions. *Faraday Disc.* **98**, 245–252.

Carpick, R. W., Ogletree, D. F. & Salmeron, M. (1999). A general equation for fitting contact area and friction vs. load measurements. *J. Colloid Interface Sci.* **211**, 395–400.

Carrion-Vazquez, M., Oberhauser, A. F., Fowler, S. B., Marszalek, P. E., Broedel, S. E., Clarke, J. & Fernandez, J. M. (1999). Mechanical and chemical unfolding of a single protein: a comparison. *Proc. natn. Acad. Sci. USA* **96**, 3694–3699.

Chan, D., Healy, T. W. & White, L. R. (1976). Electrical double-layer Interactions under regulation by surface ionization equilibria-dissimilar amphoteric surfaces. *J. Chem. Soc. Faraday Trans. I* **72**, 2844–2865.

Chan, D. Y. C. & Horn, R. G. (1985). The drainage of thin liquid films between solid surfaces. *J. chem. Phys.* **83**, 5311–5324.

Chan, D. Y. C., Mitchell, D. J., Ninham, B. W. & Pailthorpe, B. A. (1980a). Solvent structure in

https://doi.org/10.1017/S0033583501003687 Published online by Cambridge University Press

particle interactions – low-pressure effects and analytic limits. *J. Chem. Soc. Faraday Trans. II* **76**, 776–784.

Chan, D. Y. C., Pahsley, R. M. & White, L. R. (1980b). A simple algorithm for the calculation of the electrostatic repulsion between identical charged surfaces in electrolyte. *J. Colloid Interface Sci.* **77**, 283–285.

Chang, K.-C. & Hammer, D. A. (1996). Influence of direction and type of applied force on the detachment of macromolecularly-bound particles from surfaces. *Langmuir* **12**, 2271–2282.

Chelsea, S., Selveraj, P. & Zhu, C. (1998). Measuring two-dimensional receptor–ligand binding kinetics by Micropipette. *Biophys. J.* **75**, 1553–1572.

Chelsea, S. & Zhu, C. (1996). Validation and accuracy assessment of the micropipet piconewton force transducer. In *Advances in Bioengineering* (ed. Rastegar), vol. 30. New York: ASME.

Chen, Y. L., Chen, S., Frank, C. & Israelachvili, J. N. (1992). Molecular mechanisms and kinetics during the self-assembly of surfactant layers. *J. Colloid Interface Sci.* **153**, 244–265.

Chen, Y. L., Helm, C. A. & Israelachvili, J. N. (1991a). Measurements of the elastic properties of surfactant and lipid monolayers. *Langmuir* **7**, 2694–2699.

Chen, Y. L., Helm, C. A. & Israelachvili, J. N. (1991b). Molecular mechanisms associated with adhesion and contact angle hysteresis of monolayer surfaces. *J. phys. Chem.* **95**, 10737–10746.

Chernomordik, L., Melikyan, G. B. & Chizmadzhev, Y. A. (1987). Biomembrane fusion: a new concept derived from model studies using two interacting planar lipid bilayers. *Biochim. biophys. Acta* **906**, 309–352.

Chilkoti, A., Boland, T., Ratner, B. D. & Stayton, P. S. (1995). The relationship between ligand-binding thermodynamics and protein–ligand interaction forces measured by atomic force microscopy. *Biophys. J.* **69**, 2125–2130.

Chilkoti, A. & Stayton, P. S. (1995). Molecular-originas of the slow streptavidin–biotin dissociation kinetics. *J. Am. chem Soc.* **117**, 10622–10628.

Chiruvolu, S., Israelachvili, J., Leckband, D., Schmitt, F.-J., Walker, S. & Zasadzinski, J. (1994). Higher order self-assembly of vesicles via site-specific binding. *Science* **264**, 1753–1756.

Chiruvolu, S., Israelachvili, J. N., Naranjo, E., Xu, Z. & Zasadzinski, J. A. (1995). Measurement of forces between spontaneous vesicle-forming bilayers. *Langmuir* **11**, 4256–4266.

Christenson, H. K. (1988). Non-DLVO forces between surfaces – solvation, hydration and capillary effects. *J. Dispersion Sci. & Technol.* **9**, 171–206.

Christenson, H. K. & Claesson, P. M. (2001). Direct measurements of the force between hydrophobic surfaces in water. *Adv. Colloid Interface Sci.* **91**, 391–436.

Christenson, H. K., Claesson, P. M., Berg, J. & Herder, P. C. (1989). Forces between fluorocarbon surfactant monolayers: salt effects on the hydrophobic interaction. *J. phys. Chem.* **93**, 1472–1478.

Christenson, H. K., Fang, J., Ninham, B. W. & Parker, J. L. (1990). Effect of divalent electrolyte on the hydrophobic attraction. *J. phys. Chem.* **94**, 8004–8006.

Christenson, H. K. & Horn, R. G. (1983). Direct measurement of the force between solid surfaces in polar liquid. *Chem. Phys. Lett.* **28**, 45.

Christenson, H. K. & Horn, R. G. (1985). Solvation forces measured in non-aqueous liquids. *Chemica Scripta* **25**, 37–41.

Christenson, H. K. & Yaminsky, V. V. (1993). Adhesion and solvation forces between surfaces in liquids studied by vapor-phase experiments. *Langmuir* **9**, 2448–2454.

Chu, S., Bjorkholm, J. E. & Ashkin, A. (1986). Experimental observation of optically trapped atoms. *Phys. Rev. Lett.* **57**, 314–317.

Claesson, P. M., Blom, C. E., Herder, C. & Ninham, B. W. (1986). Interactions between water-stable hydrophobic Langmuir-Bloodgett monolayers on mica. *J. Colloid Interface Sci.* **114**, 234–242.

Claesson, P. C. & Kurihara, K. (1989). Dihexadecyl phosphate monolayers – intralayer and interlayer interactions. *J. phys. Chem.* **93**, 917–922.

Claussen-Schaumann, H., Rief, M., Tolksdorf, C. & Gaub, H. E. (2000). Mechanical stability of single DNA molecules. *Biophys. J.* **78**, 1997–2007.

Cleveland, J. P., Manne, S., Bocek, D. & Hansma, P. K. (1993). A nondestructive method for determining the spring contstant of cantilevers for scanning force microscopy. *Rev. Sci. Instrum.* **64**, 403–405.

Coulson, C. A. (1961). *Valence*, 2nd edn. London and New York: Oxford University Press

Creighton, T. (1993). *Proteins: Structures and Molecular Properties*, 2nd edn. New York: Freeman.

Dai, J. W. & Sheetz, M. P. (1999). Membrane tether formation from blebbing cells. *Biophys. J.* **77**, 3363–3370.

de Gennes, P. (1988). *Scaling Concepts in Polymer Physics*. Ithaca, New York: Cornell University Press.

de Gennes, P. G. (1976). Dynamics of entangled polymer solutions. 1. Rouse model. *Macromolecules* **9**, 587–593.

de Gennes, P. G. (1987). Polymers at an interface: a simplified view. *Adv. Colloid Interface Sci.* **27**, 189–209.

Dean, P. M. (1987). *Molecular Foundations of Drug–Receptor Interactions*, pp. 121, 254. London and Cambridge: Cambridge University Press.

Del Pennino, U., Mezzega, E., Valeri, S., Alietti, A., Brigatti, M. F. & Poppi, L. (1981). Interlayer water and swelling properties of monoionic montmorillonites. *J. Colloid Interface Sci.* **84**, 301–309.

https://doi.org/10.1017/S0033583501003687 Published online by Cambridge University Press

Dembo, M., Torney, D. C., Saxman, K. & Hammer, D. (1988). The reaction-limited kinetics of membrane-to-surface adhesion and detachment. *Proc. R. Soc. Lond. B.* **234**, 55–83.

Dembo, M. & Wang, Y. L. (1999). Stresses at the cell-to-substrate interface during locomotion of fibroblasts. *Biophys. J.* **76**, 2307–2316.

Derjaguin, B. V. (1934). Untersuchungen über die Reibung und Adhaesion, IV. Theorie des Anhaftens Kleiner Teilchen. *Kolloid Zeits* **69**, 155–164.

Derjaguin, B. V. & Landau, L. (1941). *Acta Physiochim URSS* **14**, 633.

Dori, Y., Bianco-Peled, H., Satja, S. K., Fields, G. B., McCarthy, J. B. & Tirrell, M. (2000). Ligand accessibility as a means to control cell response to bioactive bilayer membranes. *J. Biomed. Mat. Res.* **50**, 75–81.

Dow, L., Jones, D. N. M., Wolfe, S. A., Verdine, G. L. & Churchill, M. E. A. (2000). Structural studies of the high mobility group globular domain and basic tail of HMG-D bound to disulfide cross-linked DNA. *Biochemistry* **39**, 9725–9736.

Ducker, W., Xu, Z. G. & Israelachvili, J. N. (1994). Measurements of hydrophobic and DLVO forces in bubble-surface interactions in aqueous solutions. *Langmuir* **10**, 3279–3289.

Ducker, W. A. & Senden, T. J. (1992). Measurement of forces in liquids using a Force Microscope. *Langmuir* **8**, 1831–1836.

Dzyaloshinskii, I. E., Lifshitz, E. M. & Pitaevskii, L. P. (1961). The General Theory of van der Waals Forces. *Advances Phys.* **10**, 165–209.

Enachescu, M., van den Oetelaar, R. J. A., Carpick, R. W., Ogletree, D. F., Flipse, C. F. J. & Salmeron, M. (1999). Observation of proportionality between friction and contact area at the nanometer scale. *Tribology Lett.* **7**, 73–78.

Essavaz-Roulet, B., Bockelmann, U. & Heslot, F. (1997). Mechanical separation of the complementary strands of DNA. *Proc. natn. Acad. Sci. USA* **94**, 11935–11940.

Evans, D. F. & Wennerstrom, H. (1999). *The Colloidal Domain: Where Physics, Chemistry, Biology, and Technology Meet*, 2nd edn. New York: VCH Publishers.

Evans, E. (1985). Detailed mechanics of membrane–membrane adhesion and separation. II. Discrete kinetically trapped molecular cross-bridges. *Biophys. J.* **48**, 185–192.

Evans, E. (1988). Mechanics of cell deformation and cell–surface adhesion. In *Physical Basis of Cell Adhesion* (ed. Bongrand), pp. 173–190. Boca Raton: CRC Press.

Evans, E. (1999). Looking inside molecular bonds at biological interfaces with dynamic force spectroscopy. *Biophys. Chem.* **82**, 83–97.

Evans, E., Berk, D. & Leung, A. (1992). Detachment of agglutinin-bonded red blood cells: I. forces to rupture molecular-point attachments. *Biophys. J.* **59**, 838–848.

Evans, E. & Metcalfe, M. (1984). Free-energy potential for aggregation of giant, netural lipid bilayer vesicles by van der Waals attraction. *Biophys. J.* **46**, 423–426.

Evans, E. & Needham, D. (1988). Attraction between lipid bilayer membranes in concentrated solutions of nonadsorbing polymers: comparison of mean-field theory with measurements of adhesion energy. *Macromolecules* **21**, 1822–1831.

Evans, E. & Rawics, W. (1990). Entropy-driven tension and bending elasticity in condensed-fluid membranes. *Phys. Rev. Lett.* **64**, 2094–2097.

Evans, E. & Ritchie, K. (1997). Dynamic strength of molecular adhesion bonds. *Biophys. J.* **72**, 1541–1555.

Evans, E. & Ritchie, K. (1999). Strength of a weak bond connecting flexible polymer chains. *Biophys. J.* **76**, 2439–2447.

Evans, E., Ritchie, K. & Merkel, R. (1995). Sensitive force technique to probe molecular adhesion and structural linkages at biological interfaces. *Biophys. J.* **68**, 2580–2587.

Evans, E. N. (1987). Physical properties of surfactant bilayer membranes: thermal transitions, elasticity, rigidity, cohesion, and colloidal interactions. *J. phys. Chem.* **91**, 4219–4228.

Evert, L. L., Leckband, D. E. & Israelachvili, J. N. (1994). Structure and dynamics of ion-induced domains in free and supported monolayers and bilayers. *Langmuir* **10**, 303–315.

Falsafi, A., Deprez, P., Bates, F. S. & Tirrell, M. (1997). Direct measurement of adhesion between viscoelastic polymers: a contact mechanical approach. *J. Rheology* **41**, 1349–1364.

Fisher, L. R. & Israelachvili, J. N. (1981). Direct measurement of the effect of meniscus forces on adhesion-study of the applicability of macroscopic thermodynamics to microscopic liquid interfaces. *Colloids & Surfaces* **3**, 303–319.

Fisher, T., Oberhauser, A. F., Carrion-Vasquez, M., Marszalek, P. E. & Fernandez, J. M. (1999). The study of protein mechanics with the atomic force microscope. *Trends biochem. Sci.* **24**, 379–384.

Florin, E.-L., Moy, V. T. & Gaub, H. E. (1994). Adhesion forces between individual ligand–receptor pairs. *Science* **264**, 415–417.

Fredriksson, C., Kihlman, S., Rodahl, M. & Kasemo, B. (1998). The piezoelectric quartz crystal mass and dissipation sensor: A means of studying cell adhesion. *Langmuir* **14**, 248–251.

Frens, G. & Overbeek, J. Th. G. (1972). Repeptilization and theory of electrocratic colloids. *J. Colloid Interface Sci.* **38**, 376–387.

https://doi.org/10.1017/S0033583501003687 Published online by Cambridge University Press

Galbraith, C. G. & Sheetz, M. P. (1997). A micromachined device provides a new bend on fibroblast traction forces. *Proc. natn. Acad. Sci. USA* **94**, 9114–9118.

Gee, M. L., Tong, P., Israelachvili, J. N. & Witten, T. A. (1990). Comparison of light scattering of colloidal dispersions with direct force measurements between analogous macroscopic surfaces. *J. chem. Phys.* **93**, 6057–6064.

Gijs, J., Wuite, R., Davenport, J., Rappaport, A. & Bustamante, C. (2000). An integrated laser trap/flow control video microscope for the study of single biomolecules. *Biophys. J.* **79**, 1155–1167.

Gingell, D. & Parsegian, V. A. (1972). Computation of van der Waals interaction in aqueous systems using reflectivity data. *J. theor. Biol.* **36**, 41–52.

Grakoui, A., Bromley, S. K., Sumen, C., Davis, M. M., Shaw, A. S., Allen, P. M. & Dustin, M. L. (1999). The immunological synapse: a molecular machine controlling T-cell activation. *Science* **285**, 221–226.

Granfeldt, M. K., Jonsson, B. & Woodward, C. E. (1991). A Monte Carlo simulation study of the interaction between charged colloids carrying adsorbed polyelectrolytes. *J. phys. Chem.* **95**, 4819–4826.

Gregory, J. (1973). Approximate expression for the interaction of diffuse electrical double layers at constant charge. *J. Chem. Soc. Faraday Trans. II* **69**, 1723–1728.

Gregory, J. (1975). Interaction of unequal double layers at constant charge. *J. Colloid Interface Sci.* **51**, 44–51.

Gristina, A. (1987). Biomaterial-centered infection: microbial adhesion versus tissue integration. *Science* **237**, 1588–1595.

Guldbrand, L., Jonsson, V., Wennerstrom, H. & Linse, P. (1984). Electrical double-layer forces – a Monte-Carlo study. *J. chem. Phys.* **80**, 2221–2228.

Gullingsrud, J., Braun, R. & Schulten, K. (1999). Reconstructing potentials of mean force through time series analysis of steered molecular dynamics simulations. *J. comp. Phys.* **151**, 190–211.

Hamaker, H. (1937). The London–van der Waals attraction between spherical particles. *Physica* **4**, 1058–1072.

Harris, A., Wild, P. & Topak, D. (1980). Silicone-rubber substrata – new wrinkle in the study of cell locomotion. *Science* **208**, 177–179.

Harris, J. M. (1992). *Poly(ethylene glycol) Chemistry: Biotechnical and Biomedical Applications*. New York: Plenum Press.

Helfrich, W. (1978). Steric interaction of fluid membranes in multilayer systems. *Z. Naturforsch.* **33a**, 305–315.

Helm, C. A., Israelachvili, J. N. & McGuiggan, P. M. (1989). Molecular mechanisms and forces involved in the adhesion and fusion of amphiphilic bilayers. *Science* **246**, 919–922.

Helm, C. A., Israelachvili, J. N. & McGuiggan, P. M. (1992). Role of hydrophobic forces in bilayer adhesion and fusion. *Biochemistry* **31**, 1794–1805.

Henderson, D. & Lozada-Cassou, M. (1986). A simple theory for the force between spheres immersed in a fluid. *J. Colloid Interface Sci.* **114**, 180.

Henderson, D. & Lozada-Cassou, M. (1994). Dielectric saturation provide a plausible explanation of the hydration solvent force? *J. Colloid Interface Sci.* **162**, 508.

Herron, J., He, X.-M., Mason, M. L., Voss, E. W. & Edmundson, A. B. (1989). Three-dimensional structure of a fluorescein-Fab complex crystallized in 2-methyl-2,4-pentanediol. *Proteins* **5**, 271–280.

Hertz, H. (1881). Über die Behrüng fester elastischer Körper. *J. Reine Angew. Math.* 92.

Heuberger, M., Dietler, G. & Schlapbach, L. (1996). Elastic deformations of tip and sample during atomic force microscope measurements. *J. Vac. Sci. Technol. B* **14**, 1250–1254.

Heuberger, M., Luengo, G. & Israelachvili, J. (1997). Topographic information from multiple beam interferometry in the Surface Forces Apparatus. *Langmuir* **13**, 3839–3848.

Hogg, R., Healy, T. W. & Fuerstenau, D. W. (1966). Mutual coagulation of colloidal dispersions. *Trans. Faraday Soc.* **62**, 1683–1651.

Homola, A. & Robertson, A. A. (1976). A compression method for measuring forces between colloidal particles. *J. Colloid Interface Sci.* **54**, 286–297.

Honig, B. & Nicolls, A. (1995). Classical electrostatics in biology and chemistry. *Science* **268**, 1144–1149.

Höök, F., Rodahl, M., Kasemo, B. & Brzezinski, P. (1998). Structural change in hemoglobin during adsorption to solid surfaces: Effects of pH, ionic strength, and ligand binding. *Proc. natn. Acad. Sci. USA* **95**, 12271–12276.

Horn, R. (1984). Direct measurements of the force between two lipid bilayers and observation of their fusion. *Biochim. Biophys. Acta* **778**, 224–228.

Horn, R. G. (1990). Surface forces and their action in ceramic materials. *J. Am. ceram. Soc.* **73**, 1117–1135.

Horn, R. G., Israelachvili, J. N., Marra, J., Parsegian, V. A. & Rand, R. P. (1988). Comparison of forces measured between phosphatidylcholine bilayers. *Biophys. J.* **54**, 1185–1187.

Horn, R. G., Israelachvili, J. N. & Pribac, F. (1987). Measurement of the deformation and adhesion of solids in contact. *J. Colloid Interface Sci.* **115**, 480–492.

Horn, R. G. & Smith, D. T. (1992). Contact electrification and adhesion between dissimilar materials. *Science* **256**, 362–363.

https://doi.org/10.1017/S0033583501003687 Published online by Cambridge University Press

Horn, R. G., Smith, D. T. & Haller, W. (1989). Surface forces and viscosity of water measured between silica sheets. *Chem. Phys. Lett.* **162**, 404–408.

Hui, S. W., Kuhl, T. L., Guo, Y. Q. & Israelachvili, J. (1999). Use of poly(ethylene glycol) to control cell aggregation and fusion. *Colloids & Surfaces B: Biointerfaces* **14**, 213–222.

Hunter, R. J. (1987). *Foundations of Colloid Science*. Oxford: Clarendon Press.

Hwang, W. C. & Waugh, R. E. (1997). Energy of dissociation of lipid bilayer from the membrane skeleton of red blood cells. *Biophys. J.* **72**, 2669–2678.

Idziak, S. H. J., Safinya, C. R., Hill, R., Kraiser, K. E., Ruths, M., Warriner, H., Steinberg, S., Liang, K. S. & Israelachvili, J. (1994). The X-ray Surface Forces Apparatus: structure of a smectic liquid crystal under confinement and flow. *Science* **264**, 1915–1918.

Israelachvili, J. & Wennerström, H. (1996). Role of hydration and water structure in biological and colloidal interactions. *Nature* **379**, 219–225.

Israelachvili, J. & Wennerström, H. (1997). Hydration in electrical double layers. *Nature* **385**, 689–690.

Israelachvili, J. N. (1973). Thin film studies using multiple beam interferometry. *J. Colloid Interface Sci.* **44**, 259–272.

Israelachvili, J. N. (1983). Molecular layering of water at surfaces and origin of repulsive hydration forces. *Nature* **306**, 249–250.

Israelachvili, J. N. (1986). Measurement of the viscosity of liquids in very thin films. *J. Colloid Interface Sci.* **110**, 263–271.

Israelachvili, J. N. (1989). Techniques for direct measurements of forces between surfaces in liquids at the atomic scale. *Chemtracts – Anal. Phys. Chem.* **1**, 1–12.

Israelachvili, J. N. (1990). Adhesion and short-range forces between surfaces I – new apparatus for surface force measurements. *J. Mater. Res.* **5**, 2223–2231.

Israelachvili, J. N. (1991). *Intermolecular and Surface Forces*, 2nd edn. London & New York: Academic Press.

Israelachvili, J. N. (1994). Strength of Van Der Waals Attraction between Lipid Bilayers. *Langmuir* **10**, 3369–3370.

Israelachvili, J. N. & Adams, G. E. (1978). Measurement of forces between two mica surfaces in aqueous electrolyte solutions in the range 0–100 nm. *J. Chem. Soc., Faraday Trans. I* **74**, 975–1001.

Israelachvili, J. N. & Berman, A. (1995). Irreversibility, energy dissipation and time effects in intermolecular and surface interactions. *Israel J. Chem.* **35**, 85–91.

Israelachvili, J. N. & Pashley, R. M. (1984). Measurement of the hydrophobic interaction between two hydrophobic surfaces in aqueous electrolyte solutions. *J. Colloid Interface Sci.* **98**, 500–514.

Israelachvili, J. N. & Wennerström, H. (1990). Hydration or steric forces between amphiphilic surfaces? *Langmuir* **6**, 873–876.

Israelachvili, J. N. & Wennerström, H. (1992). Entropic forces between amphiphilic surfaces in liquids. *J. phys. Chem.* **96**, 520–531.

Izrailev, S., Stepaniants, S., Isralewitz, B., Kosztin, D., Lu, H., Molnar, F., Wriggers, W. & Schulten, K. (1998). Steered molecular dynamics. In *Computational Molecular Dynamics: Challenges, Methods, Ideas* (eds. H Deuflhard, M. Leimkuhler & S. Reich), pp. 39–65. New York: Springer.

Izrailev, S., Stepaniants, S., Balsera, M., Oono, Y. & Schulten, K. (1997). Molecular dynamics study of unbinding of the avidin–biotin complex. *Biophys. J.* **72**, 1568–1581.

Jencks, W. (1969). *Catalysis in Chemistry and Enzymology*. Toronto: Dover.

Jeppesen, C., Wong, J. Y., Kuhl, T. L., Israelachvili, J. N., Mullah, N., Zalipsky, S. & Marques, C. M. (2001). Impact of polymer tether length on multiple ligand–receptor bond formation. *Science*. **293**, 465–468.

Joesten, M. D. & Schaad, L. J. (1974). *Hydrogen Bonding*. New York: Dekker

Johnson, K. L. (1985). *Contact Mechanics*. New York: Cambridge University Press.

Johnson, K. L., Kendall, K. & Roberts, A. D. (1971). Surface energy and the contact of elastic solids. *Proc. R. Soc. Lond. A* **324**, 301–313.

Jones, D., Searles, M. A., Shaw, G. L., Churchill, M. E. A., Ner, S. S., Keeler, J., Travers, A. A. & Neuhaus, D. (1994). The solution structure and dynamics of the DNA-binding domain of HMG-D from *Drosophila melanogaster*. *Structure* **2**, 609–627.

Jonsson, B. W. & Halle, B. (1980). Ion distributions in Lamellar liquid-crystals – a comparison between results from solutions of the Poisson–Boltzmann equation. *J. phys. Chem.* **84**, 2179.

Kaplanski, G., Famarier, C., Tissot, O., Pierres, A., Benoliel, A.-M., Alessi, A.-C., Kaplanski, S. & Bongrand, P. (1993). Granulocyte–endothelium initial adhesion: analysis of transient binding events mediated by E-selectin in a laminar shear flow. *Biophys. J.* **64**, 1922–1933.

Katrich, V., Bustamante, C. & Olson, W. K. (2000). Pulling chromatin fibers: computer simulations of direct physical micromanipulations. *J. molec. Biol.* **295**, 29–40.

Katsaras, J. (1998). Adsorbed to a rigid substrate, dimyristoylphosphatidylcholine multibilayers attain full hydration in all mesophases. *Biophys. J.* **75**, 2157–2162.

https://doi.org/10.1017/S0033583501003687 Published online by Cambridge University Press

Kauzmann, W. (1959). Some factors in the interpretation of protein denaturation. *Adv. Protein Chem.* **14**, 1–63.

Keller, C. A. & Kasemo, B. (1998). Surface specific kinetics of lipid vesicle adsorption measured with a quartz crystal microbalance. *Biophys. J.* **75**, 1397–1402.

Kellermayer, M., Smith, S. B., Granzier, H. L. & Bustamante, C. (1997). Folding–unfolding transitions in single titin molecules characterized with laser tweezers. *Science* **276**, 1112–1115.

Kendall, K. (1994). Adhesion: molecules and mechanics. *Science* **263**, 1720–1725.

Kjellander, R. & Florin, E. (1981). Water-structure and changes in thermal-stability of the system poly(ethylene oxide)–water. *J. chem. Soc. Faraday Trans. I*, **77**, 2053.

Kjellander, R. & Marcelja, S. (1985a). Polarization of water between molecular-surfaces – a molecular-dynamics study. *Chemica Scripta* **25**, 73–80.

Kjellander, R. & Marcelja, S. (1985b). Perturbation of hydrogen-bonding in water near polar surfaces. *Chem. Phys. Lett.* **120**, 393–396.

Klapper, I., Hagstrom, R., Fine, R., Sharp, K. & Honig, B. (1986). Focusing of electric fields in the active site of Cu–Zn superoxide dismutase: effects of ionic strength and amino acid modification. *Proteins: Structure, Function and Genetics* **1**, 47–59.

Klein, J. (1986). Surface forces with adsorbed polymers: direct measurements and model calculations. *Macromol. Chem. Macromol. Symp.* **1**, 125–137.

Kloboucek, A. B., Faix, J. & Sackmann, E. (1999). Adhesion-induced receptor segregation and adhesion plaque formation: a model membrane study. *Biophys. J.* **77**, 2311–2328.

Kozack, R., d'Mello, M. J. & Subramaniam, S. (1995). Computer modeling of electrostatic steering and orientational effects in antibody–antigen association. *Biophys. J.* **68**, 807–814.

Kramers, H. A. (1940). Brownian motion in a field of force and the diffusion model of chemical reactions. *Physica* **VII**, 284–304.

Kuhl, T. J., Berman, A. D., Hui, S. W. & Israelachvili, J. N. (1998a). Direct measurement of depletion attraction and thin-film viscosity between lipid bilayers in aqueous polyethylene oxide solutions. *Macromolecules* **31**, 8250–8257.

Kuhl, T. J., Leckband, D. E., Lasic, D. D. & Israelachvili, J. N. (1994). Modulation of interaction forces between bilayers exposing short-chained ethylene oxide headgroups. *Biophys. J.* **66**, 1479–1488.

Kuhl, T. L., Guo, Y., Aldferfer, J. L., Berman, A., Leckband, D., Israelachvili, J. & Hui, S. W. (1996). Direct measurement of polyethylene glycol induced depletion attraction between lipid bilayers. *Langmuir* **12**, 3003–3014.

Kuhl, T. L., Leckband, D. E., Lasic, D. D. & Israelachvili, J. N. (1995). Modulation and modeling of interaction forces between lipid bilayers exposing terminally grafted polymer chains. In *CRC Handbook on Stealth Liposomes* (ed. D. L. F. Martin), ch. 8, pp. 73–91. Boca Raton, FL: CRC Press.

Kuhl, T. L., Majewski, J., Wong, J. Y., Steinberg, S., Leckband, D. E., Israelachvili, J. N. & Smith, G. S. (1998b). A neutron reflectivity study of polymer-modified phospholipid monolayers at the solution-solid interface-poly(ethylene glycol)-lipids on silane-modified supports. *Biophys. J.* **75**, 2352–2362.

Kuo, S. & Lauffenburger, D. A. (1993). Relationship between receptor/ligand binding affinity and adhesion strength. *Biophys. J.* **65**, 2191–2200.

Kuo, S. & Sheetz, M. P. (1993). Force of single kinesin molecules measured with optical tweezers. *Science* **260**, 232–234.

Kuzmenka, D. & Granick, S. (1988a). The collapse of poly(ethylene oxide) monolayers. *Macromolecules* **21**, 779–786.

Kuzmenka, D. J. & Granick, S. (1988b). Kinetics of polymer adsorption measured *in situ* at the solid liquid interface – utility of the infrared total internal-reflection method. *Colloids and Surfaces* **31**, 105–116.

Kwok, R. & Evans, E. (1981). Thermoelasticity of large lecithin bilayer vesicles. *Biophys. J.* **35**, 637–652.

Kwong, D., Tees, D. F. J. & Goldsmith, H. L. (1996). Kinetics and locus of failure of receptor ligand-mediated adhesion between latex spheres. II. Protein-protein bond. *Biophys. J.* **71**, 1115–1122.

Landman, U., Luedtke, W. D., Burnham, N. A. & Colton, R. J. (1990). Atomistic mechanisms and dynamics of adhesion, nanoindentation, and fracture. *Science* **248**, 454–461.

Langmuir, I. (1938). The role of attractive and repulsive forces in the formation of tactoids, thixotropic gels, protein crystals and coacervates. *J. chem. Phys.* **6**, 873–896.

Lau, A. W. C., Levine, D. & Pincus, P. (2000). Novel electrostatic attraction from plasmon fluctuations. *Phys. Rev. Lett.* **84**, 4116–4119.

Leckband, D., Chen, Y.-L., Israelachvili, J., Wickman, H. H., Fletcher, M. & Zimmerman, R. (1993). Measurements of conformational changes during adhesion of lipid and protein (polylysine and S-layer) surfaces. *Biotech. & Bioeng.* **42**, 167–177.

Leckband, D. (1995). The surface forces apparatus – a tool for probing molecular protein interactions. *Nature* **376**, 617–618.

Leckband, D. (2000). Measuring the forces that control protein interactions. *Annu. Rev. Biophys. biomol. Struct.* **29**, 1–26.

Leckband, D., Müller, W., Schmitt, F.-J. & Ringsdorf, H. (1995). Molecular mechanisms determining the strength of receptor-mediated intermembrane adhesion. *Biophys. J.* **69**, 1162–1169.

https://doi.org/10.1017/S0033583501003687 Published online by Cambridge University Press

Leckband, D. E., Helm, C. A. & Israelachvili, J. (1992). Role of calcium in the adhesion and fusion of bilayers. *Biochemistry* **32**, 1127–1140.

Leckband, D. E., Kuhl, T. L., Wang, H. K., Müller, W. & Ringsdorf, H. (1995). 4-4-20 anti-fluorescyl IgG Fab′ recognition of membrane bound hapten: direct evidence for the role of protein and interfacial structure. *Biochemistry* **34**, 11467–11478.

Leckband, D. E., Schmitt, F.-J., Israelachvili, J. N. & Knoll, W. (1994). Direct force measurements of specific and nonspecific protein interactions. *Biochemistry* **33**, 4611–4624.

Lee, G., Kidwell, D. A. & Colton, R. J. (1994). Sensing discrete streptavidin–biotin interactions with atomic force microscopy. *Langmuir* **10**, 354–357.

Leikin, S., Parsegian, V. A., Rau, D. C. & Rand, R. P. (1993). Hydration forces. *Annu. Rev. phys. Chem.* **44**, 369–395.

LeNeveu, D. M., Rand, R. P. & Parsegian, V. A. (1976). Measurement of forces between lecithin bilayers. *Nature* **259**, 601–603.

Leuedtke, W. D. & Landman, U. (1992). Solid and liquid junctions. *Computational Mat. Sci.* **1**, 1–24.

Leung, K. & Luzar, A. (2000). Dynamics of capillary evaporation. II. Free energy barriers. *J. chem. Phys.* **113**, 5845–5852.

Lifschitz, E. (1956). *Soviet Phys. JETP* (English trans.) **2**, 73–83.

Lindermann, J. & Lauffenburger, D. A. (1993). *Receptors*. Oxford: Oxford University Press.

Lis, L., McAlister, M., Fuller, N. L., Rand, R. P. & Parsegian, V. A. (1982). Interactions between neutral phospholipid–bilayer membranes. *Biophys. J.* **37**, 657–666.

London, F. (1937). The general theory of molecular forces. *Trans. Faraday Soc.* **33**, 8–26.

Lu, H., Isralewitz, B., Krammer, A., Vogel, V. & Schulten, K. (1998). Unfolding of titin immunoglobulin domains by steered molecular dynamics simulation. *Biophys. J.* **75**, 662–671.

Luengo, G., Pan, J.-M., Heuberger, M. & Israelachvili, J. N. (1998). Temperature and time effects on the 'adhesion dynamics' of poly-butyl methacrylate (PBMA) surfaces. *Langmuir* **14**, 3873–3881.

Lum, K., Chandler, D. & Weeks, J. D. (1999). Hydrophobicity at small and large length scales. *J. phys. Chem.* **103**, 4570–4577.

Luzar, A., Bratko, D. & Blum, L. (1987). Monte-Carlo simulation of hydrophobic interaction. *J. chem. Phys.* **86**, 2955–2959.

Luzar, A. & Leung, K. (2000). Dynamics of capillary evaporation. I. Effect of morphology of hydrophobic surfaces. *J. chem. Phys.* **113**, 5836–5844.

Lyle, I. G. & Tiddy, G. J. T. (1986). Hydration forces between surfactant bilayers – an equilibrium binding description. *Chem. Phys. Lett.* **124**, 432–436.

Madura, J. D., Briggs, J. M., Wade, R. C., Davis, M. E., Luty, B. A., Ilin, A., Antosiewicz, J., Gilson, M., Bagheri, B., Scott, L. R. & McCammon, J. A. (1995). Electrostatics and diffusion of molecules in solution: simulations with the University of Houston Brownian Dynamics Program. *Computer Physics Commun.* **91**, 57–95.

Mahanty, J. & Ninham, B. W. (1976). *Dispersion Forces*. New York: Academic Press.

Majewski, J., Wong, J. Y., Park, C. K., Seitz, M., Israelachvili, J. N. & Smith, G. S. (1998). Structural studies of polymer-cushioned lipid bilayers. *Biophys. J.* **75**, 2363–2367.

Mangipudi, V., Tirrell, M. & Pocius, A. V. (1995). Direct measurement of the surface-energy of corona-treated polyethylene using the Surface Forces Apparatus. *Langmuir* **11**, 19–23.

Manning, G. S. (1969). Limiting laws and counterion condensation in polyelectrolyte solutions. I. Colligative properties. *J. chem. Phys.* **51**, 924–933.

Marcelja, S. (1997). Effects of ion hydration in double layer interaction. *Colloids and Surfaces A* **130**, 321–326.

Markova, N., Sparr, E., Wadso, L. & Wennerstrom, H. (2000). A calorimetric study of phospholipid hydration. Simultaneous monitoring of enthalpy and free energy. *J. phys. Chem. B* **104**, 8053–8060.

Marra, J. (1985). Controlled deposition of lipid monolayers and bilayers onto mica and direct force measurements between galactolipid bilayers in aqueous-solutions. *J. Colloid Interface Sci.* **107**, 446–458.

Marra, J. (1986a). Effects of counterion specificity on the interactions between quaternary ammonium surfactants in monolayers and bilayers. *J. phys. Chem.* **90**, 2145–2150.

Marra, J. (1986b). Direct measurement of the interaction between phospatidylglycerol bilayers in aqueous-electrolyte solutions. *Biophys. J.* **50**, 815–825.

Marra, J. & Israelachvili, J. N. (1985). Direct measurements of forces between phosphatidylcholine and phosphatidylethanolamine bilayers in aqueous electrolyte solutions. *Biochemistry* **24**, 4608–4618.

Marsh, D. (1989). Water adsorption isotherms and hydration forces for lysolipids and diacyl phospholipids. *Biophys. J.* **55**, 1093–1100.

Marszalek, P., Lu, H., Li, H., Carrion-Vazquez, M., Oberhauser, A. F., Schulten, K. & Fernandez, J. M. (1999). Mechanical unfolding intermediates in titin modules. *Nature* **402**, 100–103.

McCammon, A. J. (1998). Theory of biomolecular recognition. *Curr. Opin. struct. Biol.* **8**, 245–249.

McCammon, J. & Harvey, S. (1987). *Dynamics of Proteins and Nucleic Acids*. New York: Cambridge University Press.

McFarlane, J. S. & Tabor, D. (1950). Adhesion of solids and the effect of surface films. *Proc. R. Soc. Lond. A* **202**, 224–243.

https://doi.org/10.1017/S0033583501003687 Published online by Cambridge University Press

McGuiggan, P. M. & Israelachvili, J. N. (1990). Adhesion and short-range forces between surfaces. Part II: Effects of surface lattice mismatch. *J. Mater. Res.* **5**, 2232–2243.

McIntosh, T. J. & Simon, S. A. (1986). Hydration force and bilayer deformation – a reevaluation. *Biochemistry* **25**, 4058–4066.

McIntosh, T. J. & Simon, S. A. (1994). Hydration and steric pressures between phospholipid-bilayers. *Annu. Rev. Biophys. biomol. Struct.* **23**, 27–51.

McIntosh, T. J., Simon, S. A., Needham, D. & Huang, C. H. (1992a). Structure and cohesive properties of sphingomyelin cholesterol bilayers. *Biochemistry* **31**, 2012–2020.

McIntosh, T. J., Simon, S. A., Needham, D. & Huang, C. H. (1992b). Interbilayer interactions between sphingomyelin and sphingomyelin cholesterol bilayers. *Biochemistry* **31**, 2020–2024.

Mehta, A., Rief, M., Spudich, J. A., Smith, D. A. & Simmons, R. A. (1999). Single-molecule biomechanics with optical methods. *Science* **283**, 1689–1695.

Merkel, R., Nassoy, P., Leung, A., Ritchie, K. & Evans, E. (1999). Energy landscapes of receptor-ligand bonds explored with dynamic force spectroscopy. *Nature* **397**, 50–53.

Moy, V., Jiao, Y., Hillmann, T., Lehmann, H. & Sano, T. (1999). Adhesion energy of receptor-mediated interaction measured by elastic deformation. *Biophys. J.* **76**, 1632–1638.

Moy, V. T., Florin, E.-L. & Gaub, H. E. (1994). Intermolecular forces and energies between ligands and receptors. *Science* **266**, 257–259.

Murphy, F., Sweet, R. M. & Churchill, M. E. A. (1999). The structure of a chromosomal high mobility group protein–DNA complex reveals sequence-neutral mechanisms important for non-sequence-specific DNA recognition. *EMBO J.* **18**, 6610–6618.

Murray, D., Ben-Tal, N., Honig, B. & McLaughlin, S. (1997). Electrostatic interaction of myristoylated proteins with membranes: simple physics, complicated biology. *Structure* **5**, 985–989.

Nardi, J., Feder, T., Bruinsma, R. & Sackmann, E. (1997). Electrostatic adhesion between fluid membranes-phase separation and blistering. *Europhys. Lett.* **38**, 159–160.

Ninham, B. W. & Parsegian, V. A. (1971). Electrostatic potential between surfaces bearing ionizable groups in ionic equilibrium with physiologic saline solution. *J. theor. Biol.* **31**, 405.

Noppl-Simson, D. A. & Needham, D. (1996). Avidin–biotin interactions at vesicle surfaces: adsorption and binding, cross-bridge formation, and lateral interactions. *Biophys. J.* **70**, 1391–1401.

Northrup, S., Sllison, S. A. & McCammon, J. A. (1984). Brownian dynamics simulation of diffusion-influenced bimolecular reactions. *J. chem. Phys.* **80**, 1517–1524.

Ohnuchic, J., Wolynes, P. G., Luthey-Schulten, Z. & Socci, N. D. (1995). Toward an outline of the topography of a realistic protein-folding funnel. *Proc. natn. Acad. Sci. USA* **92**, 3626–3630.

Ohshima, H. (1994). Electrostatic interaction between two dissimilar spheres: an explicit analytic expression. *J. Colloid Interface Sci.* **162**, 487–495.

Ohshima, H. (1995). Electrostatic interaction between two dissimilar spheres with constant surface charge density. *J. Colloid Interface Sci.* **170**, 432–439.

Ohshima, H., Chan, D. Y. C., Healy, T. W. & White, L. R. (1983). Improvement on the Hogg–Healy–Fuerstenau Formulas for the interaction of dissimilar double layers II. Curvature correction to the formula for the interaction of spheres. *J. Colloid Interface Sci.* **92**, 232–242.

Onsager, L. (1949). The effects of shape of the interaction of colloidal particles. *Ann. NY Acad. Sci.* **51**, 627–659.

Paci, E. & Karplus, M. (2000). Unfolding proteins by external forces and temperature: The importance of topology and energetics. *Proc. natn. Acad. Sci. USA* **97**, 6521–6526.

Parsegian, V. A. & Brenner, S. L. (1976). The role of long range forces in ordered arrays of tobacco mosaic virus. *Nature* **259**, 632–635.

Parsegian, V. A., Fuller, N. & Rand, R. P. (1979). Measured work of deformaiton and repulsion of lecithin bilayers. *Proc. natn. Acad. Sci. USA* **76**, 2750–2754.

Pashley, R. M. & Israelachvili, J. N. (1984). Molecular layering of water in thin films between mica surfaces and its relation to hydration forces. *J. Colloid Interface Sci.* **101**, 511–523.

Patel, S. S. & Tirrell, M. (1989). Measurement of forces between surfaces in polymer fluids. *Annu. Rev. Phys. Chem.*, 40.

Peachey, J., VanAlsten, J. & Granick, S. (1991). Design of an apparatus to measure the shear response of ultrathin liquid-films. *Rev. Sci. Instrum.* **62**, 463–473.

Peitzsch, R. M., Eisenberg, M., Sharp, K. A. & McLaughlin, S. (1995). Calculations of the electrostatic potential adjacent to model phospholipid bilayers. *Biophys. J.* **68**, 729–738.

Pelham, R. J. & Wang, Y. L. (1997). Cell locomotion and focal adhesions are regulated by substrate flexibility. *Proc. natn. Acad. Sci. USA* **94**, 13661–13665.

Persson, P. K. T. & Bergenstahl, B. A. (1985). Repulsive forces in lecithin glycol lamellar phases. *Biophys. J.* **47**, 743–746.

Petsev, D., Thomas, B. R., Yau, S. T. & Vekilov, P. G. (2000). Interactions and aggregation of apoferritin molecules in solution effects of added electrolytes. *Biophys. J.* **78**, 2060–2069.

https://doi.org/10.1017/S0033583501003687 Published online by Cambridge University Press

Petsev, D. N. & Vekilov, P. G. (2000). Evidence for non-DLVO hydration interactions in solutions of the protein apoferritin. *Phys. Rev. Lett.* **84**, 1339–1342.

Pfeiffer, W. H., Sackmann, E., Knoll, W. & Richter, D. (1989). Local dynamics of lipid bilayers studied by incoherent quasi-elastic neutron-scattering. *Europhys. Lett.* **8**, 201–206.

Pierres, A., Benoliel, A.-M. & Bongrand, P. (1995). Measuring the lifetime of bonds made between surface-linked molecules. *J. biol. Chem.* **270**, 26586–26592.

Pierres, A., Benoliel, A. M., Bongrand, P. & VanderMerwe, A. P. (1996). Determination of the lifetime and force dependence of interactions of single bonds between surface-attached CD2 and CD48 adhesion molecules. *Proc. natn. Acad. Sci. USA* **93**, 15114–15118.

Pincet, F., Perez, E., Bryant, G., Lebeau, L. & Mioskowski, C. (1994). Long-range attraction between nucleosides with short-range specificity: direct measurements. *Phys. Rev. Lett.* **73**, 2780–2783.

Pincus, P. (1976). Excluded volume effects and stretched polymer chains. *Macromolecules* **8**, 386–388.

Pincus, P. (1977). Dynamics of stretched polymer chains. *Macromolecules* **9**, 386–388.

Ploehn, H. J. & Russel, W. B. (1990). Interactions between colloidal particles and soluble polymers. *Adv. chem. Eng.* **15**, 137–227.

Podgornik, R. J., Rau, D. C. & Parsegian, V. A. (1989). The action of interhelical forces on the organization of DNA double helices – fluctuation-enhanced decay of electrostatic double-layer and hydration forces. *Macromolecules* **22**, 1780–1786.

Pollock, H. M., Barquins, M. & Maugis, D. (1978). The force of adhesion between solid surfaces in contact. *Appl. Phys. Lett.* **33**, 798–799.

Portigliatti, M., Koutsos, V., Hervet, H. & Leger, L. (2000). Adhesion and deformation of a single latex particle. *Langmuir* **16**, 6374–6376.

Poste, G. & Nicholson, G. L. (1978). *Membrane Fusion*. Amsterdam: North Holland.

Prieve, D. & Alexander, B. M. (1986). Hydrodynamic measurement of double-layer repulsion between colloidal particle and flat-plate. *Science* **231**, 1269–1273.

Prieve, D. & Frej, N. A. (1990). Total internal-reflection microscopy – a quantitative tool for the measurement of colloidal forces. *Langmuir* **6**, 396–403.

Prieve, D. C. (1999). Measurement of colloidal forces with TIRM. *Adv. Coll. Int. Sci.* **82**, 93–125.

Rädler, J. & Sackmann, E. (1992). On the measurement of weak repulsive and frictional colloidal forces by Reflection Interference Contrast Microscopy. *Langmuir* **8**, 848–853.

Ramsden, J. J. (1995). Puzzles and paradoxes in protein adsorption. *Chem. Soc. Rev.* **24**, 73–78.

Rand, R. P. & Parsegian, V. A. (1989). Hydration forces between phospholipid-bilayers. *Biochim. biophys. Acta* **988**, 351–376.

Rau, D. C., Lee, B. & Parsegian, V. A. (1984). Measurement of the repulsive force between polyelectrolyte molecules in ionic solution – hydration forces between parallel DNA double helices. *Proc. natn. Acad. Sci. USA* **81**, 2621–2625.

Raucher, D. & Sheetz, M. P. (1999). Characteristics of a membrane reservoir buffering membrane tension. *Biophys. J.* **77**, 1992–2002.

Richetti, P. & Kekicheff, P. (1992). Direct measurement of depletion and structural forces in a micellar system. *Phys. Rev. Lett.* **68**, 1951–1954.

Rief, M., Gautel, M., Oesterhelt, F., Fernandez, J. M. & Gaub, H. E. (1997a). Reversible unfolding of individual titin immunoglobulin domains by AFM. *Science* **276**, 1109–1116.

Rief, M., Gautel, M., Schemmel, A. & Gaub, H. E. (1998). The mechanical stability of immunoglobulin and fibronectin III domains in the muscle protein titin measured by atomic force microscopy. *Biophys. J.* **75**, 3008–3014.

Rief, M., Oesterhelt, F., Heymann, B. & Gaub, H. E. (1997b). Single molecule force spectroscopy on polysaccharides by atomic force microscopy. *Science* **275**, 1295–1297.

Rief, M., Pascuel, J., Saraste, M. & Gaub, H. E. (1999). Single molecule force spectroscopy of spectrin repeats: Low unfolding forces in helix bundles. *J. molec. Biol.* **286**, 553–561.

Rodahl, M., Hook, F., Krozer, A., Brzezinski, P. & Kasemo, B. (1995). Quartz-crystal microbalance setup for frequency and Q-factor measurements in gaseous and liquid environments. *Rev. Sci. Instrum.* **66**, 3924–3930.

Rodgers, K. K., Pochapsky, T. C. & Sligar, S. G. (1988). Probing the mechanisms of macromolecular recognition: the cytochrome b5–cytochrome c complex. *Science* **240**, 1657–1659.

Rosenthal, P., Zhang, X. D., Formanowski, F., Fitz, W., Wong, C. H., Meierewert, H., Skehel, J. J. & Wiley, D. C. (1998). Structure of the haemagglutinin-esterase-fusion glycoprotein of Influenza C virus. *Nature* **396**, 92–96.

Rouzina, I. & Bloomfield, V. A. (1996). Macroion attraction due to electrostatic correlation between screening counterions. 1. Mobile surface-adsorbed ions and diffuse ion cloud. *J. phys. Chem.* **100**, 9977–9989.

Ruths, M., Israelachvili, J. N. & Ploehn, H. J. (1997). Effects of time and compression on the interactions of adsorbed polystyrene layers in a near-θ solvent. *Macromolecules* **30**, 3329–3339.

Sackmann, E. (1996). Supported membranes: scientific and practical applications. *Science* **271**, 43–48.

https://doi.org/10.1017/S0033583501003687 Published online by Cambridge University Press

Saenger, W. (1984). *Principles of Nucleic Acid Structure*. New York: Springer.

Saterbak, A. & Lauffenburger, D. A. (1996). Adhesion mediated by bonds in series. *Biotechnol. Prog.* **12**, 682–699.

Schmidtke, D. W. & Diamond, S. L. (2000). Direct observation of membrane tethers formed during neutrophil attachment to platelets or P-selectin under physiological flow. *J. Cell Biol.* **149**, 719–729.

Schmitz, K., Holcomb-Wygle, D. L., Oberski, D. J. & Lindermann, C. B. (2000). Measurement of the force produced by an intact bull sperm flagellum in isometric arrest and estimation of the dynein stall force. *Biophys. J.* **79**, 468–478.

Schneider, J., Berndt, P., Haverstick, K., Kumar, S., Chiruvolu, S. & Tirrell, M. (1998). Force and adhesion measurements between hydrogen-bonded layers of glycine-functionalized amphiphiles. *J. Am. chem. Soc.* **120**, 3508–3509.

Schneider, J. & Tirrell, M. (1999). Direct measurement of molecular level forces and adhesion in biological systems. *Bioadhesive Drug Delivery Systems: Fundamentals, Novel Approaches, and Development* **98**, 223–256.

Seifert, U. (2000). Rupture of multiple parallel bonds under dynamic loading. *Phys. Rev. Lett.* **84**, 2750–2753.

Seitz, M., Ter-Ovanesyan, E., Hausch, M., Park, C. K., Zasadzinski, J., Zentel, R. & Israelachvili, J. N. (2000). Formation of tethered supported bilayers by vesicle fusion onto lipopolymer monolayers promoted by osmotic stress. *Langmuir* **16**, 6067–6070.

Seitz, M., Wong, J. Y., Park, C. K., Alcantar, N. A. & Israelachvili, J. (1998). Formation of tethered supported bilayers via membrane-inserting reactive lipids. *Thin Solid Films* **329**, 767–771.

Servuss, R. M. & Helfrich, W. (1989). Mututal adhesion of lecithin membranes at ultralow tensions. *J. Phys. France* **50**, 809–827.

Sharp, K. A. & Honig, B. (1990). Electrostatic interactions in macromolecules: theory and applications. *Annu. Rev. biophys. Biophys. Chem.* **19**, 302–332.

Shatzky-Schwartz, M., Arbuckle, N. D., Eisenstein, M., Rabinovich, D., Baraket-Samish, A., Haran, T. E., Luisi, B. F. & Shakked, Z. (1997). X-ray and solution studies of DNA oligomers and implications for the structural basis of A-tract-dependent curvature. *J. molec. Biol.* **267**, 595–603.

Sheth, S., Efremova, N. & Leckband, D. (2000). Interactions of poly(ethylene oxide) brushes with chemically selective surfaces. *J. phys. Chem. B* **104**, 7652–7662.

Sheth, S. R. & Leckband, D. (1997). Measurements of attractive forces between proteins and end-grafted poly(ethylene glycol) chains. *Proc. natn. Acad. Sci. USA* **94**, 8399–8404.

Shklovskii, B. I. (1999). Wigner crystal model of counterion induced bundle formation of rodlike polyelectrolytes. *Phys. Rev. Lett.* **82**, 3268–3271.

Shoemaker, B., Portman, J. J. & Wolynes, P. G. (2000). Speeding molecular recognition by using the folding funnel: The fly-casting mechanism. *Proc. natn. Acad. Sci. USA* **97**, 8868–8873.

Shubin, V. E. & Kékicheff, P. (1993). Electrical double layer structure revisited via a surface force apparatus: mica interfaces in lithium nitrate solutions. *J. Colloid Interface Sci.* **155**, 108–123.

Simson, R., Wallraff, E., Faix, J., Niewohner, J., Gerisch, G. & Sackmann, E. (1998). Membrane bending modulus and adhesion energy of wild-type and mutant cells of *Dictyostelium* lacking talin or cortexillins. *Biophys. J.* **74**, 514–522.

Sivasankar, S., Brieher, W., Lavrik, N., Gumbiner, B. & Leckband, D. (1999). Direct molecular force measurements of multiple adhesive interactions between cadherin ectodomains. *Proc. natn. Acad. Sci. USA* **96**, 11820–11824.

Sivasankar, S., Gumbiner, B. & Leckband, D. E. (2001). Direct measurements of multiple adhesive alignments and unbinding trajectories between cadherin extracellular domains. *Biophys. J.*, in press.

Sivasankar, S., Subramaniam, S. & Leckband, D. (1998). Direct molecular level measurements of the electrostatic properties of a protein surface. *Proc. natn. Acad. Sci. USA* **95**, 12961–12966.

Skehel, J. J. & Wiley, D. C. (1998). Coiled coils in both intracellular vesicle and viral membrane fusion. *Cell* **95**, 871–874.

Socci, N., Onuchic, J. N. & Wolynes, P. G. (1999). Stretching lattice models of protein folding. *Proc. natn. Acad. Sci. USA* **96**, 2031–2035.

Soto, G. & Hultgren, S. J. (1999). Bacterial adhesins: common themes and variations in architecture and assembly. *J. Bacteriol.* **181**, 1059–1071.

Sowers, A. E. (1987). *Cell Fusion*. New York: Plenum.

Stayton, P., Olinger, J. M., Jiang, M., Bohn, P. W. & Sligar, S. G. (1992). Genetic engineering of surface attachment sites yields oriented protein monolayers. *J. Am. chem. Soc.* **114**, 9298–9299.

Sterba, M. & Sheetz, M. P. (1998). Basic laser tweezers. *Methods Cell Biol.* **55**, 29–41.

Strunz, R., Oroszlan, K., Schäfer, R. & Güntherodt, H. J. (1999). Dynamic force spectroscopy of single DNA molecules. *Proc. natn. Acad. Sci. USA* **96**, 11277–11282.

Stuart, J. & Hlady, V. (1995). Effects of discrete protein surface interactions in Scanning Force Microscopy. *Langmuir* **11**, 1368–1374.

Sutton, R., Fasshauer, D., Jahn, R. & Brunger, A. T. (1998). Crystal structure of a SNARE complex

https://doi.org/10.1017/S0033583501003687 Published online by Cambridge University Press

involved in synaptic exocytosis at 2·4 Angstrom resolution. *Nature* **395**, 347–353.

Svoboda, K. & Block, S. M. (1994). Biological applications of optical forces. *Annu. Rev. Biophys. biomolec. Struct.* **23**, 247–285.

Svoboda, K., Schmidt, C. F., Schnapp, B. J. & Block, S. M. (1993). Direct observation of kinesin stepping by optical trapping interferometry. *Nature* **365**, 721–727.

Swift, D. G., Posner, R. G. & Hammer, D. A. (1998). Kinetics of adhesion of IgE-sensitized rat basophilic leukemia cells to surface-immobilized antigen in couette flow. *Biophys. J.* **75**, 2597–2611.

Tanford, C. (1980). *The Hydrophobic Effect*. New York: John Wiley & Sons.

Tarazona, P. & Vichente, L. (1985). A model for the density oscillations in liquids between solid walls. *Mol. Phys.* **56**, 557–572.

Tees, D., Waugh, R. E. & Hammer, D. A. (2001). A microcantilever device to assess the effect of force on the lifetime of selectin–carbohydrate bonds. *Biophys. J.* **80**, 668–682.

Tees, D. F., Coenen, O. & Goldsmith, H. L. (1993). Interaction forces between red cells agglutinated by antibody. IV. Time and force dependence of breakup. *Biophys. J.* **65**, 1318–1334.

Tees, D. F. J. & Goldsmith, H. L. (1996). Kinetics and locus of failure of receptor–ligand mediated adhesion between latex spheres. I. Protein-carbohydrate bond. *Biophys. J.* **50**, 1109–1116.

Tirrell, M. (1996). Measurement of interfacial energy at solid polymer surfaces. *Langmuir* **12**, 4548–4551.

Tirrell, M., Falsafi, A., Deprez, P. & Bates, F. S. (1997). Direct measurement of adhesion between viscoelastic polymers: a contact mechanical approach. *J. Rheology* **41**, 1349–1364.

Tolansky, S. (1948). *Multiple Beam Interferometry of Surfaces and Films*. Oxford University Press.

Tolansky, S. (1955). *An Introduction to Interferometry*. London: Longmans, Green & Co.

Tskhovrebova, L., Trinick, J., Sleep, J. A. & Simmons, R. M. (1997). Elasticity and unfolding of single molecules of the giant muscle protein titin. *Nature* **387**, 308–312.

Tucker, E. E., Lane, E. H. & Christian, S. D. (1981). Vapor-pressure studies of hydrophobic interactions – formation of benzene–benzene and cyclohexane–cyclohexanol dimers in dilute aqueous-solutions. *J. Solution Chem.* **10**, 1–20.

Verwey, E. J. W. & Overbeek, J. T. G. (1948). *Theory of the Stability of Lyophobic Colloids*, 1st edn. Amsterdam: Elsevier Publishing Co.

Viani, B. E., Low, P. F. & Roth, C. B. (1983). Direct measurement of the relation between interlayer force and interlayer distance in the swelling of montmorillonites. *J. Colloid Interface Sci.* **96**, 229.

Viani, M., Schaffer, T. E., Chanad, A., Rief, M., Gaub, H. E. & Hansma, P. K. (1999a). Small cantilevers for force spectroscopy of single molecules. *J. appl. Phys.* **86**, 2258–2262.

Viani, M., Schaffer, T. E., Palocai, G. T., Pietrasanta, L. I., Smith, B. L., Thompson, J. B., Rief, M., Gaug, H. E., Plaxco, K. W., Cleland, A. N., Hansma, H. G. & Hansma, P. K. (1999b). Fast imaging and fast force spectroscopy of single biopolymers with a new atomic force microscope designed for small cantilevers. *Rev. Sci. Instr.* **70**, 4300–4303.

Vigil, G., Xu, Z., Steinberg, S. & Israelachvili, J. (1994). Interactions of silica surfaces. *J. Colloid Interface Sci.* **165**, 367–385.

Vijayendran, R., Hammer, D. & Leckband, D. (1998). Simulations of the adhesion between molecularly bonded surfaces in direct force measurements. *J. chem. Phys.* **108**, 7783–7793.

Visscher, K., Gross, S. P. & Block, S. M. (1996). Construction of multiple-beam optical traps with nanometer-resolution position sensing. *IEEE J. Selected Top. Quant. Electron.* **2**, 1066–1076.

Visscher, K., Schnitzer, M. J. & Block, S. M. (1999). Single kinesin molecules studied with a molecular force clamp. *Nature* **400**, 184–189.

Voet, D. & Voet, J. G. (1995). *Biochemistry*. Somerset, NJ: John Wiley & Sons.

Walker, S. A., Kennedy, M. T. & Zasadzinski, J. A. (1997). Encapsulation of bilayer vesicles by self-assembly. *Nature* **387**, 61–64.

Walker, S. A. & Zasadzinski, J. A. (1997). Electrostatic control of spontaneous vesicle aggregation. *Langmuir* **13**, 5076–5081.

Wang, M. D., Schnitzer, M. J., Yin, H., Landick, R., Gelles, J. & Block, S. M. (1998). Force and velocity measured for single molecules of RNA polymerase. *Science* **282**, 902–907.

Wendoloski, J. J., Matthew, J. B., Weber, P. C. & Salemme, F. R. (1987). Molecular dynamics of a cytochrome c–cytochrome b5 electron transfer complex. *Science* **238**, 794–797.

Wiener, M. C. & White, S. H. (1992). Structure of a fluid dioleoylphosphatidylcholine bilayer determined by joint refinement of X-ray and neutron-diffraction data 3. Complete structure. *Biophys. J.* **61**, 434–447.

Wong, J. Y., Kuhl, T. J., Israelachvili, J. N., Mullah, N. & Zalipsky, S. (1997). Direct measurement of a tethered ligand–receptor interaction potential. *Science* **275**, 820–822.

Wong, J. Y., Majewski, J., Seitz, M., Park, C. K., Israelachvili, J. N. & Smith, G. S. (1999a). Polymer-cushioned bilayers – I. A structural study of various preparation methods using Neutron Reflectometry. *Biophys. J.* **77**, 1445–1457.

https://doi.org/10.1017/S0033583501003687 Published online by Cambridge University Press

Wong, J. Y., Park, C. K., Seitz, M. & Israelachvili, J. (1999b). Polymer-cushioned bilayers – II. An investigation of interaction forces and fusion using the Surface Forces Apparatus. *Biophys. J.* **77**, 1458–1468.

Wong, S. S., Joselevich, E., Woolley, A. T., Cheung, C. L. & Lieber, C. M. (1998). Covalently functionalized nanotubes as nanometre-sized probes in chemistry and biology. *Nature* **394**, 52–54.

Xu, C., Guild, J., Webb, W. W. & Denk, W. (1995). Determination of absolute two-photon excitation cross sections by *in situ* second-order autocorrelation. *Optics Lett.* **20**, 2372–2374.

Xu, Z. & Yoon, R.-H. (1989a). The role of hydrophobic interactions in coagulation. *J. Colloid Interface Sci.* **132**, 532–541.

Xu, Z. & Yoon, R.-H. (1989b). A study of hydrophobic coagulation. *J. Colloid Interface Sci.* **134**, 427–434.

Yeung, C. & Leckband, D. (1997). Molecular level characterization of microenvironetal influences on the properties of immobilized proteins. *Langmuir* **13**, 6746–6754.

Yeung, C., Purves, T., Kloss, A., Sligar, S. & Leckband, D. (1999). Cytochrome c recognition of immobilized, orientational variants of cytochrome b5: direct force and equilibrium binding measurements. *Langmuir* **15**, 6829–6836.

Yoneda, M. (1960). Force exerted by a single cilium of *Mytilus edulis I. J. exp. Biol.* **37**, 461–468.

Yoon, R.-H., Flinn, D. H. & Rabinovich, Y. I. (1997). Hydrophobic interactions between dissimilar surfaces. *J. Colloid Interface Sci.* **185**, 363–370.

Zacharias, M., Luty, B. A., Davis, M. E. & McCammon, J. A. (1992). Poisson–Boltzmann analysis of the λ repressor–operator interaction. *Biophys. J.* **63**, 1280–1285.

Zasadzinski, J. (1997). Novel approaches to lipid-based drug delivery. *Curr. Opin. Solid State. Mater. Sci.* **2**, 345–349.

Zilker, A., Ziegler, M. & Sackmann, E. (1992). Spectral analysis of erythrocyte flickering in the 0·3–0·4 μm–1 regime by microinterferometry combined with fast image processing. *Phys. Rev. A* **46**, 7998–8001.

https://doi.org/10.1017/S0033583501003687 Published online by Cambridge University Press